Spring 2002

Development of icejet-based surface processing technology

Dimitri V. Shishkin
New Jersey Institute of Technology

ABSTRACT

DEVELOPMENT OF ICEJET-BASED SURFACE PROCESSING TECHNOLOGY

by
Dimitri V. Shishkin

The objective of the proposed work is to acquire knowledge needed for the development and deployment of manufacturing processes utilizing the enormous technological potential of water ice. Material removal by blasting with ice media such as particles, pellets and slugs was investigated. The ice media was accelerated by entrainment in a fluid stream (air, steam, liquid water, supercritical CO_2), impact of rotating blades, fluid expansion, etc. The ice-airjet has to replace sand blasting and the ice-waterjet has to replace the abrasive waterjet. Based on these results, technical approaches for surface processing and machining will be improved. A primary advantage of the ice media is movement toward more complete pollution prevention. With this technique, it is possible to eliminate both contamination of the substrate and generation of contaminated waste streams. In addition to the obvious environmental benefits, use of ice media has improved a number of key operational techniques, such as cleaning, decoating, polishing, deburring, drilling, cutting, etc.

Production of ice media "just-in-time" at minimal environmental cost constitutes another advantage of ice-based technologies. A key objective of this research is to improve ice blasting so that it is not just feasible, but also technologically and economically efficient. An understanding of process physics and its application to the manufacturing operations are necessary in order to attain this objective. The feasibility

and effectiveness of other than blasting ice-based technologies, such as precision temperature control, mixing, forming, etc. was also investigated.

The principal issue in the use of the ice abrasives is formation of the ice particles. Two technologies of the particles formation were investigated. One of these technologies involves crushing and subsequent grinding of ice blocks. It is applicable at conditions when ice is readily available, for example at Arctic. Another process involved integration of water freezing and decomposition of the generated ice. It was shown that the size distribution of the particles is determined by the rate of the water supply and cooling conditions.

The results of the experiments were used to suggest a technology for surface processing using ice powder. A process for formation of the powder of brittle materials was also discussed.

DEVELOPMENT OF ICEJET-BASED SURFACE PROCESSING TECHNOLOGY

by
Dimitri V. Shishkin

A Dissertation
Submitted to the Faculty of
New Jersey Institute of Technology
in Partial Fulfillment of the Requirements for the Degree of
Doctor of Philosophy in Mechanical Engineering

Department of Mechanical Engineering

May 2002

APPROVAL PAGE

DEVELOPMENT OF ICEJET-BASED SURFACE PROCESSING TECHNOLOGY

Dmitri V. Shishkin

Dr. Ernest S. Geskin, Dissertation Adviser — Date
Professor of Mechanical Engineering, NJIT

Dr. Bernard Koplik, Committee Member — Date
Professor of Mechanical Engineering, NJIT

Dr. Raj Sodhi, Committee Member — Date
Associate Professor of Mechanical Engineering, NJIT

Dr. Zhiming Ji, Committee Member — Date
Associate Professor of Mechanical Engineering, NJIT

Dr. Sanchoy Das, Committee Member — Date
Professor of Industrial and Manufacturing Engineering, NJIT

BIOGPAPHICAL SCETCH

Author: Dimitri V. Shishkin

Degree: Doctor of Philosophy

Date: May 2002

Undergraduate and Graduate Education:

- Doctor of Philosophy in Mechanical Engineering
  New Jersey Institute of Technology, Newark, NJ, 1999
- Master of Science in Mechanical Engineering
  New Jersey Institute of Technology, Newark, NJ, 1999
- Master of Science in Electrical Engineering
  Krivoy Rog Technical University, Ukraine, 1995
- Bachelor of Science in Electrical Engineering
  Krivoy Rog Technical University, Ukraine, 1994

Major: Mechanical Engineering

Presentations and publications:

E. Geskin, Tismenetskiy, E. F. Li, D. Shishkin, Investigation of Icejet Machining, *Proceedings of 1997 NSF Design and Manufacturing Grantees Conference*, Seattle, 1997.

E. Geskin, L. Tismenetskiy, F. Li, P. Meng and D. Shishkin, Investigation of Icejet Machining, *Proceedings of 9th American Waterjet Conference*, Houston, TX August 1997, pp. 281-290.

E. Geskin, L. Tismenetskiy, D. Shishkin, "Development of a robotic system for cleaning of chemical reactors", *Proceedings of the 9th American Waterjet Conference*, Houston, Texas, August 1997, pp. 631- 644.

E. Geskin, D. Watts, L. Tismenetskiy, E. Bachromi, and D. Shishkin, "Testing of the waterjet based system for reactors cleaning", *Proceeding of the 14th International Conference on JETTING TECHNOLOGY*, Brugge, Belgium, September 1998, pp. 535-544.

E. Geskin, D. Shishkin, K. Babets, *Ice, Cryogenic and Polymer Added Jets* ", Chapter in the Book, "Abrasive Water Jet, a View on Future", published by Institute for Industrial Technologies and Automation, June 1999.

E. Geskin, D. Shishkin, K. Babets, Investigation of Ice Jet Machining, *Proceedings of 1999 NSF Design and Manufacturing Grantees Conference*, Long Beach, January 1999.

E. Geskin, B. Goldenberg, D. Shishkin, K. Babets, O. Petrenko, "Water Based Machining Technology", 6th Annual Exhibition of The Coalition for National Science Funding, Rayburn House Office Building, Washington, DC, May 2000.

E. Geskin, D. Shishkin, K. Babets," Ice, Cryogenic and Polymer Added Jets," Chapter in the book Abrasive Waterjet, A View on Future, Italian Institute of for Industrial Automation and Technology, Milan, 1999.

D. Shishkin, E. Geskin, K. Babets, Application of Ice Particles for Precision Cleaning of Sensitive Surfaces, *International Symposium On Surface Contamination and Cleaning*, Newark, NJ, May 2001.

D. Shishkin, E. Geskin, B. Goldenberg, Development of a Technology for Fabrication of Ice Abrasives, *International Symposium On Surface Contamination and Cleaning*, Newark, NJ, May 2001.

D. Shishkin, E. Geskin, B.Goldenberg, A Practical Application of Ice Jet Technology, *Cleaner Times*, August 2001.

D. Shishkin, E. Geskin, B. Goldenberg, Application of Ice Particles for Precision Cleaning of Sensitive Surfaces, *Electronic Packaging Magazine*, September 2001.

D. Shishkin, E. Geskin, B. Goldenberg, Development of a Technology for Fabrication of Ice Abrasives, *Proceeding of the 2001 WJTA American Waterjet Conference*, Minneapolis, Minnesota, August 2001.

D. Shihskin, E. Geskin, B. Goldenberg, "Application of Ice Particles for Precision Cleaning of Sensitive Surfaces", ASME Transaction, Journal of Electronic Packaging Magazine, to be published.

D. Shishkin, K. Babets, "Ice Based Surface Decontamination," Proceedings of Fourth DOE International Decommissioning Symposium, Knoxville, TN, June 2000.

To the eternal memory
of my love,
Lord rests her soul

ACKNOWLEDGMENT

The author wishes to express his sincere gratitude to his advisor, Dr. E. S. Geskin, for his remarkable guidance, constant encouragement, patience and moral support throughout this investigation. A special appreciation is devoted to Dr. B. S. Goldenberg for his efforts, advice and high-level expertise during this work. This dissertation could not be possible without their support.

Special thanks to Dr. B. Koplik, Dr. Z. Ji, Dr. R. Sodhi, and Dr. S. Das for their various help, serving as a member of the Dissertation Committee, having kindly read through the original manuscript, and providing many valuable suggestions. Additionally, sincere thanks to Dr. I. Cochin and Dr. H. Surjanhata for their timely help and suggestions during this study.

The author is grateful to the Department of Mechanical Engineering at New Jersey Institute of Technology for providing funding throughout this research. The author appreciates the encouragement and friendship from all of the Waterjet Laboratory members and NJIT friends: Dr. K. Babets, Dr. L. Tismentskiy, Mr. O. Petrenko, and Mr. Ceasar Guerra.

The author would also like to express his sincere gratitude to Dr. R. Kane, Director of the Office of Graduate Studies and Ms. G. Katz.

And finally, the warmest and deep appreciation to Ms. Annette L. Damiano, Lord rests her soul, to the author's mother, Svetlana Shishkina, author's sister, Irina Shishkina for their eternal love.

TABLE OF CONTENTS

TABLE OF CONTENTS
(Continued)

Chapter **Page**

TABLE OF CONTENTS
(Continued)

Chapter **Page**

LIST OF TABLES

LIST OF FIGURES

LIST OF FIGURES
(Continued)

LIST OF FIGURES
(Continued)

LIST OF FIGURES
(Continued)

Figure **Page**

LIST OF FIGURES
(Continued)

Figure **Page**

LIST OF FIGURES
(Continued)

LIST OF FIGURES
(Continued)

Figure **Page**

LIST OF FIGURES
(Continued)

Figure **Page**

LIST OF FIGURES
(Continued)

Figure **Page**

LIST OF FIGURES
(Continued)

Figure **Page**

CHAPTER 1

INTRODUCTION

1.1 Objective

Thermodynamic analysis of material removal and common sense indicate that an ideal tool for material shaping is a high energy beam, having infinitely small cross-section, precisely controlled depth and direction of penetration and no effect on the generated subsurface. The production of the beam should be relatively inexpensive and environmentally sound while the material removal rate should be high and should exceed the rates of existing material removal techniques. No such beam currently exists. The laser beam, embodying some of the above features, constitutes an effective material-processing tool. Laser applications for surface modification, welding and precision machining is well understood and documented. At the same time, the physics of the laser-material processing limits the use of this beam. Laser processing is based on the material evaporation and results in the formation of the heat-affected zone, which irreversibly changes the properties of the material. In some cases, for example during surface modification, such a change is necessary. In other cases, for example in eye surgery, such change is damaging. Another shortcoming of the laser processing is its limited ability to control energy density and the shape of the beam. Still another shortcoming of the lasers is the complexity and high cost of the equipment.

A narrow stream of high-energy water, so called waterjet, comes close to becoming an ideal tool. Waterjet (WJ) is able to remove a material without subsurface damage. Because of this, WJ constitutes one of the most common tools for surface processing. During last 30 years high speed WJ was adopted by industry as a machining

tool. At water pressure at the order of 340 MPa (50,000 psi), water velocity approaches 800 m/s and specific energy of the jet is comparable with that of the laser beam. However, machining ability of WJ is far below than that of the laser. The principal shortcoming of WJ is the low efficiency of the energy transfer between the jet and the workpiece. This results in low productivity of WJ machining. More important, WJ can be applied to machining of comparatively soft materials only.

The energy transfer and subsequently the mode of material removal change dramatically by addition of abrasive particles into the water stream. The abrasive waterjet (AWJ) generated as the result of such an addition enables machining practically any engineering material. The rate of removal of "hard-to-machine materials" by the use of AWJ is comparative if not superior to other material removal processes. Due to its capability, AWJ in a short time became one of leading machining technologies. In the course of AWJ, particles are sucked into a mixed chamber due to vacuum created by the jet. Mixing of water and particles and formation of a homogeneous flow occurs in a focusing tube, which form a highly erosive slurry jet. The various applications of AWJ are well understood and documented.

However, AWJ is a mixture of water and particles and this imposes a number of limitations and inconveniences. The energy efficiency of AWJ is still low, although acceptable, mixing of the water and particles imposes a severe limitation on the minimal usable jet diameter, special provisions are required for particles supply and disposal, the addition of abrasive particles increases the cost of processing and its environmental impact.

It would be highly desirable to enhance the productivity of WJ and yet avoid solid emission. This objective can be achieved by the replacement of conventional abrasive materials by ice particles, thus resulting in formation of ice-waterjet (IWJ). The solid particles, regardless of their properties, are able to erode the material in the impingement site. Thus, ice can be used as an abrasive media. Termination of the negative environmental effects of AWJ machining constitutes a significant advantage of IWJ. Most important, however, is the feasibility of the use IWJ for shaping of material in food, electronic, space and other branches of industry where any contamination in the course of processing is impossible. One of the potential applications of IWJ is medicine. Another significant advantage of the water ice abrasives is their availability and low cost. There is no need to deliver and store ice. The only commodities needed for fabrication of water ice particles are water and electricity.

It is highly desirable to convert an environmentally unfriendly, but widely adopted, AWJ machining into a green ice blasting process. However, it is necessary to overcome significant technological difficulties in order to attain adoption of IWJ by the practice. The erosion of substrate by impinging particles is due to stress waves generated in the course of impact. The strength and duration of these waves depends on mechanical properties of the impinging particles. The elastic characteristics of conventional abrasives are superior to that of ice. Thus, these abrasives constitute much more effective machining tool. Despite a low productivity, the use of water ice will be readily acceptable by food, biomedical and other industries where the contamination of the substrate constitutes the primary concern of users.

The most important problem, which actually impedes adoption of the ice-jet technology, is the difficulties in the generation and handling of ice abrasives. Regular abrasives are stable at all practical ranges of operational conditions, while ice particles can exist only at subzero temperature. Maintaining such a temperature within the nozzle and within the jet is an extremely difficult task. Ice particles tend to pack and clog the supply lines. The adherence between the particles increases dramatically, as the temperature approaches 0°C. Thus, prior to entrance in the nozzle ice particles should be maintained at a low temperature. These and some other problems prevent adoption of IWJ. In order to assure the acceptance of IWJ by the industry, it is necessary to develop a practical technology for formation of the ice-water slurry. IWJ jet is one of little practically available green machining tools. The need in such tools is rapidly growing. Although no practical application of IWJ is reported so far, it is safe to predict that water ice constitutes one of the most promising technological tools.

There are several reports of the application of the air-ice jets (Herb and Visaisouk, 1996, Liu et al, 1998, Geskin et al, 1999). The advantage of air driven system is the feasibility to maintain a low temperature of the stream and a high-pressure gradient in suction lines. Because of this, it is expected that this technology will be adopted by the practice fairly soon. However, machining ability of the ice airjet (IAJ) is insufficient for removal of the most of engineering material. Thus, most probably, this technology will be adopted for surface processing, while material shaping will be carried out by IWJ.

The substantial advantage of IAJ is elimination of off-products, solid or liquid, while its disadvantage is the use of gas as a source of momentum. Low density of the gas media limit machining ability of the jet. The use of cryogenic fluid (liquid nitrogen,

ammonia, and carbon dioxide) enables us to eliminate off-products as well as substrate contamination, while the sufficient momentum is delivered to the impact zone (Dunsky and Hashish, 1996, Hashish and Dunsky, 1998, Sherman and Adams, 1996). The obvious difficulty of this technology is the necessity to maintain a working fluid at a cryogenic temperature.

The use of particles as energy carriers in the impingement zone is one of ways of improving momentum transfer from the fluid to the substrate. The increase of the density of the fluid momentum at the impingement zone is another approach to this problem. Highly coherent fluid flow readily passes through a layer of a rejected fluid. Thus, momentum losses of the jet are reduced. However, the mechanisms of the energy delivery to a substrate by a coherent jet and impacting particles are quite different. Material removal by particles is due to the erosion, while penetration of a fluid jet is due to the stagnation pressure. Due to this, even coherent jet can penetrate only comparatively soft materials. The most effective way to increase jet coherence without water contamination is addition of small amount of polymers (Summers, 1995, Lombari, 1997). The improvement of the jet penetration by the addition of polymers is widely adopted by the industry.

In this study, the potential of the reduction of emission of jet processing and the obstacles to the creation of the green jetting technology was discussed. Although various approaches to this issue are examined, the main attention is paid to the application of water ice, particularly to the contribution of the authors to this problem.

Current cleaning technologies are based on the use of chemicals or sand and water blasting. All of these technologies bring about heavy environmental pollution. The air-ice

blasting constitutes the unique cleaning technology, which involves practically no off-products, thus has no negative environmental impact. The use of ice blasting for such diverse operations as graffiti removal, food cleaning, car wash, etc. will result in the reduction of pollution and thus improvement of the quality of life in urban areas. Ice based industrial cleaning can improve labor conditions. Ice blasting can be effectively used for elimination of the consequences of the chemical and biological attacks. The fine ice powder is constituted an effective medical tool.

Currently, ice is used as cooling media for food preservation. The fine ice powder generated by the developed devices made this operation more efficient. This reduces food cost and improves its quality. The ice particles reduces the environmental impact of the graffiti removal, car wash, industrial cleaning, food processing. They could also be used for antiterrorist activity.

1.2 Mission Statement

During the course of the previous NSF sponsored research, it was found that the addition of ice particles into the air stream results in a formation of an effective cleaning media. The use of the ice-airjet enabled carrying out a number of highly sensitive cleaning and decoating operations, which cannot or at least cannot effectively, be accomplished by other means. However, the industrial scale ice blasting would be practical if a reliable, energy effective technology for the formation of particles of a given size and temperature is developed. During previous experiments, it was shown that the desired particles could be reproducibly generated by an auger icemaker.

Conventionally, solidification of a continuous liquid flow, e.g. water flow, brings about a formation of solid blocks. However, it was found that if definite conditions (high rate of solidification, low final temperature of the solid, high stresses, motion along a given trajectory) are met the solidification results in the formation of particles, rather than blocks. The change of process conditions enabled to control wide range of particles properties, such as size, integrity, temperature. The performed laboratory experiments demonstrated the feasibility to fabricate the desired particles using the auger type icemaker. The principal features of this device (continuous mode of operation, flexibility, ability to handle large flows and to generate large temperature gradients) make it suitable for industrial scale production. However, the technology of the direct conversion of a liquid into particles of a given size does not exist. Thus additional knowledge is needed in order to upscale the laboratory set up, used in the previous research to an industrial scale reactor. It is the objective of the proposed work to acquire such knowledge. In order to attain this goal the experimental data describing water-to-particles conversion would be acquired and used to construct temperature and stress fields and phase distribution within the icemaker. In addition to investigation of steady state conditions, the effect of the change of variable, including very rapid changes will be explored. The obtained information was enable to identify and to quantify the sequence and coupling of phenomena, which bring about particles formation. As the result, the dimensionless equations representing the process of particles formation and suitable for the reactor design was constructed. The special attention in the course of the proposed study was paid to the formation of fine, perhaps submicron-particles of ice and some other materials.

It is objective of the proposed work to investigate particles formation in the course of freezing of moving water, to use the acquired information in order to construct process model and to use the developed model in order to develop a knowledge needed for industrial scale particles production.

1.3 Properties of Water Ice

The practical application of the water ice as a machining media is determined by ice properties. The phase diagram showing the regions of the existence of various forms of solid ice as well as the boundary between the solid and liquid states is depicted on Figure 1.1 [1,2]

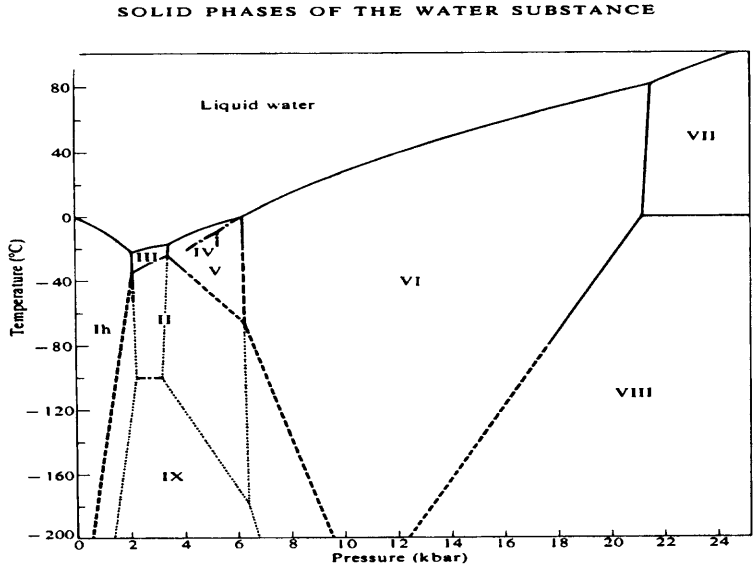

Figure1.1 Phase diagram of water. [1]

Although the properties of various phase modification of ice vary in a wide range, a practical importance has Ice I existing at the modest pressure (below 200 MPa).

The important feature of ice I is the reduction of a melting temperature with increase of the pressure. The minimum temperature of the liquid water is attained at the pressure about 200 MPa and is equal to -20°C. The reduction of the water solidification temperature from 0°C to -20°C as the pressure rises from 0.1 MPa to 200 MPa is almost linear. This property determines the feasibility of ice formation by cooling of compressed water to the temperature slightly exceeding solidification temperature at this pressure and subsequent isoenthalpic water decompression in a nozzle. After the nozzle water pressure drops to 0.1 MPa, a part of water is converted to ice. The energy balance of the flow prior and after the nozzle determines the fraction of the frozen water. This fraction is determined by the equation:

$$x = \frac{C_p(T_2)T_2 - C_p(T_1)T_1}{h + C_p T_2} \tag{1.1}$$

where x is the fraction of water converted into ice during an expansion, *Cp(Tp)* is the specific heat of water at constant pressure at temperature T, kJ/kg C, T_1 and T_2 are the temperatures of water prior and after an expansion, C, h is the latent heat of water freezing at T_2, kJ/kg.

Another important ice feature determining particle behavior in the course of impact is ice elasticity. At the temperature range of -3°C to -40°C, ice behaves as almost perfect elastic body. Hook's Law is obeyed if the stresses in the ice are below than certain level and are applied during a short period of time [1]. The dynamic elastic properties of ice [2] at -5°C are characterized by the following data: Young modulus (E) = 8.9-9.9 GPa, Rigidity modulus (G) = 3.4-3.8 GPa, Bulk modulus (K) =8.3-11.3 GPa, Poison's ratio (χ) = 0.31-0.36. For comparison, for Aluminum Alloy 1100-H14 E = 70

GPa and G=26 GPa. For silica glass, E=70 GPa. If a columnar ice is stressed perpendicular to the long direction of the column, the static Young modulus in bars is determined by the equation:

$$E=(5.69-0.64T)\times 10^4 \qquad (1.2)$$

where, temperature T is given in C. The dynamic Young modulus of ice increases almost linearly from 7.2 GPa at -10°C to 8.5 GPa at -180°C, and is independent from direction of loading. The data above shows that the ice powder can be consider as a soft blasting material and used accordingly.

One of the main issues in the use of the ice powder is sintering of ice particles and their adhesion to the surface of the enclosure. The strength of the adhesion of ice particles depends on the ice temperature. The effect of the temperature on the adhesion forces is shown in Figure 1.2.

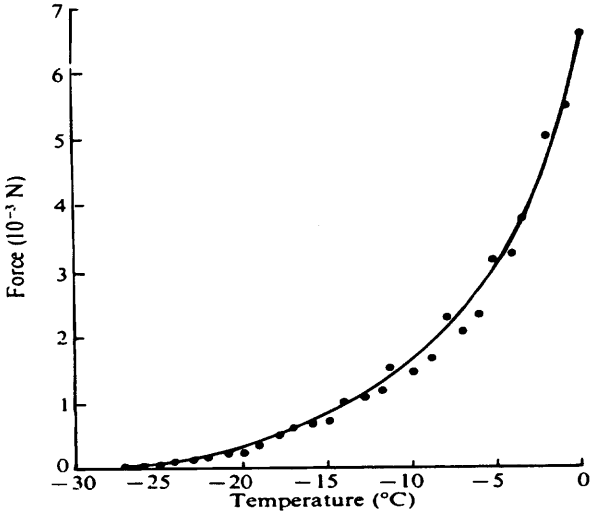

Figure 1.2 Strength of the adhesion of ice particles. [1]

As it follows from this figure it is necessary to maintain ice temperature below -30°C to prevent sintering of the particles. The sintering is also determined by the duration of the particles contact.

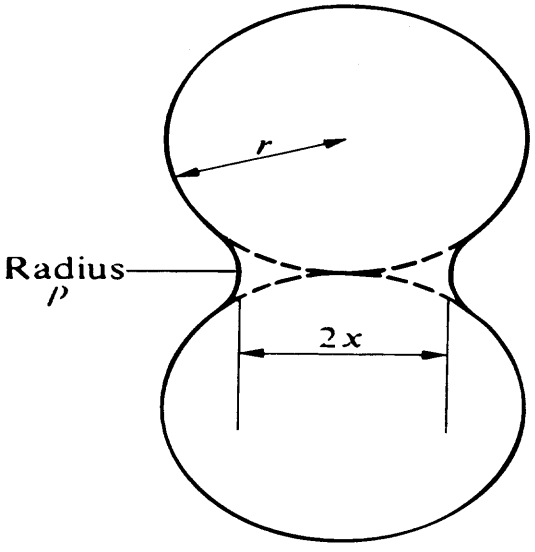

Figure 1.3 Schematic of the sintering of ice particles [1].

The radius of the neck, which forms between two ice spheres, brought into contact during time t at temperature T and presented in Figure 1.3 is determined by the equation

$$\left(\frac{x}{r}\right)^n = \frac{A(T)}{r^m} t \qquad (1.3)$$

where x is the radius of the neck, r is the radius of sphere, $A(T)$ is a function of the temperature, which depends on the mechanism of sintering, n and m are the constants, which are also determined by the mechanism of sintering. As it follows from equation (1.3), it is necessary to prevent the contact between particles in order to avoid particles

sintering. Ice tends to adhere to a solid surface where the ice nuclei are generated. The strength of the adhesion to the polished steel is illustrated by Figure 1.4.

The moisture contained in the atmosphere in the course of ice transportation will bring about the adherence of the ice to walls or sintering of ice particles. Both phenomena result in the formation of a plug and clogging of the conduits (Figure 1.4).

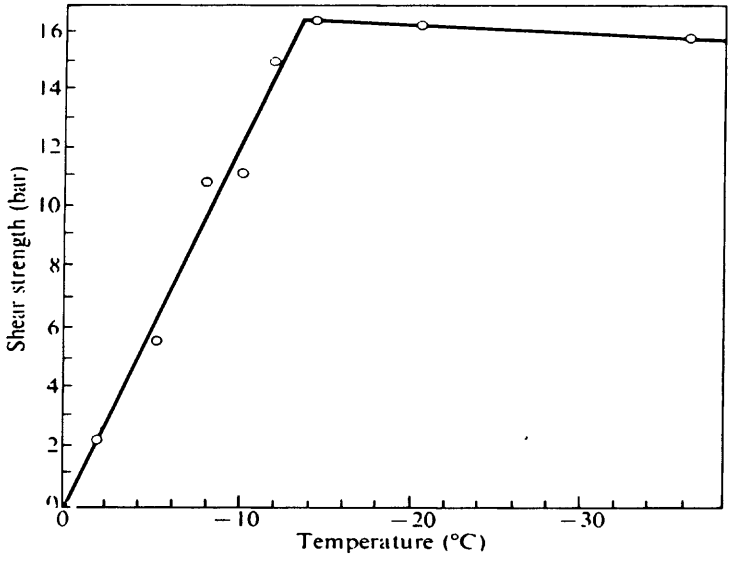

Figure 1.4 Shear strength of ice adhesion to stainless steel [1].

CHAPTER 2

EXPERIMENTAL SET UPS

The preliminary experiments involved cooling of the compressed water prior to the water nozzle. Cooling was accomplished by submerging of the supply pipe into the liquid nitrogen bath and resulted in the improvement of WJ performance. However, no ice particles have been found in the stream. The most probable cause of the observed improvement was reduction of steam generation in the course of jet formation and thus increase in the stream coherence.

In order to evaluate the effect of ice particles on the jet-workpiece interaction, a simple system for ice-particles generation and entrainment by WJ was constructed (Figure 2.1). In this system ice cubes produced by a regular icemaker were fed into a grinder. In order to prevent ice melting the dry ice, (solid CO_2) was added to ice. The particles generated in the grinder were fed into a conventional abrasive nozzle via a conventional system for abrasive supply. A coil installed prior to the nozzle was submerged into liquid nitrogen and used for water cooling prior to expansion. The nozzle in the system Figure 2.1 is motionless and thus was used for drilling only. IJ material cutting was carried out at the 5-axes robotics workcell. The compressed water for the performed experiments were supplied by Ingersoll-Rand Co. made intensifier with maximum available pressure of 340 MPa.

The experiments were carried out at the water pressure of 320 MPa. The nozzle diameter was 0.175 mm, the diameters of the focusing tube were 0.75 and 1.075 mm while the stand off distance ranged from 3 to 5 mm. The traverse rate during cutting was

25 mm/min. The experiments involved cutting and drilling of steel, aluminum, titanium and composite samples. The machining was carried out by IJ and WJ at similar operational conditions. The developed ice supply system was not able to provide steady flow of ice particles as well as to assure the control of particles size and prevent particles melting. In order to evaluate the effect of particles addition on the machining, water during the reported experiments was not precooled.

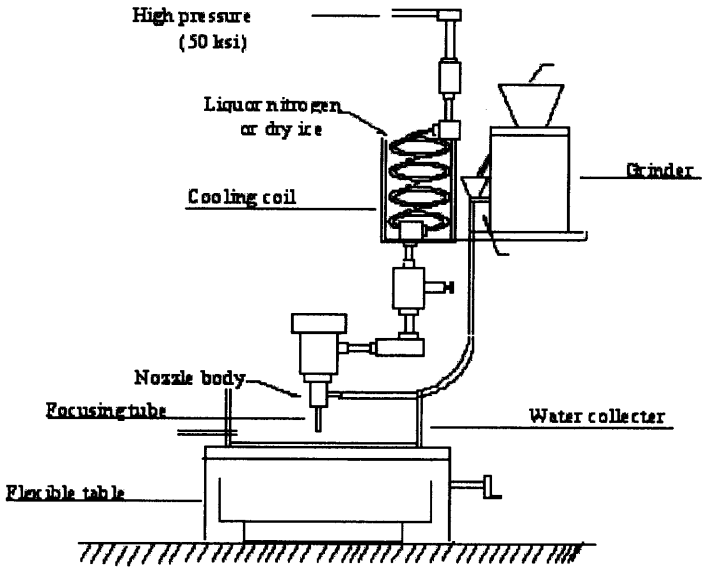

Figure 2.1 Schematic of the IJ cell.

Clogging of ice particles in the course of ice supply from the source (bunker, ice grinder, etc.) to the focusing tube constitutes the main barrier in the system design. The clogging occurs as a result of any appearance of water within the particles stream. When started, the chain reaction of clogging is developing almost instantaneously. Water within the ice stream can be generated due to the local melting or moisture condensation, and it is difficult to prevent its appearance.

The thermodynamic analysis of conditions of the ice formation, transportation and entrainment by the waterjet enabled us to determine the potential site of the moisture generation within the ice supply system. It was found that clogging could be prevented if a part of the ice supply line is maintained at a subzero temperature so no moisture is generated. The temperature of the rest of the supply system is 0°C so moisture generation does not result in particles agglomeration. Another barrier in the system operation is generation of an adequate driving force acting on the ice flow. This was attained by the use of air ejector. Because the ejector is fed by a compressor without aftercooler, the walls the ejector are heated. In order to eliminate the effect of the stream exiting the ejector on the jet formation in the mixing chamber, there is a gap between the exit of the ejector and the receiving port of the mixing chamber. With these conditions, the entering of the practical ice particles in the nozzle is assured, while the interference between the air-particles and water streams are eliminated.

2.1 Milling System Prototype

Another experimental set up system was introduced during IJ System development. An experimental set up for injection of ice particles into the water stream is shown in Figure 2.2. Ice was prepared in a conventional ice making machine and fed into an ice milling system. After two stages of milling, ice particles of desired dimensions were separated and via a vibrational feeder delivered into a bunker. Dry ice was used to prevent melting and lamping of particles. Injector transfers particles from the bunker to the waterjet machining cell. The particles transport was carried out by CO_2, which was also used as a cooling media. Gas and particles were separated in a cyclone. After the cyclone particles

were moved to the second bunker located at the site of the abrasive bunker, the gas was returned to the first bunker and used for additional cooling of the particles.

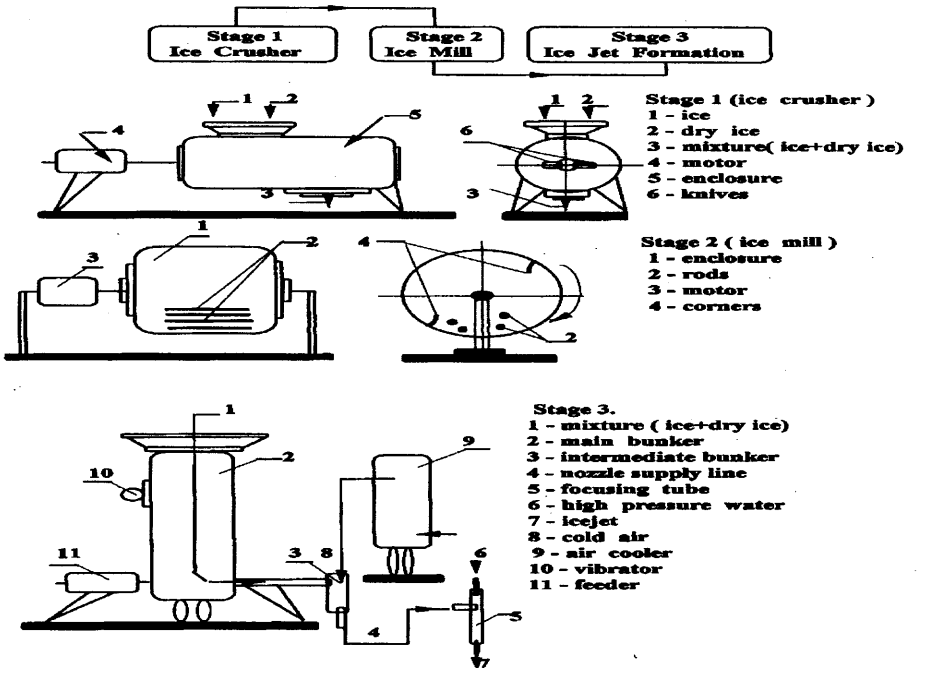

Figure 2.2 Schematic of milling machine used to produce subzero ice particles.

Dry ice was used for the cooling of the second bunker. Particles stored in the second bunker were supplied via hose to the abrasive port of the cutting head. Similarly to abrasive particles, ice is driven to the cutting head by suction developed by the waterjet. Mixing of the particles and water and formation of ice jet is similar to the formation of AWJ.

The developed IJ was used for cutting of various metals (titanium, stainless steel, aluminum). The same samples were cut by WJ and AWJ in order to compare these three technologies. The cutting was carried out at the water pressure of 340 MPa, water nozzle

diameter of 250 micron, focusing tube diameter of 1100 micron, stand off distance of 2.5 mm, traverse rate at IJ and WJ cutting was 5 cm/min and 25 cm/min during AWJ cutting. Barton Mines garnet 220 was used for abrasive cutting. The rate of abrasive flow was 65 g/min, while the estimated rate of ice particles supply was 63 g/min and estimated size of ice particles was 2.5-3.0 mm. The traverse rate of 5 cm/min was the maximum traverse rate at which IJ cutting was possible.

2.2 Crushing System Prototype

Experimental set up system was introduced during IJ System development. An experimental set up for injection of ice particles into the water stream is shown in Figure 2.3. Ice was prepared in a conventional ice making machine and fed into an ice milling system. After two stages of milling, ice particles of desired dimensions were separated and via a vibrational feeder delivered into a bunker. Dry ice was used to prevent melting and lamping of particles. Injector transfers particles from the bunker to the waterjet-machining cell. The particles transport was carried out by CO_2, which was also used as a cooling media. Gas and particles were separated in a cyclone. After the cyclone particles were moved to the second bunker located at the site of the abrasive bunker, the gas was returned to the first bunker and used for additional cooling of the particles. Dry ice was used for the cooling of the second bunker. Particles stored in the second bunker were supplied via hose to the abrasive port of the cutting head. Similarly to abrasive particles, ice is driven to the cutting head by suction developed by the waterjet. Mixing of the particles and water and formation of ice jet is similar to the formation of AWJ.

The developed IJ was used for cutting of various metals (titanium, stainless steel, aluminum). The same samples were cut by WJ and AWJ in order to compare these three technologies. The cutting was carried out at the water pressure of 340 MPa, water nozzle diameter of 250 micron, focusing tube diameter of 1100 micron, stand off distance of 2.5 mm, traverse rate at IJ and WJ cutting was 5 cm/min and 25 cm/min during AWJ cutting. Barton Mines garnet 220 was used for abrasive cutting. The rate of abrasive flow was 65 g/min, while the estimated rate of ice particles supply was 63 g/min and estimated size of ice particles was 2.5-3.0 mm. The traverse rate of 5 cm/min was the maximum traverse rate at which IJ cutting was possible.

The system for formation of ice particles, accounted for the requirements above were constructed. The system operated as following. Ice and dry ice are supplied into the first stage of the crushing. Here the piston 1 moves ice to the rotating knives 2. The obtained coarse particles are supplied to the screw conveyer of the second stage. This conveyer delivers particles to the rotating knives, which generate fine particles. These particles are supplied into bunker 8 and then to the vibrator 10. The vibrating rod 9 assures continuity of the flow through the bunker 9. The vibrator 10 supplies particles to the bunker 12 and then to the tube 13. The suction created by the water nozzle assures delivery of the particles to the nozzle head. The heater 14 prevents clogging of the of the entrance port. Vibration of the crushers, bunkers and intermediate lines assures continuity of the powder flow. The rate of the vibration as well as operations of both stages of the crushing is controlled by PC via the microprocessor MP. The crusher bunkers and vibrator 10 are located within the insulated enclosure. The supply line 13 is also located

in the enclosure. The air at the temperature of -70°C is supplied into the enclosures. The tests showed the stability of the operation of this system.

The experimental study of crushing of the ice block by rotating knives will involve monitoring of the torque applied to the knife, stresses in the blades, temperature of the ice surface and the size distribution of the generated ice particles.

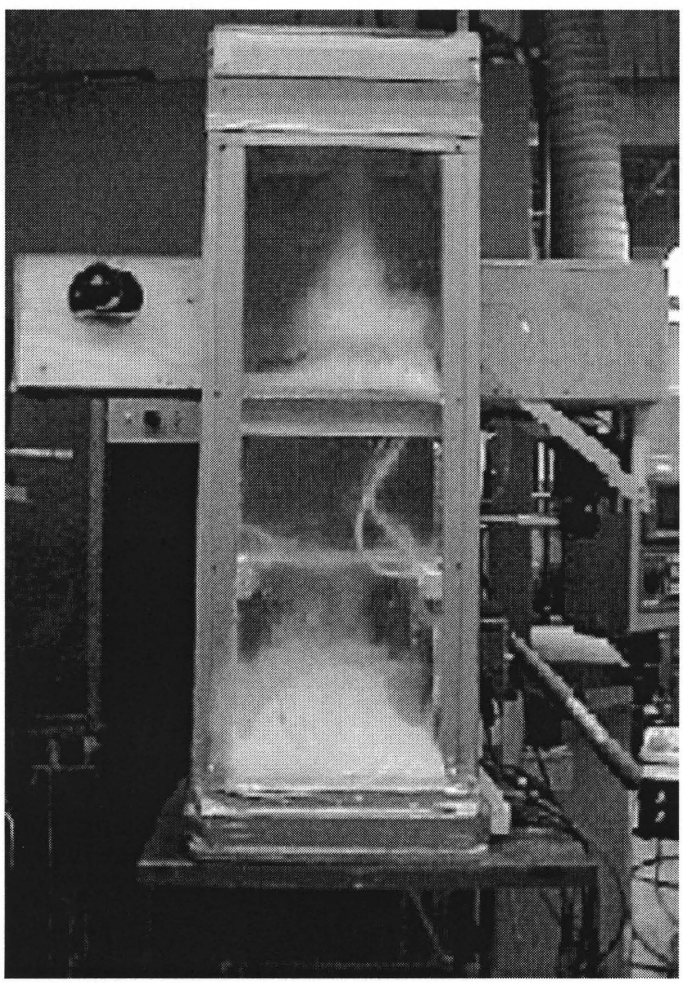

Figure 2.3 System for ice formation (general view).

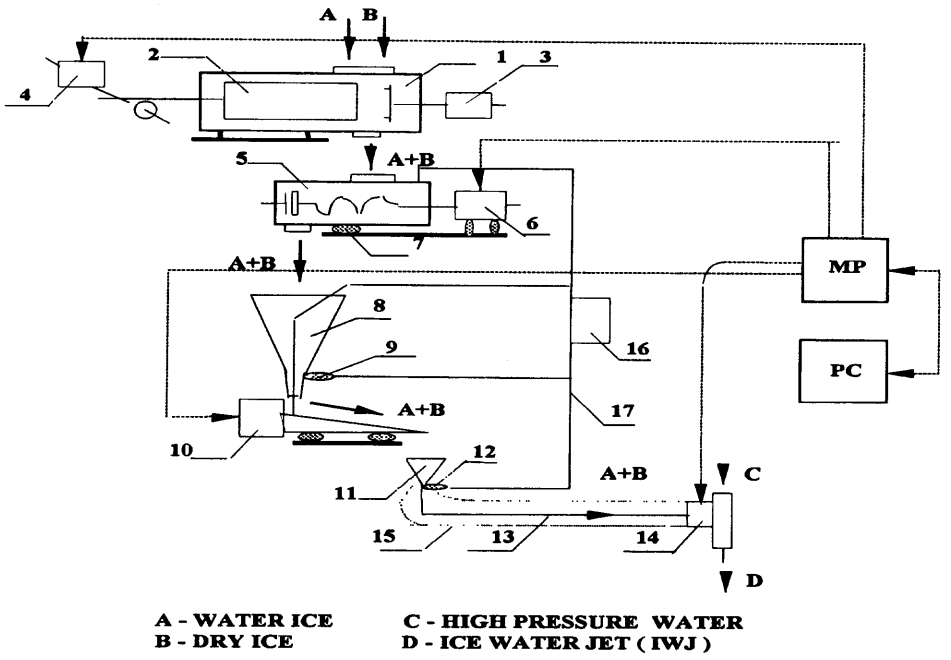

1- the first stage of crushing, 2- the piston, 3- the knives motor of the first stage of crushing, 4- the piston motor, 5- the second (precise) stage of crushing, 6- the knives motor of the second stage of crushing, 7- the amortizator of the second stage of crushing, 8- the intermediate supply bunker #1, 9- the amortizator of the intermediate supply bunker #1, 10- the electromagnetic vibrator, 11- the intermediate supply bunker #2, 12- the amortizator of the intermediate supply bunker #2, 13- the intermediate supply line, 14- the electrical heater, 15- the insulation enclosure of the intermediate supply line, 16- the adjustable speed and force vibrator, 17- the vibration transfer stainless steel rods.

Figure 2.4 Schematic of the system for ice formation.

The size reduction of the ice particles generated by the auger icemaker or by the ice crushing will be carried out by the particles impact by the vibrating plates. A vibration crusher was constructed along with monitoring system for the dimension of the generated particles for corresponding operational conditions. The detailed description of this system and feedback control system is given in the Appendix A.

2.3 Evaporator-Auger Based Freezer System Prototype

The third laboratory prototype of the ice maker machine was completed at the April 2000. The machine, general view is illustrated in Figure 2.5 consists of few functionally separated blocks:

- ice making block includes the evaporator, auger, auger driver, sealing and TurboJet cooling apparatus;
- ice unloading mechanism includes the driver for traverse movement, drivers for feeder springs, flexible tubing and support sliding part;
- nozzle block includes two parallel nozzles with focusing tubes and focusing device.

The parts for ice making block were manufactured by Hoshizaki America, Inc. The other blocks were designed and manufactured by Waterjet laboratory, NJIT. Hoshizaki flaker series evaporator has maximum productivity of 8.4 kg/hour and produce supercooled ice powder with temperature range from -20°C in high water flow rate regime to -60°C in low water flow rate regime. Turbo Jet cooling apparatus supplies refrigerant Galden perfluorinated fluid by Ausimont Co. with average flow rate of 9.8 liters per minute with stabilized temperature of -72°C and pressure about 150 kPa. Water supplies through water port with water flow rate range 0-500 ml/min and room temperature. Water flow rate controls precisely by valve. The schema of evaporator – auger ice making machine is presented on Figure 2.6. Auger driver is AC capacitor motor with reducing gearbox of speed 7.5 rpm.

Ice unloading mechanism works as an automatic feeder and use the principle of razor, which slides on the ice surface and picks up ice powder with rotating spring feeders and suction force developed by a working nozzle. Three electrical motors provide

motion to the unloading mechanism. Two of them are high-speed DC motors with speed controllers, which allow having a wide range of speed from 0 to 30,000 rpm. Traverse motion provides by the auger driver with rotational speed 7.5 rpm.

Nozzle block consists of two nozzles and special focusing device. For these experiments, the nozzles of three distinct diameters were used and it was determined that the optimal nozzle to focusing tube ratio is 1:2. Ice supplies to the nozzles through flexible plastic tubes, which remain elasticity under the low temperature.

The water, air, refrigerant and ice are grouped into three channels such as input channel, output and control channels. The system requires a water source to provide a flow rate at least 30 litter/hour. A city water system is adequate for this purpose. Water pressure is equivalent to the pressure in city water net system. The water can be considered as an input and control channel at the same time. Refrigerant can also be considered as input with constant flow rate and temperature. The output channel for the system is ice powder with predicted parameters.

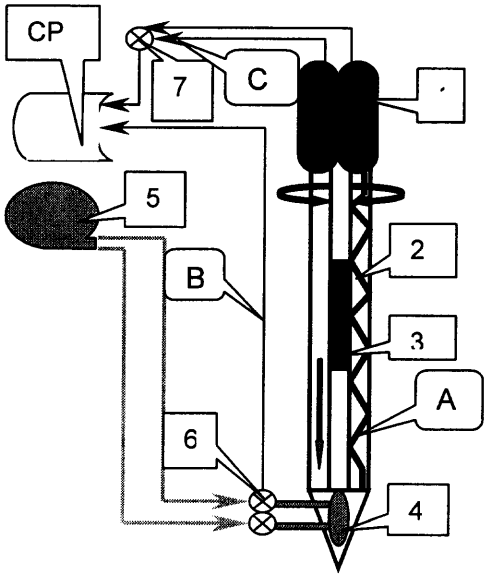

1 – precisely controlled spring feeder drivers
2 – spring feeder
3 – slot which provides traverse motion of the block nozzle
4 – focusing tube block
5 – high pressure air compressor
6 – CPU-controlled valves control air flow rate
7 – speed of the spring feeders controlled by CPU

A – the direction of ice flow movement
B – CPU
C – feedback to the CPU from the spring feeder drivers

Figure 2.5 Schematic of the nozzle block.

The following chapter will discuss experimental technique being used to control and predict ice behavior inside of the evaporator and allowed develop experimental database. It should be mentioned that obtained database is valid for the following range of water flow rates:

- from 0 to 150 ml/min for coolant media Galden HT-55;
- from 0 to 200 ml/min for liquid nitrogen coolant media.

In the course of the performed experiments a modified commercial icemaker of he Hoshizaki of America was used for ice particles production. Thus, the dimensions of the auger, heat exchanger, water supply port etc. were determined in advance. The rate of the supply of the cooling media was determined by the design of the refrigeration system or pressure in the nitrogen tank. The desired way of water solidification, that is size distribution and the temperature of the ice particles was determined by the rate of the water supply, which change gradually from 0 to 200 ml/min. The torque of the auger driver in order to prevent jamming of the icemaker was increased also. In the final analysis, the ability of the industrial system to generate the desired kind of the particles by the selection of the water flow rate at the given cooling conditions was shown. The attempts to improve ice production by the increase of the water pressure or control the supply of the cooling media were unsuccessful. It was determined however, that it is absolutely necessary to eliminate any obstructions to the ice flow in order to prevent jamming of the heat exchanger.

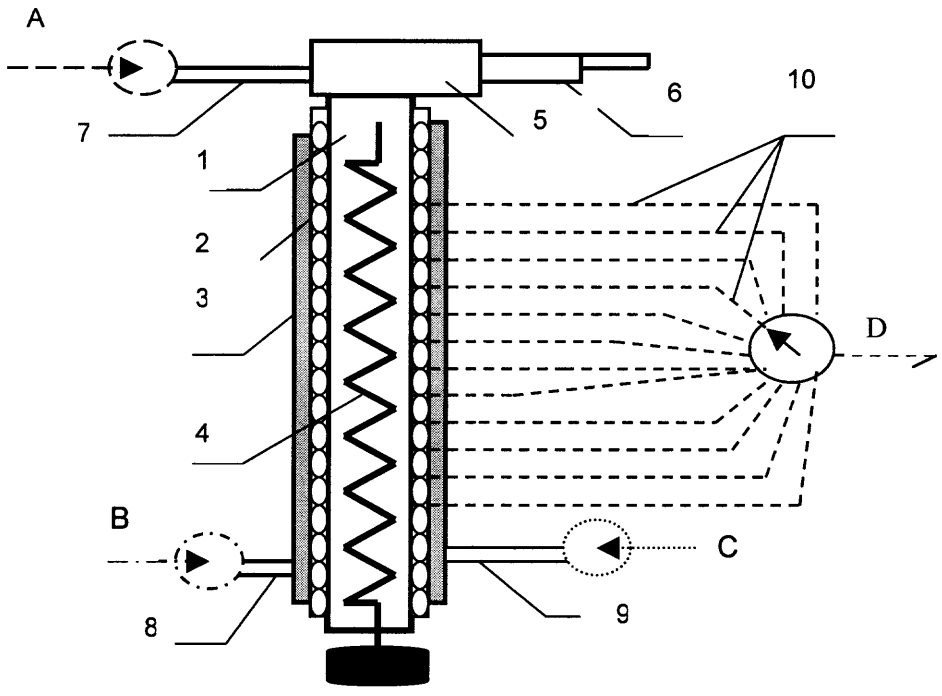

1 – evaporator
2 – refrigerant coils
3 – insulation
4 – auger
5 – ice reloading device
A – air flow rate gauge
C – flow rate gauge for liquid refrigerant
D – thermocouples
6 – air gun
7 – air supply port
8 – water supply port
9 – port for liquid refrigerant
10 – thermocouples
B – water flow rate gauge

Figure 2.6 Schematic of evaporator-auger type icemaker.

It is quite obvious that the conditions of the ice production (specific cost and energy consumption, process stability, uniformity of the generated particle, output per 1 kg of the facility or 1 cm^2 of the outlet crossection area etc.) will be dramatically improved by the process optimization. However, the shear number of the control variables (rate of the supply of the water and coolant, rate of the auger rotation, the diameter and the length of the heat exchanger, distribution of the temperature and heat

flow along the refrigerator, the geometry of the auger) exclude practicality of empirical process optimization. At the same time, complexity of the phenomena which occur in the course of the powder formation (water freezing and simultaneous decomposition in the spiral moving layer) exclude the use of a conventional physical models.

Thus, the only practical approach to the process design entails experimental study of the water properties distribution within the icemaker, construction of the process phenomenology using the acquired information and then to use commercial packages (Pro/ENGINEER, FIDAP, etc.) to evaluate the design parameters of the icemaker as well as the correlation between input variables and the ice properties. Appendix B contains detailed views of the evaporator-auger unit and nozzle block.

CHAPTER 3

INVESTIGATION OF ICE WATERJET AND ICE AIRJET FORMATION

Abrasive nozzle head assures entrainment of abrasive particles by water stream and formation of the homogeneous or almost homogeneous slurry. However, as it was shown earlier (Raissi et al., 1996, Osman et. al, 1996) [16,17] the mixing chamber constitutes an "intermediate storage" of particles, fed from the inlet port and feeding the focusing tube. The FIDAP modeling of particle entrainment by the waterjet (Figure 3.1) demonstrates this conclusion. Because conventional abrasive particles constitute a thermodynamically stable system, the dwell time in the mixing chamber has no effect on the system performance. At the same time, the ice particles can survive at a temperature above 0°C only very short time.

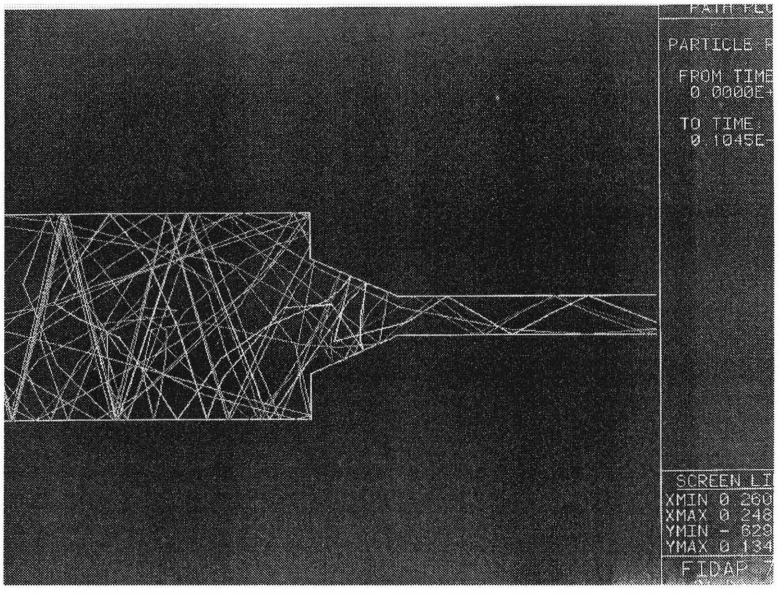

Figure 3.1 FIDAP modeling of particles motion in the mixing chamber. Notice extended dwell time of particles in the mixing chamber.

It is necessary to maintain water temperature after the nozzle at a near zero level in order to deliver solid ice particles to the impact surface. Another way to address this issue is to reduce the dwell time of the particles in the mixing tube. Appendix C shows the results of FIDAP modeling on ice particles motion into the mixing chamber developed in course of this research.

3.1 Formation of Ice WaterJet

There are several possible techniques for IWJ formation. Ice particles can be produced separately and then injected into the water stream similarly to abrasive particles. In this case, at least in principle, the generation of the ice particles of the desired dimensions, having maximal hardness is feasible. The obvious shortcoming of this technology is the need of auxiliary systems for the particles production and transportation. More important deficiency of particles entrainment into the water jet is a necessity to use a focusing tube for the formation of a slurry flow. The minimal diameter of a focusing tube, that is the minimal diameter of the stream, exceeds 350 micron.

Ice waterjet can be created by the formation of the ice particles in the course of jet expansion in the nozzle. The movements of ice particles in the mixing chamber shown in Figure 3.2. Thermodynamics of ice [1] allows us to reduce the temperature of the compressed water much below 0°C without freezing. At the pressure of 13.8 MPa, water temperature can be reduced down to -25°C. During the expansion in the nozzle, while water pressure reaches 1 bar part of water is converted into ice. Due to enthalpy release during the solidification, water temperature increases, but it cannot exceed 0°C. The fraction of water converted into ice is determined by the difference between water

enthalpies prior and after the nozzle and by the enthalpy conversion into kinetic energy of the stream during water acceleration. The shortcomings of this technology are the difficulties of the control of particle nucleation and growth and, the most of all, a small margin of enthalpy available for the solidification.

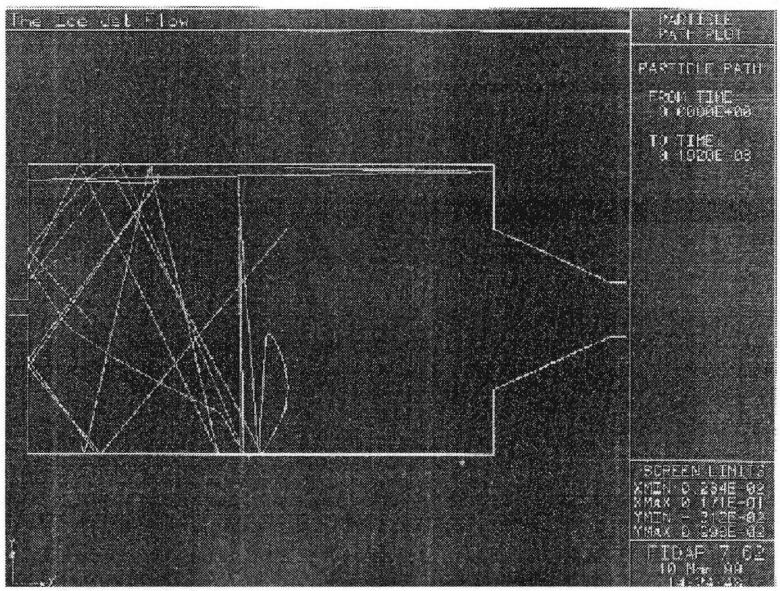

Figure 3.2 FIDAP modeling of particles motion in the mixing chamber. The end of a trajectory is due to melting.

Finally, ice formation is possible by cooling compressed water prior to the nozzle and additional water cooling in the focusing tube. Heat removal in the focusing tube can be attained, for example, by submerging the focusing tube into a cooling media. This technique enables us to increase the rate of the ice generation, but results in the increase of IWJ diameter due to the use of the focusing tube. However, in this case, the focusing tube is not used for mixing of water and particles. Due to this, the diameter of the focusing tube and thus, stream diameter are significantly less than those during particles addition. Cooling of the focusing tube requires much simpler facility than preparation and

handling of ice particles. Thus, each of the above technologies has shortcomings and benefits and further experiments are required to specify the areas of applications of each technology.

Previous studies of IWJ machining reported by Galecki and Vickers [18] and Truchot et al [19] involved the examination of stream freezing and ice particles supply in the water stream. These authors reported that addition of ice particles into WJ improves cutting of soft materials, that is the materials that can be cut by a conventional WJ. The study of the formation and the use of the ice jet (IWJ) have been carried by Waterjet Technology laboratory of NJIT since 1993 (Geskin et al, Li at al) [20-27].

3.1.1 Experimental Study of IWJ Machining

The addition of ice to WJ completely changed the mode of the jet-substrate interaction. Particularly, cutting of different metals became possible. The principal shortcoming of the system was particles clogging at a high rate of particles supply. The process was stable until a particle or several particles are stuck at the entrance of the cutting head. Then ice plug developed. The formation of this plug was readily detectable by the change of the noise of the jet. If, however, ice supply was stopped, the nozzle suction destroyed the plug.

The performed experiments showed the strong effect of ice addition. If WJ is able to remove a thin layer, IJ assures metal cutting. The rate of cutting was, however, much less than that of AWJ. The low productivity of IJ is due to the low cutting ability of ice particles, comparative to that of abrasive particles. It is also due to low flow rate of ice supply. At this stage, it was impossible to evaluate the comparative contribution of each

of these factors. It is expected that improvement of the procedure of particles formation and prevention of system clogging will improve process productivity, which might reach the level AWJ machining.

The important feature of IJ cutting of stainless steel is a narrow kerf. The width of the kerf is equal to that of WJ and substantially less than that of AWJ. Most probably, this reduction is due to prevention of steam formation in IJ and, thus, reduction of the jet diameter. Similar kerf width reduction was observed in the course of cutting of titanium, aluminum and copper. In all the cases above, the observed IJ kerf was less than that of AWJ. At the same time, in the course of copper cutting, a wide strip of eroded surface was developed. The width of this strip is comparable to the width of AWJ kerf. The formation of the eroded area on the copper surface is probably due to formation of an array of slow particles outside the main stream. The kinetic energy of these particles is not sufficient for significant surface modification of metals, such as steel, titanium and even aluminum occurs. This energy, however, is sufficient for substantial erosion of a copper surface.

Another series of experiments involved partial freezing of the water stream. Ice particles were generated in the water stream passing the copper heat exchanger. The presence of these particles was identified by the erosion of a surface subjected to the impact of the jet. No change in the surface topography occurs without water cooling, while when the heat exchanger was submerged into the liquid nitrogen surface erosion was readily observed. Moreover, the dimples generated by the cooled jet are similar to that generated by the impinging AWJ. Another indication of the formation of ice particles is the change of the noise generated by jet. The character of this noise changed

substantially when the nozzle head was submerged in the nitrogen bath. Control variable in this case was the depth of submerging of the copper tube into the nitrogen bath. This depth in the final analysis determines the rate of heat removal from water. An excessive cooling rate results in water freezing, while at an insufficient rate of heat removal no ice formation was observed.

The results of the surface erosion by the impinging IJ, generated by the stream cooling were also investigated. The impinging jet was able to drill steel and remove rust. No change of the surface geometry was observed without jet cooling.

The results of IJ and WJ drilling and cutting are shown in Tables 3.1 and Table 3.2. The presented results show the substantial improvement due to the ice entrapment. For example, WJ was not able to cut an aluminum sample while the ice addition assured process completion. Icejet was able to create a through hole, while WJ was not able to bring about any noticeable material removal. Waterjet was not able to penetrate through a graphite composite and IJ impact resulted in the composite delimitation while the ice addition assured hole generation.

Performed research evidently demonstrates potential effectiveness of IJ machining. It is possible to use IJ for shaping of various materials, for example steel and titanium. IJ machining is uniquely clean as well as efficient technology. As it is shown, IJ cutting results in the formation of a clean surface with minimal material removal. No existing technology is able to assure material separation at such kerf width without modification of the generated surface. At the same time, substantial improvement in the process technology is necessary. The performed work showed that IJ could be generated by cooling of the water flow after the nozzle exit or by ice particles supply into the

stream. However, a reliable technique for formation of ice particles is yet to be developed. The pictures of WJ and IJ cutting and drilling profiles are presented in Appendix D.

Table 3.1 Comparative Study of Material Drilling by WJ and IJ

Number of samples	Materials	Thickness (mm)	Time of Drilling (min)	Depth of Penetration (mm) Water / Water-Ice	Diameter of Holes (mm) Water / Water-Ice	Size of Ice Particles
1	AL	20	2	4.3 10.5	1.4 2.8	Large
2	AL	3.1	1	throu throu	~ ~	Large
3	AL	5.4	3.5	3.6 throu	1.1 1.1	large
4	AL	5.3	2.0	3.2 throu	1.1 1.1	Large
5	Regular Steel	6.4	5.6	2.5 throu	1.1 1.1	Large
6	Regular Steel	2.9	2.1	2.1 throu	1.1 1.1	Small
7	Ti-alloy	12.9	4.2	3.1 4.3	1.2 1.2	Small
8	Graphite Epoxy-Based Composite	7.4	5 sec	5.3 throu	1.3 1.2	Large
9	Stainless Steel	3.2	3.0	2.5 2.9	1.1 1.1	Small
10	Stainless Steel	2	8.0	0 1.7	1.1 1.1	Large

Table 3.2 Comparative Results of Material Cutting by IJ and WJ

Number of Samples	Materials	Thickness (mm)	Speed (cm/min)	Depth of Penetration (mm WJ IWJ	Size of Ice Particles
1	Al	5	2.5	3.1 Total Perforation	Large
2	Al	5.4	2.5	3.6 Total Perforation	Large
3	Stainless Steel	1.3	2.5	0.5 Total Perforation	Large
4	Stainless Steel	1.3	2.5	0.5 0.7	Large
5	Stainless Steel	3.2	2.5	0.7 2.1	Large
6	Stainless Steel	3.2	2.5	0.7 1.0	Small

3.2 Formation of IAJ

The use of ice particles is simplified if the particles are entrained in the air stream. There is a number of suggested air-ice based technologies. One of the firsts of such technologies is a car washing machine, utilizing ice particles. The stream of the charged frozen particles controlled by a set of coils was directed at treated surfaces [6]. Szijcs [7] proposed cleaning of the sensitive surfaces by the impact of the fine grade blast material and air. The atomization of the liquid in the air stream and subsequent freezing of the generated fine droplets form the blast material. The freezing is achieved by the addition of the refrigerant (N_2, CO_2, Freon) into the stream in the mixing chamber or by the addition of refrigerant into the jet after the mixing chamber. The use of ice particles, which have the uniform grain size of ultra-fine water for cleaning the surface and grooves

of the ferrite, block [8]. Ice blasting devise using stored particles was suggested by Harima [9]. Vissisouk [10] proposed to use ice particles near melting temperature in order to effectively remove a coating. Mesher [11] suggested a nozzle for enhancement of the surface cleaning by ice blasting. Shinichi [12] suggested cleaning inexpensively various surfaces by mixing ice particles, cold water and air. Niechial [13] proposed an ice blasting cleaning system containing an ice crusher, a separator and a blasting gun. Settles [14] suggested producing ice particles of a size range below 100 micrometers within the apparatus just prior to the nozzle.

3.2.1 Experimental Study of IAJ Cleaning

Although the use of ice blasting is suggested by a number of inventors, the practical application is much more limited. Herb and Vissaisouk [10] report the use of ice pellets for precision cleaning of zirconium alloys in the course of production of bimetallic tubing. It is reported that ice blasting improved the quality of bimetal. The use of air-ice blasting for steel derusting is reported by Liu et al [15]. The following operational conditions were maintained during blasting: air pressure: 02-0.76 MPa, grain diameter: below 2.5 mm, ice temperature -50°C, traverse rate 90 mm/min, and standoff distance 50 mm. At these conditions, the rate of derusting ranged from 290 mm^2/min at the air pressure of 0.2 MPa to 1110 mm^2/min at the air pressure of 0.76 MPa. The quality of the treated surface complied with ISO 8501-1 Sa 2.

The application of ice-air jet (IAJ) for surface cleaning was also investigated. It was demonstrated that at the optimal range of process conditions this jet constitutes a precision tool for selective material removal operations. A number of experiments was

carried out in order to demonstrate this ability of the air-ice jet. Various electronic devises (computers, calculators, electronic games and watches) were disassembled and electronic boards were contaminated by grease and metal powder. Then the boards were cleaned and reassembled. The computer, calculators and watches worked normally. Other experiments involved degreasing, depainting and deicing of liquid crystals, polished metals, optical glass, fabric, removal emulsion from a film, etc. The biomedical applications of the IAJ were investigated also. In the course of the experiments chicken and pork skin was treated by IAJ. The feasibility of removal of the epidermis layer without damaging the underneath laying layers of the skin was demonstrated. Extremely fine ice abrasive of average diameter of 300 microns was used for these purposes.

The feasibility of the damage free and pollution free decontamination of highly sensitive surfaces was demonstrated. Since the system was designed to produce fine particles, it was not applicable for removal of heavy deposit, for example rust. Modification of the operational conditions, including the increase of the parts size, will address this problem. A generic environmentally friendly surface processing technology is emerging as the result of the above experiments. Appendix E represents photographs of basic types of deposit and substrates, which were treated in course of IAJ experiments.

CHAPTER 4

EXPERIMENTAL STUDY OF ICE POWDER PRODUCTION

The main impediment in the experimental study of ice powder formation was inability to install the temperature, pressure and friction gauges at the inner wall of the evaporator because the cooling coils of the heat exchanger are welded to the evaporator enclosure and covered by an insulator. At these conditions, in order to monitor freezing, the thermocouples have been installed on the inner wall of the evaporator. Their tips and inner surface of the enclosure form a smooth surface to minimize the friction between the enclosure and the moving ice. Then, gauges have been attached to the enclosure firmly enough to outstay high-pressure as well as high friction generated during ice formation.

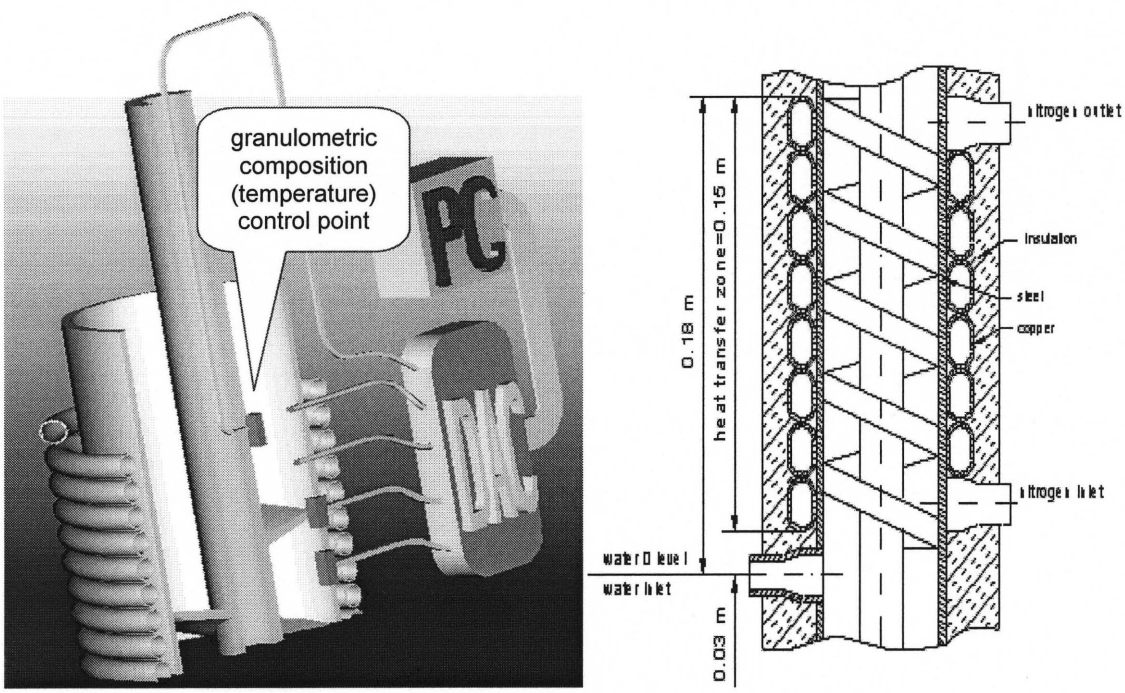

Figure 4.1 Schematic of thermocouple placement inside the evaporator and auger (distances calibrated from water inlet level): DAC – data acquisition card; TG – thermogauges; PC – personal computer.

Sixteen holes of OD = 0.75 mm were drilled along the evaporator body at the same vertical line and thermocouples were welded inside these holes. Thermocouples and gauges tips sticking out of an inner surface of the evaporator were cut off and then the inner enclosure surface was polished.

Schematic Figure 4.1 gives a detailed information about the gauges position inside the evaporator. Schematic shows positioning of the thermocouple placement inside the evaporator. The data acquired through the gauges are following.

4.1 Experimental Results for Galden HT-55 Cooling Media

4.1.1 Temperature Distribution along the Evaporator

The monitoring of the internal evaporator wall temperature in time for the different water flow rates was the objective of this experiment. The physical process of ice nucleation in helical motion combined with thermal expansion is very complicated and required the understanding of the temperature field distribution along the evaporator. The average time constant of the system for different water flow rates and two distinct cooling media was estimated.

Temperature distribution along the evaporator vs. time for distinct water flow rates the data were acquired at different water flow rates, ranging from 0 to 120 ml/min. In the course of each specific experiment, process variables were fixed. Six thermocouples were used for data acquisition.

It is quite obvious that as flow rate drops so does the temperature within the evaporator. At the top of the evaporator (the thermocouple 10), the temperature reaches –

72°C at zero flow rate. At the flow rate of 20 ml/min, the temperature of ice read by the thermocouple 10 is below -60°C and it rises to -40°C at the flow rate of 120 ml/min. Conversingly, at the thermocouple 1 (5 mm from the water entrance port) reading is always positive, except for the zero flow rate. Thus, at the bottom of the evaporator water is maintained in the liquid state. The negative temperature is observed at the thermocouple 3 (distance from the water entrance port is 23 mm). Point of crossing of time axis shifts form left to right with flow rate increases. With high flow rates, the system needed more time to bring the water to freezing point and then produce supercooled ice. Also, flow rate determined the low temperature boundary on the graphs. With low flow rates, the system produces ice of lower temperature.

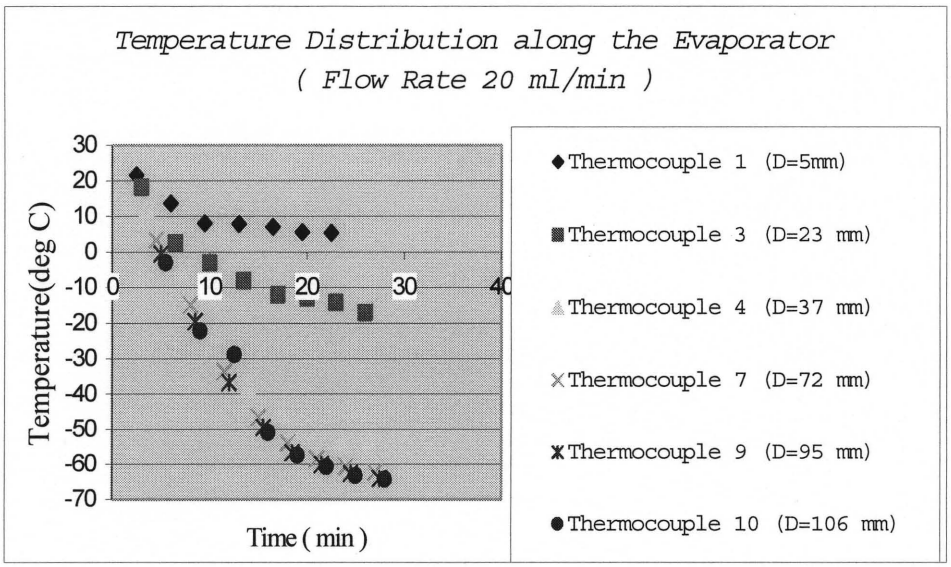

Figure 4.2 Temperature distribution along the evaporator vs. time for various water flow rates.

4.1.2 Temperature Distribution along the Evaporator versus Distance from Water Inlet Level

The zone assessment is necessary for monitoring the liquid, solid and decomposed phases of the ice powder formation. This data readily allowed estimating the heat flux through the system for all phases of the process. The resistance probes are precisely monitored the zone structure of the formation process and showed point where solidification process finished and decomposition occurred. Temperature distribution along the evaporator vs. thermocouple distances from water zero level: these graphs will complete the picture of temperature distribution along the inner evaporator wall for distinct cooling duration of 10, 15 and 20 minutes. These graphs help to understand the temperature behavior for three separate evaporator section:

- bottom or ice plug nucleation section;
- middle or plug supercooling and decomposition section;
- upper or ice abrasive supercooling section.

Bottom or liquid phase section of the evaporator mainly consists of water with small inclusion of ice particles and temperature about 0°C. Resistance between water port and resistance gauges placed in the bottom part of the evaporator gives the range from 25MΩ to 40 MΩ. This is basically confirmed that the bottom part of the evaporator holds liquid water. Middle or ice developing section of the evaporator is a region where ice starts form and grow. Resistance gauges for this part of the evaporator gave the questionable information. Some of them shown very high resistance, which eventually goes to infinity and some, gave the range between 40MΩ to 50MΩ. This understandable due to water insulation properties and then because of the dynamical character of ice development few of the resistance gauges had a direct contact to zones where ice grows

rate enable us to generate a desired particle population. For calculation of the average diameter of ice granules, the Image Tool statistical package was used. The images of the randomly selected sets of ice particles were used for the fractional particles classification appertained to a given water flow rate. Three pictures were generated for each set and the Image Tool statistical package was used to calculate average diameter of particles for each set. It was determined for example that at the water flow rate ranging between 20ml/min and 40 ml/min the average diameter of ice particles varies from 0.17 mm to 1.25 mm. Such powder constitutes an effective abrasive media for bio-medical applications. It can be used also for cleaning and surface processing of the sensitive electronic boards and electrical parts.

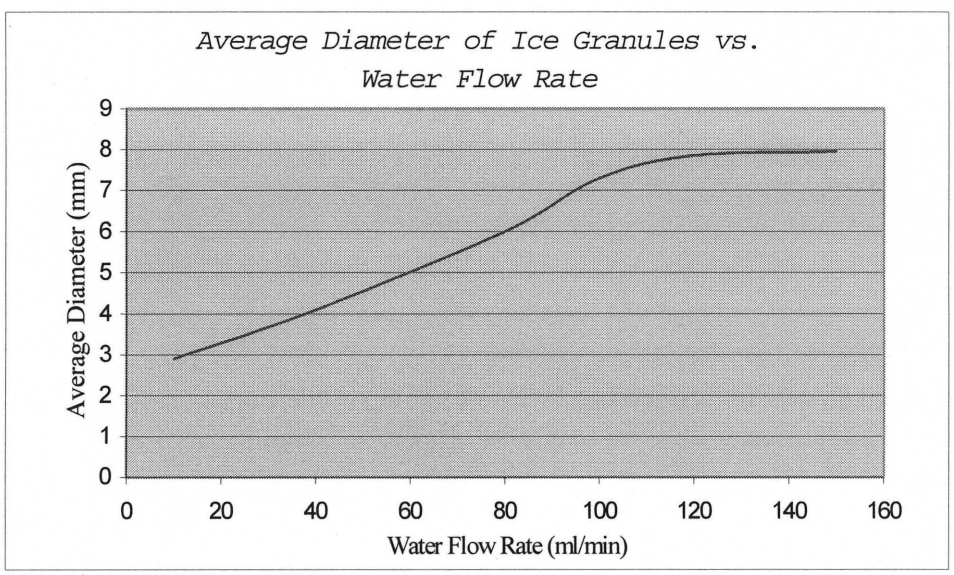

Figure 4.4 Average diameter of ice particles as a function of water flow rate for cooling media Galden HT – 55.

For the water flow rate range from 40 ml/min to 80 ml/min, the average diameter of ice granules is around 2.25 mm. This ice can be used for cleaning and degreasing of

is more intensive. Therefore, the resistance data read from these gauges varies from 50MΩ to infinity. Upper or ice supercooling section is the top portion of the evaporator. In this section ice temperature drops from -20°C to -60°C. The data for this section gave reading with very high resistance values close to infinity. This shows that this section consists of pure supercooled decomposed ice.

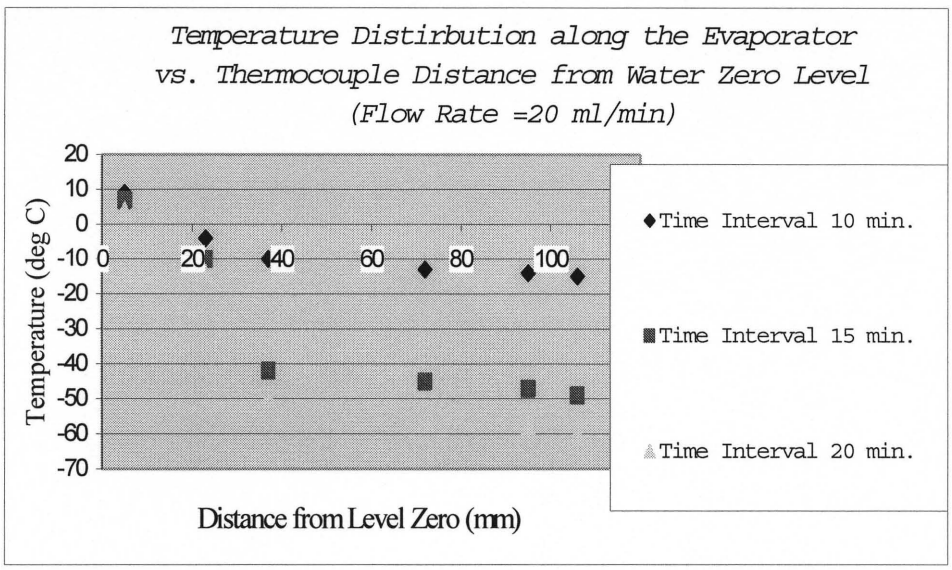

Figure 4.3 Temperature distribution along the evaporator at different cooling duration.

4.1.3 Granulometric Composition of the Ice Abrasive as a Function of Water Flow Rate

The granulometric composition is a vital parameter of IJ system. The experimental results of cleaning of the various deposits suggested the ice particles classification, which is applicable for each particular deposit type. Then, one of the technology requirements is a comprehensive information about the ice granulometric composition as a function of water flow rate for each distinct reactor set up. In the course of the experiment, it was determined that precise control of the coolant temperature at -72°C and the water flow

different types of metals and plastics. At the water flow rates higher than 200 ml/min, the average diameter of ice granules reaches its maximum value of 7.0 mm. This particles adequately accelerated can be used for metals derusting.

4.1.4 Granulometric Composition as a Function of Ice Temperature

Experimental results have shown that the granulometric composition of ice abrasive is directly related to the ice abrasive temperature at outlet point of the evaporator. This set of the experiments was conducted to monitor the above dependence and incorporate it into developing ice abrasive technology production. As it was mentioned above, the TurboJet cooling system provided coolant with fixed flow rate 9.8 l/min. In present set up the coolant flow rate was constant. However, it is highly desirable to have controllable coolant flow rate. In the future, design of IJ system along with different type of coolant the variable coolant flow rate will be used.

According to Hobbs [1] the strength of the adhesion of ice particles decreases rapidly when system subjected to the temperature below -15°C which is shown on Figure 4.5. Then, it is very important to monitor the temperature of ice particles on the outlet (control point) of IJ system. Graph, which represents correlation between average diameter of ice granules vs. ice temperature at the top control point of the evaporator shown on Figure 4.6.

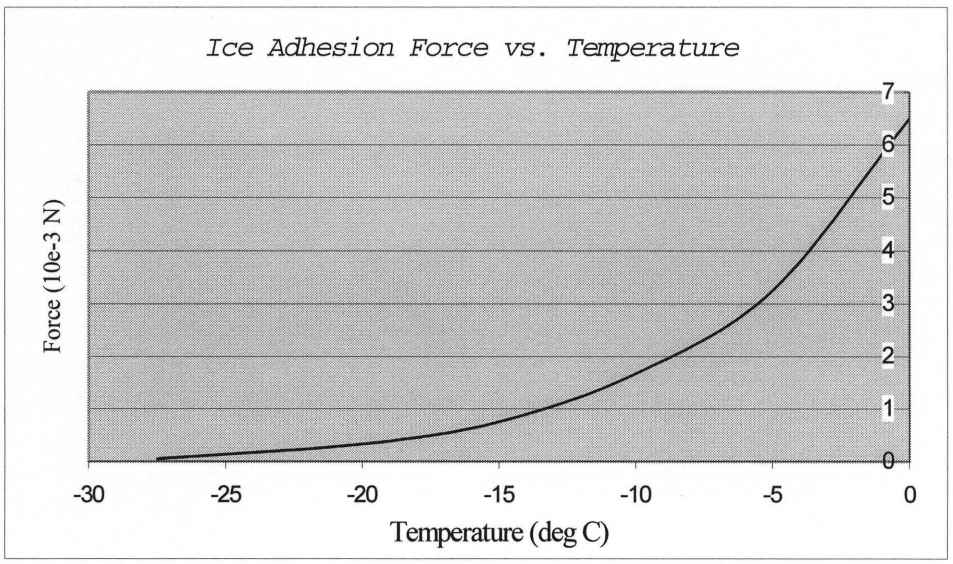

Figure 4.5 Force required separating two ice spheres at ice saturation against temperature.

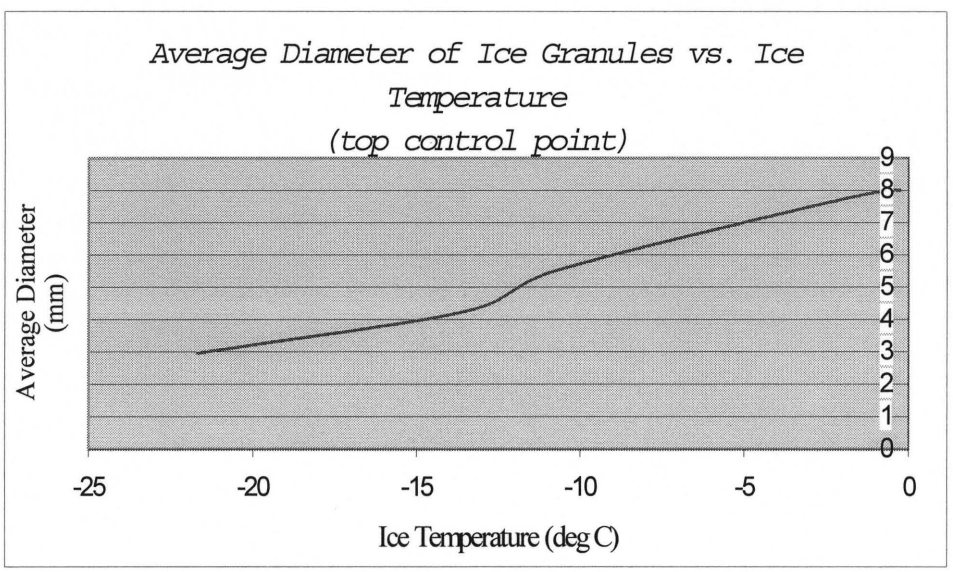

Figure 4.6 Size distribution of ice particles vs. ice temperature at evaporator outlet.

4.2 Experimental Results for Liquid Nitrogen Cooling Media

In the previous set up (HT-55 Galden as a cooling media), the ice productivity and quality were limited by coolant temperature and flow rate. TurboJet System supplies coolant media with constant temperature and flow rate. The strength of adhesion of ice particles decreases dramatically in the domain of low temperatures (Figure 4.5). Then the cooling power provided by TurboJet System is not enough for producing of ice of desired temperature and size distribution. The minimum reached temperature of ice at the top control point of IJ System did not exceed –25°C and as a result of this, the average diameter of ice granules remained high with a value ~2.95 mm according to flow rate 10-20 ml/min. Furthermore, the effectiveness of previous experimental prototype was not high because of very little amount of quality ice (ice of needed particle size distribution) provided by the system. Another disadvantage is very high time constant of the system, which not allowed to operator the prompt start and continues work with given, set up. Time constant of the system is in the range from 10 min to 20 min depends on the water flow rate into the system. Obviously, different type of cooling media has to be used to overcome these obstacles.

For the next experimental laboratory prototype, liquid nitrogen was used as a cooling media. In order to provide enough torque for ice crushing inside the evaporator, the original Hoshizaki electrical motor was substituted by high speed Dayton AC-DC universal series motor with following technical characteristics:

- motor power: 750 W;
- voltage:115 V (1 phase);

- motor speed: 10,000 rpm.

Motor was mounted on the original Hoshizaki gearbox speed reducer. Database for this set up is presented below.

4.2.1 Temperature Distribution along the Evaporator as a Function of Water Flow Rate

Based on the provided experimental data, the heat flux through the system during ice plug expansion and the time constant of the reactor for liquid nitrogen cooling media was investigated. This experiment was carried out under following experiment parameters:

- auger speed = 100 rpm;

- liquid nitrogen flow rate: 750 SCFH (air calibrated);

To remain constant, liquid nitrogen flow rate high precision release valve was welded in on the cooling coil outlet. Due to the nature of liquid nitrogen evaporation (liquid to gas phase transition), it was problematic held flow rate fixed. The fluctuations of the flow rate between 500 SCFH to 1000 SCFH constrained us from using exact value. The time constant of set up with liquid nitrogen as a cooling media is about 2.5 minutes, so it reduced by 7 times compare with previous one. In the temperature field distribution inside the evaporator attention should be emphasized on thermocouples 2 and thermocouple 10. Thermocouple 2 presents the transition zone where the crystallization of ice begins. It was technically impossible to place additional thermocouples at this region of the evaporator in order to monitor the crystallization process (cooling coils would not allowed to do this). Therefore, it lead to the conclusion that the transition zone is very narrow and at the distance 24 mm from water port inlet ice creation process is very intensive inside the water volume adjacent to the evaporator wall. Thermocouple 10

placed at the distance 167 mm from water zero level shows that the temperature of ice near the evaporator wall volume is almost the same for all flow rates and about -190°C. This is very important for understanding of ice crystallization process in the volume adjacent to the auger, where probably the speed of ice crystallization is not high enough and process is not homogeneous. This non-homogeneous process of water freezing in a closed volume may be a reason for appearance of ice particles with not desirable size and temperature. Then, some technical improvements should be done in order to avoid this problem in future.

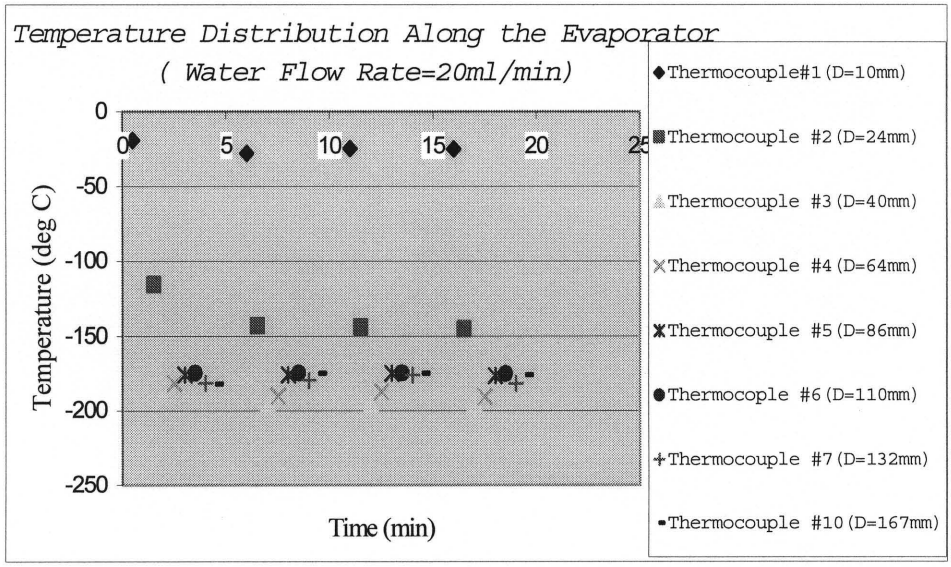

Figure 4.7 Temperature distribution along the evaporator vs. time for various water flow rates and liquid nitrogen as a cooling media.

The time constant of the system is sufficiently shorter for the liquid nitrogen cooling media.

4.2.2 Temperature Distribution along the Evaporator versus Distance from Water Inlet Level

The temperature distribution along the evaporator vs. distances from water zero level for the fixed time intervals are interesting issue. Three duration of time of 2.5, 5 and 10 minutes from the moment of coolant valve opening were considered. These graphs give an information about the time constant and the time inertia of this system. The time constant of the system is in the range from 2.5 minutes to 5 minutes depends on water flow rate into the system. Minimum temperature region for this system lies in the range from 50 mm to 80 mm from water zero level (water inlet port). Then, in this region the highest expansion forces are developed and process of crystallization and separation of ice particles is the most intensive.

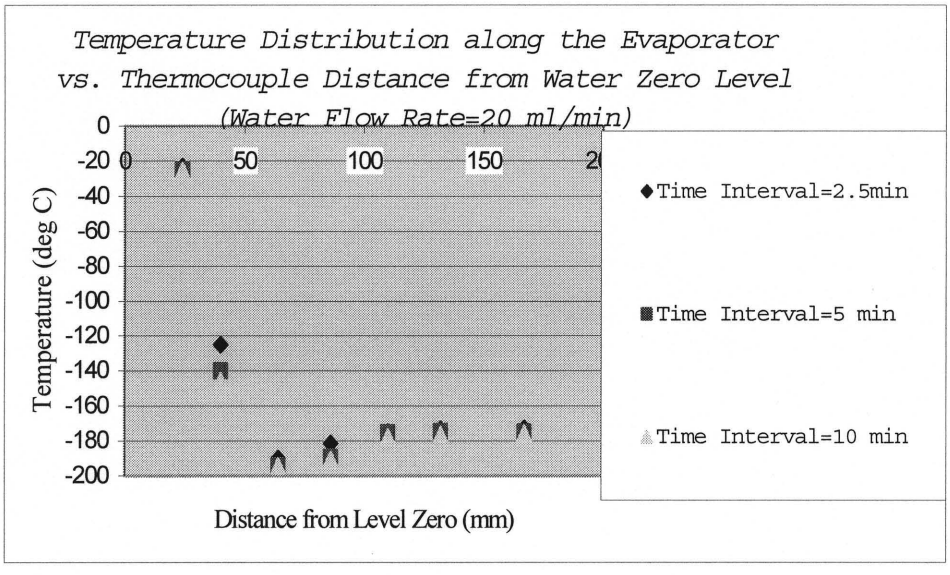

Figure 4.8 Temperature distribution along the evaporator vs. distances from water zero level for three distinct time duration.

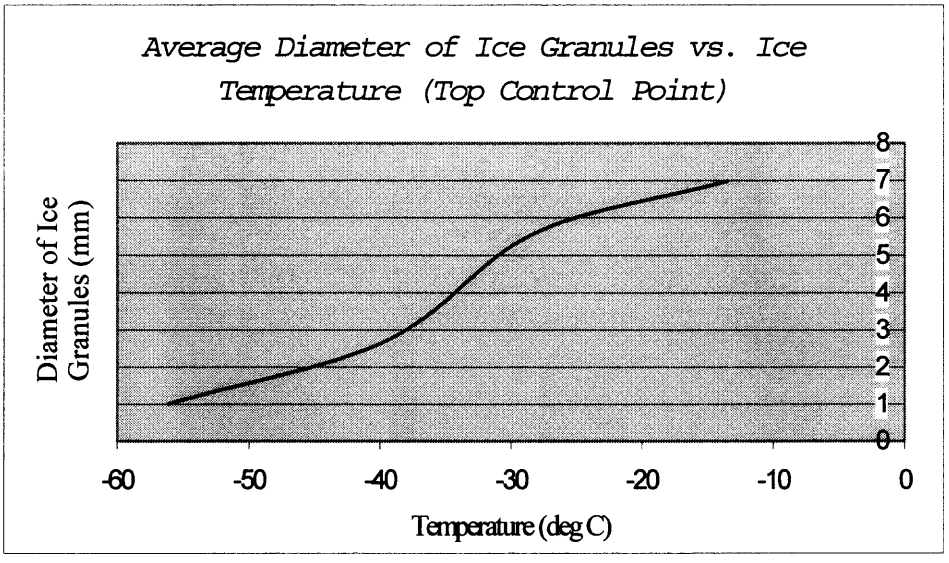

Figure 4.9 Ice granules size distribution vs. water flow rate.

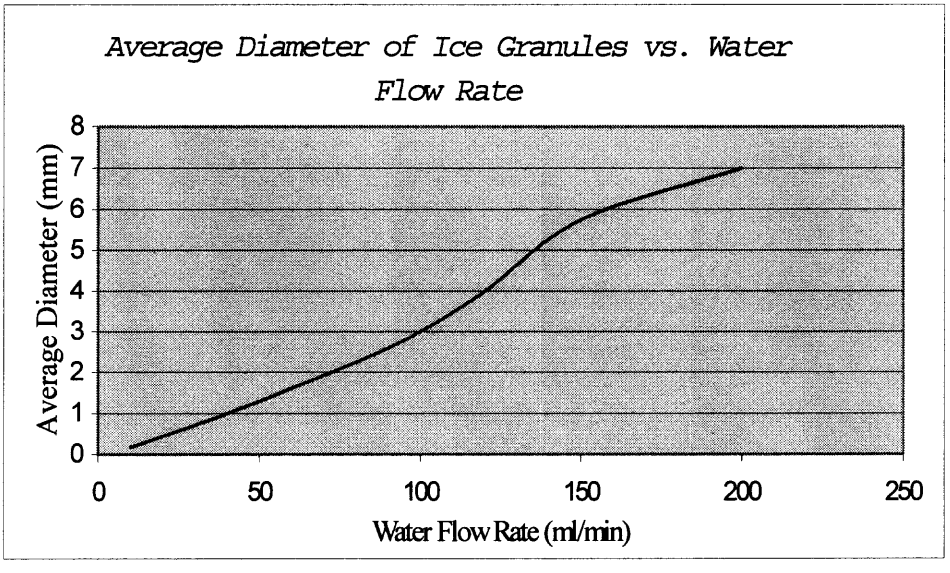

Figure 4.10 Ice particles size distribution vs. ice temperature at the top control point of the evaporator.

The process of ice particles supercooling conducted in the upper part of the evaporator and continued the process of ice particle separation. Also, this region could be possibly a reason for the process of sintering of ice particles, which had a different surface temperature. As a result, the particles of the undesirable size and shape could be formed.

4.2.3 Ice Particles Granulometric Composition as a Function of Ice Temperature at Control Point

The strength of the adhesion of ice particles decreases substantially in the low temperature domain as shown in Figure 4.5. The results are given in Figure 4.9 and provide another opportunity to control the average diameter of ice particles by controlling the temperature of the coolant media temperature and flow rate. The functional dependence of the average diameter of ice granules versus water flow rate is given in Figure 4.10.

4.3 Comparative Analysis of Experimental Results for Galden HT-55 and Liquid Nitrogen Cooling Media

The following table represents the important technical characteristics for both experimental laboratory prototypes.

Table 4.1 Technical Characteristic of Two Evaporator-Auger Experimental Set-Ups

Coolant Media Type	HT-55Galden Liquid	Liquid Nitrogen
Motor Type	one phase AC	universal AC-DC
Motor Speed (rpm)	1,000	10,000
Motor Power (W)	125	750
Gearbox Type	Hoshizaki 2 stages	Hoshizaki 2 stages
Gearbox Ratio	100:1	100:1

The properties of coolant media were presented in Table 4.2.

Table 4.2 Properties of Cooling Media

Type of Cooling Media	Cooling Media Temperature (°C)	Cooling Media Flow Rate
HT-55 Galden	-72	0.129 kg/s
Liquid Nitrogen	-196	7.866E-6 m^3/s

Two different types of coolant media were analyzed with zero water flow rate into the evaporator. The results of this analysis are presented on the Figure 4.11. The monitoring of the temperature distribution between two thermocouples were used. Thermocouples 2 and 6 were situated in the bottom (transient) and middle part of the evaporator and allowed to analyze the behavior of IJ system in the evaporator region where ice crystallization started and ice supercooling, deformation and compressive fracture process have continued. The cooling ability of the liquid nitrogen is essentially higher than Galden HT-55 coolant liquid. The ice crystallization process at the distance of 24 mm from water level input conducted very intensively. The temperature drop at the thermocouple #2 (D=24 mm) is in a range from -150°C to -80°C, and this results in the productivity of the IJ system as well as the quality of ice granules. There is a certain advantage of using liquid nitrogen as a cooling media. The time constant of the system is about 5 times higher for a low flow rates domain and 2.5-3 times higher for the high one.

Ice temperature on the output of IJ system in case with liquid nitrogen reaches -55°C that influences the mechanical properties of ice nucleus such as strength, elasticity modulus and stiffness. Then, it is possible tuning up the proper parameters of IJ system for each specific cleaning problem by simple variation of a coolant temperature.

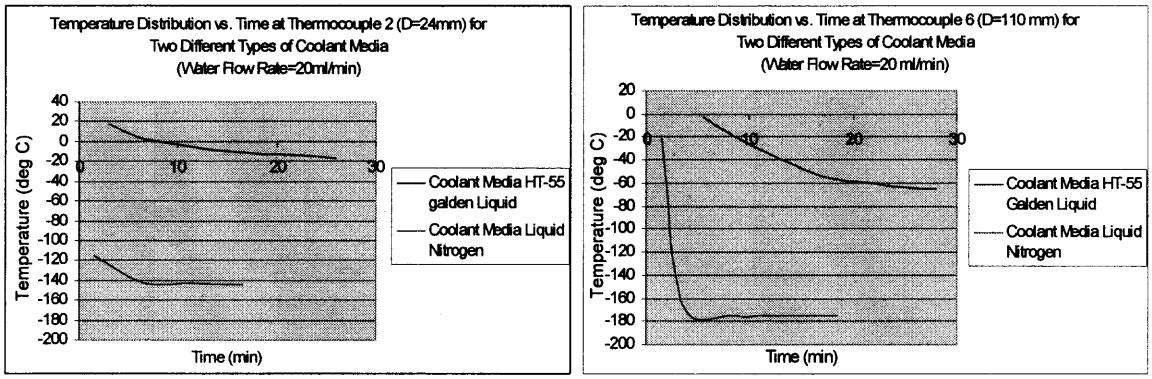

Figure 4.11 Temperature distribution at thermocouples 2 and 6 (D=24 and 110 mm from water inlet level) vs. time for two different coolant media.

The picture of temperature distribution vs. thermocouple position from water zero level for liquid nitrogen and Galden HT-55 liquid is identical to the results discussed above. The time constant of IJ system has improved about 5 times in case of liquid nitrogen. The temperature field along the evaporator is generally homogeneous except for the bottom-situated thermocouples. Appendix F presents a complete set of the experimental data for the Galden HT-55 and liquid nitrogen experimental set-ups.

4.4 Experimental Study of Particles Distribution within the Freezer

The freezer can be separated into three distinct zones along its height: water freezing and ice plug formation zone, ice formation and decomposition zone and ice particles cooling zone. In order to investigate distribution of these zones along the freezer as well as the state of the water mater (percentage, granulometric composition and space distribution of the solid phase) a special experiment was designed and executed. After steady conditions of ice particles production were attained, the auger and consequently the content of the water mater were rapidly extracted from the freezer with a specially designed pulling

device. (Figure 4.12). Adhesions as well as compressive forces that developed inside of the evaporator in course of ice nucleation assured that the ice structure that filled auger volume remained stable during the extraction.

The images of ice distribution along the extracted auger were recorded. These images are depicted on Figures 4.14 and 4.15. It has to be pointed out that two different cooling schemas were investigated in course of experiments: dual-side cooling schema, when cooling media flows through the evaporator and auger, and one side cooling schema when coolant bypasses the auger.

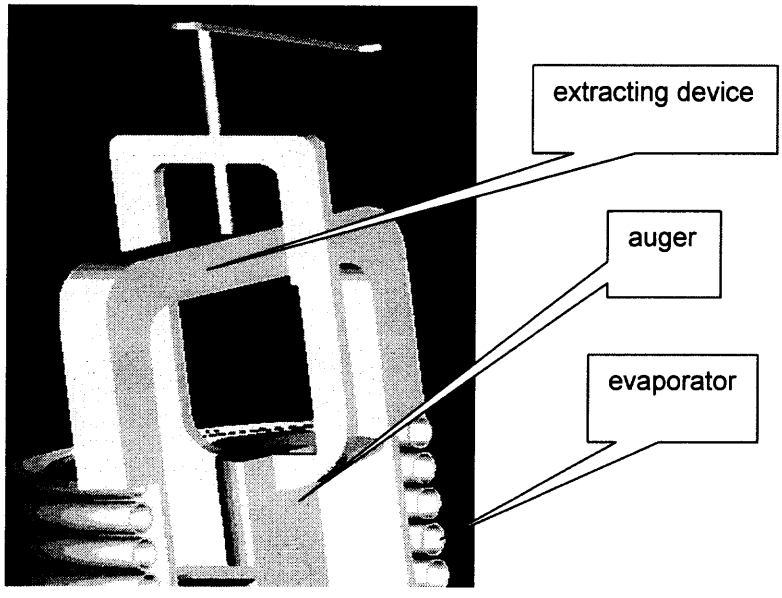

Figure 4.12 Schematic of auger extraction procedure.

Single and dual side cooling schemas are presented on Figure 6.3. Ice nucleation results for distinct cooling zones and cooling media flow rate of 5.9E-03 m^3/s are presented in Figure 4.13.

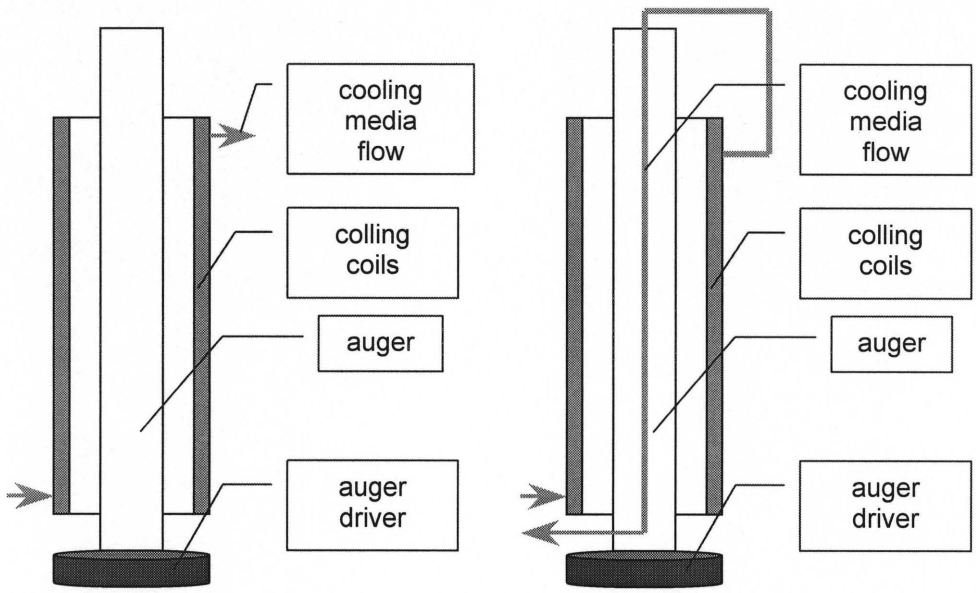

Figure 4.13 Single and dual side cooling schemas.

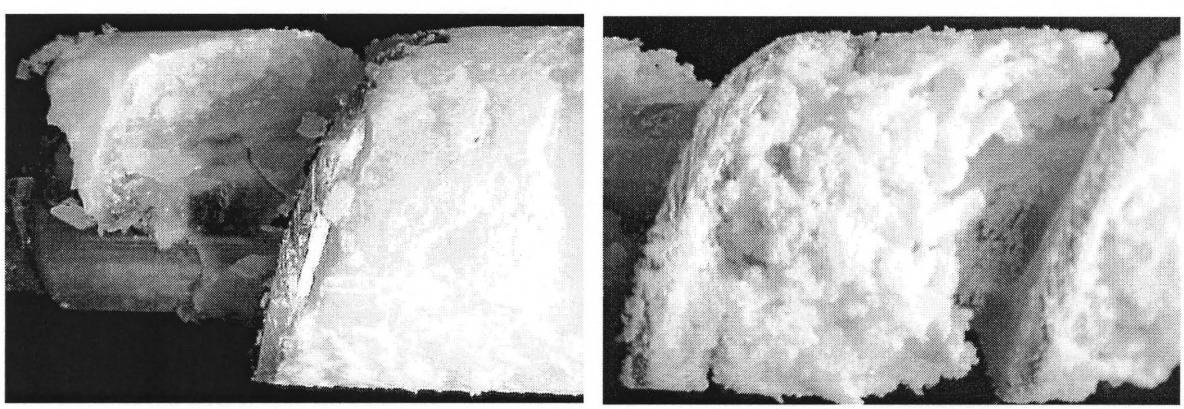

(a) (b)

Figure 4.14 Ice plug in different stages of its formation in course of single side cooling schema: a) nucleation and cooling stage, and b) supercooling and decomposition stage.

Dual side ice nucleation pictures are depicted in the Figure 4.15. Under this cooling schema, the ice nucleation process has propagated into two directions - from the inner evaporator wall to the auger stem and in the reverse direction.

Due to the character of ice propagation, the temperature field through the ice plug in the nucleation stage is homogeneous, which assures the brittle mode ice throughout its depth. Compressive stress developed under this cooling schema is commensurable with the single side cooling schema and average nucleated grain has smaller size due to the extremely fast character of nucleation.

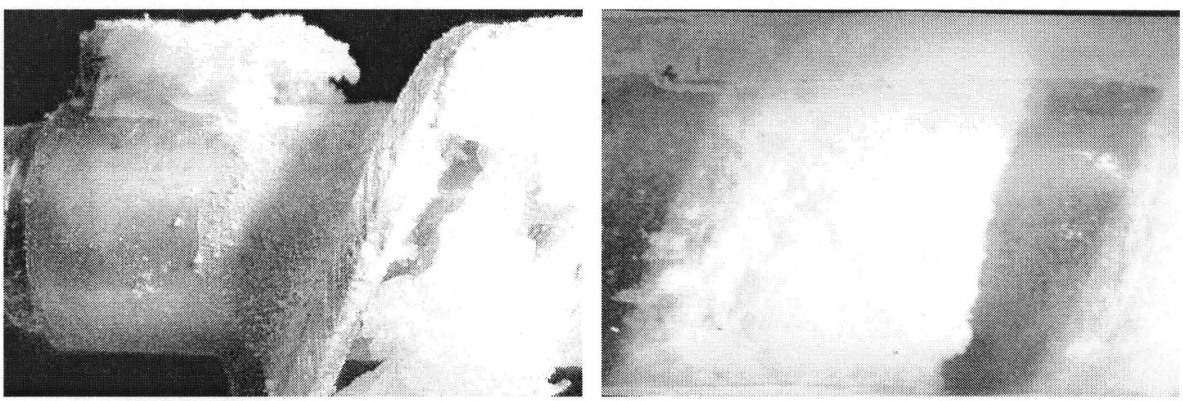

(a) (b)

Figure 4.15 Different stages of ice plug formation for dual side cooling schema: a) ice plug formation and cooling stage, and b) plug decomposition stage.

These conclusions can be drawn from the developed pictures and the corresponding granulometric compositions of the ice particles at the outlet of the system. Another important conclusion could be made: dual side cooling schema does not allowed stress relaxation of the ice plug in the near auger zone, whereas single side nucleation leads to relaxation in that zone, where ice plug is in ductile mode.

It has been taken in account that water for the IJ system provided by the city net and contains air bubbles. Michel [35] showed that Young's modulus is a function of porosity. A large volume of experiments has been made on the static modulus of

elasticity of polycrystalline ice. In general, according to Michel [35], elastic modulus can be related linearly with the porosity by an expression of the form:

$$\frac{E}{E_0} = 1 - \frac{e}{e_0} \tag{4.1}$$

where E_0 is the dynamic modulus for pure ice, e is the porosity of the ice, e_0 is the porosity of reference for each the ice is becoming a firn. This porosity is defined as the ratio of the volume of cavities to the total volume of ice. In this study, experimentally measured ice density at the specified ice temperature showed that the porosity of ice is below 3% and it did not affect the elasticity modulus much.

CHAPTER 5

GEOMETRY ANALYSIS OF EVAPORATOR AND AUGER

The geometry of the evaporator and auger are the principal parameters of the ice-making machine. Evaporator – auger geometry of three tested kinds of the icemakers (original, *A* and *B*) is presented in Table 5.1.

Table 5.1 Geometry of the Experimental Set-Ups

Set Up Type	Original	*A*	*B*
Height of the transition zone H [mm]	160	175	275
Helical way pitch P [mm]	45	15	80
Depth of helical thread d [mm]	8.4	2.5	11.2
Helical way width [mm]	4.7	2.5	6.2
Cooling coil diameter D [mm]	10	5	13
Helical way inclination θ [deg]	75	90	50

Experimental set up *A* generated the finest ice powder with the highest frequency of the fluctuations of ice powder output. The Bosch 1000 W universal AC/DC motor was chosen as the auger driver. Full course of planned experiments for this set up was not completed due to the auger failure. In this case, the duration of the ice plug formation and decomposition was very short and thus the ice powder extraction process at the evaporator outlet was almost continuous. Granulometric distribution of the generated ice particles, determined by the UTHSCSA Image Tool statistical package, obeyed the normal distribution law with average diameter of ice granules below 0.3 mm.

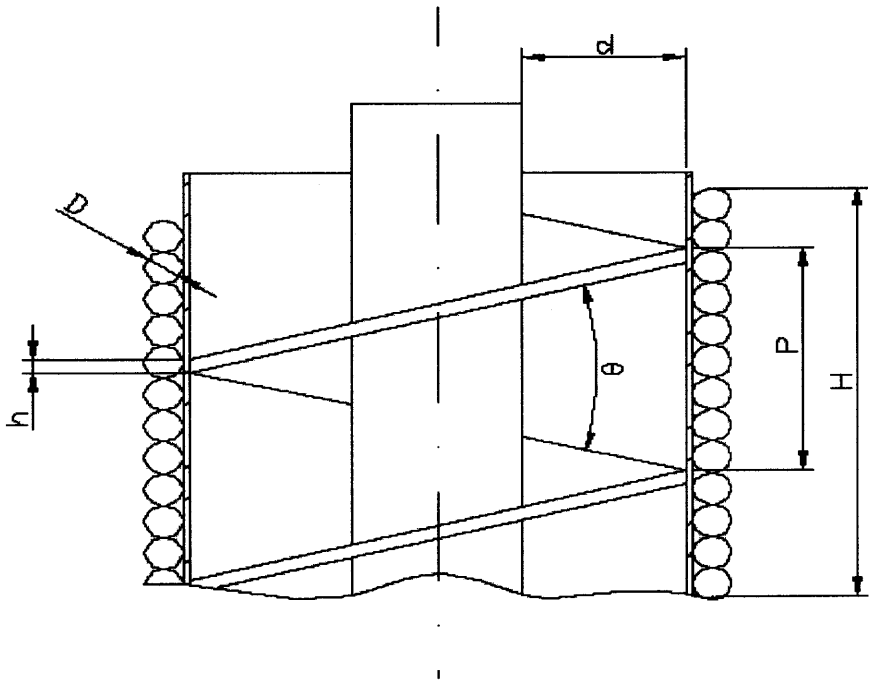

Figure 5.1 Geometry of the evaporator and auger with specified optimization parameters. Here H is the height of the heat transition zone, P is the pitch of the auger, θ is the angle developed by ascending and descending branches of helical way, d is the depth of helical thread, h is the helical way width, D is the cooling coils diameter.

It is suggested that this mode of operation of the icemaker is due to the conditions of water solidification, determined by the ratio of the thickness of the water layer between the evaporator and auger walls or so-called auger thread depth. The liquid nitrogen flow rate was in the range of ~ 0.177 m^3/min.

Experimental set up *B* was tested on a wide range of water flow rates from 20 ml/min to 250 ml/min. The liquid nitrogen flow rate was around ~ 0.8 m^3/min, which was twice higher than it was in original set up. Resulting granulometric composition was extremely non-homogeneous with a visually determined average diameter of the ice grain above 10 mm, which made the ice abrasive incompatible with existing nozzle block device. The same granulometric composition pattern was observed throughout the entire range of water flow rates. The active volume for 10 mm cross-sectional layer of the

decomposition chamber was ~ 8.96×10^{-6} m^3 in comparison with set up *A* where it was 3.75×10^{-7} m^3. The active decomposition volume of set up *B* was approximately 24 times higher than in set up *A* and the cooling power provided by the liquid nitrogen was insufficient for the fine grain nucleation and high compressive and shear stress field generation. One of the very important parameters of the evaporator-auger system is a ratio of the active decomposition volume to the actual length of the ice plug measured along the helical ways. This parameter explains where formation of the ice plug is finalized and where the decomposition process is started. It is quite difficult to determine its value without employing the series of the strain gauges along the evaporator inner wall and was impossible to achieve in the present set up.

The following parameter should be introduced: the ratio of the rotational velocity of the auger to the active decomposition volume. Based on the geometrical parameters of the presented experimental set ups and auger rotational velocities, the following conclusion could be made: the ratio ω/V_d, where ω is an angular velocity of the auger and V_d is an active decomposition volume, should be maximized. Those values are presented below in the Table 5.1.

Table 5.2 Parameter ω/V_d for Original, *A* and *B* Set-Ups.

Model #	Original	Set Up A	Set Up B
ω/V_d (rad/sec×m^3)	26.45×10^6	2667×10^6	0.837×10^6

This parameter reached its maximal value for the experimental set up *A* and shows that for small active decomposition volumes auger rotational speed can attain quite high values due to extremely fast nucleation of the ice plug in the active decomposition

volume. Furthermore, the following conclusion could be deducted from these results: helical way thread depth can be minimized down to the point when it reaches an average size of the ice granules. It means that helical thread depth of auger has an average diameter of ice granules as a physical constraint. For the system, which supposedly has to produce ice abrasive of mesh10, (average diameter 2.0 mm) the thread depth could not be less than that value. Pitch value may be flexible and has to assure the complete infill of the active decomposition volume.

Height of the heat transition zone has to be sufficient enough to complete transition of the solidified ice plug to the brittle mode. The placement of the impedance gauges along the original set up evaporator wall had proven that nucleation of the ice plug occurs at the bottom heat transition zone with consecutive decomposition and further cooling of the ice powder does not result in change of the granulometric composition or temperature of ice abrasive. All experimental set-ups had an extensive heat transition zone to ensure transition of the ice plug to the brittle mode and its decomposition.

Dual-side cooling schema was introduced in the original and *A* set ups and allowed achieving the most homogeneous temperature field distribution along the cross-section of the ice plug. Experimental data of the temperature distribution along the evaporator confirm that system time constant for the set up *A* has a lowest value, which shows that this system has the minimal thermal inertia. A main concern during the design of the set up *A* auger was optimization of its mass. Hollow auger design is necessary for two purposes: minimization of the auger and set up total mass along with its time constant and possibility to provide dual-side cooling with cooling media flow through the

auger. Although auger and total mass should be minimized, a major constraint was the structural integrity of the system and its ability to sustain the compressive and shear stresses generated in course of the ice plug formation and decomposition.

CHAPTER 6

ANALYTICAL AND NUMERICAL STUDY OF ICE PLUG DECOMPOSITION

6.1 Theoretical Techniques for Description of the Ice Decomposition under Compression

The formation and decomposition of water ice was a subject of a numerous studies and a number of theoretical techniques were suggested for process description. There are several numerical techniques, which in principle are applicable to the analysis of the system in question. The phenomenon of ice nucleation under normal conditions was fairly well investigated by Hobbs [1] and Eranti [2].

Theoretical analysis of ice failure under compressive stress includes the estimation of the flaw size in the ice plug during formation, stresses origination and finally decomposition. The flaws can be micro-cracks, grain boundaries, or any other imperfections, which are shown to behave as a flaw. The theory of compressive fracture of a flawed specimen is given by Ashby and Hallam [3]. The nucleation of cracks under compressive stress is generally due to dislocation pile-up at the grain boundaries and relief of stress concentration by parting along the grain boundaries. The phenomenon of crack nucleation has been well investigated for low to moderate loading conditions and the studies indicate that crack nucleation is well described by of the delayed elastic strain criterion [5] (Figure 6.1). In this study, the behavior of ice under dynamically applied high amplitude compressive and shear stress was investigated.

There are two broad types of ice structure which are worth distinguishing:

- granular ice, which is a conglomerate of randomly oriented crystals of ice, typically of grain size 1-3 mm. It is also known as random polycrystalline ice and equi-axed ice.

If the crystal orientations are truly random, then the mechanical properties of the ice are, of course, isotropic. This is known as T-1 ice.

The columnar ice, which is an arrangement of crystals oriented so their *c*-axes preferentially lie in-plane. Such crystals are generally in the size range 3-100 mm and under normal growth conditions the crystals are elongated in the vertical direction with their *c*-axes randomly distributed in the horizontal plane. This ice is generally refereed to as S-2 ice and is found in the lower levels of lake and river ice. It is transversely isotropic (orthotropic) in properties; that is, its properties are the same in all directions in the horizontal plane.

The continuum behavior of these two types of ice, granular and columnar, is markedly similar in form, with minor quantitative differences. The conditions of ice nucleation in the system (Figures 4.14 and 4.15) bring about formation of the granular ice known as T-1 ice. The fast and turbulent character of ice nucleation led to this conclusion.

When ice is subjected to a stress, it initially deforms in three distinct ways: it undergoes an immediate elastic strain ε_e, a transient time-dependent delayed elastic strain ε_d, and a time-dependent non-linear viscous creep strain ε_v. The "delayed elastic" strain ε_d is also referred to as primary creep, and is largely recoverable on unloading; the "viscous" strain ε_v is referred to as the secondary creep, and is permanent (Figure 6.1 b).

To describe this stress-strain behavior for granular ice, the well-verified constitutive laws exist. In fact these laws are well approximated by conventional equations relating deformation and stresses in a plastic-elastic material (Figure 6.1 a). Once the stage of apparently stable secondary creep has been reached, and all transient

creep effects have become negligible, the deformation process becomes more complex again, and a stage of tertiary creep may be entered [1].

A simple spring-and-dashpot model of the rheological description of ice behavior is shown in Figure 6.1 (a), and schematic illustration of the strain history during the constant load test is shown in Figure 6.1 (b). The phases of deformation are as follows (Figure 6.1 b).

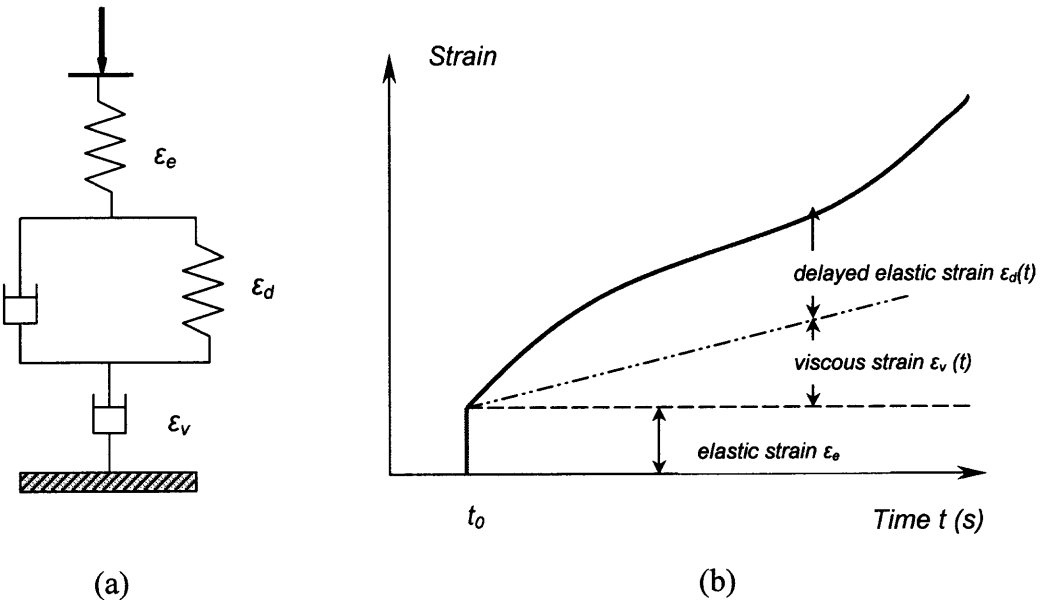

Figure 6.1 Simple spring-and-dashpot model of the rheology of ice. Deformation initially occurs in three ways: by simple elastic strain ε_e, by recoverable delayed elastic strain ε_d, and by permanent non-linear viscous creep ε_v, and strain history for a constant stress suddenly applied at time $t=t_0$.

An alternative nucleation criterion was introduced for high stress nucleation conditions [5]. This criterion assumes that the crack nucleation under compressive stress occurs simply when the lateral tensile strain induced by Poisson expansion reaches level already defined as critical for tensile crack nucleation. In case of tensile crack nucleation, the strain criterion is given by equation:

$$\varepsilon_n = \varepsilon_o + k_2/\sqrt{d} \tag{6.1}$$

where ε_0 and k_2 are constants with values $\varepsilon_0 = 6.3\times10^{-5}$, $k_2 = 2.1\times10^{-6}$ $m^{1/2}$.

Now under compressive stress σ_{11} the lateral tensile strain ε_{22} is given by:

$$\varepsilon_{22} = -\nu\sigma_{11}/E \tag{6.2}$$

where ν is a Poisson's ratio.

The compressive nature of forces is denoted by minus sign.

Another approach is based on the assumption that the size of flaws (cracks and wings) developed in the course of ice decomposition are constant. Had this assumption been accepted the flaws and wings in the case of the study are in order of a =1.5 mm and l=a/2 and the study of phenomena in question becomes rather trivial. Unfortunately, this assumption contradicts experimental results of the ice granulometric composition statistically determined for the different water flow rates. The variable fractions were observed in course of the experiments.

Another effective approach to the process modeling is the geometric scaling of the region of the water solidification. Sanderson [5] suggested that, if the whole sample is scaled up geometrically, then the larger one will contain flaws, which are proportionally scaled up. In this case fracture mechanism analysis shows that if the linear dimension of the sample increases by a factor ξ^2 then according to Bazant and Kim [4] the fracture strength will decrease by a factor $\xi^{-1/2}$. Therefore, if geometrical dimensions of the specimen will be increased by a factor of 10 then the predicted strength is 5.7 MPa. However, this statement is based on the doubted physical assumption that a larger sample contains larger flaws. This requires experimental proof that, for example doubling sample

size automatically and precisely doubles flaw size. The performed study did not substantiate this notion. Thus, it was not used for process interpretation.

One of the most practical approaches to the study of materials defects is the Weibull theory [28]. This theory is based on a realistic assumption that for the larger size samples there is a higher probability of containing the flaws from the tail ends of the statistical distribution. Thus, more probably a larger sample contains larger flaws. This theory was intended principally for tensile fracture. It is not necessarily true for the compressive fracture. However, if the compressive strength would behave in the same way one should expect the strength to be a function of volume V in the form $V^{1/bf}$ where b_f is a statistical parameter characterizing the flaw-size distribution (after Dieter) [5]. Unfortunately, the range of b_f is not well defined for water ice. The experimental study of the fresh water ice by Lavrov [29] indicates that the factor b_f is approximately equal to 15, while the direct measurements by Gold [30] for S-2 type ice ranges b_f as low as 1 or 3. To compare, for glass it lies in a range 2-5, for rocks and ceramics b_f is about 15.

According to Sanderson [5] the value of b_f varies in the range of 1-15, the most realistic magnitude of b_f for the brittle mode of ice is 3. This value was used in the presented study. The value b_f can be elaborated by the X-ray analysis of flaws distribution. This experiment however was beyond of the scope of the study in question. Compressive fracture stress or stress required to bring about the decomposition of ice plug is proportional to the area of contact A or to the square of the linear dimension of the ice plug ξ (6.3). According to the Weibull theory these stresses can be represented by the equation:

$$\sigma \sim A^{-3/(2bf)} \tag{6.3}$$

or

$$\sigma_n = k_n A_n^{-\left(\frac{3}{2b_f}\right)} \tag{6.4}$$

where σ_n is a thermally generated compressive fracture stress developed during ice plug decomposition, A_n is an area of contact of the ice plug with the evaporator wall. The empirical coefficient k could be estimated applying the least-squire method:

$$k = \frac{\sum_{i=1}^{n} \sigma_i A_i^{-\left(\frac{3}{2b_f}\right)}}{\sum_{i=1}^{n} \left[A_i^{-\left(\frac{3}{2b_f}\right)} \right]^2} \tag{6.5}$$

In the case in question Ai is the area of the interface between the ice plug and the heat sink and σ_i is the maximal thermally generated compressive stress at a corresponding water flow rate. Coefficient k calculated for the statistical parameter b_f lying in the range of 3-15 and determined by Gold [29] and Lavrov [30] is presented in table 6.1

Table 6.1 Coefficient k of Weibull Distribution Determined for Distinct Values of Statistical Parameter b_f

b_f	3	5	10	15
k [Pa×m^3]	0.572E06	1.797E06	4.197E06	5.557E06

It can be assumed that the statistical parameter b_f determines the ice structure. For the ice of S-1 type this coefficient is in an order of magnitude higher than that for the T-1 polycrystalline type of ice. The conditions of ice formation prescribed the major differences in the ice compressive decomposition behavior. The duration of ice formation as well as the temperature gradient throughout the ice plug resulted in different size and

structure of crystals, which formed the ice plug. This leads to the higher compressive or tensile stresses required decomposing the ice plug.

The ice granulometric composition could be used for the thermal compressive stress analysis. The existing mathematical techniques (6.1,6.2) for description of the system in the case (the T1 granular ice) adequately describes process at moderate stresses. An additional study, however, is needed to address this phenomenon at high stresses.

6.2 Analytical Study of the Heat Exchange between Evaporator and Freezer

Both water freezing and ice decomposition are determined by the heat removal from water flow. In order to investigate this process, heat transfer analysis of the evaporator part was conducted. Heat flux through the system was calculated using Pro/MECHANICA 2001 thermal analysis mode and approximate estimation of the coefficient of heat transfer from the water matter to nitrogen. In the system shown in Figure 6.2, heat is transferred from the water to nitrogen. Heat extracted from the water matter is generated in the course of cooling of liquid water and ice and in the course of ice formation. Heat absorbed by the nitrogen flow is consumed for nitrogen vaporization and in a small degree for vapor heating. Heat transfer involved convection heat exchange between the water and ice and the wall and between the liquid and vapor nitrogen and the coil. It also involves heat conduction through the wall of the water freezer and the evaporator's coils. All processes of heat transfer and generation occur simultaneously (Figure 6.2).

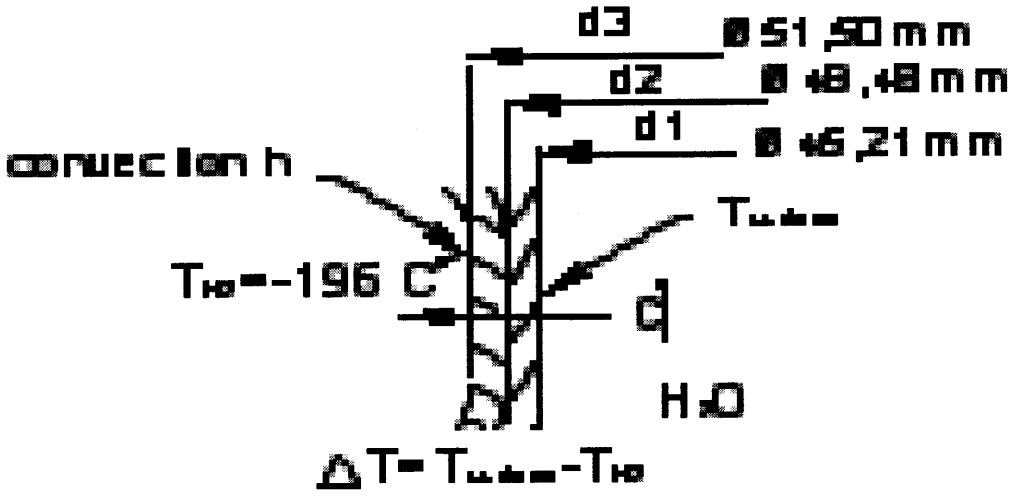

Figure 6.2 Schematic of the heat flow path.

Total average thermal resistances between nitrogen and the internal surface of the freezer wall and heat flux absorbed by the water stream in the course of ice production were chosen as parameters specifying the process of ice powder formation. The average coefficient of heat transfer from the stream of nitrogen to the internal wall of the copper pipe was determined as the result of the analysis. The temperature of the internal freezer wall T_s is graphically presented on Figure 6.3. The tabulated data for T_s are presented in Table 6.2. The temperature Ts was measured by the thermocouples located at levels of 24, 40, 64, 86,110, 132, and 167 mm from water inlet. The measurements were performed for the several water flow rates.

Table 6.2 Temperature of Inner Freezer Wall for Selected Water Flow Rates

0 ml/min			20 ml/min		40 ml/min	
Location [mm]	$T_{surface}$ [C°]	ΔT [C°]	$T_{surface}$ [C°]	ΔT [C°]	$T_{surface}$ [C°]	ΔT [C°]
24	-149	47	-25.3	170.7	-24.5	171.5
40	-187	9	-145.7	50.3	-149	47
64	-187.3	8.7	-192	4	-191.1	4.9
86	-187.5	8.5	-190.3	5.7	-174.3	21.7
110	-187.9	8.1	-177.7	18.3	-173.2	22.8
132	-188.2	7.8	-176.5	19.5	-174.7	21.3
167	-188.7	7.3	-175.6	20.4	-173.9	22.1
80 ml/min			100 ml/min		150 ml/min	
Location [mm]	$T_{surface}$ [C°]	ΔT [C°]	$T_{surface}$ [C°]	ΔT [C°]	$T_{surface}$ [C°]	ΔT [C°]
24	-110.5	85.5	-73.5	122.5	-58	138
40	-186.3	9.7	-172.7	23.3	-152.5	43.5
64	-189.6	6.4	-180.6	15.4	-165	31
86	-170.3	25.7	-175.9	20.1	-160	36
110	-171.5	24.5	-168.5	27.5	-159	37
132	-172.7	23.3	-167.7	28.3	-158.7	37.3
167	-172.9	23.1	-169.9	26.1	-158	38

The temperature gradient between the interior of the freezer wall and the liquid nitrogen flowing through the cooling coils ΔT and is presented on Figure 6.3.

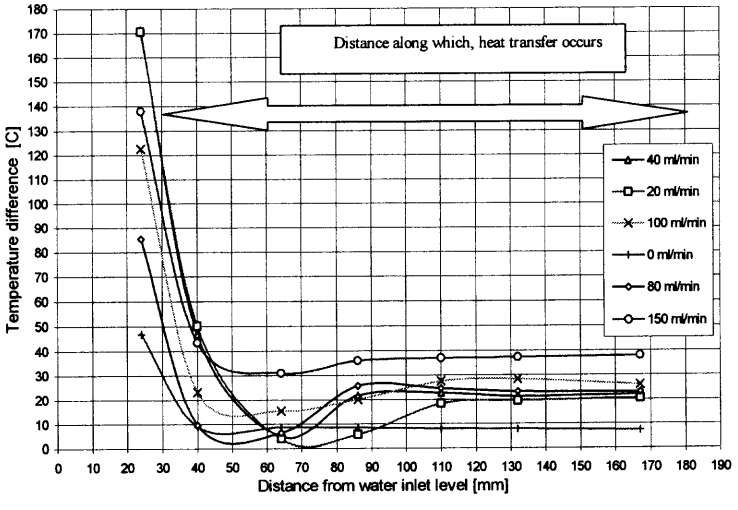

Figure 6.3 ΔT parameter plotted against the distance from water inlet level.

The integral $\int_{0.03}^{0.18} \Delta T(x)dx$ determined from Figure 6.3 was used for assessment of an average heat transfer in the system. The total resistance of the system can be calculated as follows:

$$R_{tot} = \frac{1}{\pi \cdot x_{tot}} \cdot \left[\frac{ln\left(\frac{d_2}{d_1}\right)}{2 \cdot k_{1-2}} + \frac{ln\left(\frac{d_3}{d_2}\right)}{2 \cdot k_{2-3}} + \frac{1}{h \cdot d_3} \right] \tag{6.6}$$

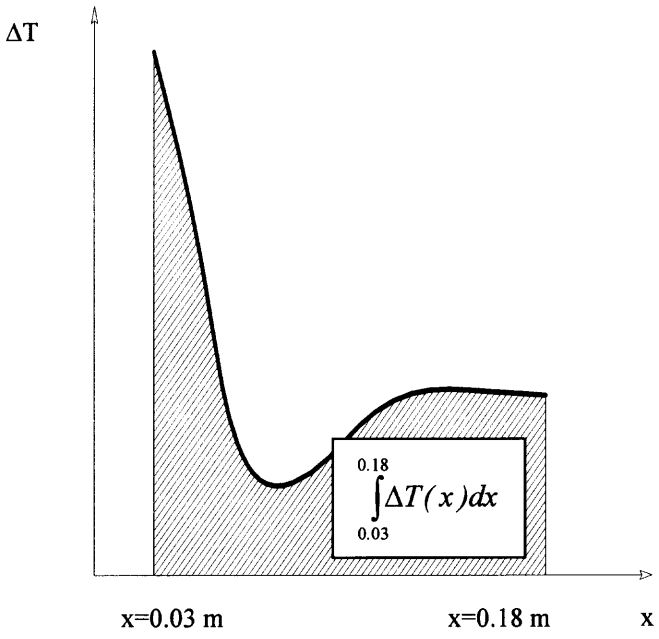

Figure 6.4 Characteristic curve of the temperature distribution at the inner evaporator wall vs. distance from the water inlet level.

where x_{tot} = 0.15 m is the length of the heat transition zone along which heat transfer occurs, k_{1-2} = 11 W/ m×K is a heat transfer coefficient for stainless steel at temperature -150°C, k_{2-3} = 408 W/ m×K is a heat transfer coefficient for copper at temperature -150°C, d_1 is an inside diameter of the evaporator, d_2 is an outside diameter of the evaporator, d_3 is

a distance from the evaporator center line to the inside surface of the cooling coil, h is convection coefficient of the liquid nitrogen to the inner surface of copper tubing.

Since $x_{tot} = \int_{0.03}^{0.18} dx$, the formula for total resistance can be expressed as follows:

$$R_{tot} = \frac{1}{\pi \cdot \int_{0.03}^{0.18} dx} \cdot \left[\frac{ln\left(\frac{d_2}{d_1}\right)}{2 \cdot k_{1-2}} + \frac{ln\left(\frac{d_3}{d_2}\right)}{2 \cdot k_{2-3}} + \frac{1}{h \cdot d_3} \right] \tag{6.7}$$

where R_{tot} is the total resistance along the heat flow path, k_{1-2}, k_{2-3}, d_1, d_2 and d_3 are the parameters described above.

Heat absorbed by nitrogen is given as follows:

$$\dot{Q}_{tot} = \frac{\int_{0.03}^{0.18} \Delta T(x)dx}{R_{tot} \cdot \int_{0.03}^{0.18} dx} = \frac{\int_{0.03}^{0.18} \Delta T(x)dx}{\frac{1}{\pi \cdot \int_{0.03}^{0.18} dx} \cdot \left[\frac{ln\left(\frac{d_2}{d_1}\right)}{2 \cdot k_{1-2}} + \frac{ln\left(\frac{d_3}{d_2}\right)}{2 \cdot k_{2-3}} + \frac{1}{h \cdot d_3} \right] \cdot \int_{0.03}^{0.18} dx} \tag{6.8}$$

where $\dot{Q}_{tot}$ is the heat absorbed by liquid nitrogen and the other terms are as described above.

To make calculations more convenient let:

$$R_{tot} \cdot \int_{0.03}^{0.18} dx = \frac{1}{\pi \cdot \int_{0.03}^{0.18} dx} \cdot \left[\frac{ln\left(\frac{d_2}{d_1}\right)}{2 \cdot k_{1-2}} + \frac{ln\left(\frac{d_3}{d_2}\right)}{2 \cdot k_{2-3}} + \frac{1}{h \cdot d_3} \right] \cdot \int_{0.03}^{0.18} dx = R_{av} \tag{6.9}$$

where R_{av} is the average out total resistance along the heat flow path, and the rest of the terms are as described above.

$$\overset{\circ}{Q}_{tot} = \frac{\int_{0.03}^{0.18} \Delta T(x)dx}{R_{av}} \tag{6.10}$$

where R_{av} is presented in (6.11), and:

$$R_{av} = \frac{\int_{0.03}^{0.18} \Delta T(x)dx}{\overset{\circ}{Q}_{tot}} \tag{6.11}$$

where $\overset{\circ}{Q}_{tot}$ is total absorbed heat calculated in (6.10).

Having, values of R_{av} for different water flow rates, the average heat transfer coefficient can be readily calculated:

$$h = \frac{1}{\left[R_{av} \cdot \pi - \frac{ln\left(\frac{d_2}{d_1}\right)}{2 \cdot k_{1-2}} - \frac{ln\left(\frac{d_3}{d_2}\right)}{2 \cdot k_{2-3}} \right] \cdot d_3} \tag{6.12}$$

where R_{av} was calculated in (6.11) and values in denominator are presented in (6.13) and (6.14).

$$\frac{ln\left(\frac{d_2}{d_1}\right)}{2 \cdot k_{1-2}} = \frac{ln\left(\frac{49.48}{45.21}\right)}{2 \cdot 11} = 0.0041 \tag{6.13}$$

$$\frac{ln\left(\frac{d_3}{d_2}\right)}{2 \cdot k_{2-3}} = \frac{ln\left(\frac{51.50}{49.48}\right)}{2 \cdot 408} = 0.000049 \tag{6.14}$$

Furthermore, the heat absorbed by the liquid nitrogen can be determined by the use of the average heat transfer coefficient. The total heat flow Q_{tot} is divided into three essential components: Q_1, which is the heat flow from liquid water, Q_2, which is the heat flow

required to freeze water, Q_3, which is the heat flow for ice cooling. The following data are required to perform this calculation: T_2, is the temperature of ice at the outlet of the system, h_1, the enthalpy of water at 20°C, is 83.9 kJ/kg, h_2, the enthalpy of water at 0°C, is 0 kJ/kg, h_3 the enthalpy of phase change for water equal to 344 kJ/kg, C_p, the specific heat for ice, is 2.26 kJ/kgK, and m, which is the flow of water. The water-cooling component of the heat flow is determined as:

$$\dot{Q}_1 = \dot{m} \cdot (h_1 - h_2) \tag{6.15}$$

where the values of h_1 and h_2 are described above.

To freeze water inside of the active decomposition volume heat flow can be calculated as:

$$\dot{Q}_2 = \dot{m} \cdot h_3 \tag{6.16}$$

where h_3 is the enthalpy of the water phase change.

The heat flow required for supercooling of the ice plug is:

$$\dot{Q}_3 = \dot{m} \cdot C_p \cdot (0 - T_2) \tag{6.17}$$

where C_p is the specific heat of ice and T_2 is the temperature of ice at the outlet of the evaporator.

Then the total heat flow is:

$$\dot{Q}_{tot} = \dot{Q}_1 + \dot{Q}_2 + \dot{Q}_3 \tag{6.18}$$

The result of the described above calculations is presented in Table 6.3.

Table 6.3 Heat Flow and Its Components

				Heat absorbed by nitrogen		
water flow [ml/min]	ice temp. at the outlet [C]	water flow [m3/s]	water flow [kg/s]	water cooling [kW]	water freezing [kW]	ice cooling [kW]
10	-71.5	1.667E-07	0.0002	0.0140	0.0561	0.0269
40	-54.9	6.667E-07	0.0007	0.0558	0.2242	0.0824
80	-41.2	1.333E-06	0.0013	0.1116	0.4484	0.1238
100	-37.4	1.667E-06	0.0017	0.1396	0.5605	0.1405
120	-34.7	2.000E-06	0.0020	0.1675	0.6727	0.1563
150	-27.6	2.500E-06	0.0025	0.2093	0.8408	0.1555
200	-12.9	3.333E-06	0.0033	0.2791	1.1211	0.0966

The numerical calculation of the ice-cooling component of the heat flow was performed by Pro/MECHANICA 2001 package. The analysis was carried out for three different water flow rates of 50, 100, and 150 ml/min and results are presented in Figure 6.5. The heat flow component for ice freezing for the analytical and numerical calculations are tabulated now for the water flow rates of 50, 100, 150 ml/min.

Table 6.4 Comparative Results of Average out Numerical and Analytical Calculations of the Heat Flow for Ice Freezing

			Heat Flow Component for Ice Freezing	
water flow rate [ml/min]	water flow rat [m^3/s]	water flow rate [kg/s]	numerical calculation [W]	analytical calculation [W]
50	1.857E-7	0.00085	113.4	107.5
100	1.667E-6	0.0017	135.95	140.5
150	2.500E-6	0.0025	146.25	155.5

The compliance of the results of both computations demonstrates the validity of the obtained data. The performed analysis shows that the freezer design could be improved to reduce the thermal resistance of the wall. Another potential improvement of

the system efficiency is the distributed cooling of the freezer. This will allow optimizing the coolant usage.

6.3 Numerical Modeling of Ice Plug Decomposition

The compressive fracture behavior of the ice plug in auger spiral motion was analyzed using the Pro/ENGINEER 2001 software package. Thermal mode of Pro/MECHANICA 2001 was chosen to analyze the thermal expansion phase of the solidified ice plug. The principal input data parameters of the model are the physical properties of ice along with its volume and boundary temperature of the evaporator and auger walls. The geometry of the solid model and the boundary conditions of thermally loaded and insulated boundary surfaces are shown on Figure 6.5. Physical properties of ice in general depend on its temperature and type. The ice crystallization conditions predetermine the ice type. Extremely short duration of freezing under very low temperature as well as turbulent character of crystallization lead to a conclusion that ice is T-1 polycrystalline type ice.

Accordingly to the chosen ice type, the model has acquired the following input data:

- ice density as a function of temperature (Figure 6.6). The functional dependency can be established through the trend line added to the curve:

$$\rho = 0.9152e^{(-0.0001T)} \tag{6.19}$$

where ρ is ice density, T is ice temperature.

- coefficient of linear expansion α of T-1 ice type is shown on Figure 6.7. The tabulated data of the coefficient of linear expansion of polycrystalline bulk ice can be found at

Hobbs [1]. Superimpose the exponential trade line into given curve the functional dependence is:

$$\alpha = 7E\text{-}05e^{0.0102T} \tag{6.20}$$

where α is a coefficient of linear expansion, T is ice temperature.

Measurements of the static elastic module of polycrystalline ice have been made by Mantis [31], Gold [30], and Voytkovskiy [32]. Values of the static Young's modulus for polycrystalline ice obtained by different workers range from 0.3 to 11 GPa. The observation indicate that when polycrystalline ice is stressed in a complete load cycle between 5 to 10 s relative movements between the grains contribute significantly to the elastic strain. Gold [30] found that the static Young's modulus Y_s increased with decreasing temperature according to the relation:

$$Y_s=(5.69\text{-}0.0648\times T) \tag{6.21}$$

where Y_s is the static Young's modulus in GPa and T is the temperature in °C.

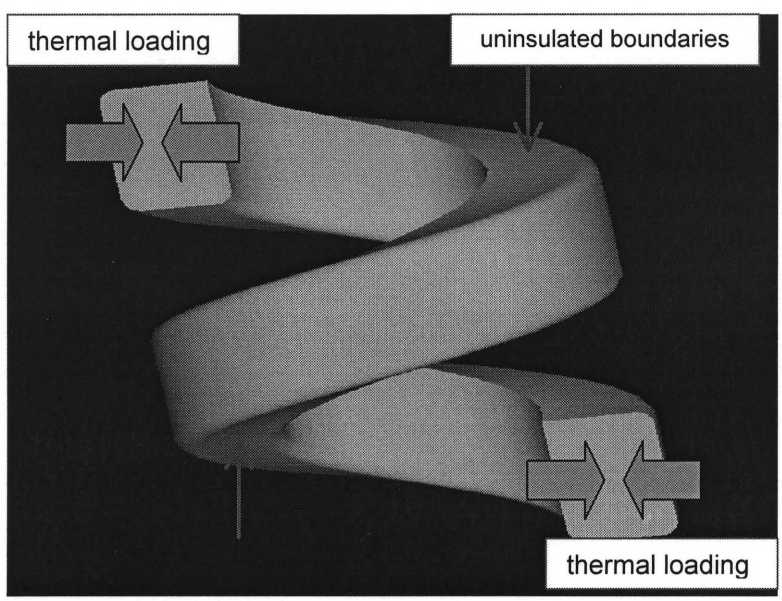

Figure 6.5 Solid model geometry with specified thermal loading and boundary conditions.

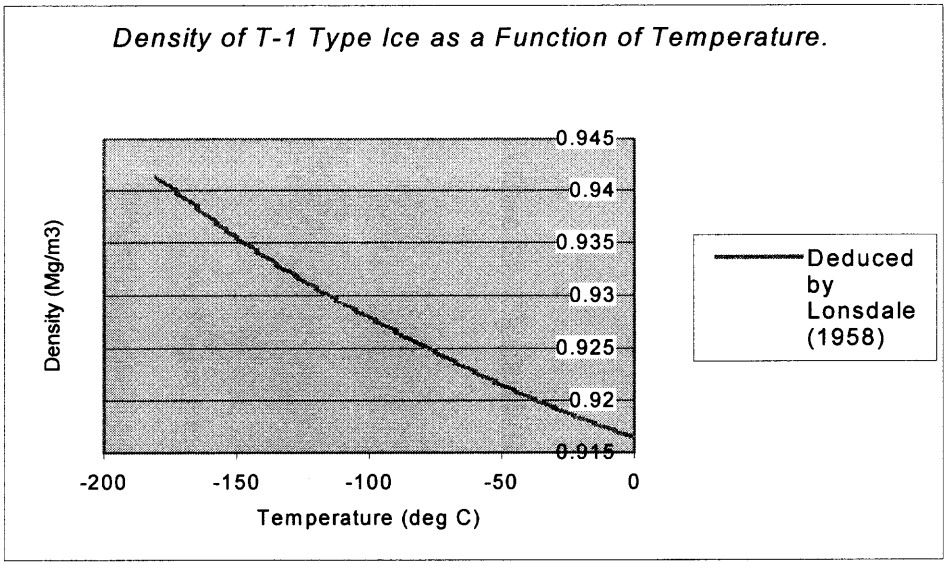

Figure 6.6 Density of T-1 ice type as a function of temperature at atmospheric pressure[1].

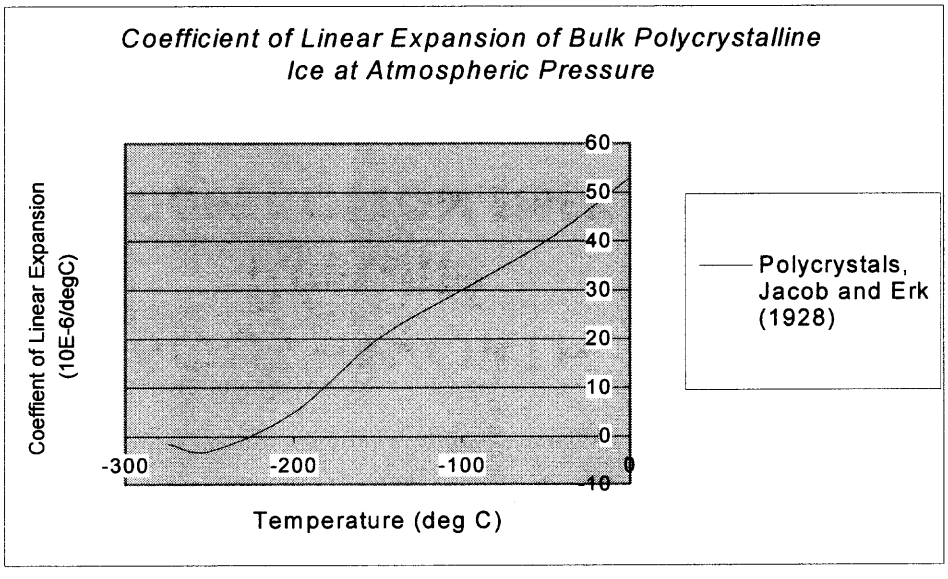

Figure 6.7 Coefficient of linear expansion of T-1 type polycrystalline ice at atmospheric pressure according to Jacob and Erk [1].

The Poisson's ratio v has almost linear dependence on the temperature T and is presented in Figure 6.16. It appears that the Poisson's ratio of polycrystalline ice is due to the temperature dependence of grain boundary slip and also of the reversible movement of dislocations. Poisson's ratio tabulated data were used in numerical modeling procedure. The specific heat was chosen accordingly to the ice type and has average value [1]:

$$\zeta=4.62\times10^{3}\ m^2/(s^2C) \tag{6.22}$$

Powell (1958) took measurements of the thermal conductivity coefficient, but recently more extensive measurements of the thermal conductivity coefficient of polycrystalline ice have been conducted Ratcliffe (1962), Dean and Timmerhaus (1963), and Dillard and Timmerhaus (1966) [1]. The thermal conductivity coefficient graph is presented on Figure 6.9. Exponential trend line added to this curve described it functionally as:

$$\lambda=1.7358e^{(-0.007T)} \tag{6.23}$$

where λ is the thermal conductivity coefficient, and T is the temperature.

Maximum shear stress was selected as a failure criterion for this material based on the forces and torque diagram presented on Figure 6.10. The infinitesimal element of the ice plug was analyzed under applied forces and two separated cases were taken into consideration (Figure 6.10). The temperature of the internal freezer wall is a boundary condition at the adjacent ice plug surface. Boundary temperature for few distinct water flow rates is shown at Figure 6.19. This temperature was measured by the thermocouple # 3 positioned at the distance of 40 mm from water inlet level. Two other surfaces of the ice plug in the model are prescribed as being uninsulated (Figure 6.13). This assumption is valid based upon the consideration of the actual device when no internal convection,

radiation and heat transfer, except due to liquid nitrogen flow, is allowed into the system, however along the helical ways heat transfer was allowed.

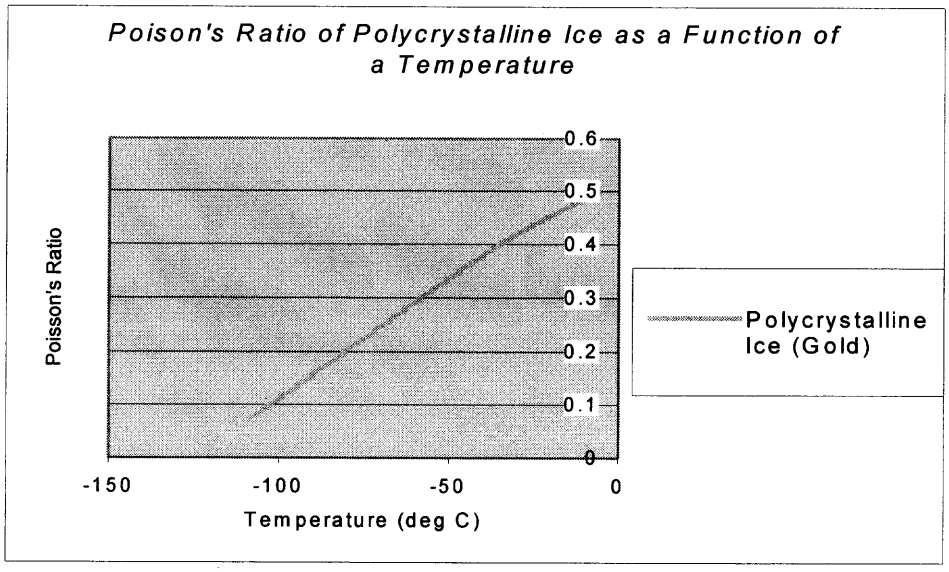

Figure 6.8 Poisson's ratio of the polycrystalline ice as a function of the temperature [1].

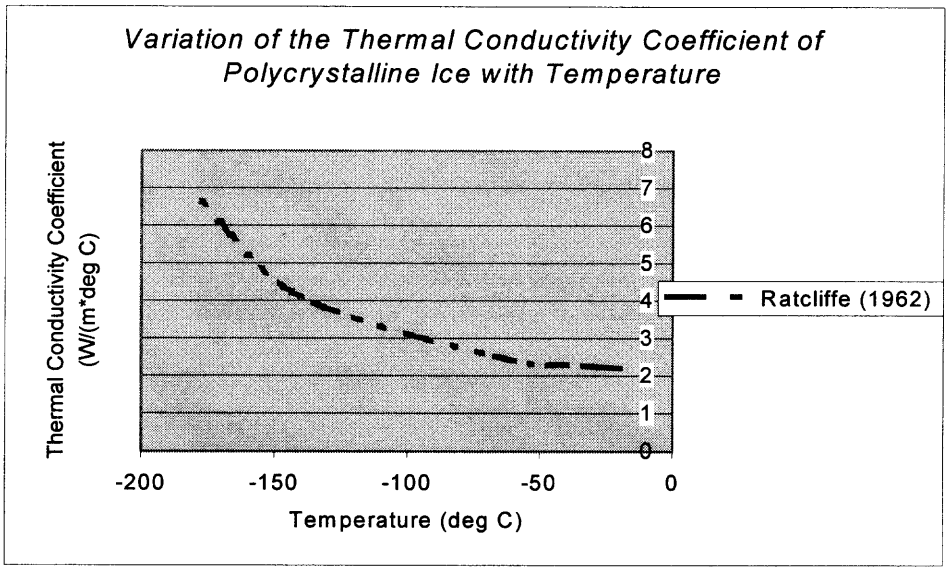

Figure 6.9 Thermal conductivity of polycrystalline ice as a function of temperature according to Ratcliffe [1].

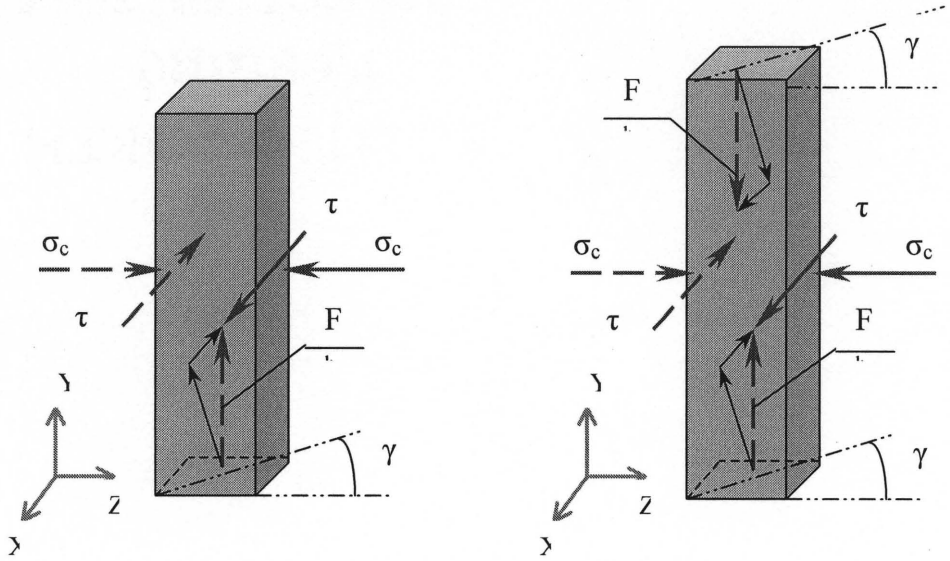

Figure 6.10 Geometry of the infinitesimal element of the ice plug subjected to the compressive and shearing stresses and vertical force: a) space between helical ways not entirely filled up, uniaxial compression case is present, and b) space is completely occupied by the ice plug and biaxial compression case is present.

σ_c – thermal expansion compressive stress; τ_s – shearing stress developed in auger agitated motion; F_h- vertical motion force generated by the helical ways; γ – angle between helical way and vertical Y – axis.

Tabulated data of the temperature of the ice plug surface adjacent to the evaporator wall was measured by the thermocouple # 3 and presented in Table 6.5.

Tables 6.5 Temperature of Inner Plug Surface at the Distance 40-mm from Water Inlet Level

Water Flow Rate (ml/min)	50	100	150
Temperature (° C)	-40.5	-21.7	-14.8

Tensile yield strength of the commercial polycrystalline ice as a function of the temperature used in the model is presented on Figure 6.12. Functional dependency, which was established through the superimposed trend line, is:

$$S_T = 0.0045T^2+0.0246T+14.107 \qquad (6.24)$$

where S_T is a tensile strength of a polycrystalline ice, T is a temperature.

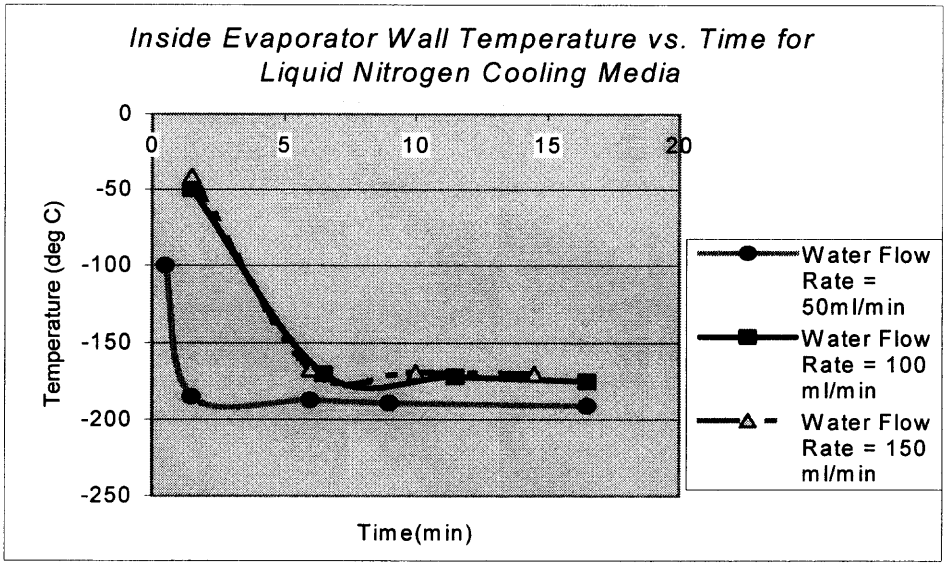

Figure 6.11 Temperature of the internal evaporator wall is a prescribed boundary condition for the outside ice plug wall.

Time of the actual ice crystallization procedure was established through the current-torque diagram for the distinct water flow rates presented on Figure 6.13. The ice plug thermal expansion time is equal to the duration of half of the current wave on the current-torque diagram. This conclusion is supported by the fluctuating character of ice powder flow at the outlet of the evaporator with distinct frequencies for different water flow rates. The frequency of the ice powder fluctuations on the evaporator outlet directly corresponds to those on current-torque diagram (Figure 6.13). Raising half of the wave is responsible for the ice plug formation with thermal stress development while lowering half corresponds to ice plug decomposition and the stress releasing stage of the process.

Thermal analysis was carried out to determine the temperature distribution at the ice plug. The heat flux and temperature fields thought the ice plug were determined during this modeling. Modeling results for water flow rates of 50, 100 and 150 ml/min are presented on Figure 6.14.

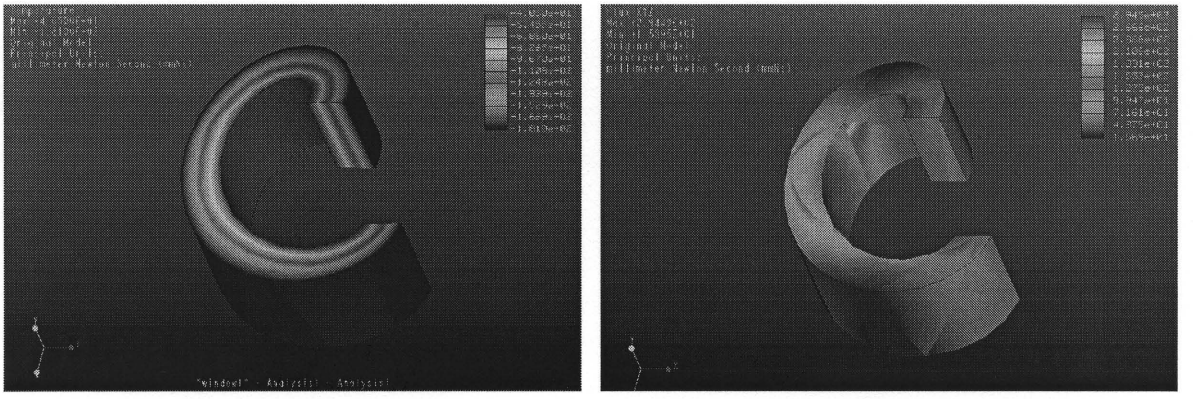

(a)

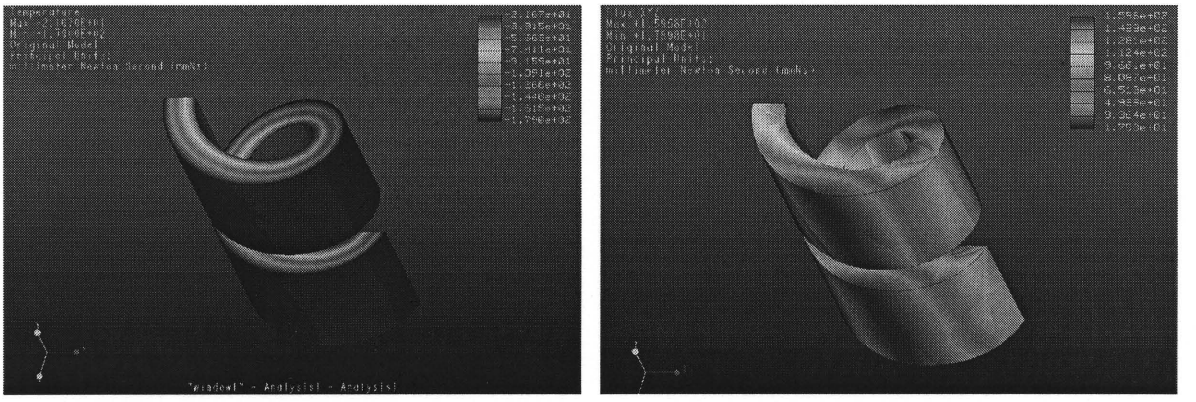

(b)

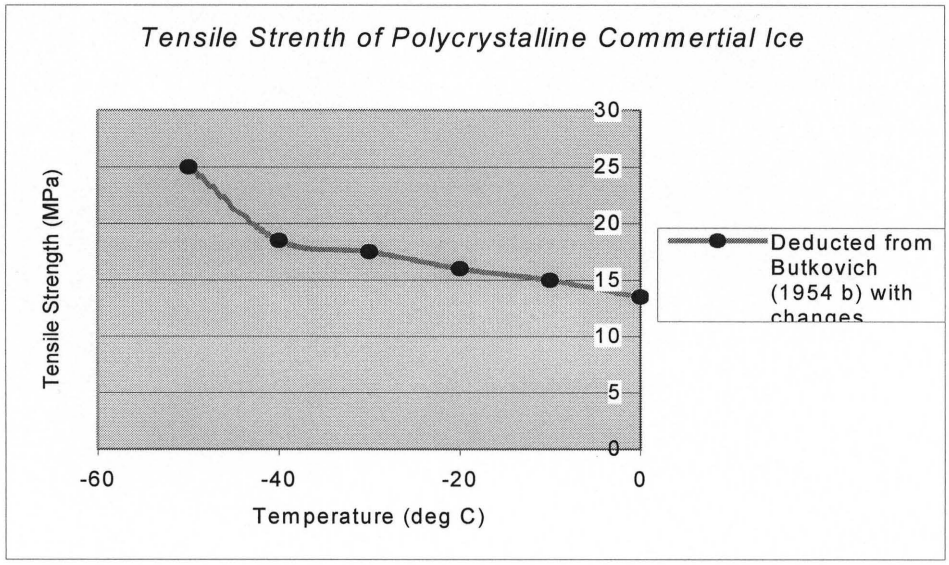

Figure 6.12 Tensile strength of polycrystalline ice as a function of a temperature. From Butkovich with changes [1].

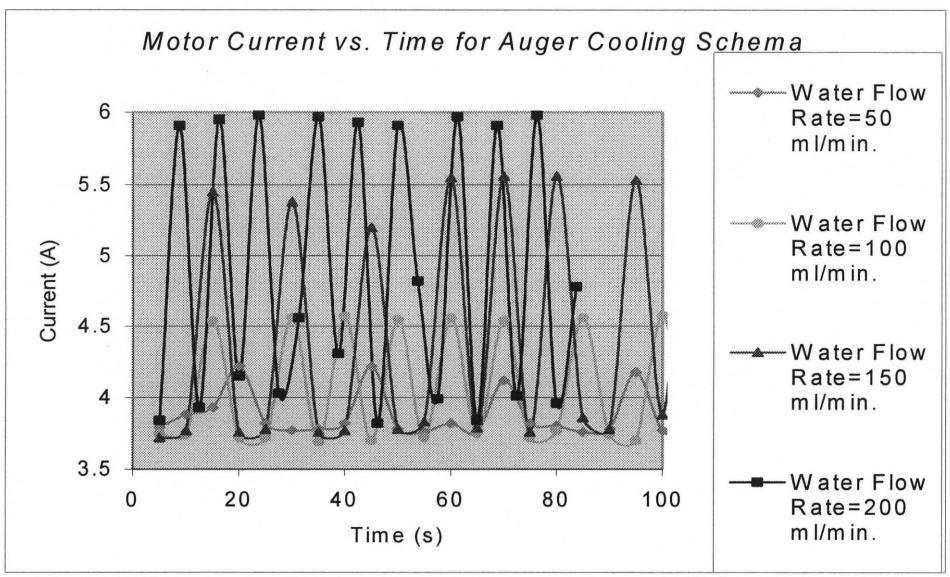

Figure 6.13 Variation of the motor current at the different water flow rates and single side-cooling schema.

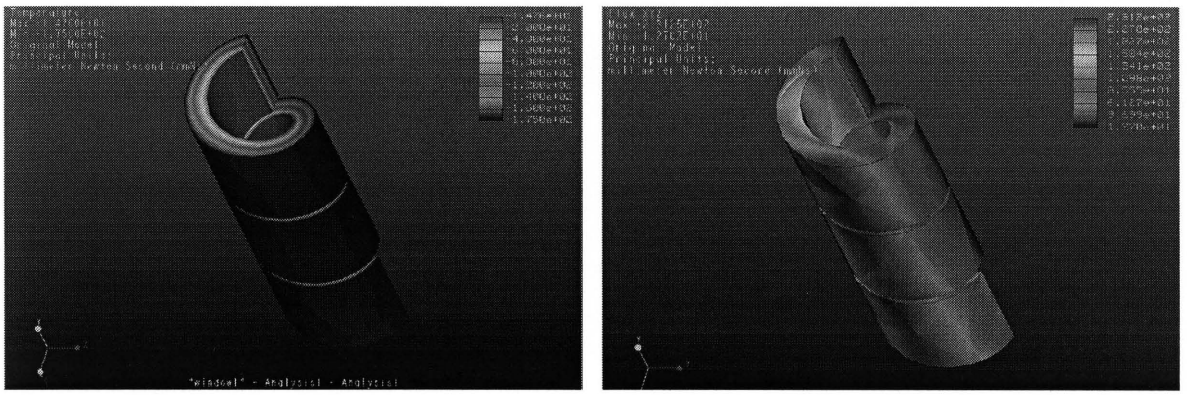

(c)

Figure 6.14 Pictures of temperature distribution and heat flux for the single side cooling schema and water flow rates correspondingly: a) 50 ml/min, b) 100 ml/min, and c) 150 ml/min.

6.4. Analytical Study of Ice Plug Decomposition

Temperature field distribution through the ice plug at the different water flow rates was determined and results are presented on Figure 6.14. Geometry of the ice plug cross-section area for different water flow rates is presented on Figure 6.15. Thermal stress developed in the ice plug can be calculated employing the temperature field within the plug obtained by the use of Pro/MECHANICA 2001. The coefficient of the linear expansion of the T-1 polycrystalline ice is presented on Figure 6.7. Then the absolute thermal elongation of the ice plug in the *Z*-direction (Figure 6.10) Δl can be determined as:

$$\Delta l = l_1 \alpha \Delta T \tag{6.25}$$

where l_1 = 9 mm is the initial length of the ice plug in Z-direction, α is the coefficient of linear expansion of the ice plug for the given temperature, ΔT is the averaging-out temperature between the inside and outside walls of the ice plug and determined as:

$$\Delta T = (T_i + T_o)/2 \tag{6.26}$$

where T_i is the inside wall temperature, T_o is the outside wall temperature.

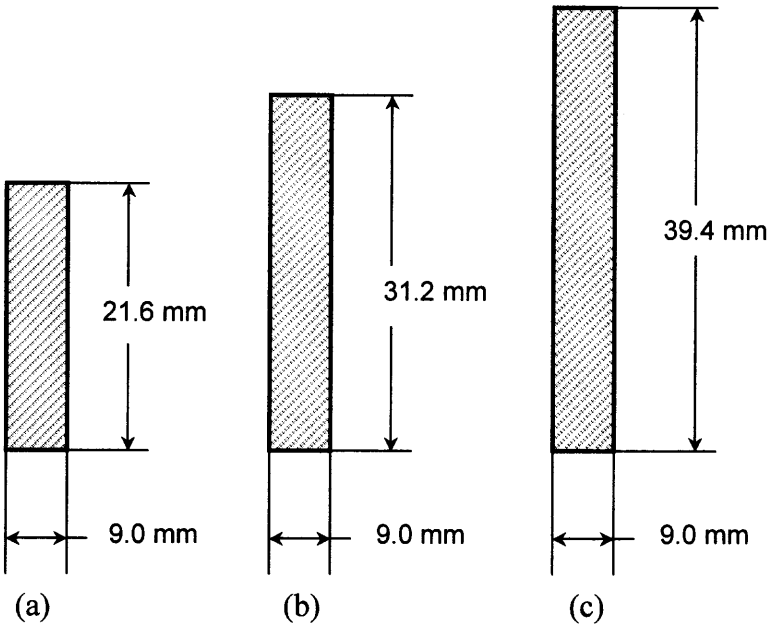

Figure 6.15 Cross-section geometry of the ice plug for the water flow rates: a) 50 ml/min, b) 100 ml/min, and c) 150 ml/min.

Then the strain in the horizontal direction can be determined as:

$$\varepsilon_{11} = \Delta l / l_1 = \alpha \Delta T \tag{6.27}$$

where ε_{11} is the strain in z-direction (Figure 6.18).

Principal stress σ_{11} in z-direction then can be found as:

$$\sigma_{11} = Y_s \varepsilon_{11} \tag{6.28}$$

where Y_s is the static Young's modulus determined in (6.21).

Experimental studies conducted by Sanderson [5] show that ice formed by the freezing of compressed water contains a wide variety of cracks. The cracks lying at various angles have the length of the order of the grain size and are clustered around the axis of loading. Experimental studies by Cole provide data of the length and density of cracks in polycrystalline T-1 ice [5]. The length of nucleated cracks, 2a, is proportional to grain size d and obeys the approximate relationship:

$$2a = 0.65d \tag{6.29}$$

where 2a is a mean crack length, d is an average grain diameter.

The density or frequency of crack appearance is also grain-size dependent and for larger grain sizes (exceeding about 5 mm) it is reasonable to assume the formation of approximately one crack per grain. The study of single crack propagation under compressive stress σ_{11} was conducted by Nemet-Nasser and Horii [34] and approximate analytic treatment of this problem has been presented by Ashby and Hallam [4]. As the load σ_{11} applied, the crack tries to slide along its boundary and two tensile zones are formed at the ends of the initial crack. When the compressive stress reaches the critical value, "wing cracks" forms and propagates roughly perpendicularly to the crack ends. As the wing cracks grow, they tend to align themselves with the principal axis of compression.

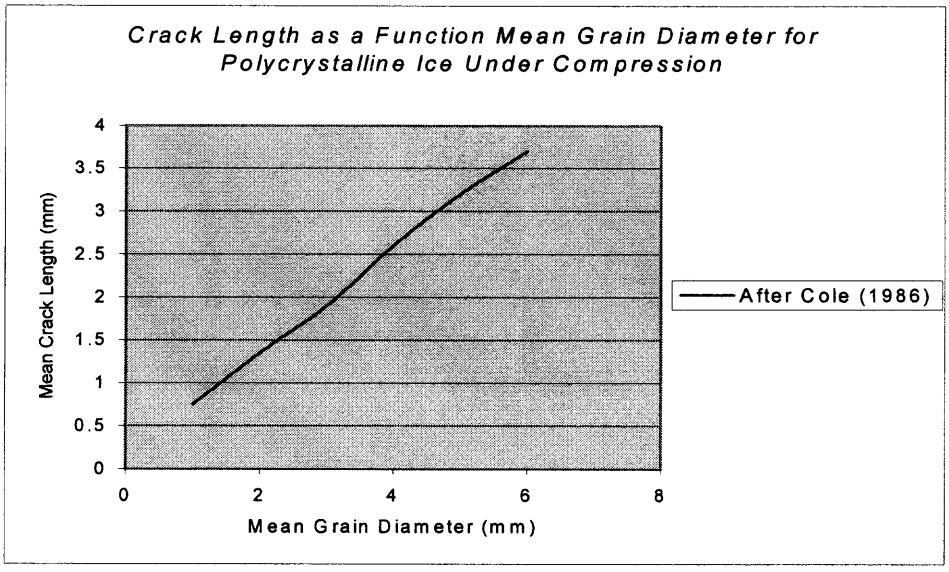

Figure 6.16 Cracks nucleated in polycrystalline ice under compression as a function of grain diameter.

The analysis by Ashby and Hallam [4] specifies a two-dimensional idealized model of crack propagation. The crack of length 2a lies at the angle of ψ to the direction to the principle compressive stress σ_{11}. As thermal stress increases wing cracks form and grow to a length l, which can be related to the stress conditions and the mechanical properties of ice. It is proven experimentally that crack wings propagation angle ψ lies in the range 35-45° [5]. Then the technique described by Sanderson [5] could be applied for the thermal compressive stress amplitude analysis.

$$K_{IC} = \frac{\sigma_{11}\sqrt{\pi a}}{(1+L)^{3/2}}\left[1-\lambda-\mu(1+\lambda)-\frac{\lambda L\sqrt{3}}{\beta}\right]\times\left[\frac{\beta L}{\sqrt{3}}+\frac{1}{\sqrt{3}(1+L)^{1/2}}\right] \tag{6.30}$$

where K_{IC} is the fractural toughness, 2a is the initial length of the crack, l is the length of the wing cracks and $L=l/a$, λ is σ_{33}/σ_{11} which is the ratio of the confining stress to compressive stress, β is approximately 0.4 which is a coefficient determined empirically, and μ is the coefficient of friction across the crack, which is not very well known.

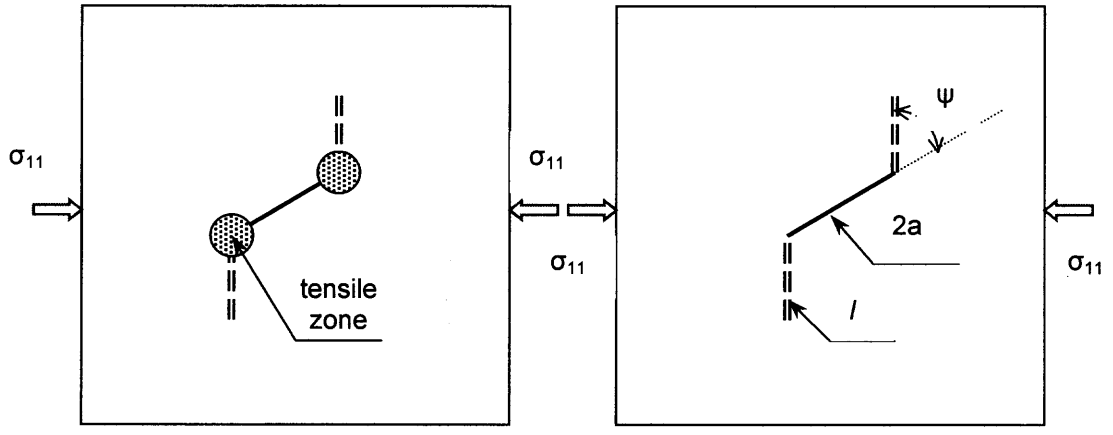

Figure 6.17 Scheme of: a). formation of wing cracks in a brittle solid under compression, b) idealized model of wing crack formation.

For the uniaxial compression when:

$$\sigma_{22} = \sigma_{33} = 0 \tag{6.31}$$

the equation (6.30) with $\lambda = 0$ will transform to:

$$K_{IC} = \frac{\sigma_{11}(1-\mu)\sqrt{\pi a}}{(1+L)^{3/2}}\left[\frac{\beta L}{\sqrt{3}} + \frac{1}{\sqrt{3}(1+L)^{1/2}}\right] \tag{6.32}$$

It was empirically proven by Sanderson [5] that on the later stages of the wing crack propagation its length is no longer then the initiating crack itself. Then if l>>a, then L>>1 and equation (6.32) can be further simplified to:

$$K_{IC} \sim \frac{\sigma_{11}\sqrt{\pi a}(1-\mu)\beta}{\sqrt{3}L} \tag{6.33}$$

The coefficient of the friction across the crack μ, is not well determined. A limited experimental data is available. Most likely it is very temperature dependent and lies in the

range 0-0.3 for the ice in brittle mode Adopting the value of $\mu = 0.3$ and setting $\beta = 0.4$, equation (6.33) becomes:

$$K_{IC} = 0.29\sigma_{11}\sqrt{\frac{a}{L}} \tag{6.34}$$

and the principal stress as a function of the initial crack and wing crack length can be written as:

$$\sigma_{11} = 3.5K_{IC}\sqrt{\frac{l}{a^2}} = 3.5\frac{K_{IC}}{a}\sqrt{l} \tag{6.35}$$

The fracture toughness of ice is empirically determined as:

$$K_{IC} = 0.1 \text{ MPa}\times\text{m}^{1/2} \tag{6.36}$$

The average diameter of the ice particles for single side-cooling schema and different water flow rates was statistically determined and presented on Figure 6.18.

For failure to occur in the ice plug the linkage of a large number of propagating wings has to interact with each other, until the material under compression loses strength. If initial flaws are separated by an average distance of order Δ_f, it is likely that wing cracks will have to propagate in a distance no more than about $\Delta_f/2$, which is in an order of the average grain diameter before the ice plug is damaged so that failure occurs (Figure 6.17). However what has not been taken into account is that if not all cracks are appropriately oriented and with orientation angles of 0 and 90° to the principal compressive stress, they will not contribute significantly to failure. Principal compressive stress σ_{11} calculated through the thermal and Sanderson approach for given water flow rates of 50, 100, and 150 ml/min are presented on Figure 6.19.

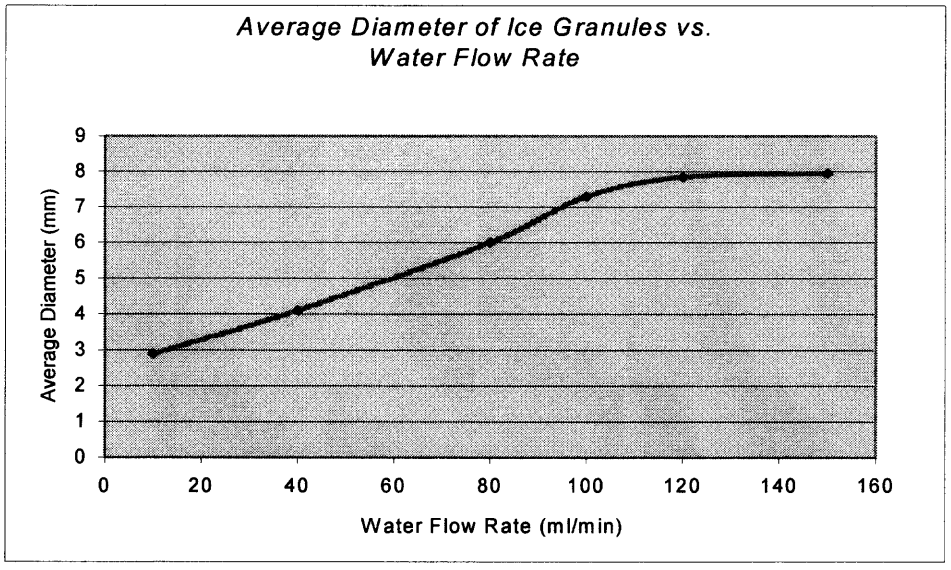

Figure 6.18 Statistically determined average diameter of ice grain for single side cooling schema.

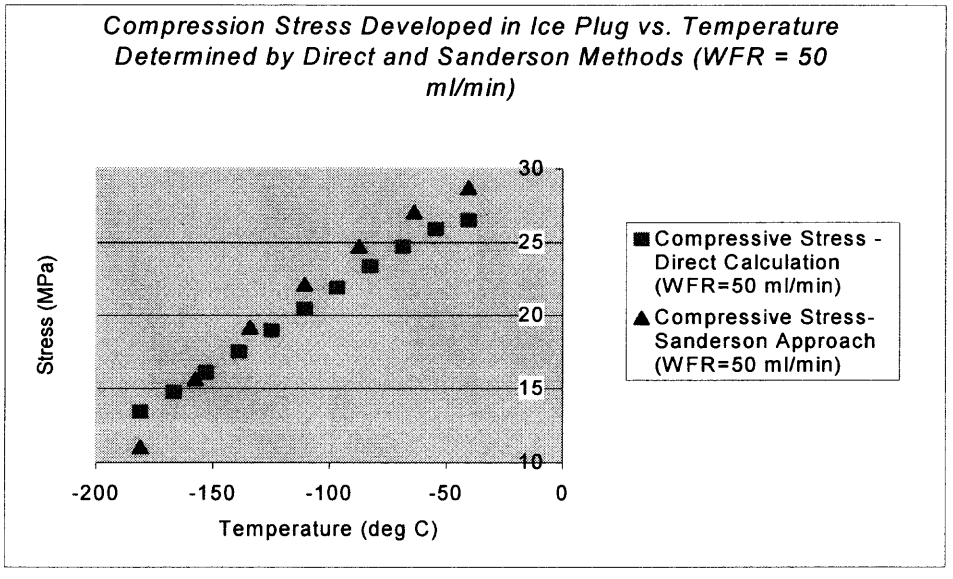

(a)

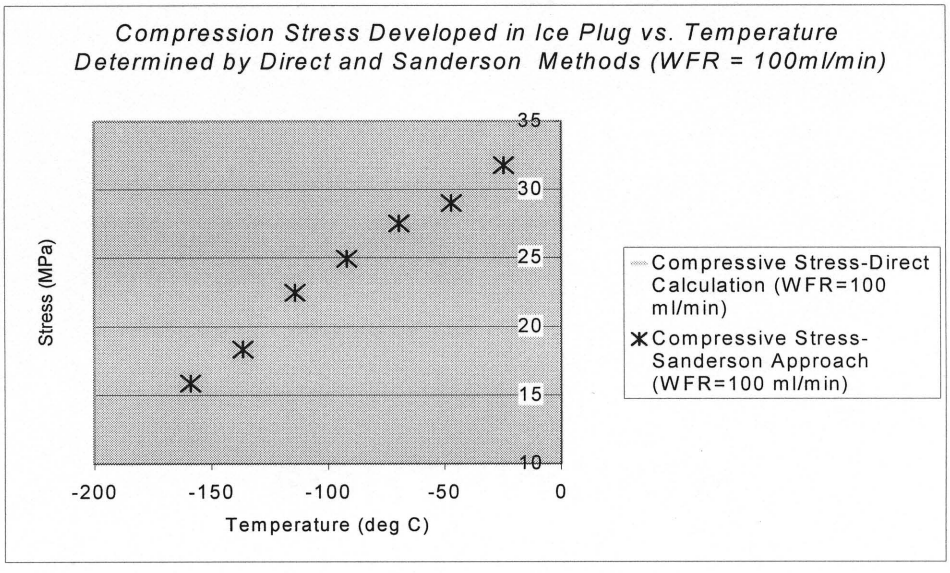

(b)

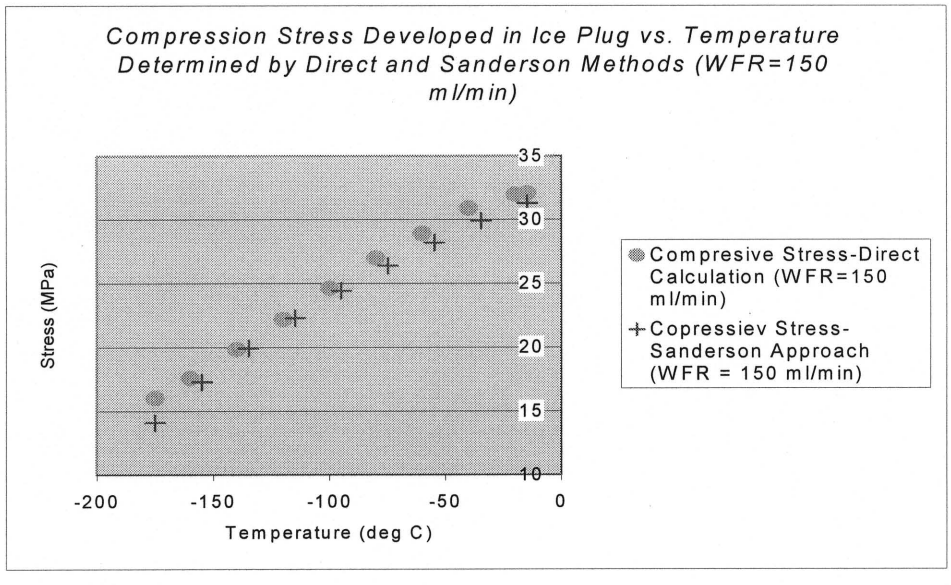

(c)

Figure 6.19 Compressive fracture stresses developed in the ice plug and calculated through thermal field distribution and average diameter of the ice grain methods for the flow rates: a) 50 ml/min, b) 100 ml/min, and c) 150 ml/min.

Compressive force can be calculated directly employing the following formula:

$$F_{11} = \sigma_{11} A_{act} \tag{6.37}$$

where F_{11} is a compressive force due to thermal expansion, σ_{11} is the principal compressive stress, A_{act} is an area of actual contact surface of the ice plug with the evaporator wall. The planar geometry of the ice plug is presented on Figure 6.20, where A is a length of the ice plug, B is a planar pitch height defined as:

$$B = A/\tan \psi \tag{6.38}$$

where ψ is an angle between helical ways and axis of auger rotation, and C is a height of the ice plug.

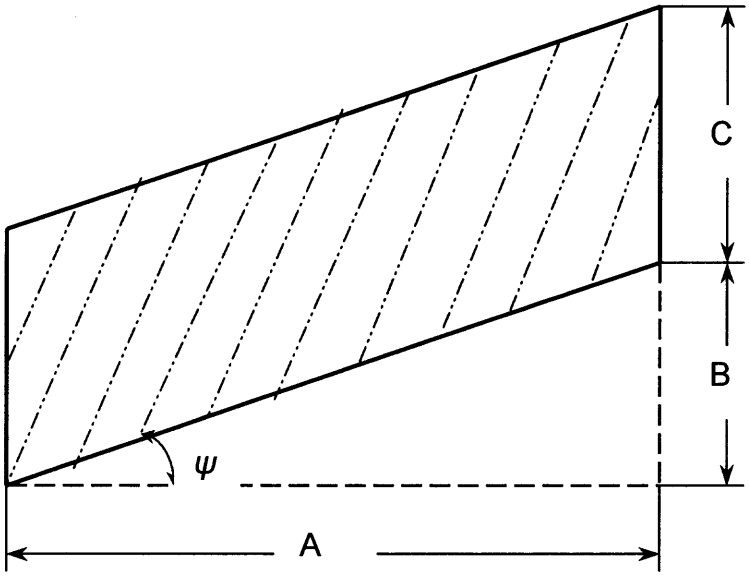

Figure 6.20 Planar geometry of the ice plug.

The actual contact area between the ice plug and the evaporator wall correlate to the planar geometry through the following formula:

$$A_{act} = 0.5A(B+2C)-0.5AB = AC \tag{6.39}$$

where A was determined in (6.38).

Then the thermally driven compressive force can be expressed as:

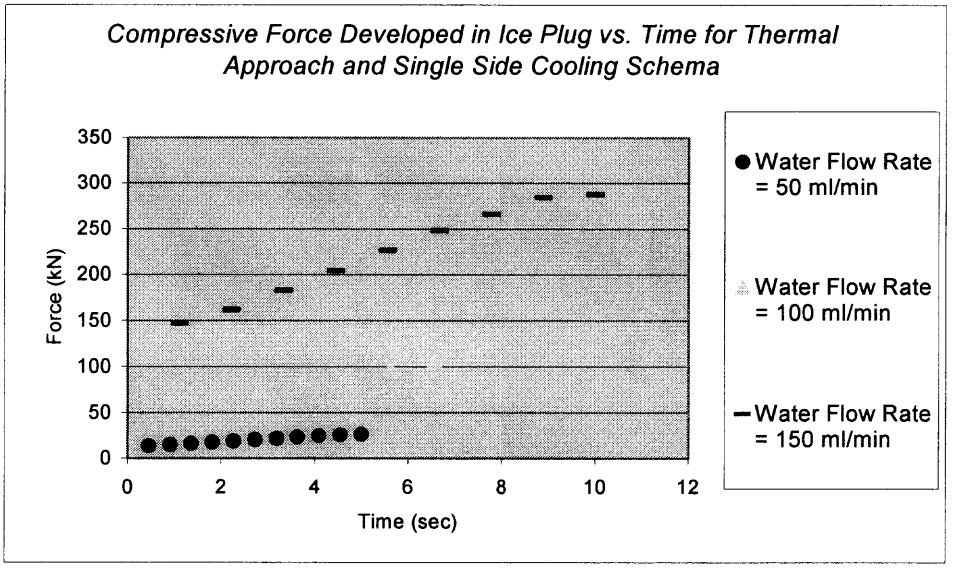

(a)

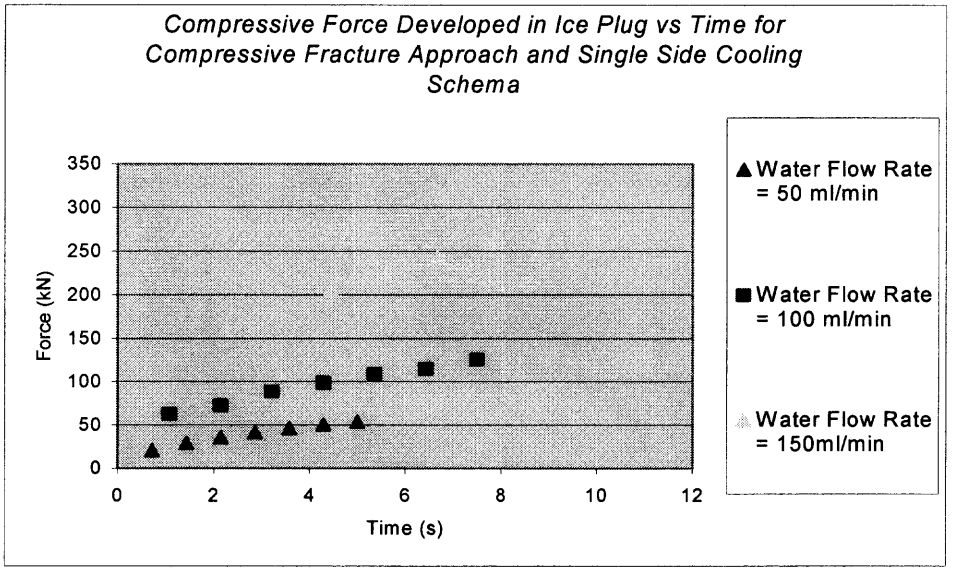

(b)

Figure 6.21 Compressive force developed during ice plug expansion for correspondingly, a) thermal and, b) compressive fracture methods.

$$F_{11} = \sigma_{11} / A_{act} \tag{6.40}$$

where σ_{11} for thermal and compressive fracture approaches was determined in (6.35) and (6.37). The compressive forces determined by the thermal and compressive fracture approaches are presented in Figure 6.21.

To estimate maximal shear force applied to the ice plug, the following technique was used. Maximum shear force occurs at the outside surface of the ice plug at the most remote point from the axis of auger rotation. Work done on the ice plug decomposition by the AC/DC type motor are determined by the motor voltage and current as well as the coefficient of active power which lies in the range 0.75 to 0.80. From the current-time diagram, work done in one cycle of decomposition for the different water flow rates and cycle duration can be determined as:

$$A = U \cos\theta \int_{t1}^{t2} I(t)dt \tag{6.41}$$

where A is the work performed by the motor during one cycle, U is a motor current, $\cos\theta$ is a coefficient of the active power. $I(t)$ is approximated by cubic function current-time dependence (6.42) and t_1, t_2 are the time limits of the duration of decomposition cycle. The current variation during the ice plug formation and decomposition cycle is given as following:

$$I(t) = k_0 + k_1 t + k_2 t^2 + k_3 t^3 \tag{6.42}$$

where k_i are the coefficients of the cubic approximation, t is the time.

Then the maximum shearing force tangential to the outside surface of the ice plug can be determined employing the following formula:

$$Fs_{\max} = \frac{A}{X\omega} \tag{6.43}$$

where Fs_{max} is a maximal shearing force exerted on the outside surface of the ice plug, A has been determined in (6.41), X is a distance of the outside surface from the axis of revolution and ω is a relative angle of plug rotation during decomposition which was empirically determined being:

$$\omega = \frac{\pi}{(H/p)} \tag{6.44}$$

where π = 1 radian, H is a height of the ice plug for each given water flow rate, p is the pitch of the auger. The relative angle of plug rotation was established experimentally based on the duration of the ice plug decomposition, its geometry and the auger pitch value. The determined shear force plotted against the water flow rate is presented on Figure 6.22.

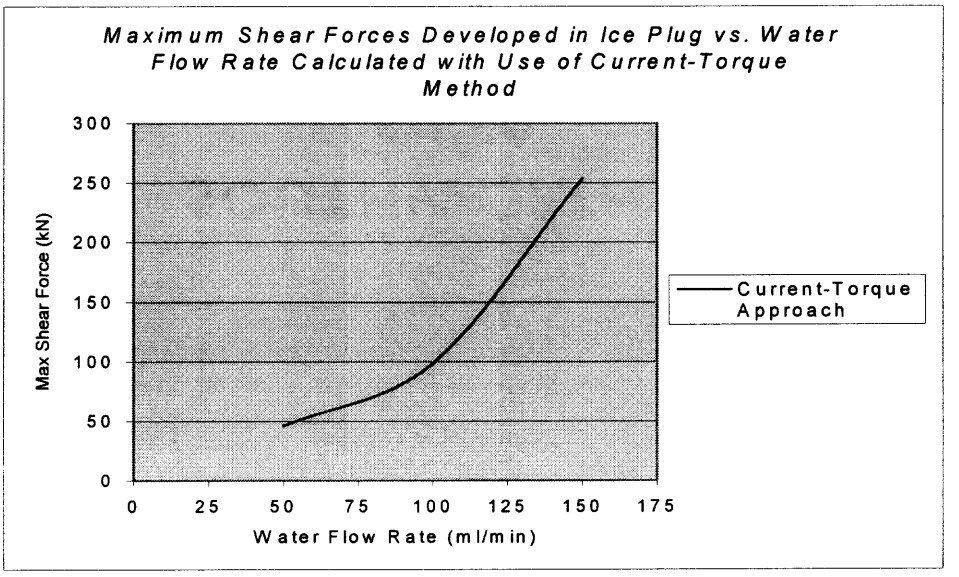

Figure 6.22 Shear force as a function of water flow rate calculated using current-torque method.

As it is depicted on Figure 6.23 the values of the maximal compressive stresses determined by the thermally generated compressive stress (6.28) and compressive fracture model (6.35) are practically identical. This validates the outcome of the presented analysis.

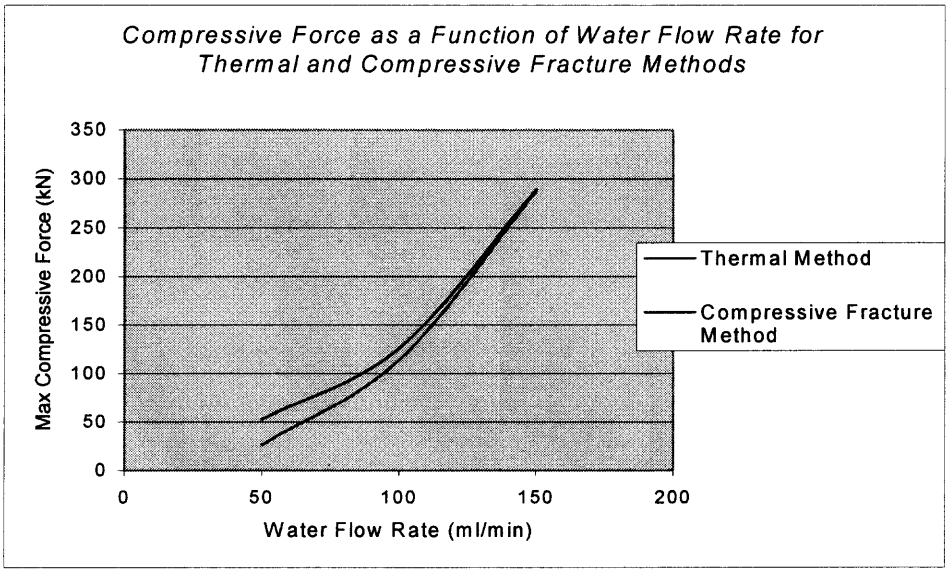

Figure 6.23 Maximum compressive force developed in the ice plug due to thermal expansion and calculated for direct and compressive fracture methods.

CHAPTER 7

PHENOMENOLOGICAL PROCESS MODEL

Water ice is a viscoelastic material with a nonlinear flow law. When polycrystalline ice is subjected to external forces, the elastic deformation followed by the transient creep until the steady viscous flow called secondary creep is reached. At high stresses, exceeding 400 kPa, the creep curve accelerates. This phenomenon is termed tertiary creep. Several physical processes are responsible for ice deformation: movement of dislocations, sliding along grain boundaries, and recrystallizations. The ultimate strength of an ice plug at a particular temperature depends on the way in which ice was formed, the size and the shape of the plug, and the way of the application of the external forces. The fracture is generally initiated through the growth of existing or newel cracks, which spreads through the plug in interaction with ice imperfections.

Data representing ice compression at the high stresses domain and temperature below -50°C was unavailable. However, the crushing strength of commercial ice, which belongs to the polycrystalline ice family by a load parallel to the axis of compression, is available at Hobbs [1] and presented on Figure 7.1. Empirical databases of ice behavior under applied compressive and shear stresses and extremely low temperature domain is not available. The most general correlation between the yield stress σ and $_{the}$ strain rate and the temperature could be presented as:

$$\sigma = (cons\tan t)\left(\dot{\varepsilon}_{st}^{1/n}\right)e^{\frac{Q}{nkT}} \tag{7.1}$$

where n is a coefficient of the ice crystal smoothness and Q is an activation energy [1].. The value of n is about 4.5 for the polycrystalline ice at the temperature below -10°C and Q = 0.76 eV for crystals indented parallel to the c – axis (after Butkovich) and n = 5.4 and Q = 0.76 eV for indentation perpendicular to the c – axis (Barnes *et al.* 1971) and $\dot{\varepsilon}_{st}$ is a steady-state creep rate (7.2).

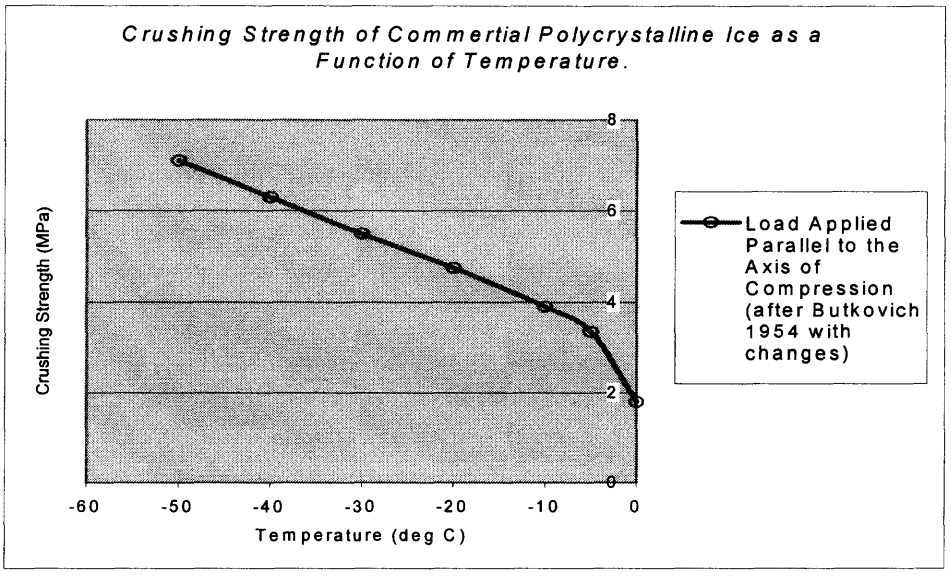

Figure 7.1 Crushing strength of the commercial ice against temperature for load applied parallel to the axis of compression. From Butkovich with changes [1].

Hobbs, [1] suggested that the polycrystalline ice creep rate at higher stresses could be expressed in the following form:

$$\frac{d\varepsilon}{dt} = A\sigma^n e^{-\left[\frac{Q}{kT}\right]} \tag{7.2}$$

where A is a temperature independent constant, Q is an activation energy for creep, n is nonlinear exponent, k is the Boltzman constant, and T is the absolute temperature. Values of A, Q, and n depend to some extend on the grain size, grain orientation distribution, and impurity content of the polycrystalline material.

The torsional shear strength of the clear lake ice is strongly temperature dependent and increasing from about 0.8 MPa at 0°C to 2.1 MPa at -50°C when the shear force was normal to the principal axis of loading. According to Butkowich, [1] the torsional shear strength versus temperature curves for the commercial ice was nearly the same as that obtained for the clear lake ice at -5°C. Thus the data available for lake ice are readily adaptable for commercial polycrystalline ice. The maximum compressive stress which has been attained in the course of thermal expansion for water flow rate of 100 ml/min and temperature ~ -30°C was about 32.5 MPa. Complete ice plug decomposition was achieved at this regime with optimal granulometric composition for ice jet cleaning purposes.

Compressive stress – strain curves for various types of ice are presented on Figure 7.2.

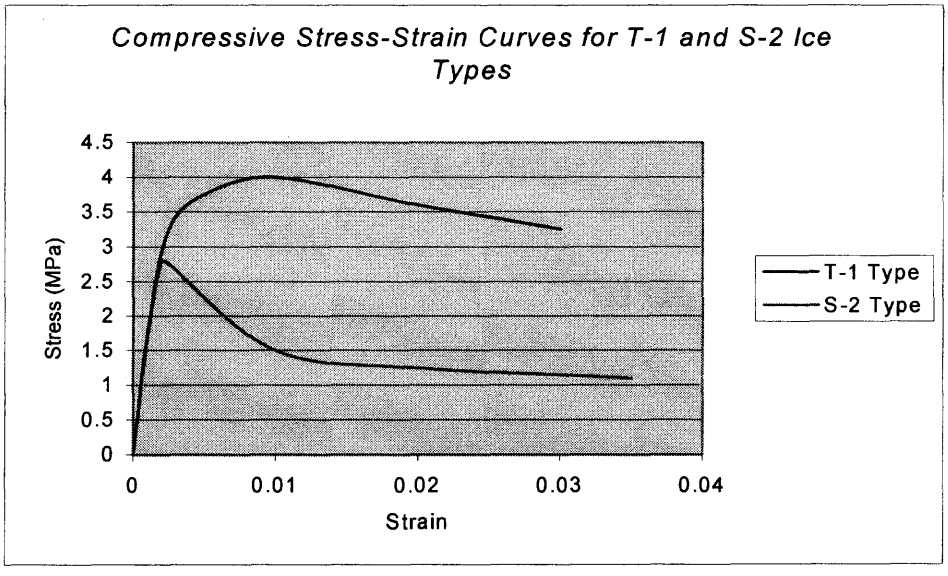

Figure 7.2 Compressive stress-strain curves for various ice types with T = -9.5°C and $\varepsilon^{\bullet}$ = 1.67 *10^{-5} s^{-1}. T1 – snow ice, S1 – columnar grained ice.

This conclusion was based on the granulometric composition of the generated powder presented on Figure 6.18. Simple comparison of the attained compressive stress with crushing strength of the polycrystalline ice under the same conditions shows that the thermal expansion crushing strength has exceeded it by 5 to 6 times. The maximum shear stress can be determined from maximum shear force and calculated as:

$$\sigma_{s\,max} = \frac{F_{s\,max}}{A} \tag{7.3}$$

where F_{smax} is the maximum shear force, and A is the actual area of contact of ice plug with evaporator wall.

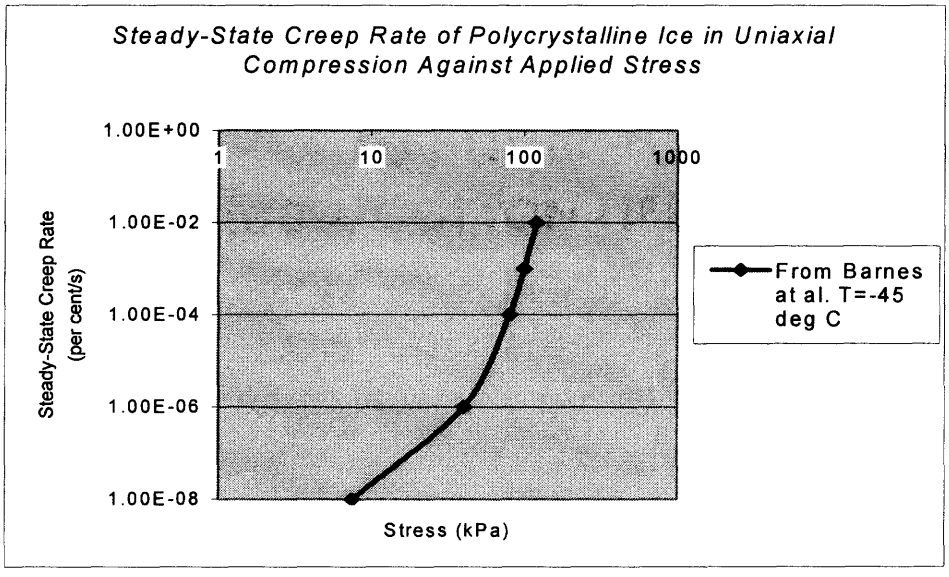

Figure 7.3 Steady-state creep rate of polycrystalline ice in uniaxial compression as a function of principal compressive stress for experimental at -48° C. From Barnes *et al.* with changes [1].

The maximum shear stress developed under thermal expansion in auger agitated motion exceeds the torsional shear strength of the polycrystalline ice in 12 to 13 times, which brings the ice plug to complete decomposition in course of auger rotation.

The stress field initiated due to thermal expansion combined with the brittle mode of the ice plug and auger agitated motion shows that under appropriately chosen conditions compressive as well as shear forces of the very high magnitude and short duration could be generated. Hypothetically then, it is possible to show that under an appropriate cooling schema and speed of the auger as well as the geometry of the auger helical ways the homogeneous stress and temperature field through the ice plug can be generated. The duration of the compressive as well as shearing stresses acting on the plug would be shorter and impulse type of impact could be generated during the thermal expansion.

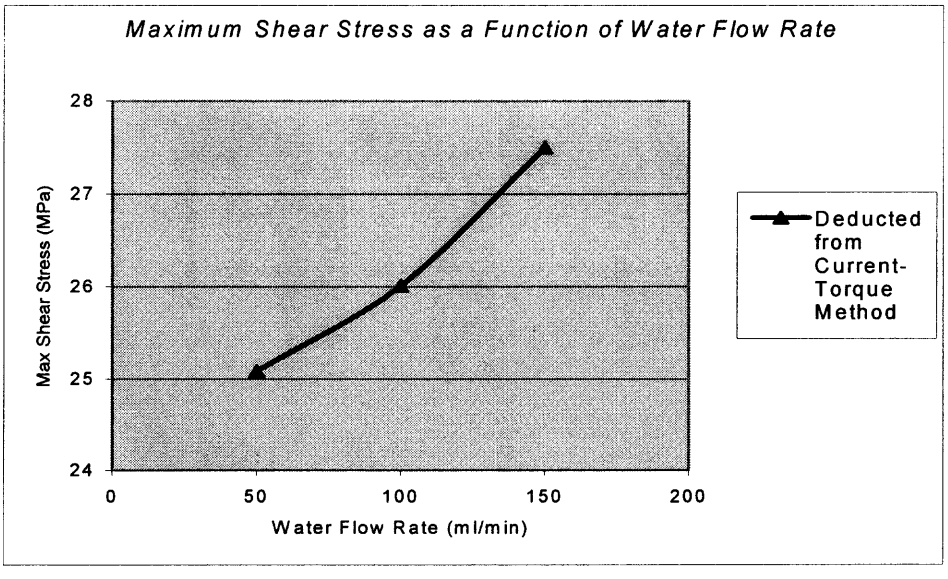

Figure 7.4 Maximum shear stress determined from current-torque method plotted against water flow rate at the ice grains temperature range -20 to -50°C.

The frequency of the decomposition peaks would have to increase and this brings to the complete decomposition of the ice plug in a continuous mode.

Expression 6.35 allowed to calculate failure stresses for any combination of flaw-size $2a$ and flaw separation Δ_f. It is reasonable to assume that for the present model flaw separation Δ_f and crack wing length l are of the same geometrical scale range. Then (6.35) can be altered and represented in the following form:

$$\sigma_{11} = \chi \frac{K_{IC}}{a} \sqrt{\frac{\Delta_f}{2}} \tag{7.4}$$

where χ is a constant of proportionality.

Then the ice mode and its mechanical properties could be approximated by the expression:

$$\sigma_{11} = \alpha \sqrt{\frac{\Delta_f}{2}} \tag{7.5}$$

where α= 3.5 MPa×m$^{1/2}$ is a combined coefficient, which describes ice behavior under given conditions [1].

The results of the computations using (7.5) (Table 7.1) show that compressive strength is highly flaw-size dependent. It proves that the formation of the extremely fine ice grains requires generation of high compressive stresses along with transition of the ice plug into brittle mode. The conclusion that the highest concentration of the flaws occurs at the boundaries of the grains also can be extracted out of these results. Increasing distance of the separation of flaws (Figure 7.5) leads to almost proportional raising of the theoretical failure stresses. Then the optimization of the ice plug shape and geometry required achieving a desirable granulometric decomposition of ice plug. The optimization suggestions will be given in Chapter 8.

Table 7.1 Theoretical Failure Stress for Polycrystalline Ice under Compression Containing Flaws of Length *2a* with Flaws Separation Distance Δ_f.

Length of flaws, 2a (m)	Separation of flaws, Δ_f (m)	Theoretical compressive failure stress, (MPa)
0.0003	0.0003	14.29
0.00075	0.00075	9.037
0.0015	0.0015	6.39
0.0015	0.003	9.037
0.0015	0.005	11.67
0.005	0.005	3.5
0.0075	0.0075	2.858
0.0075	0.01	3.3
0.0075	0.015	4.041

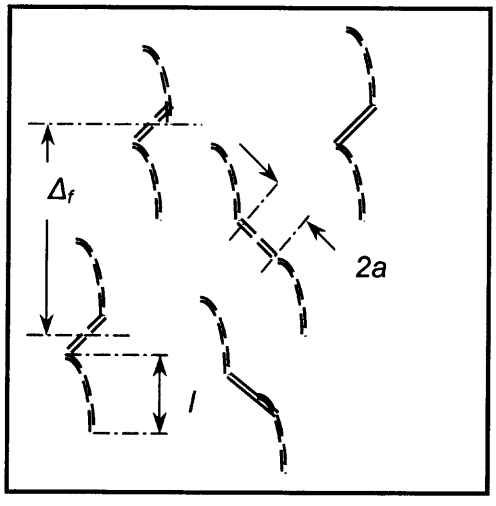

Figure 7.5 Schematic of wings propagation and separation distanses between cracks.

Furthermore, the time of the ice plug formation was extremely short comparing to the case with HT-55 Galden cooling media. The fast nucleation resulted in the formation of fine grains in the direction of the compressive stress [1]. The speed of the auger driver

rotation ranged from 750 to 1000 rpm. The propagation of the cracks generated under compression complies with the model described above (Figure 7.5).

Based on the experimental results, the most homogeneous granulometric composition at the various water flow rates was obtained using set up *A* (Table 5.1). The temperature of the ice powder for the entire range of water flow rates was about -50°C for the experimental set up A. The angle of helical ways inclination to the auger axis of rotation is 45°, which resulted in the equal distribution of the auger driving force along the *X*- and *Y*-axes along ice plug surfaces (Figure 7.5). The optimal angle between the descending and ascending helical ways has to hold ~90° value. Depth of the helical thread stipulates the duration of the ice plug composition because of the duration of water-cooling and solidification in active decomposition volume. Next, the optimal value of the helical way height has to be chosen based on the desired average ice particle size and expected productivity of the ice-making machine. According to the experimental observation, the auger of the set up *B* had the worst performance producing highly non-homogeneous ice powder. This leads to a conclusion that the intensive nucleation along with the homogeneous temperature field within the ice plug, which transformed the ice plug to the brittle mode could be achieved by controlling the d parameter or the depth of auger thread of the evaporator-auger assembly.

Furthermore, the solidification time depends on the cooling power provided to the evaporator and the water volume between the helical ways. This volume will further referred as an active decomposition volume. This parameter is a function of the helical thread depth. The auger rotational velocity determines the duration of the contact of ice plug with the evaporator wall and the amount of heat absorbed from the ice plug.

According to the current-time diagram (Figure 6.13), its ascending half-wave specifies the actual time of the ice plug formation. The ice plug started moving up along the helical ways when thermally generated compressive forces overcome the combined friction and adhesion forces between the ice plug and the evaporator-auger walls.

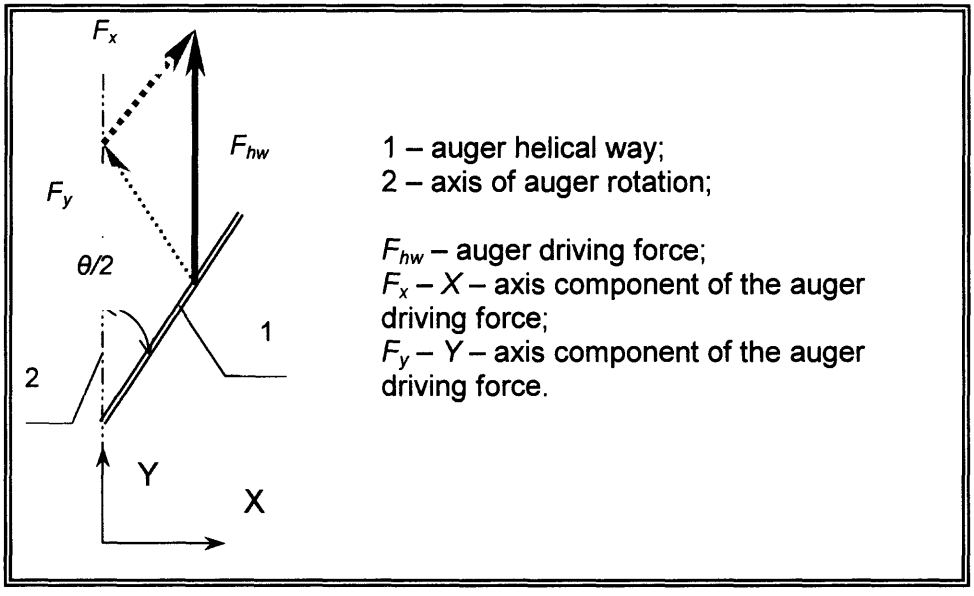

Figure 7.6 Decomposition of the helical way driving force into the X andY-components.

For the single side cooling schema, water freezing is sufficiently intensive in the region adjacent to the evaporator wall. At the same time, the rate of the solidification is near the auger stem is much lower. The ice plug decomposition schematic diagram is illustrated below (Figure 7.7). The schematic (Figure 7.7 a) shows the entrance of the freezer. The ice nucleation in this zone initiates as soon as the liquid water meets the evaporator wall having temperature of -196°C. The ice plug propagates toward the auger stem and due to the high rate of heat removal the isotropic polycrystalline structure has

formed. Due to disparity of the solidification condition, a multilayer ice plug is formed throughout the ice plug volume. The supercooling and rate of the heat removal at various sites of the plug determine the distribution of ice properties. At the beginning of the ice plug formation, the value of the current is minimal and raised gradually along with the thermal expansion forces. The point of current maximal value specified the maximum of the compressive stress.

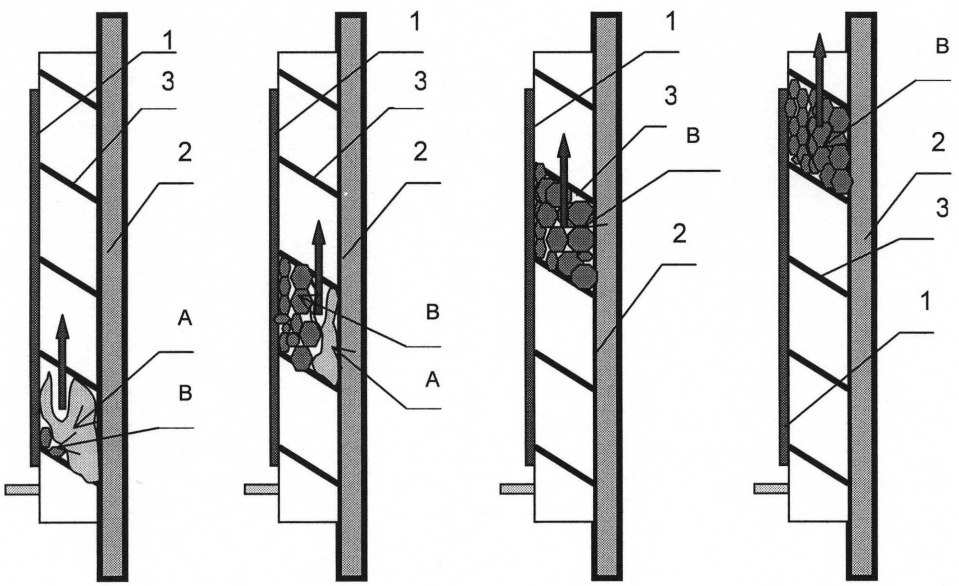

(a) (b) (c) (d)

1 - cooling media flows through evaporator cooling coils;
2 - auger stem;
3 - auger helical way.
A - supercooled ice granules;
B - moving boundary layer between supercooled and subzero ice granules;
↑ - direction of auger agitated movement.

Figure 7.7 Schematic of ice nucleation inside of the evaporator during the course of auger agitated movement for single side cooling.

The frequency of the ice powder fluctuations is differing for the variable water flow rate. High rate of water freezing near the evaporator internal wall leads to the thermal

expansion of the ice plug inside the volume constrained by the evaporator and auger stem walls. This results in the plug compression. As a result, crack propagation has started and continued through the next stage of the ice plug formation. The ice temperature at the specified region was in a range from -15°C to -150°C. The zone where ice plug formation conducted was laying in the range from 10 to 24 mm measured from water inlet level. Ice powder was periodically removed from the freezer. The frequency of the powder removal corresponds to the frequency of the picks of the current of the auger driver. (Figure 6.13). This phenomenon is determined by the ice plug thermal expansion, which produces an intensive compressive force against the evaporator wall. As soon as the compressive force runs up to its threshold value, the forward movements of the ice plug begins and continues until complete plug decomposition has achieved. A new portion of water occupies a vacant space and the process of ice plug formation recurs.

At this stage (Figure 7.6 b) of freezing, ice undergoes the following transformations: the frozen boundary layer thermal conductivity is sufficiently higher then that for water and ice plug formation process accelerated along with generation of the intensive thermal expansion stress. This phenomenon was clearly indicated by the current-time diagram. The ice plug polycrystalline structure undergoes the recrystallizations process with tensile zone formation along the grain boundaries. Now, the plug is populated with a wide variety of cracks of length of the order of the grain size, lying at various angles clustered around the axis of loading (after Cole [33]).

At the following stage (Figure 7.6 c), the continuing supercooling leads to a tremendous rise of the thermally generated stress due to the ice thermal expansion. There are two quite distinct cases, which correspond to the different boundary conditions. The

ice plug could fill the helical way volume completely and partially (Figure 7.7). When the ice plug entirely fills up the active decomposition volume, the biaxial thermal expansion case is present. Biaxial compression exists until the compressive force along the boundary surface of ice plug does not exceed the friction force between the ice plug, evaporator and auger walls and auger helical ways. Water flow rate and geometry of the active decomposition volume are two principal parameters that determine the compression mode of the ice plug. The uniaxial compression case exists in low water flow rate regimes, which for original experimental set up lies in the range of 20 ml/min to 60 ml/min. In this case ice expansion is restricted in horizontal direction and compressive stress of just sufficient magnitude to prevent it from expanding arises. The ice plug decomposition starts under combined thermoexpansion conditions, transition of the ice plug to a brittle mode occurs, as well as tunnel and wing crack propagation along the grain boundaries. The shearing stress of the necessary magnitude provided by auger rotation finalizes the decomposition of the plug.

The stage (Figure 7.6 d) finalizes the procedure of ice powder formation. The ice powder continued moving along the helical ways towards the evaporator outlet. The supercooling process continued without any substantial changes in the granulometric composition. It was mentioned before that ice crystallization pattern was random for this system and chosen cooling conditions. Experimental results show that efficiency of the dual side cooling schema is much higher than for single side, so it should be chosen as a preferable cooling schema for the future industrial device.

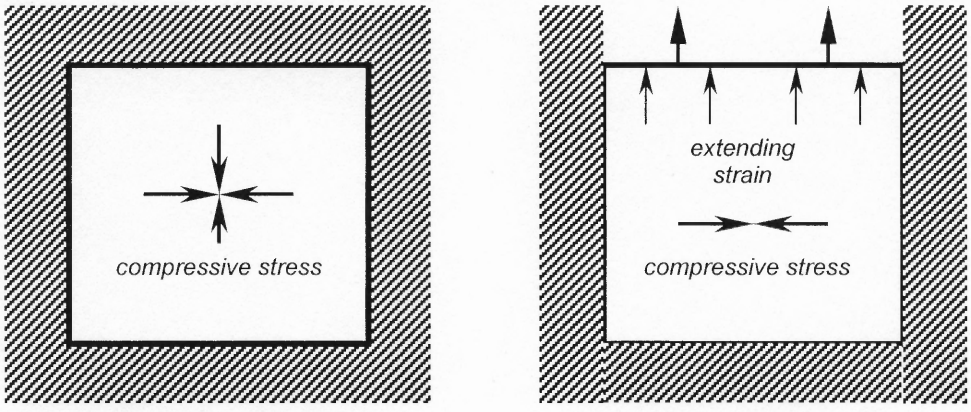

Figure 7.8 Thermally generated force: a). restricted expansion, where no movement occurs and compressive stresses develop; b). unrestricted expansion, where movement occurs in one direction and uniform uniaxial case is applicable.

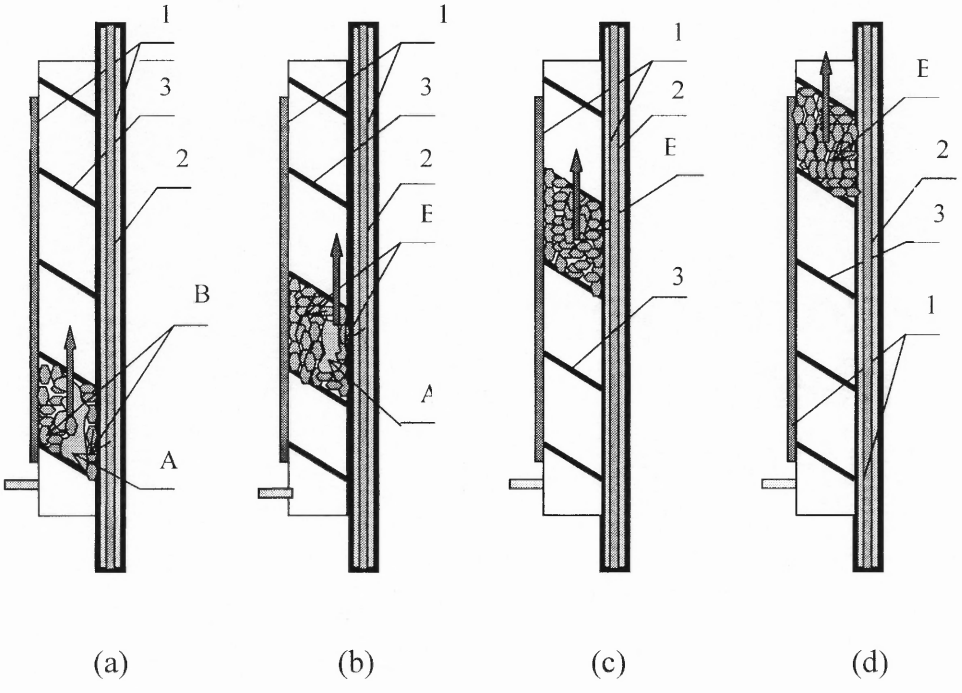

1 – cooling media flows through evaporator cooling coils and auger internal wall;
2 – auger stem;
3 – auger helical way.
A – supercooled ice granules;
B – moving boundary layer between supercooled and subzero ice granules;
⇑ - direction of auger agitated movement.

Figure 7.9 Schematic of ice nucleation inside of the evaporator in course of agitated auger movement for dual side cooling schema.

Ice plug formation started at the bottom part of evaporator with a propagation of two frozen boundaries from the internal evaporator and auger walls (Figure 7.8 a). Velocity of the heat propagation trough the both frozen boundaries were sufficiently higher then in previous cases and the plug formation occurred faster. As it was stated above, the randomly oriented polycrystalline ice structure was formed. The Weibull statistical theory suggests that in the course of ice plug solidification, defects in the form of cracks, lattice dislocations, etc, populated ice plug. The temperature gradients contribute to the thermal compression and cracks nucleation due to dislocation pile-up at grain boundaries and relief of stress concentration by parting along the grain boundaries. However, cracks may also form across grains. The studies by Hallam et al. [4] indicate that as many as 50% of nucleated cracks under compression are transgranular in character.

The ice plug populated with flaws and cracks transformed to the second stage of formation (Figure 7.8 b) where its relatively high temperature core undergoes transition to brittle mode. Cracks propagate in the ice plug volume and failure occurs by a linkage of a large number of cracks, not simply by the catastrophic propagation of a single crack. Tunnel cracks developed in the direction of the generated compressive stress. The crack wings started spreading through the ice plug and generated the crack net throughout the ice plug. During this time, the thermal expansion force is increasing rapidly with the supercooling of the ice plug. On the evaporator and auger stem internal walls a combined friction and adhesion force proportional to the thermal expansion strain rate has initiated ice plug movement towards the evaporator outlet. The new portion of water immediately

occupies an empty space between the auger and evaporator and the first stage of plug nucleation has repeated.

At this stage (Figure 7.8 c), the thermal expansion force reaches its maximum value and ice plug transformation to brittle mode is finalized. The shear stress field acting on the ice plug boundaries leads to its decomposition. The decomposed ice plug moves forward to the evaporator outlet without any substantial changes in the granulometric composition. The supercooling of the newborn ice particles continue. Their temperature directly correlated to the water flow rate.

CHAPTER 8

ADVANCED DESIGN OF THE ICE BASED JET SYSTEM

Numerical and analytical calculations of the evaporator – auger components of the ice jet system were presented in previous chapters. Based on the analysis results, the following conclusions should be made: the diameters of the evaporator and auger can be minimized, with optimization of the thickness of the ice plug or d-parameter of the system (Figure 5.1). According to the experimental results, the efficiency of the evaporator – auger set up evaluated by the average diameter of the ice particles, and ice powder flow on the evaporator outlet is very high for type *A* set up. An auger driver torque is a limitation for the design of the evaporator-auger set up with higher diameter values. It was shown that during ice nucleation compressive stresses superimposed on the evaporator and auger wall require an extremely high torque to provide ice plug vertical movement. Then the dimensions of the auger driver depend on the diameter of evaporator – auger assembly. In order minimize the dimensions of the advanced system the dimensions of the ice-making unit itself has to be optimized in accordance with the granulometric composition range and ice powder flow rate.

The number of the evaporator – auger units working in parallel can readily control productivity of the ice-making machine. The ice delivery unit can be equipped with conventional air gun or high-speed turbine mounted on the top of the evaporator – auger unit. Schematic of the advanced ice based jet system is presented on the Figure 8.1.

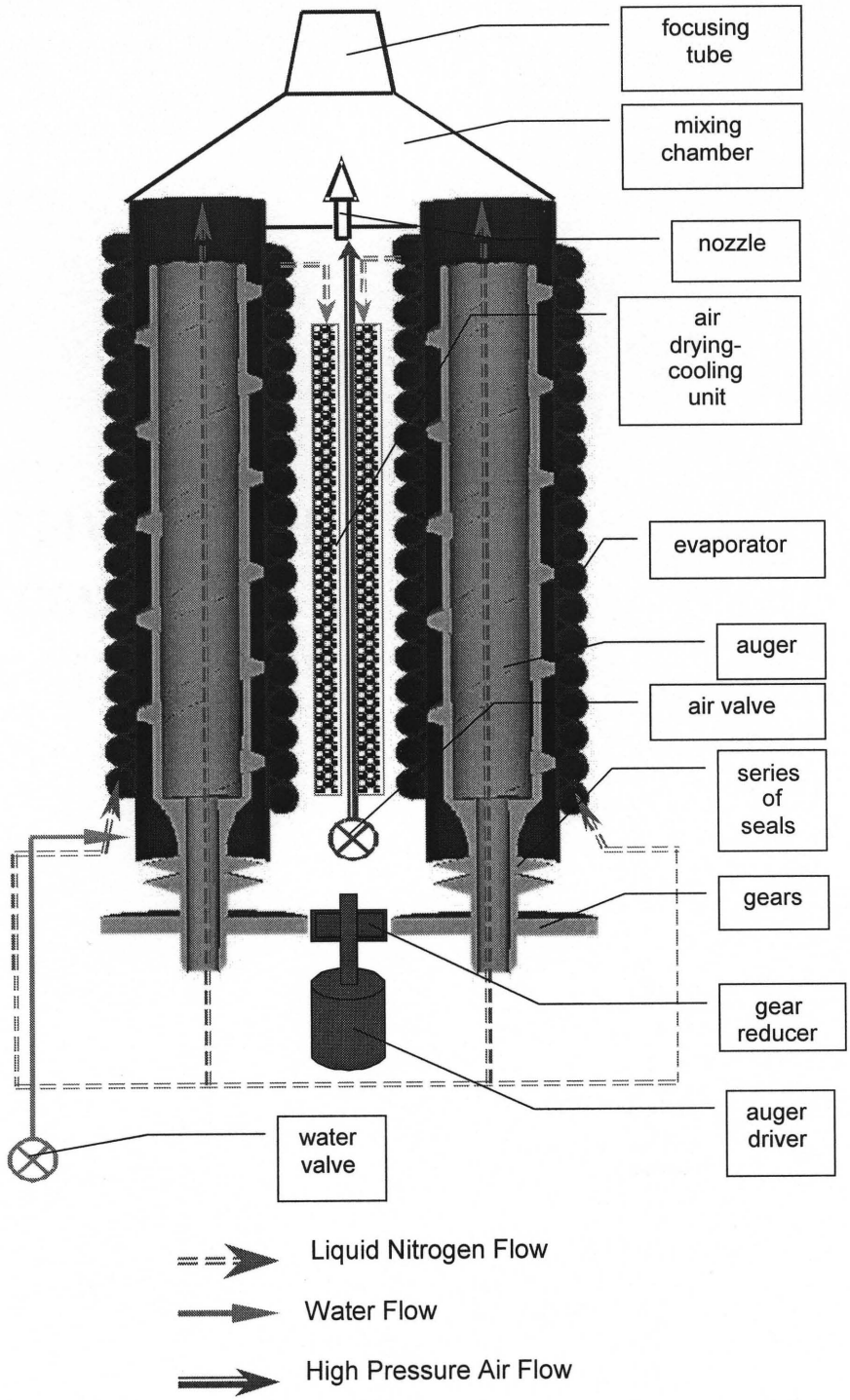

Figure 8.1 Schematic of the advanced ice based jet system.

New high pressure air drying and cooling unit was introduced in advanced design schema. The main purpose of this unit is air drying and cooling using dry desiccant dehydrant and liquid nitrogen subflow elapsing from evaporator cooling coils. Analysis of the experimental results has shown that evaporator cooling coils has to be made out of variable diameter tubing sections. Analytical results of the ice plug solidification have proven that one of the crytical parameters is solidification time which depends on the heat flux provided by the cooing media. Then, the heat flux through the water cooling and solidification zones has to be more intensive. Table 7.1 presents analyticaly determined zones distribution along the original set up evaporator.

Table 8.1 Distribution of Zones along the Evaporator

	Zones From Water Inlet Level		
water flow [ml/min]	water cooling [m]	ice freezing [m]	ice cooling [m]
20	0.03-0.0334	0.0334-0.0543	0.0543-0.18
40	0.03-0.0341	0.0341-0.1361	0.1361-0.18
80	0.03-0.0782	0.0782-0.1581	0.1581-0.18
100	0.03-0.0429	0.0429-0.1286	0.1286-0.18

Those results perfectly comply with the experimentaly determined zones.

The ice delivery unit can be equiped with the conventional air gun or high-speed turbine as it was mentioned before. It is highly recommended that suction force developed in the mixing chamber has to be precisely controlled and comparable with ice flow at the evaporator outlet. Then in the advanced design, special screen valve in mixing chamber will be introduced for precise control of the ice flow into the focusing tube. The water and high pressure air valves allowed wide range of the control for specified

parameters. Feedback control system will allow controlling the the rotational speed of the auger in wide range with high precision in accoradance with the coolant and water flow rates into the system.

CHAPTER 9

CONCLUSIONS AND RECOMMENDATIONS

9.1 Conclusions

The following conclusions can be drawn based on the experimental, analytical and numerical results found in this work:

9.1.1 General

1. The feasibility of damage free surface processing of various surfaces including highly sensitive surfaces using IAJ was demonstrated. The results of the experiments were presented at US Congress Exhibition and at several international symposiums. Boeing Inc. and Air Force requested the information pertinent to this technology. The mechanism and details of IAJ and IWJ technologies were investigated. Although the feasibility of such a technology was suggested earlier, the first comprehensive experimental, analytical and numerical study of the technology feasibility was presented in this work.

2. A prototype of industrial scale device for fabrication of ice powder at given particles property was constructed and its effectiveness was validated. Several version of prototype are available for demonstration to potential technology users.

3. Experimental and numerical investigation of water solidification resulted in the development of mechanism of ice decomposition. The ice plug contains a large number of flaws and the transformation of the material into brittle mode combined with dynamically applied compressive and shear stresses brought the ice plug about

decomposition. The size of generated particles is determined by the flaws density. It was shown that solidification is resulted in formation of the fine grains.

4. A new process for particles formation was developed and validated. The process involved solid decomposition in the course of crystallization. It was shown that rapid solidification at high compressive stresses result material decomposition at small particles. Process was validated for ice formation and can be applied to a number of other materials. The developed process was used to design a system for producing ice abrasive. The exit temperature and size of the ice particles was precisely controlled by process conditions.

5. The conceptual design of an industrial system for ice air blasting was suggested. This system includes reactor for particles production, device for particles entrainment and device for particles acceleration.

9.1.2 Investigation of Systems for Ice Particles Formation

1. The system for ice crushing was tested. The system enabled us to produce desired amount of ice particles at required output temperature and granulometric composition. However, this system required the external source of the ice. The system required a sophisticated process control procedure, which is limited the potential adoption of this system by the industry.

2. A set up for ice decomposition was constructed and tested. It implemented the principle of ice powder production in the course of solidification and auger helical motion. The evaporator-auger prototype was chosen as a base model for the industrial prototype of the icejet system. The completely different principle was employed in this

set up, which combined the external source of ice production and decomposition in one readily control technological procedure. The main impediment of the system was limited ice abrasive production. However, the simplicity of this system with very few technological parameters necessary to control the ice abrasive temperature and granulometric composition was a big advantage:

9.1.3 Reactor Design

The weight of the principal parts of the reactor has to be minimized. However, this minimization does not have to undermine a structural integrity of the reactor. The customized design of the auger part is suggested. The dual side cooling schema is required a hollow auger being used in the industrial set up. The angle of inclination of the helical thread towards the axis of auger rotation has to lie in the range between 45°-50°. The adjustable sectional cooling of the evaporator is preferable. The cooling power provided to the bottom section is required being substantially higher than for the middle and upper sections. This will assure continuous process of ice pug solidification and decomposition and possibility of high compressive stress generation.

9.1.4 Design of Ice Blasting System

The principle of forced entrainment of the ice particles into the mixing chamber was introduced in this work. The coordinated action of the suction force and spring feeder generates a continuous flow of the ice particles into the mixing chamber.

9.1.5 Investigation of the Process of Ice Decomposition

1. This work investigated the influence of those parameters on the ice abrasive. Based on the results of this work the design of the evaporator-auger system was developed.

2. A computational technique is applied to analyze stress and temperature fields in a solid phase of the ice plug formation. Heat flux was numerically calculated and results were compared with analytically determined heat flux component absorbed during the solid phase of ice plug formation. The consistency of the analytical and numerical modeling results was shown. This compliance shows that applied theory for the ice decomposition in extremely high stress field is valid and acceptable for prediction of the brittle materials behavior under application of high compressive and shear stresses.

3. The conditions of ice particles generation for the crushing, milling and evaporator-auger experimental set ups were determined. Evaporator-auger set up was investigated in depth and parameters that predetermined the abrasive formation were investigated. Stress and temperature fields required for ice plug decomposition were modeled using numerical and analytical methods.

9.1.6 Mechanism of Ice Decomposition

The Weibull statistical theory of distribution suggests that in the course of ice plug solidification, defects in the form of cracks, lattice dislocations, etc, populated ice plug. Thermal velocity is contributed to thermal compression and cracks nucleation due to dislocation pile-up at grain boundaries and relief of stress concentration by parting along the grain boundaries. Ice plug populated with flaws and cracks transformed to the second stage of formation where its relatively high temperature core undergoes transition to

brittle mode. Cracks propagate in the ice plug volume and failure occurs by a linkage of a large number of cracks, not simply by the catastrophic propagation of a single crack. Tunnel cracks developed in the direction of the compressive stress, which has been applied. The crack wings started spreading through the ice plug and generated the crack net throughout the ice plug, which brings about a complete decomposition of the ice plug.

9.1.7 Ice Water Blasting

1. The series of the experiments involved IWJ cutting and drilling of various materials were conducted. The superior cutting and drilling ability of the IWJ was shown. A numerical modeling of the ice particle behavior in the mixing chamber constituted the extensive presence time of the ice particles in the mixing chamber, which caused their complete or partial disintegration.
2. Cooling of the water prior to the nozzle could be a solution of this problem. Another possible approach is producing supercooled ice abrasive. Further thermodynamic analysis of this task has to be conducted.

9.1.8 Ice Air Blasting

1. The unique properties of IAJ enable using it in the semi-conductor, electronic, bio-medical, food and other zero-pollution tolerance industries.
2. The design of the industrial device for production of the ice powder was suggested.

9.2 Recommendations

1. The precise methods for thermal compressive and shear stress measurement have to be developed. The series of strain gauges and resistance probes should be situated on the evaporator and auger walls for continuing monitoring of process parameters. For real time monitoring of the pressure, temperature and conductivity parameters a data acquisition card will be employed.

2. Series of industrial scale prototypes has to be constructed.

3. High-speed turbine with special designed blade profile will be introduced for ice particles acceleration.

4. The results of this work constitute a foundation for a number of new technologies such as etching of soft materials, cleaning of electronics, precision cleaning of mechanical parts, food cleaning, infrastructure maintenance including the graffiti removal. The possibility of damage free cleaning of the extremely sensitive surfaces such as electronic boards, soft materials, food products and human skin was shown. The use of this technology will eliminate use of the cleaning chemical solvents and have profound effect on environment. The one of the possible promising applications is decontamination of surface from chemical, bacteriological and radiological contaminants. This technology was demonstrated to US Army. As the result US has supported this research program for development of the technology for the field decontamination facilities.

5. The development of this technology will enable producing low cost fine powder. As a result, it can be adopted by the semiconductor, electronics and biomedical industries.

6. As the result of this investigation, the practical approach for brittle material decomposition is suggested. The generated high compressive stress combined with the dynamically applied shear stress will bring to a decomposition of the brittle materials.

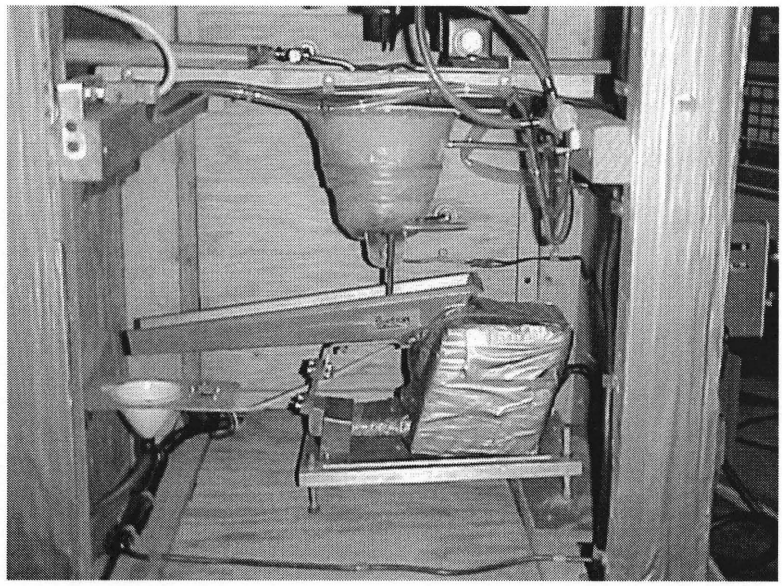

(a)

(b)

Figure A.2 (a) Photograph of the intermediate supply bunker 1and the electromagnetic vibrator, and (b) photograph of the air gun with high-pressure air supply line and intermediate supply line.

APPENDIX A

CRUSHING TECHNIQUE PROTOTYPE OF ICEJET FORMATION

The detailed view of the crushing technique prototype is presented below:

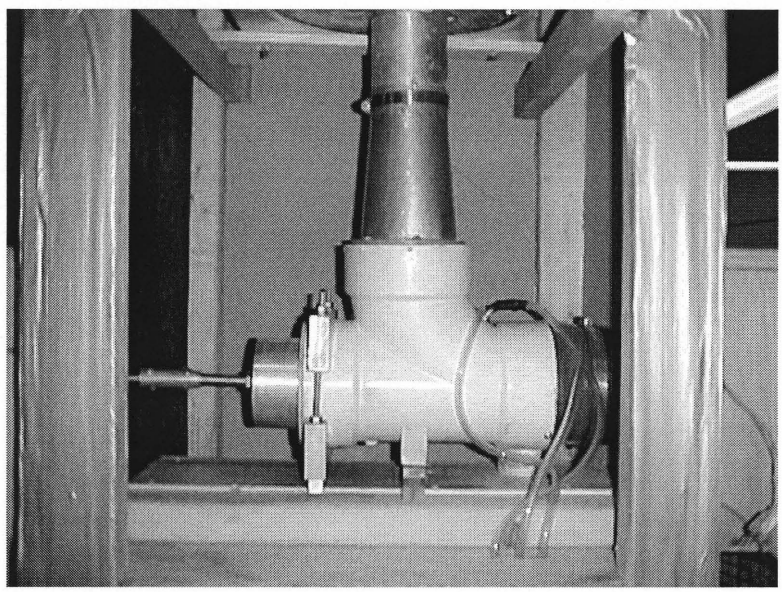

(a)

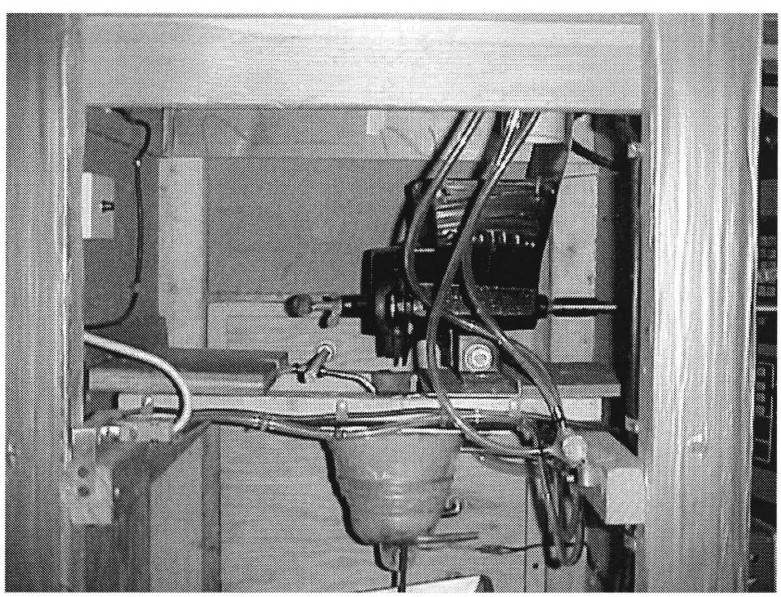

(b)

Figure A.1 (a) Photograph of the first stage of crushing (average diameter of ice particles 5.0 mm $<D_1<$ 10.0 mm), and (b) photograph of the second stage of crushing (average diameter of ice particles 1.0 mm $<D_2<$ 3.0 mm).

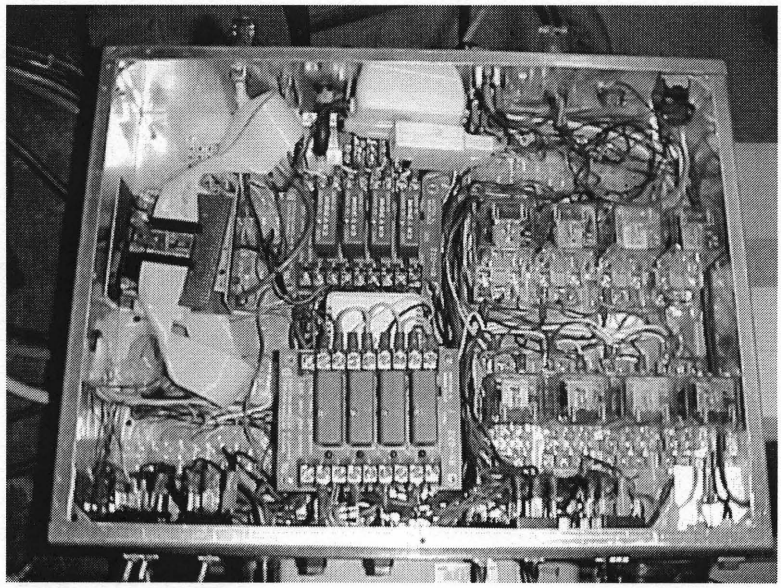

(a)

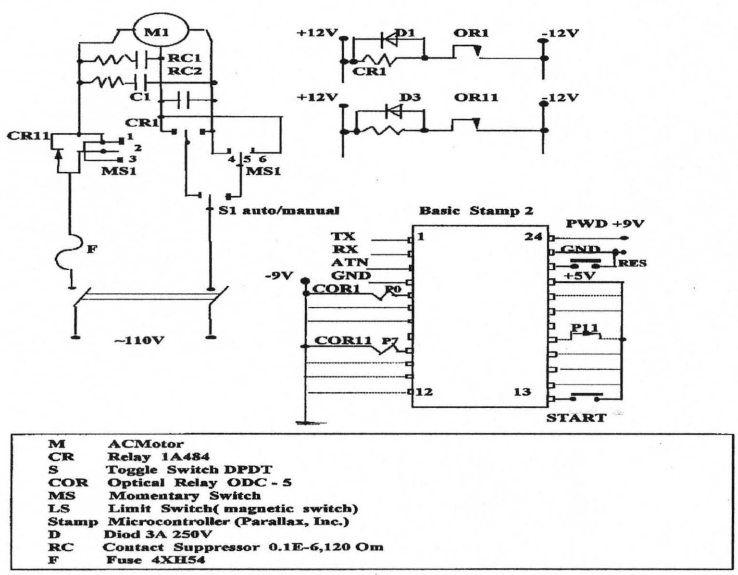

M	ACMotor
CR	Relay 1A484
S	Toggle Switch DPDT
COR	Optical Relay ODC - 5
MS	Momentary Switch
LS	Limit Switch(magnetic switch)
Stamp	Microcontroller (Parallax, Inc.)
D	Diod 3A 250V
RC	Contact Suppressor 0.1E-6,120 Om
F	Fuse 4XH54

(b)

Figure A.3 (a) Photograph of the schematic of automatic control system, and (b) electrical schematic of the automatic control system.

```
START :
DEBUG " START LOOP "
LOW 1:LOW 2:LOW 3:LOW 4:LOW 5:LOW 6:LOW 7:LOW 8:LOW 9:LOW 10:
LOW 11:
INPUT 8
LOW 8
IF IN 8=1 THEN RUN
B0=0:B1=0:WO=0:
GOTO START
RUN: DEBUG " SYSTEM WORKING "
FOR B0=0 TO 99
DEBUG ? B0
HIGH 7:HIGH 3
PAUSE 60000
LOW 7:LOW 3
DEBUG " VIBRATOR IS WORKING "
SLEEP 1
NEXT
STOP
```

Figure A.4 Example of the program written in programming language for CPU Basic Stamp II.

APPENDIX B

DESCRIPTION OF EVAPORATOR-AUGER SET UP

The detailed views of the evaporator-auger reactor and ice particles acceleration block are presented below:

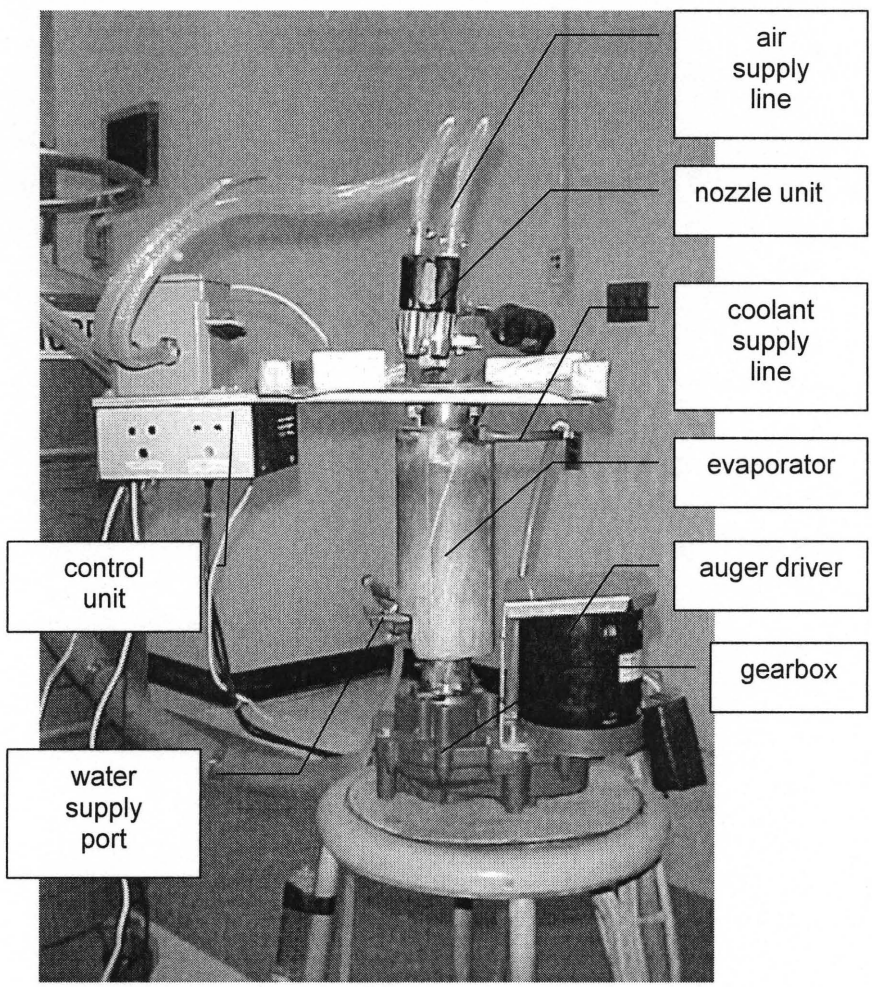

Figure B.1 Detailed view of evaporator-auger set up with nozzle unit mounted at the outlet of the reactor.

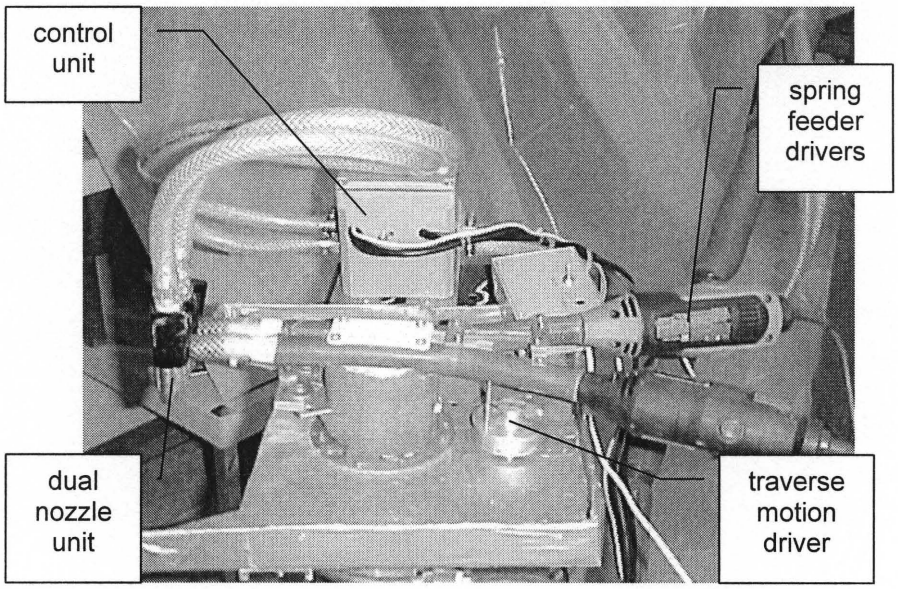

Figure B.2 Conventional air blasting gun as the ice particles accelerator device.

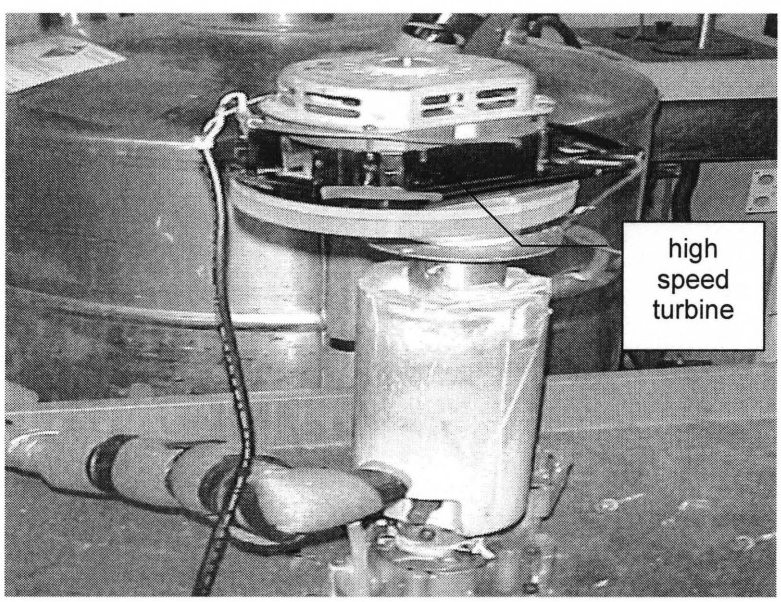

Figure B.3 High speed turbine as the ice particle accelerator device.

APPENDIX C

FIDAP MODELING OF PARTICLES MOTION

The numerical modeling results of the ice particles behavior are presented below:

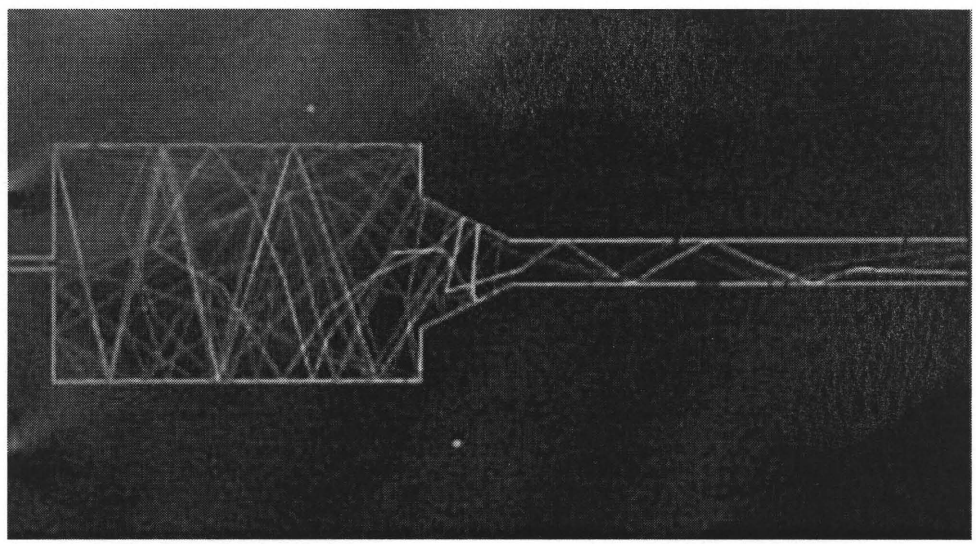

(a)

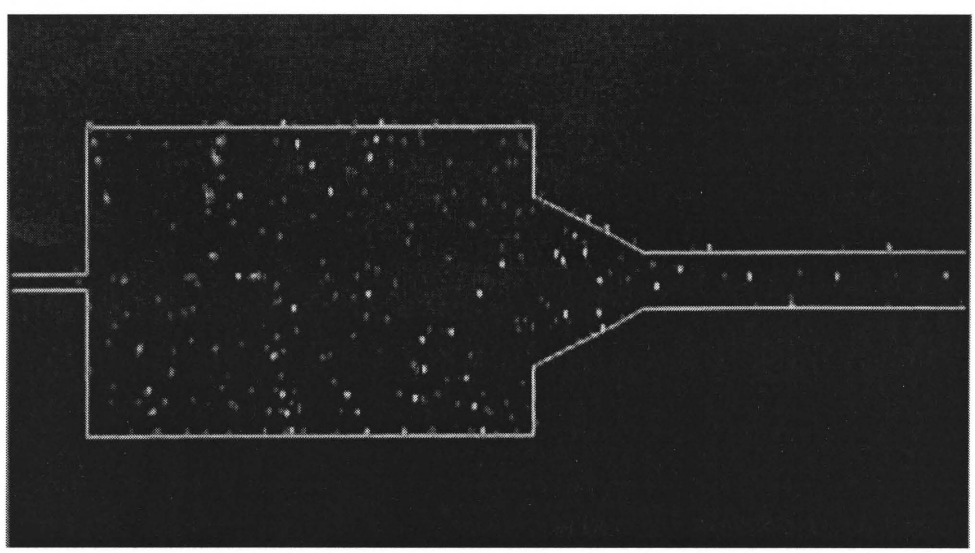

(b)

Figure C.1 (a) Monitoring of particles trajectory in the coarse of formation of the Ice Water Jet. Notice the duration of particles residence in the mixing chamber. In the case of formation of IceJet this results in melting and disappearance of ice particles, and (b) particles distribution in the mixing chamber and focusing tube. Excessive residence time in the mixing chamber brings about disappearance of ice particles.

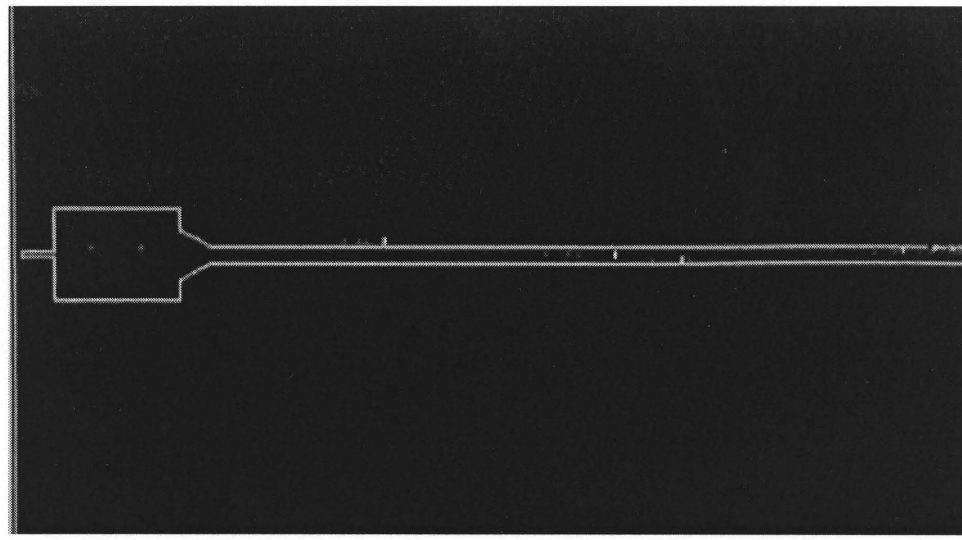

(a)

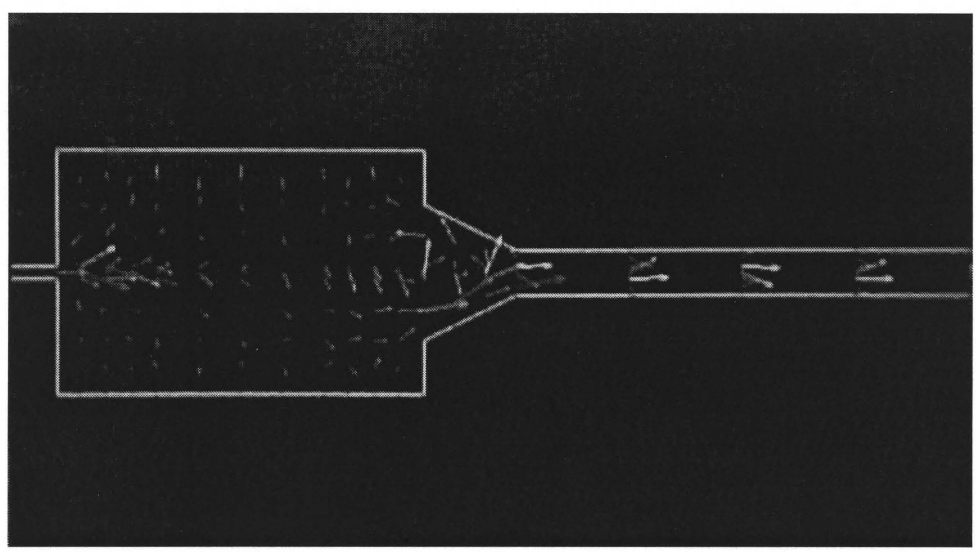

(b)

Figure C.2 (a) Particles distribution within the water flow in the case of axial particles supply. Notice short particles residence time in the mixing chamber. This mode of particles supply is effective for IceJet Formation, and (b) distribution of water velocity in the coarse of IceJet Formation. Notice high particles velocity in the entrance of focusing tube. In the case of collision this velocity brings about particles disintegration.

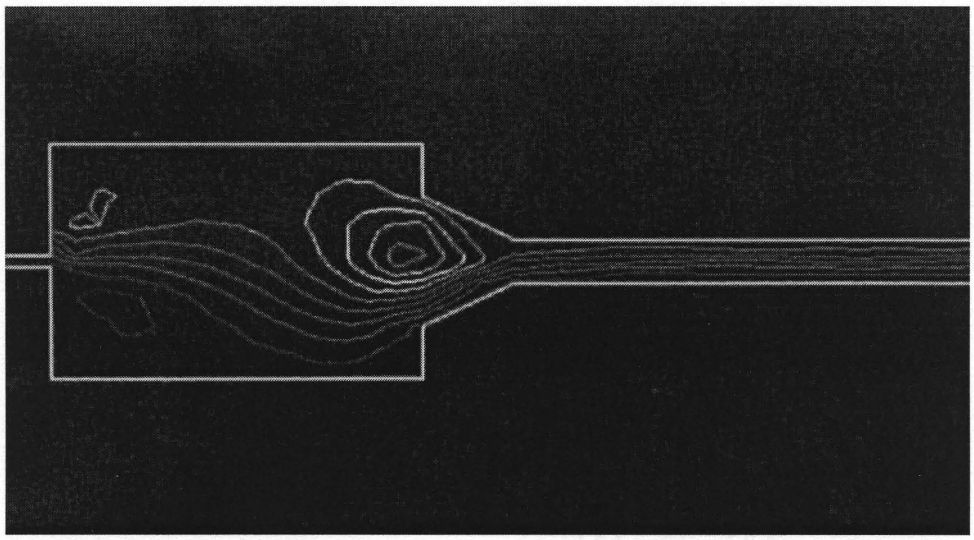

Figure C.3 Pattern of water flow in the coarse of IceJet Formation. Notice intensive water circulation in the entrance of the focusing tube. This results in melting and disappearance of ice particles.

APPENDIX D

PHOTOGRAPHS OF SAMPLES OF WATERJET AND ICEJET CUTTING

The set of waterjet and icejet cutting experimental parameters is presented below:

- water pressure : 340.0 MPa (50,000 psi);
- standoff distance : 2.5 mm;
- diameter of sapphire : 250 micron;
- diameter of focusing tube : 1100 micron;
- speed of WJ and AWJ cutting : 25 cm / min;
- speed of IJ cutting : 5cm / min.

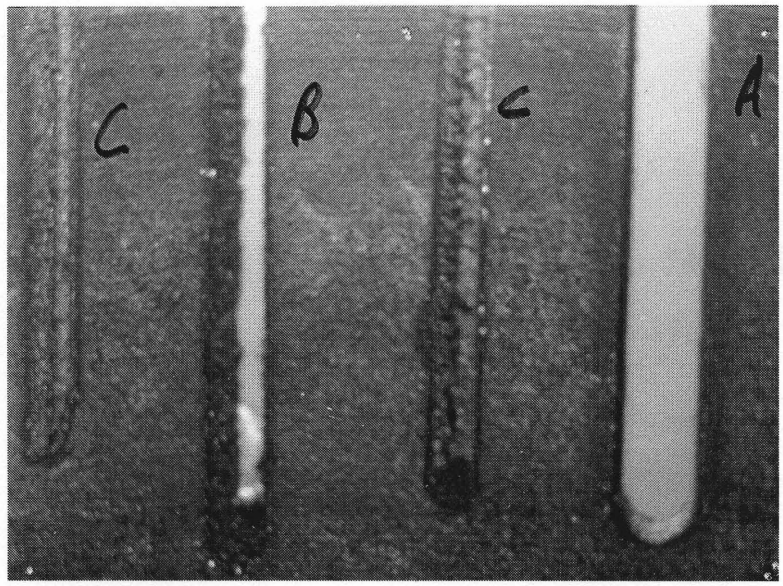

(a)

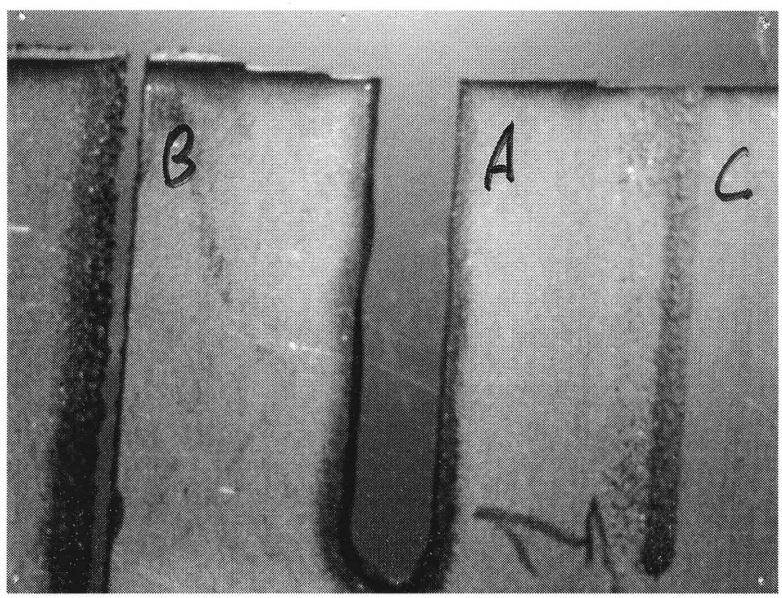

(b)

Figure D.1 Photographs of (a) cutting of copper strip of thickness 1.7-mm (X65) Notice reduced width of kerf in the coarse of IJ cutting. Notice intensive erosion of the substrate surface in the vicinity of IJ generated kerf, and (b) cutting of stainless steel strip of thickness 0.7-mm (X65). Notice superior machining ability of IJ comparative to WJ. Notice reduced width of the kerf generated by IJ.
A – Abrasive Waterjet ; B – IceJet ; C – WaterJet .

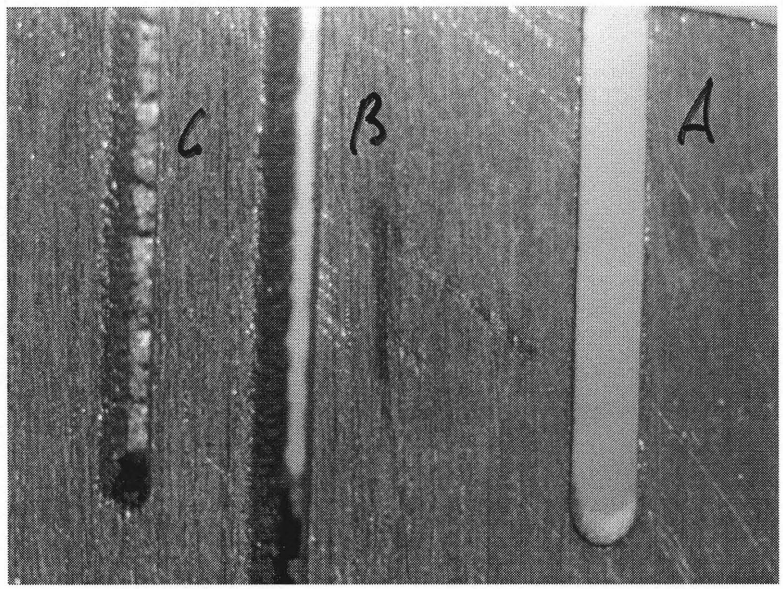

(a)

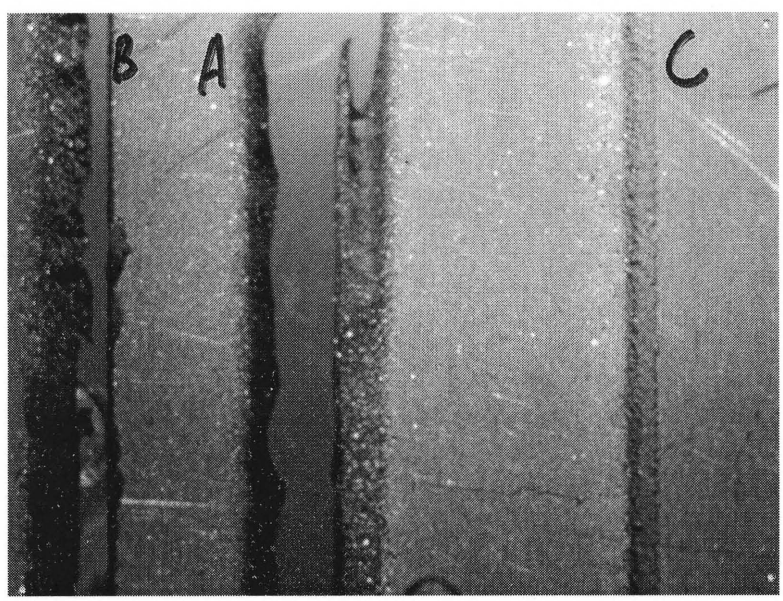

(b)

Figure D.2 Photographs of (a) cutting of aluminum strip of thickness 3.1 mm (X65). Notice reduced width of the kerf generated by IJ. Notice substrate surface erosion in the vicinity of IJ generated kerf, and (b) cutting of stainless steel strip of thickness 1.3 mm (X65). Notice superior machining ability of IJ comparative to WJ. Notice reduced width of the kerf generated by IJ.
A – Abrasive Waterjet; B – IceJet; C – WaterJet.

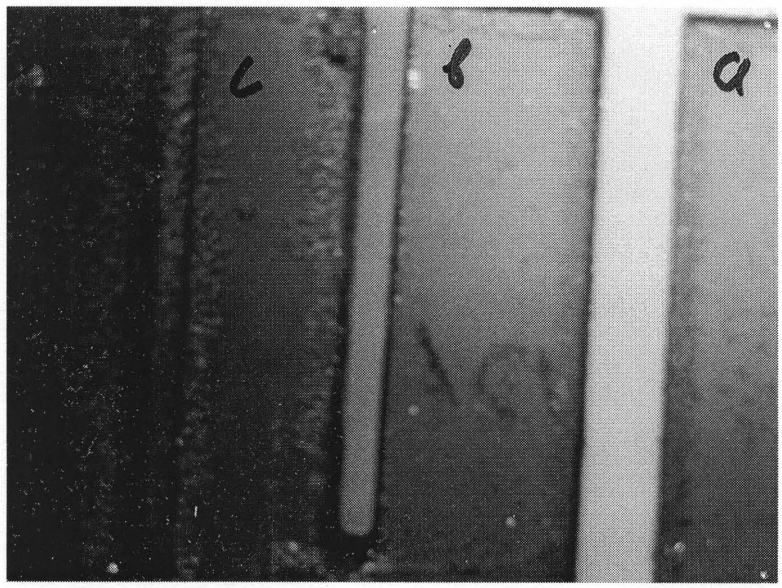

(a)

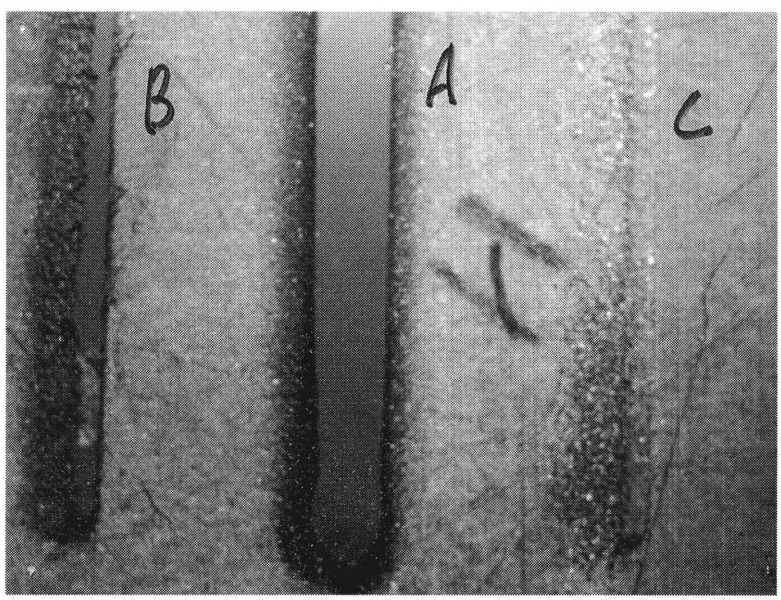

(b)

Figure D.3 Photographs of (a) cutting of carbon steel strip of thickness 0.7 mm (X65). Notice reduced width of kerf in the coarse of IJ cutting. Notice intensive erosion of the substrate surface in the vicinity of IJ generated kerf, and (b) cutting of titanium sample of thickness 0.7 mm (X65). Notice reduced width of kerf in the coarse of IJ cutting. Notice intensive erosion of the substrate surface in the vicinity of IJ generated kerf.
A – Abrasive Waterjet; B – IceJet; C – WaterJet.

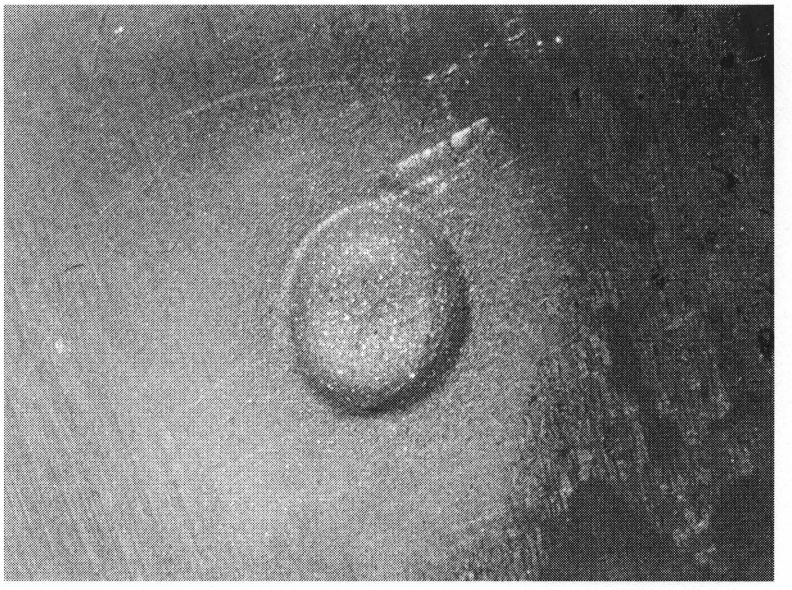

(a)

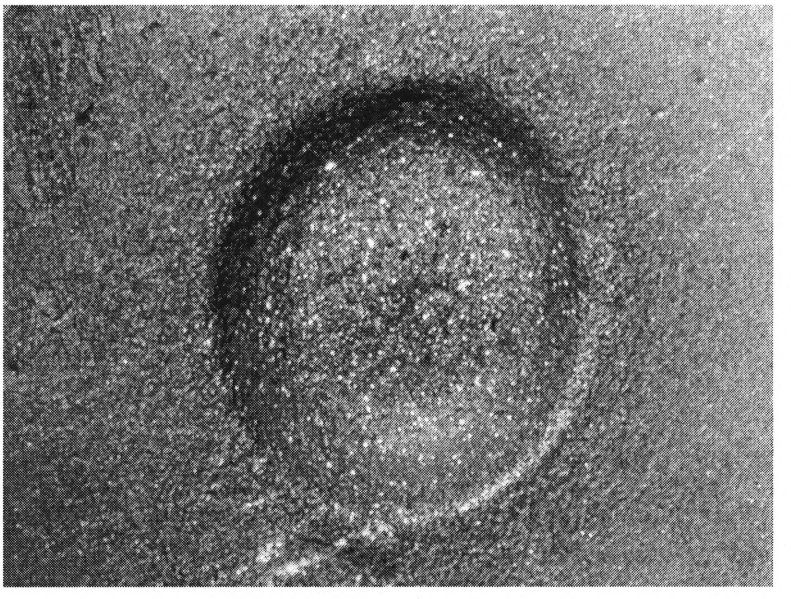

(b)

Figure D.4 Photograps of drilling of copper disk of thickness 1.7 mm, by WJ: (a) small magnification, (b) magnification (X65). Notice not complete penetration of WJ through the disc body.

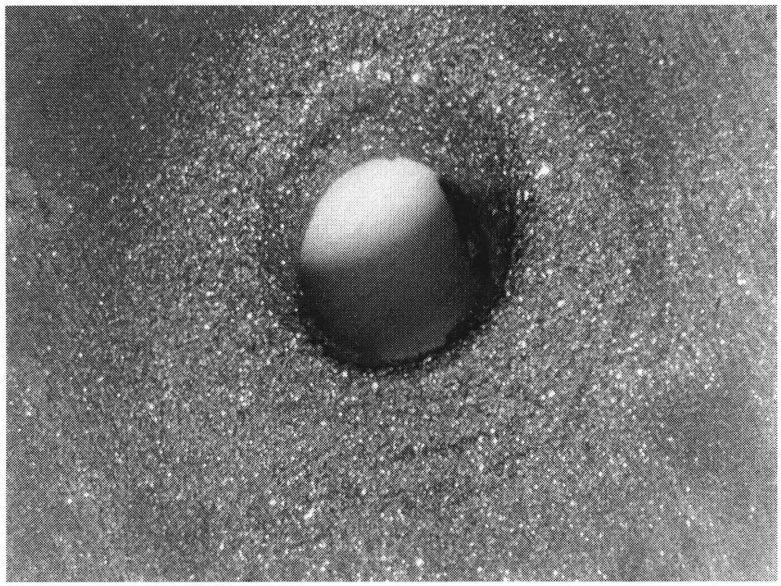

(a)

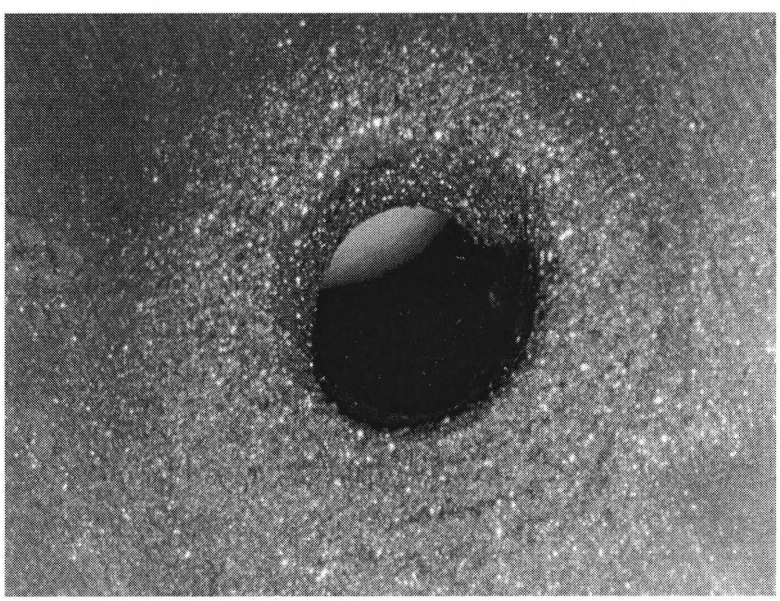

(b)

Figure D.5 Photograhs of (a) and (b) drilling of copper disk of thickness of 1.7 mm, by IJ (X65). Notice complete penetration of IJ through the disc body.

APPENDIX E

PHOTOGRAPHS OF SAMPLES OF ICE AIRJET CLEANING

The set of ice airjet cleaning experimental parameters is presented below:

- air pressure: 0.544 MPa;
- standoff distance: 25.0 mm-50.0 mm;
- diameter of nozzle: 5.0 mm;
- traverse speed of cleaning: 5.0 cm / min;
- cleaning mode: manual.

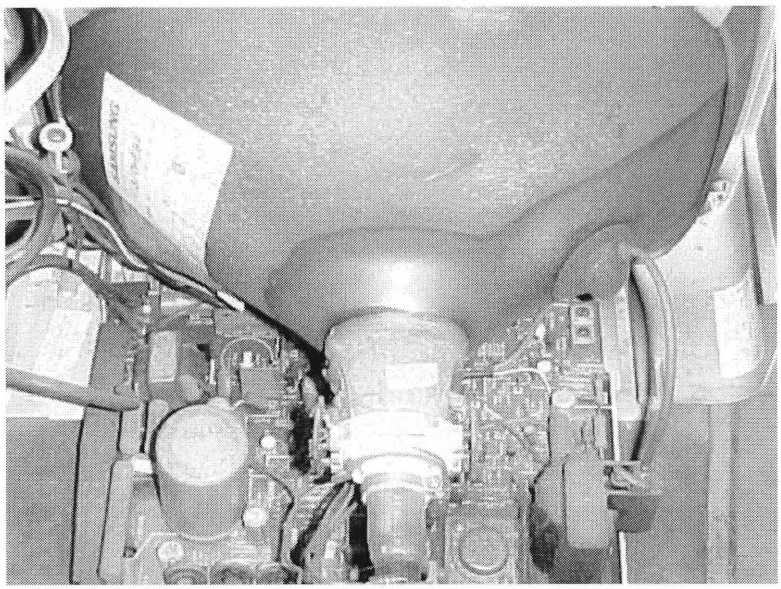

(a)

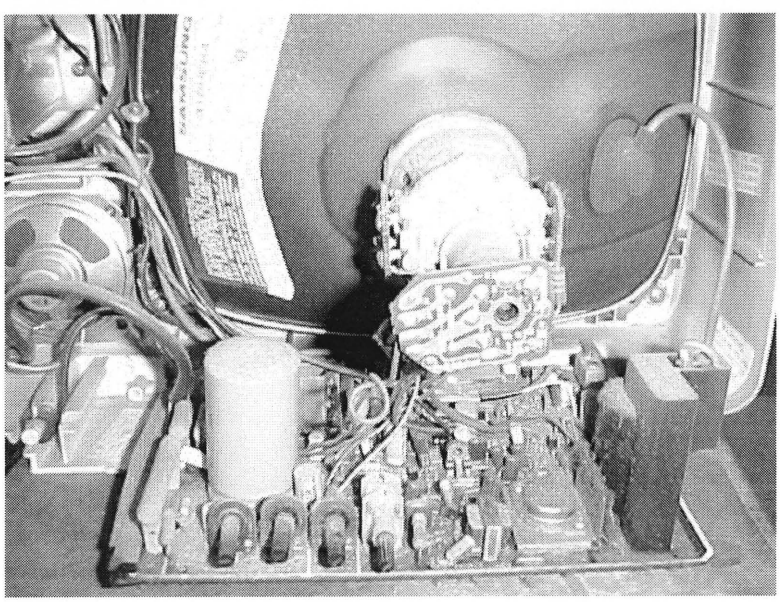

(b)

Figure E.1 (a) and (b) photographs of electronics board of TV set. Notice the heavy layers of dust and dirt on the electric and electronic components of board.

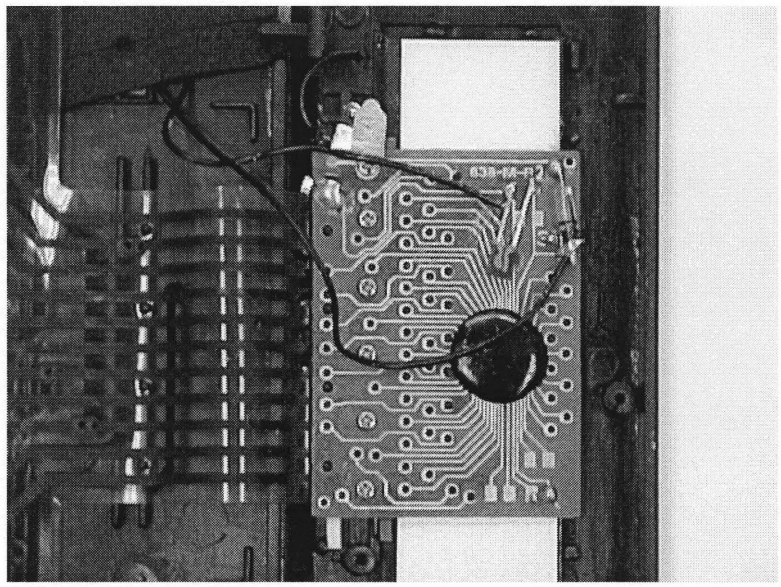

(a)

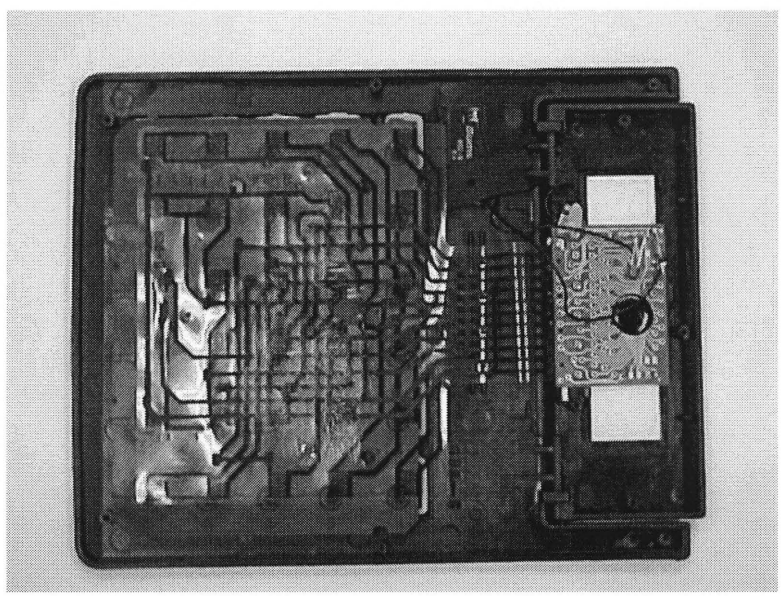

(b)

Figure E.2 (a) Photograph of the electronic board of the calculator. The calculator was disassembled and all components of the system including the LC display were covered by the mixture of lithium grease and copper powder, and (b) photograph of the calculator electronic board. Notice soft PVC electronic matrix of the calculator. The extremely sensitive surface of matrix was covered by the mixture of the lithium grease and copper powder. . After this coverage the calculator was disabled. After IJ cleaning the calculator performed normally.

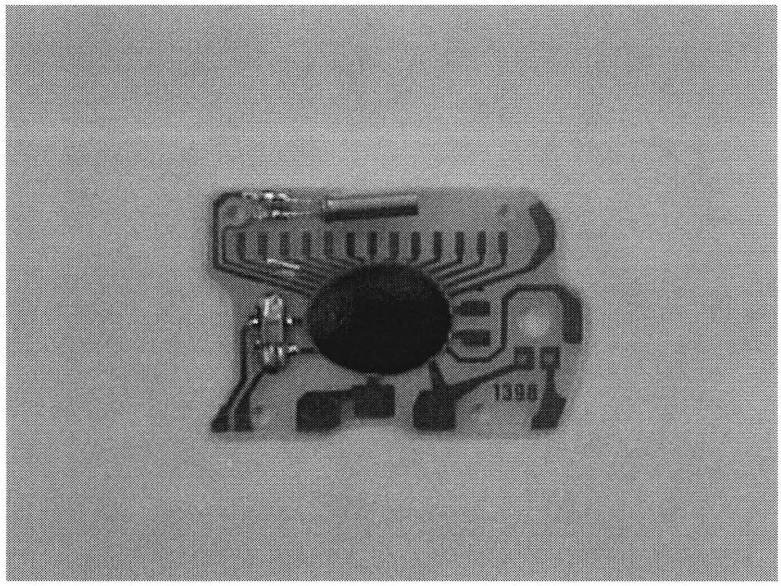

(a)

(b)

Figure E.3 (a) The electronic watches were disassembled and covered by the mixture of lithium grease and copper powder. After this the watches were disabled. Then all components of watches including microchips, conduits and LC displays were decontaminated, and (b) after IJ cleaning the watches performed normally.

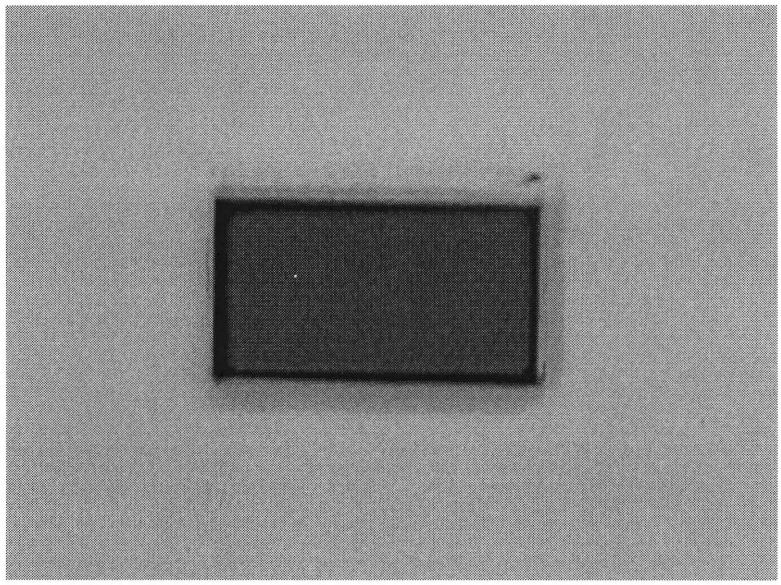

(a)

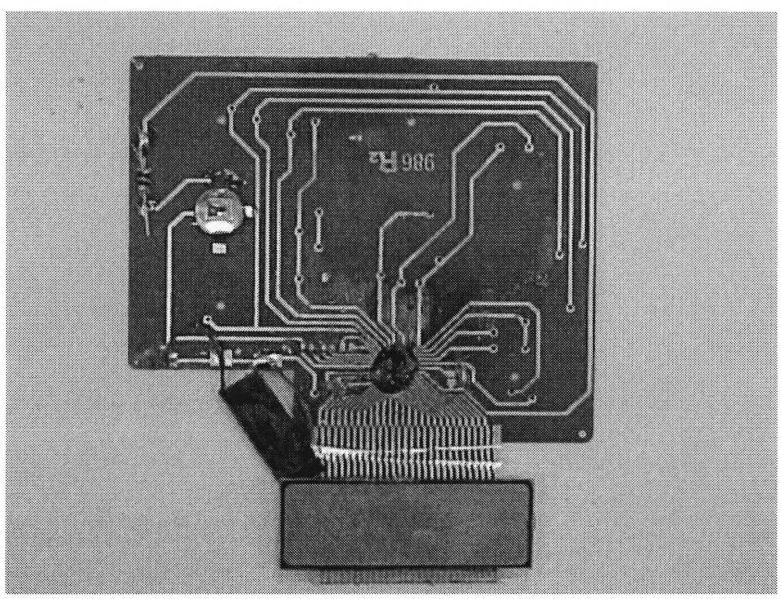

(b)

Figure E.4 (a) photograph of LC display of the electronic watch. Display was disabled by the lithium grease and then cleaned by IJ. After IJ cleaning extremely sensitive LC display performed normally, and (b) photograph of disassembled electronic board of the calculator containing microchip, LC display, solar panel element, conduits, diodes and battery. The board was contaminated by the mixture of lithium grease and copper powder and then decontaminated by IJ. After cleaning all elements of the board performed normally. No damage was induced to the vital electronic components of the system.

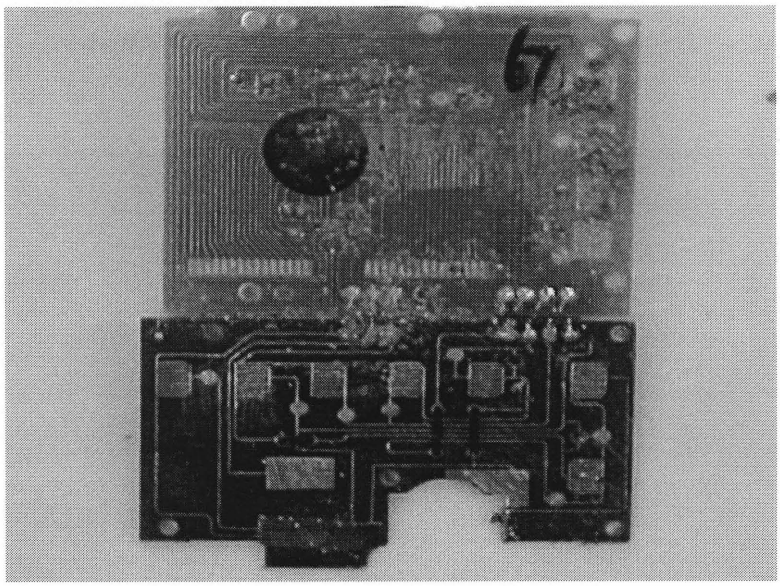

(a)

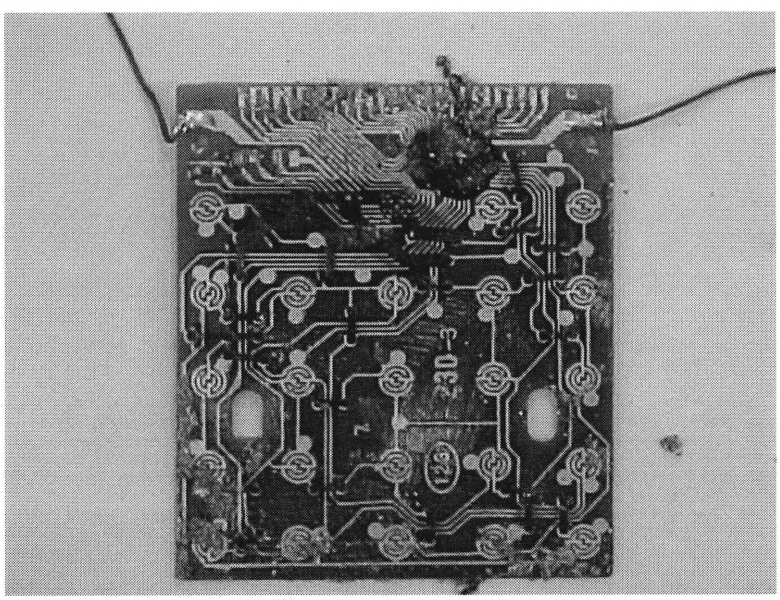

(b)

Figure E.5 (a) and (b) photographs of the board of the electronic games containing electric conduits, microchip and electronic matrix. The board was covered by the mixture of the lithium grease and copper powder and disabled. Notice the cross contamination of electric conduits of the board. After cleaning the game performed normally.

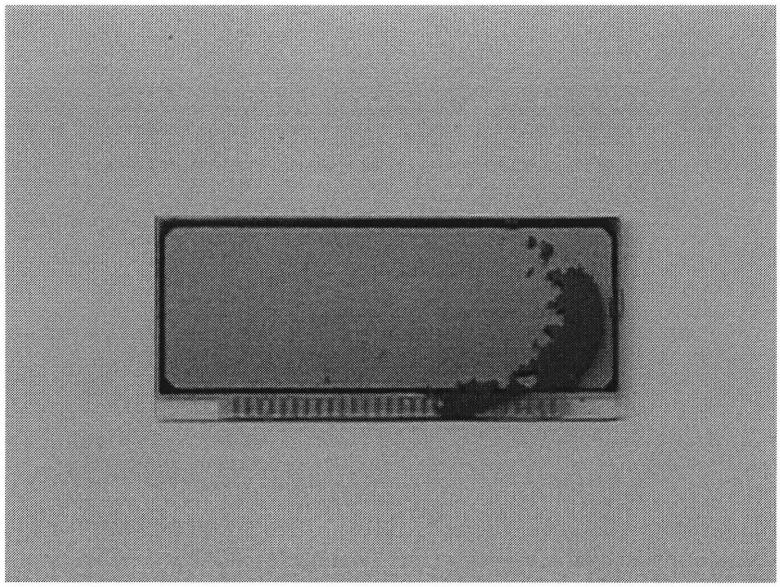

(a)

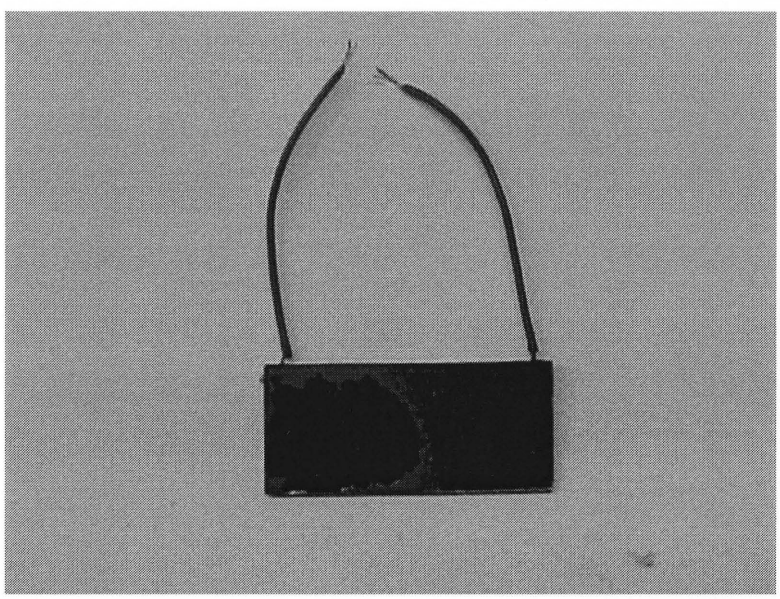

(b)

Figure E.6 (a) photograph of the LC display of the calculator containing electronic matrix and LCD conduits. The display was contaminated by Rust-Oleum gloss protective enamel. Then all elements of LC display were decontaminated by IJ. In assembly of the calculator the LC display performed normally, and (b) photograph of the solar panel element of the calculator containing electronic matrix and conduits. The solar panel was contaminated by heavy layer of Rust–Oleum gloss protective enamel and then decontaminated by IJ. In the assembly of the calculator the solar panel performed normally. Notice that the semiconductor elements of the matrix are highly sensitive.

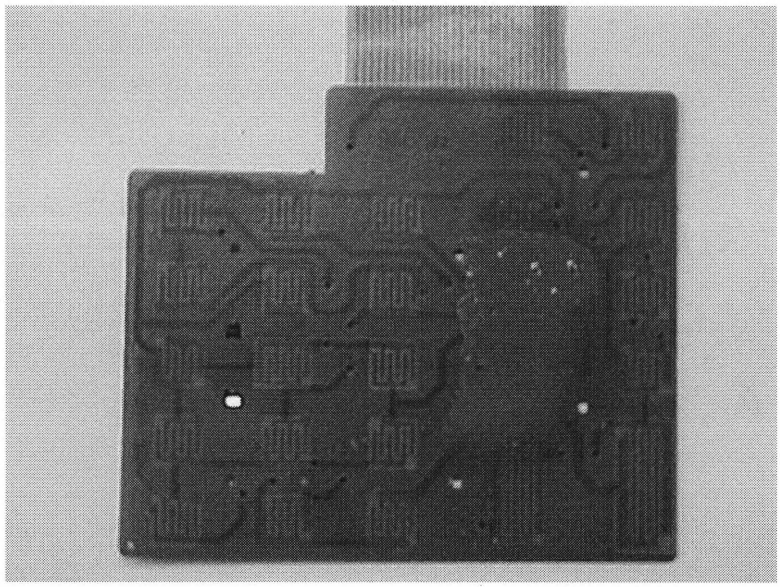

(a)

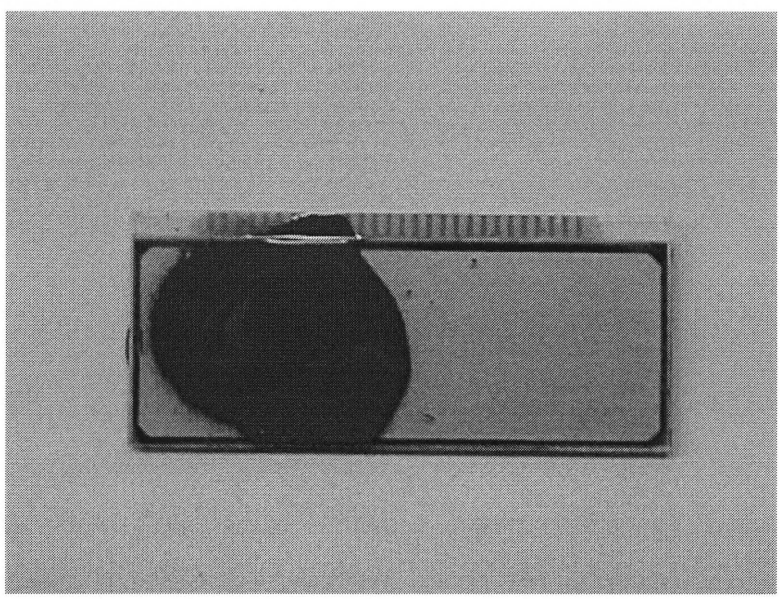

(b)

Figure E.7 (a) photograph of the electronic board of the calculator containing electronic matrix. The electronic board was contaminated by Rust-Oleum gloss protective enamel. Then electronic board was decontaminated by IJ. In assembly of the calculator the electronic board worked normally, and (b) photograph of the LC display covered by the heavy layer of Rust-Oleum gloss protective enamel. Notice the cross-contamination of the electrical conduits of LCD.

(a)

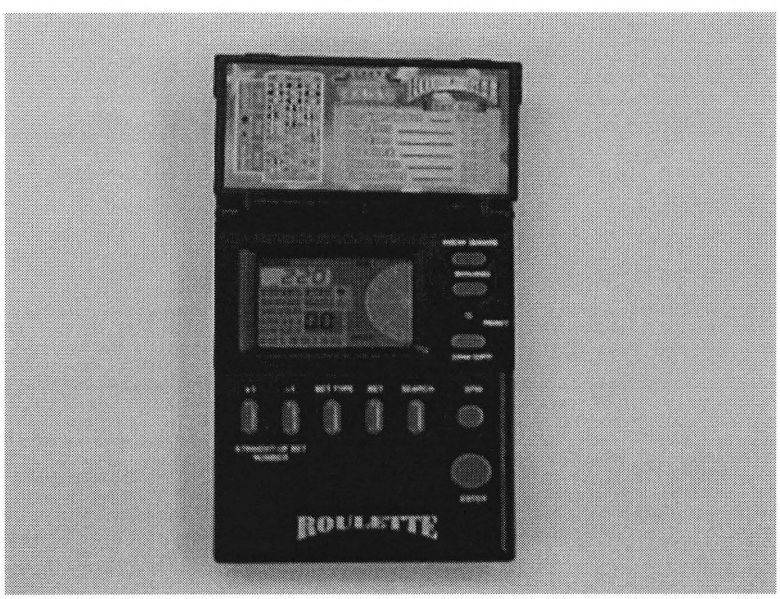

(b)

Figure E.8 (a) and (b) photographs of the electronic games in assembly after IJ cleaning. The electronic games performed normally.

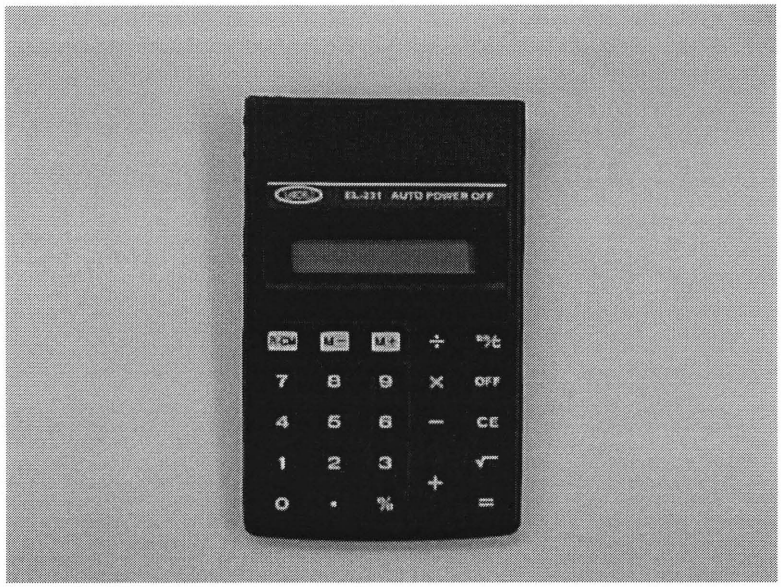

(a)

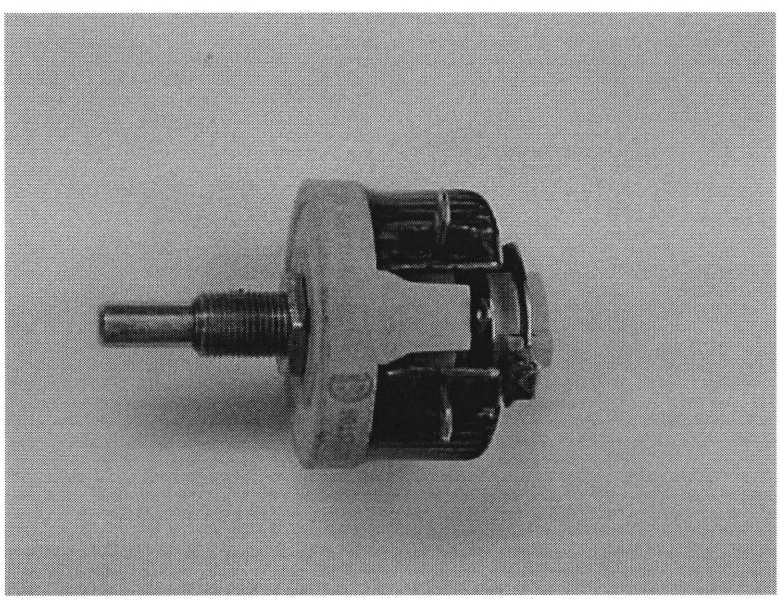

(b)

Figure E.9 (a) photograph of the calculator cleaned by IJ in assembly. The assembled electronic calculator operated normally, and (b) photograph of the electrical varistor. The varistor was contaminated by the mixture of the lithium grease and copper powder. Then the varistor was cleaned by IJ. After cleaning varistor worked normally. Notice the complicated geometry of the varistor surface. The feasibility of cleaning of complicated surfaces was demonstrated.

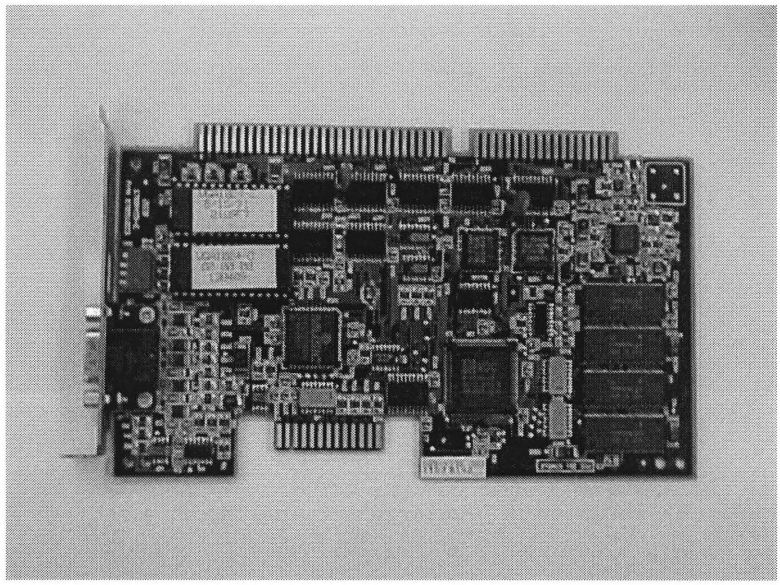

(a)

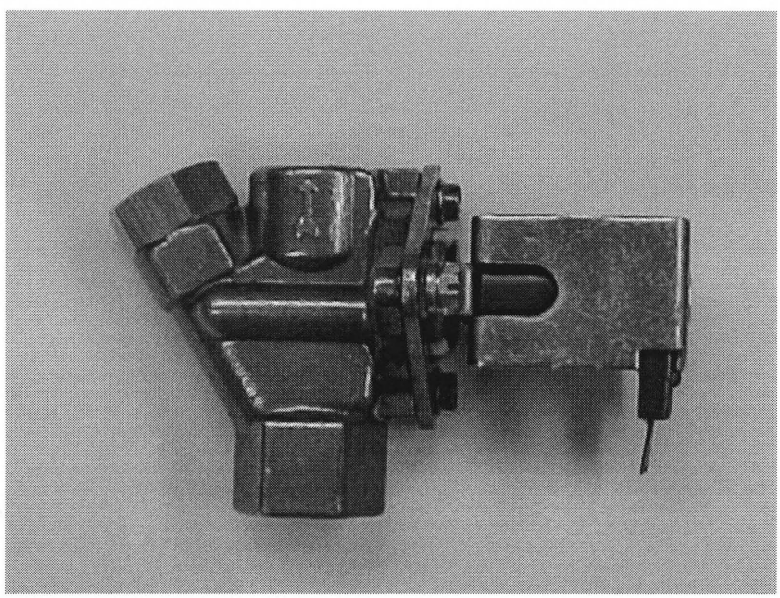

(b)

Figure E.10 (a) photograph of the monitor board of PC Brook 486DX33. The monitor board was contaminated by the heavy layer of the mixture of lithium grease and copper powder and disabled. Then the board was decontaminated by IJ. The board performance was normal in assembly with PC. The feasibility of restoration of complicated electronic parts was demonstrated, and (b) photograph of the electrical solenoid valve with connectors contaminated by Rust-Oleum gloss protective enamel. The contacts of solenoid valve were cleaned by IJ. After cleaning the solenoid valve was connected to the electrical supply source and performed normally. This experiment demonstrated the feasibility of using IJ technique for decontamination and restoration of contacts of different electronic devices.

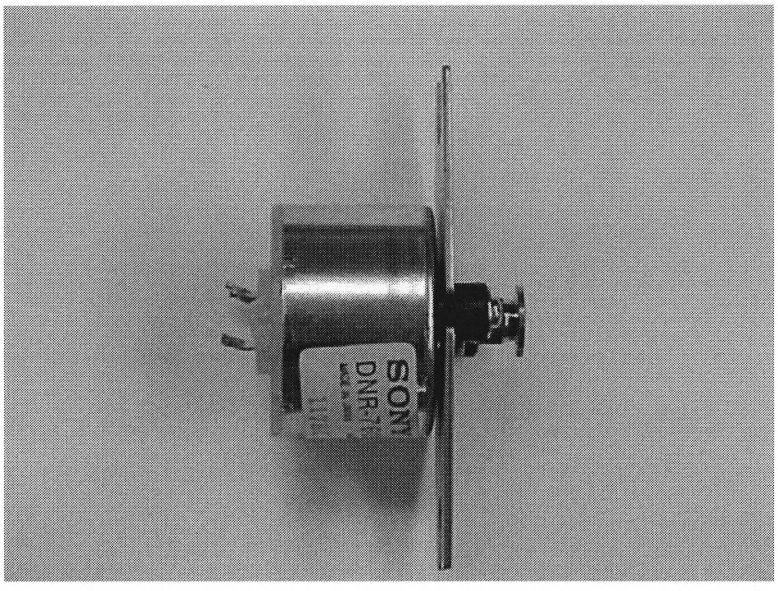

(a)

(b)

Figure E.11 (a) photograph of the DC motor. DC motor was disassembled and all elements were covered by the mixture of lithium grease and copper powder. DC motor was cleaned by IJ. In assembly DC motor performed normally, and (b) photograph of TV set in assembly. The contaminated board of TV set is shown in Figure D.1. After cleaning TV set worked normally.

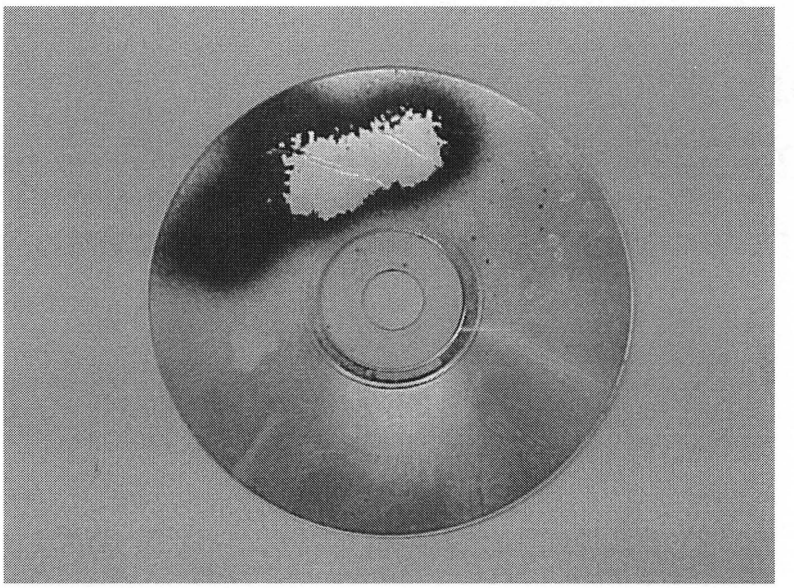

(a)

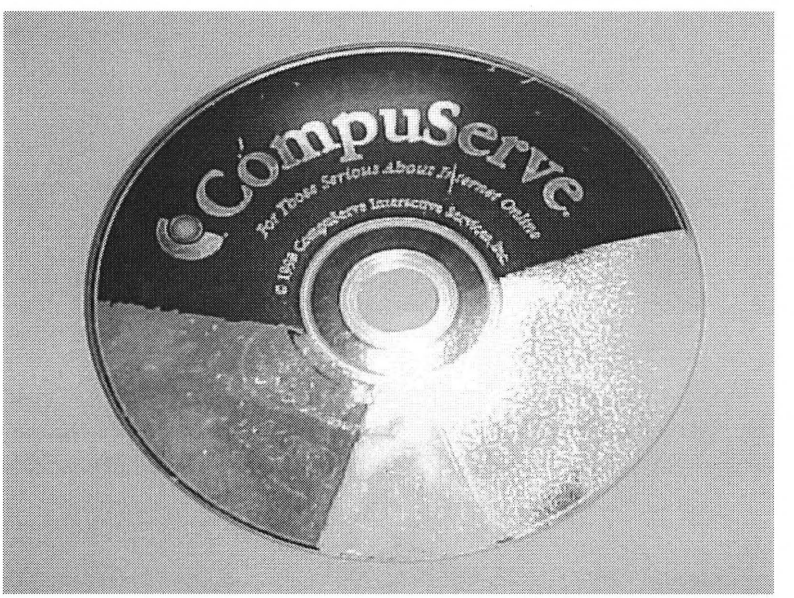

(b)

Figure E.12 (a) photograph of the CD-ROM covered by Rust-Oleum gloss protective enamel. The paint was partially removed from the CD ROM surface. No surface damage was observed in the course of IJ cleaning, and (b) photograph of the CD-ROM partially cleaned by using of IJ technique. Notice that both layers of paint and emulsion were removed. No surface damage was observed in the course of IJ processing.

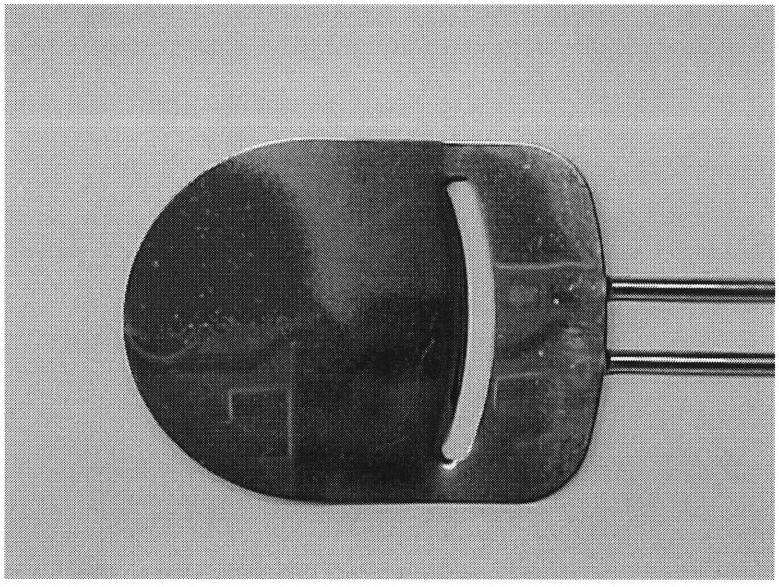

(a)

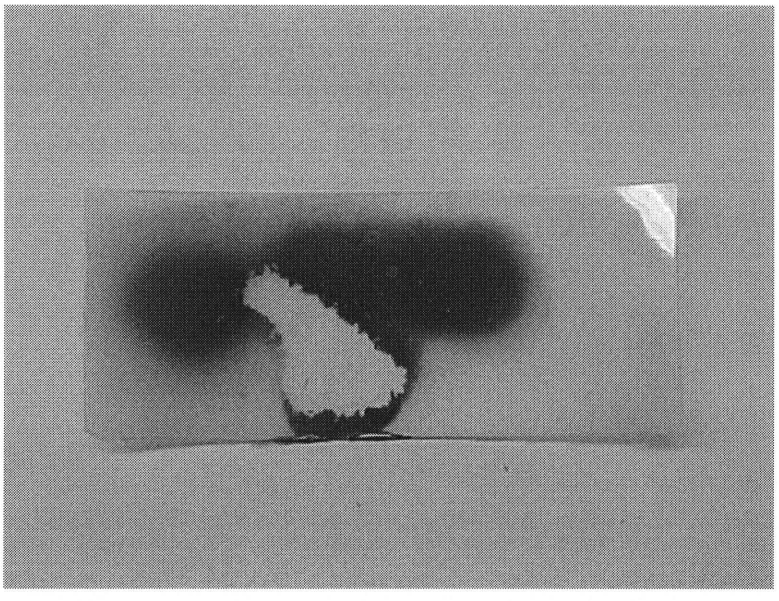

(b)

Figure E.13 (a) Photograph of the polished steel surface. The polished steel surface was contaminated by the Rust-Oleum gloss protective enamel. The paint was partially removed from the polished surface. No surface damage was observed in the course of IJ cleaning. The feasibility of the precision cleaning of polished surfaces was demonstrated, and (b) photograph of the strip of soft plastic covered by Rust-Oleum gloss protective enamel. The paint was partially removed from the plastic surface. No surface damage was observed. The feasibility of restoration and fabrication of plastic parts was demonstrated.

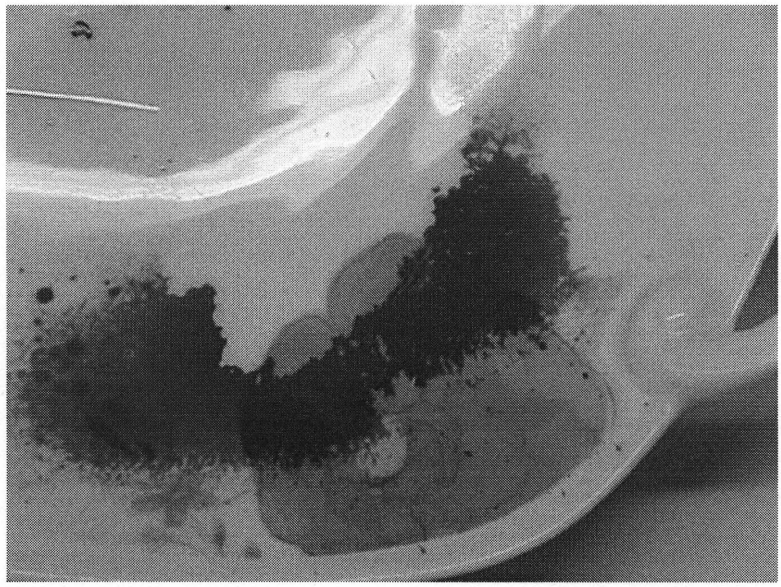

(a)

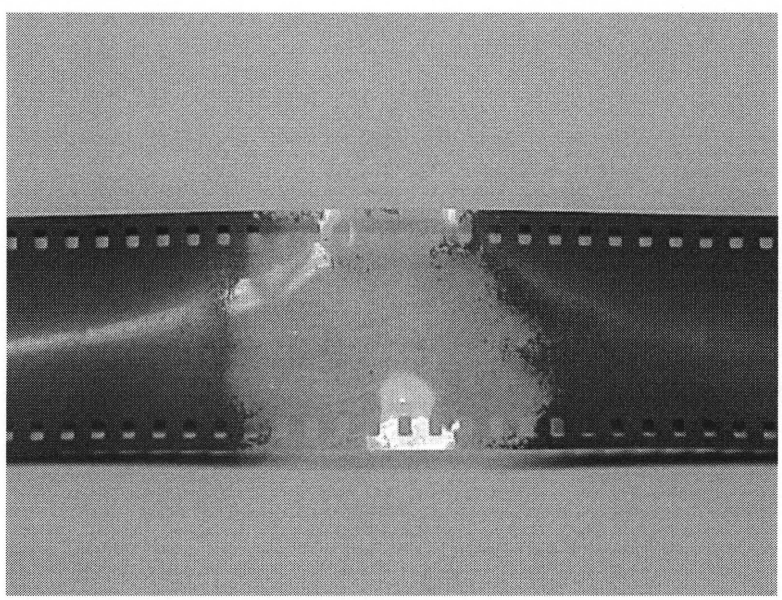

(b)

Figure E.14 (a) Photograph of the hand-painted china plate. The plate was covered by Rust-Oleum gloss protective enamel. Part of the deposited paint was removed by ice etching. No modification of the original surface was noticed. The feasibility of IJ etching of sensitive surfaces was demonstrated, and (b) photograph of the strip of the photo film. The photo emulsion was partially removed from the film surface. No surface damage was observed in the course of IJ. The feasibility of complete and selective emulsion removal from thin film was demonstrated.

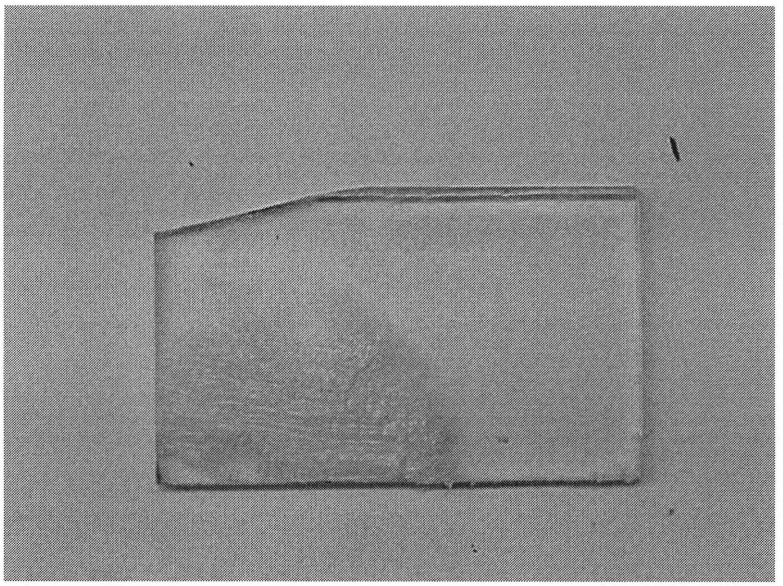

(a)

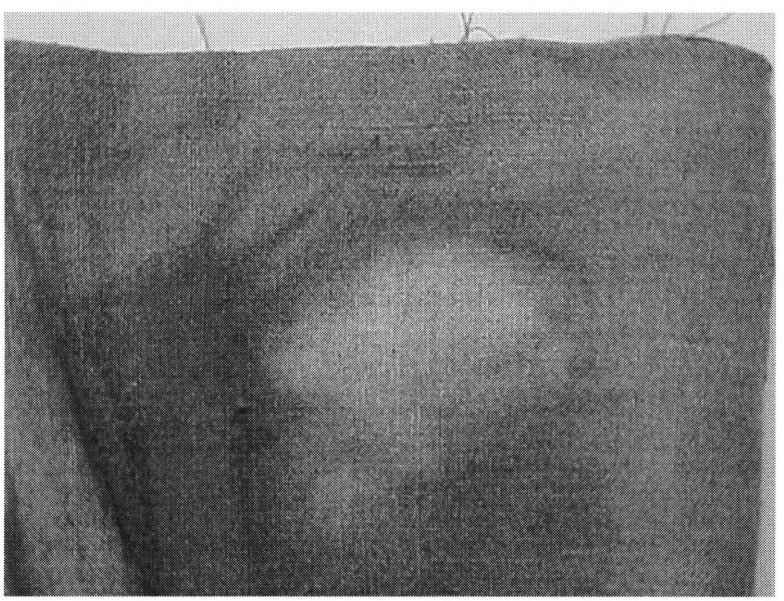

(b)

Figure E.15 (a) photograph of the strip of an organic glass covered by the lithium grease. The part of the contaminant was successfully removed by IJ. No damage of the original surface was observed. The feasibility of complete removal of the organic substances from different substrates was demonstrated, and (b) photograph of the of a cotton fabric. The fabric was contaminated by the Rust-Oleum gloss protective enamel. Then the paint was partially removed from fabric surface. The feasibility of the use of ice particles for decontamination of different fabrics was demonstrated.

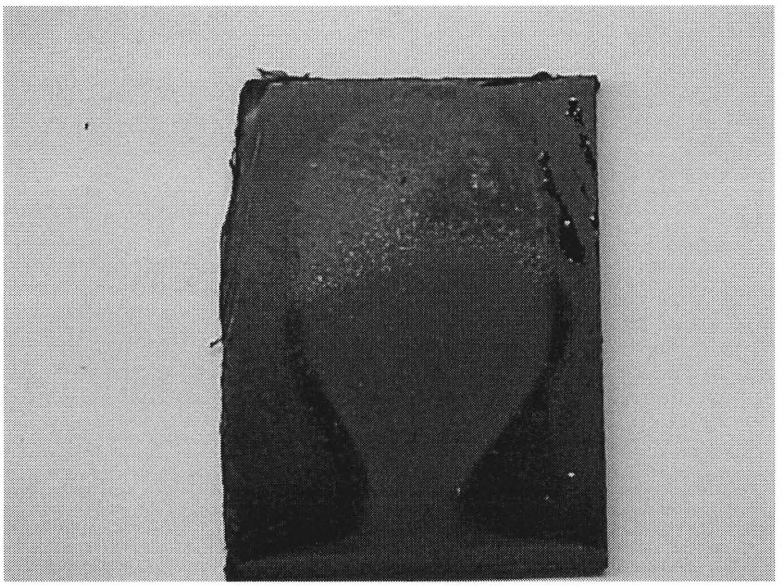

(a)

(b)

Figure E.16 (a) Photograph of the hard plastic covered by the Rust-Oleum gloss protective enamel. The paint was partially removed by IJ. The feasibility of restoration and fabrication of plastic parts was demonstrated, and (b) photograph of the cover of a pharmaceutical reactor contaminated by the lithium grease. Then the grease was partially removed from the surface of the cover by IJ. No damage of the Phaulder glass in the course of IJ cleaning was noticed.

(a)

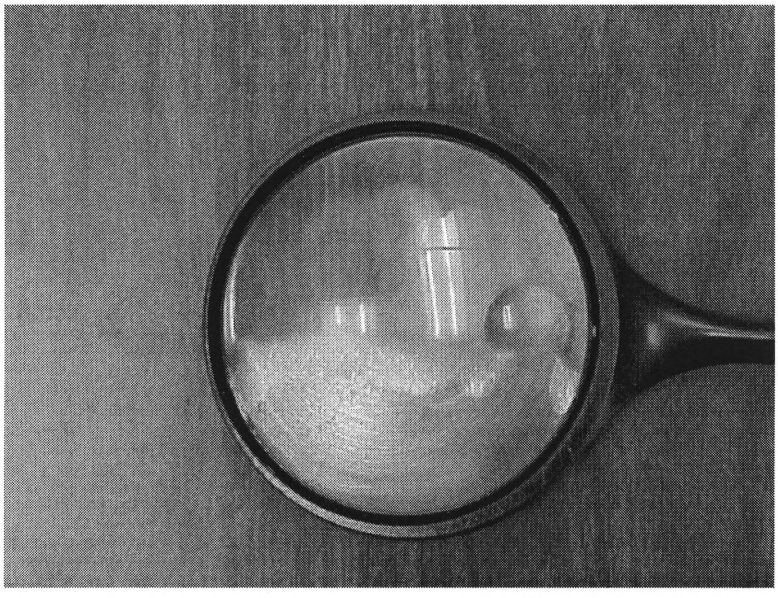

(b)

Figure E.17 (a) photograph of the photo camera. The lenses of the camera were contaminated by the lithium grease. Then the lenses were cleaned by IJ. After cleaning the camera performed normally. No damage of the surface of lenses was noticed. The feasibility of decontamination of different optical devises was demonstrated, and (b) photograph of the magnification lens. The lens was contaminated by the lithium grease. The grease was partially removed from the lens surface. Notice that no damage of the lens surface was observed.

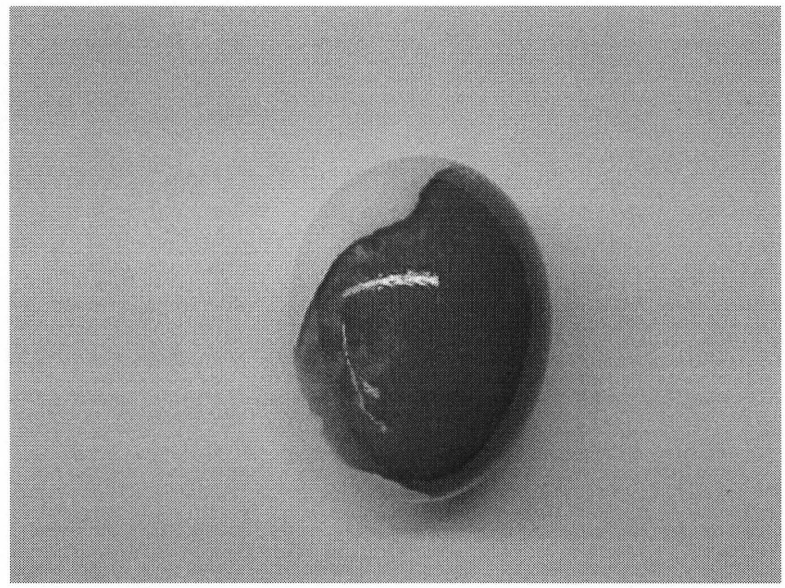

(a)

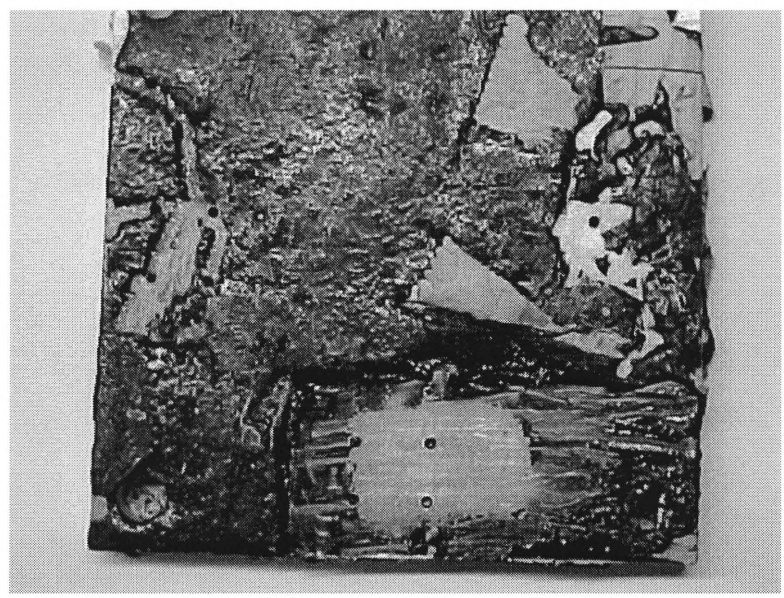

(b)

Figure E.18 (a) photograph of the egg. The egg surface was painted by Rust-Oleum gloss protective enamel. After this the egg was partially decontaminated by IJ. No damage of the egg surface or penetration of the ice particles through the eggshell was noticed. The feasibility of decontamination of highly unstable and brittle surfaces was demonstrated, and (b) photograph of the grinded aluminum surface contaminated by the thick layer of tar. The bulk of the tar was removed by WJ and knife scrubbing. The highly adhesive thin layer was removed by ice etching. No damage of the metal surface was noticed.

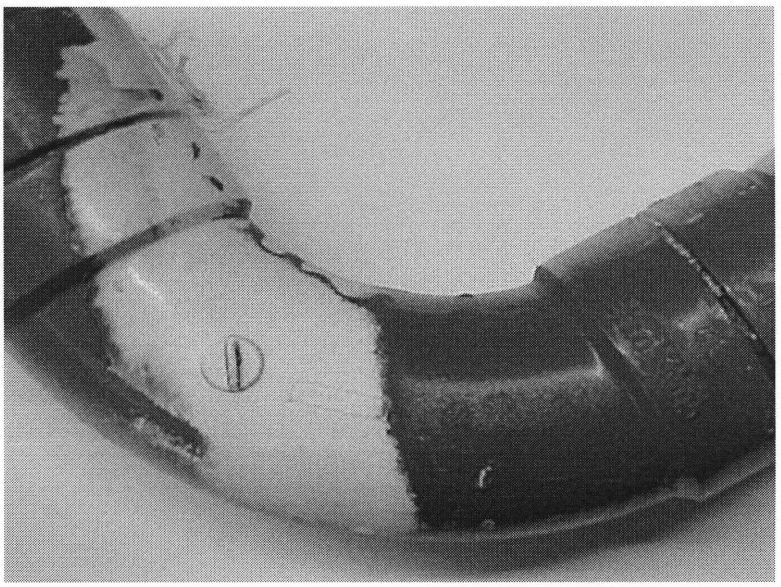

(a)

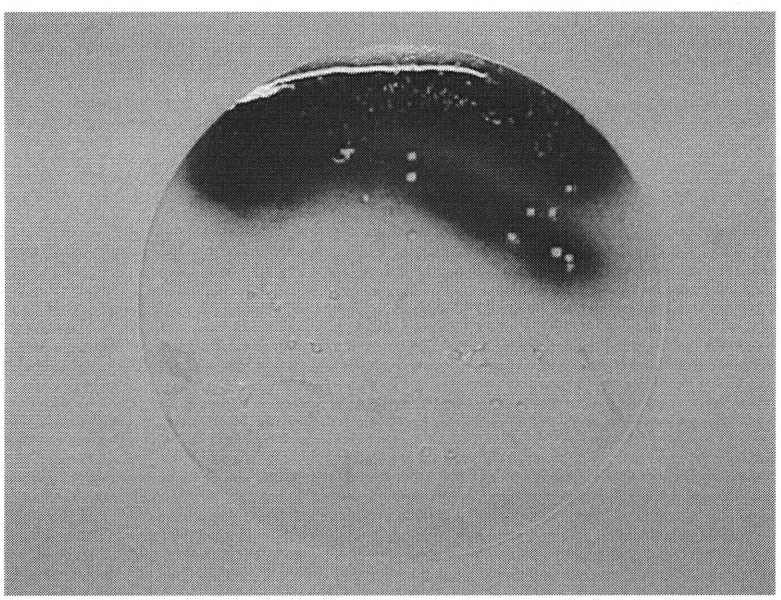

(b)

Figure E.19 (a) photograph of a PVC tube contaminated by Rust-Oleum gloss protective enamel. The tube was partially decontaminated by IJ. No damage of the tube surface in the course of IJ cleaning was noticed, and (b) photograph of the thin glass disc painted by Rust-Oleum gloss protective enamel. The paint was partially removed from the glass surface. The glass surface remains without damage. Notice that the thickness of the glass not exceed 1 mm.

(a)

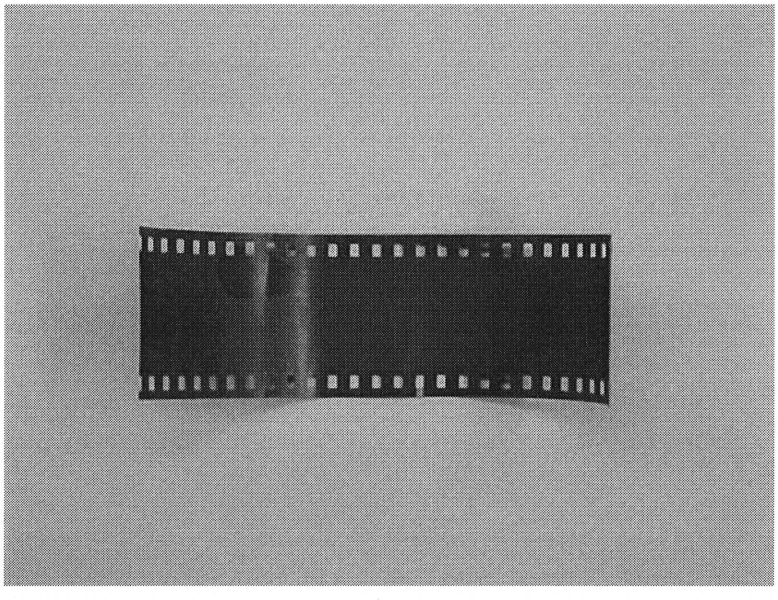

(b)

Figure E.20 (a) photograph of a plastic part. The part of coating was removed from the surface of the plastics. No damage of the substrate layer of the plastics was noticed. No penetration of the ice particles into the plastic body was noticed as well, and (b) photograph of the strip of photo film painted by Rust-Oleum gloss protective enamel. The part of the paint was removed by using of IJ technique. Notice that the underlying layer of emulsion remains without damage. The feasibility of restoration and fabrication of highly sensitive plastic parts was demonstrated.

(a)

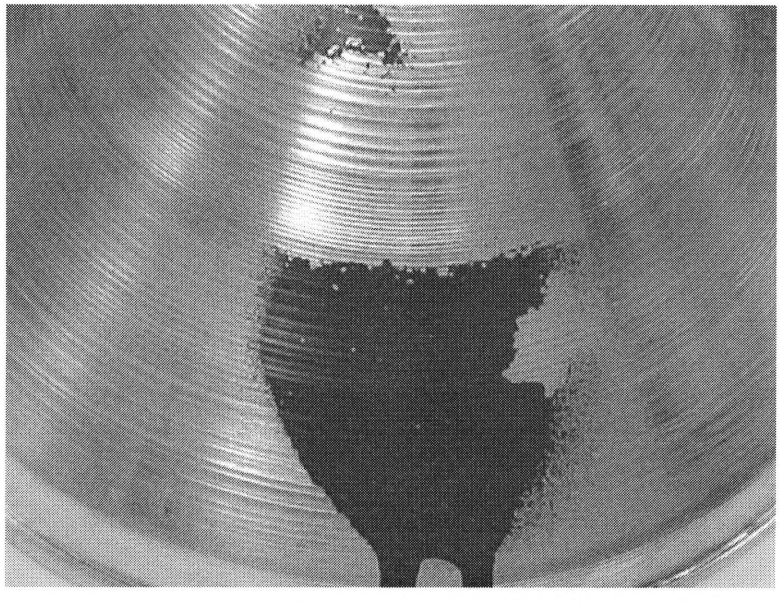

(b)

Figure E.21 (a) photograph of a magnification lens previously contaminated by the lithium grease. The grease was completely removed from the lens surface by using IJ technique. No surface damage in the course of IJ cleaning was noticed, and (b) photograph of grinded aluminum surface partially cleaned by ice particles. The aluminum surface was covered by the layer of Rust- Oleum gloss protective enamel. No surface damage was noticed.

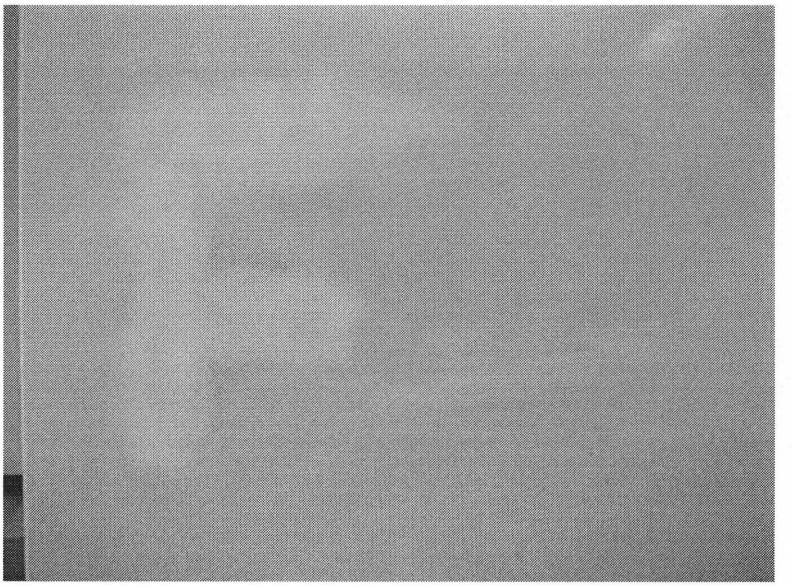

(a)

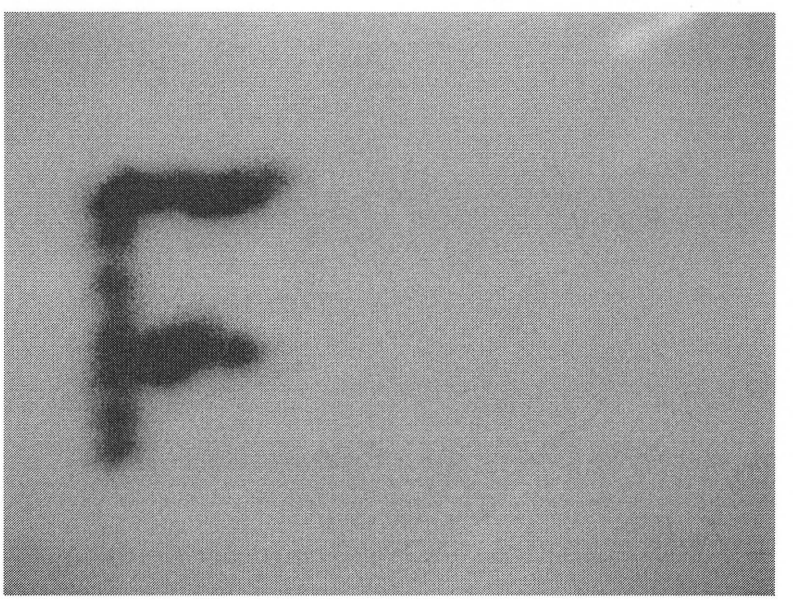

(b)

Figure E.22 Graffiti covered painted metal surface. The oil paint is highly adhesive. (a) graffiti was removed with conventional abrasive-airjet. Notice discoloration occurred on the treated region and (b) surface was decontaminated by the AIJ. No damage to the underlying paint layer was done.

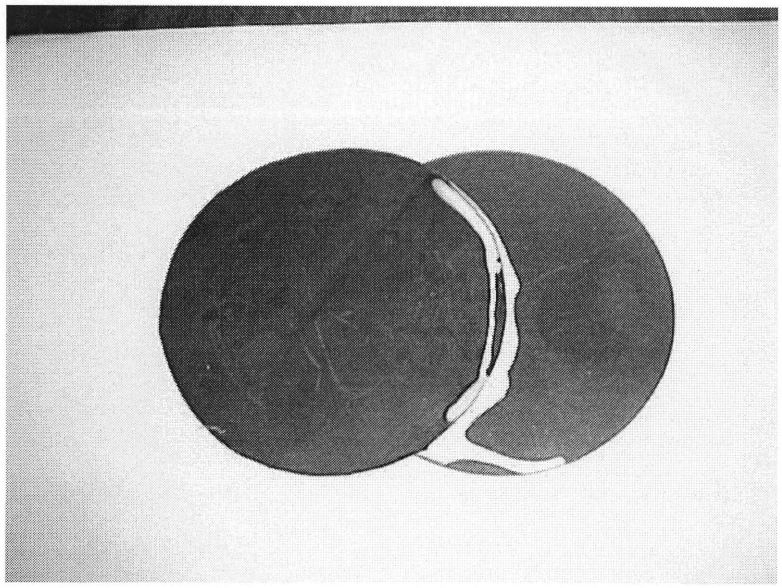

(a)

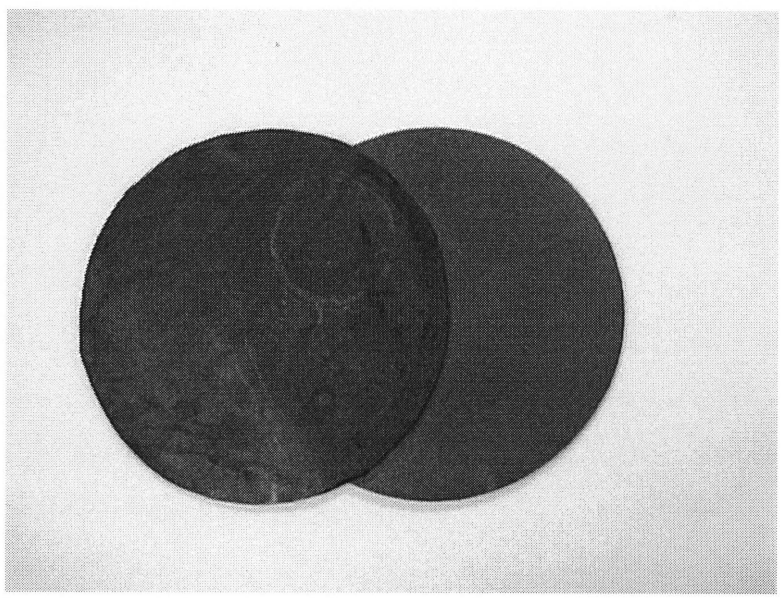

(b)

Figure E.23 (a) the Weldbond glue was used to create a joint between plastic and rubber surfaces. Notice the highly adhesive character of the glue, and (b) the glue residue was removed in course of ice-airjet cleaning. No surface damage was noticed.

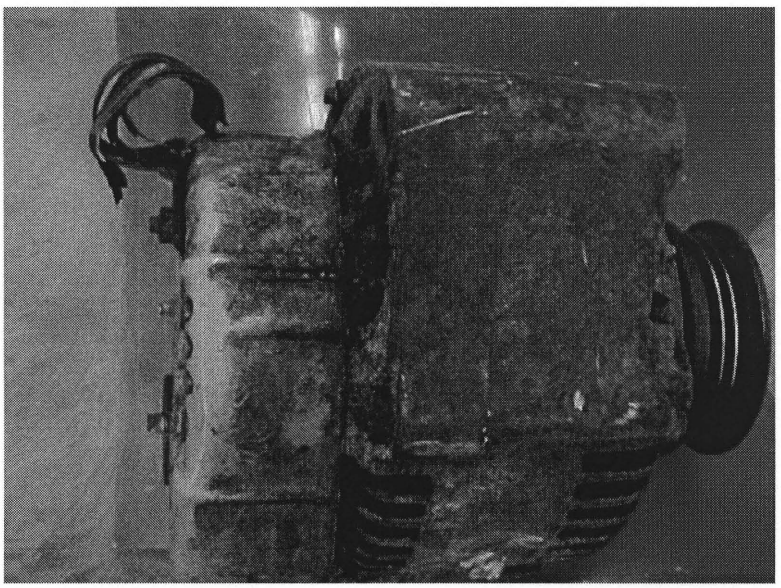

(a)

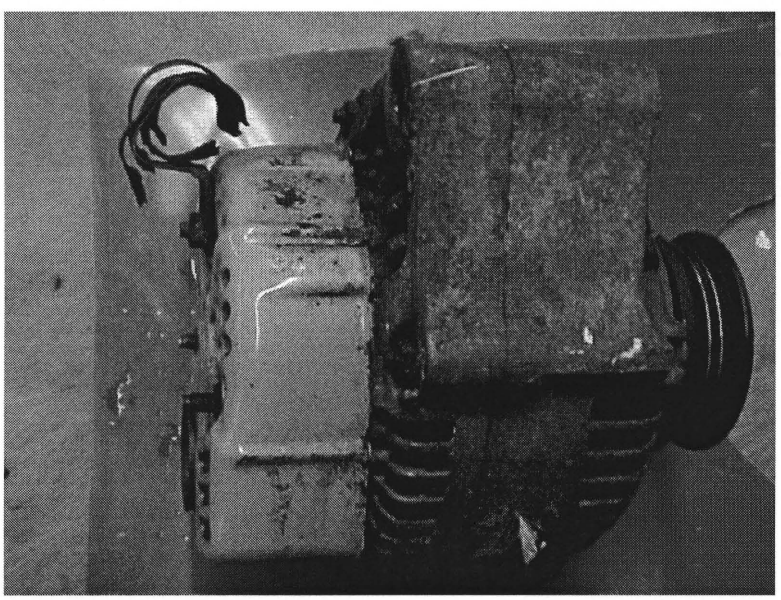

(b)

Figure E.24 (a) picture of the highly polluted with grease and dust machine part, and (b) part was decontaminated in course of ice-airjet cleaning. No damage was mentioned on underlying painted surface.

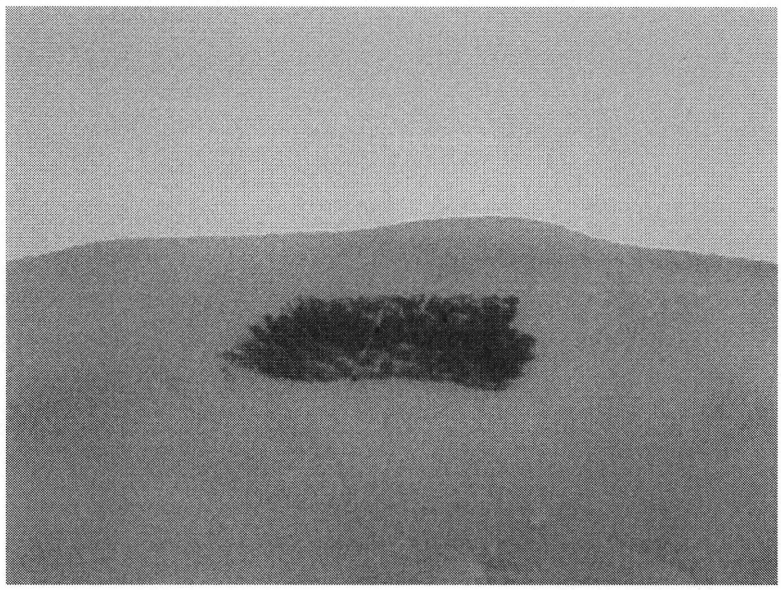

(a)

(b)

Figure E.25 Pictures of: (a) pork skin surface marked with waterproof marker, (b) marker paint was removed from skin with no noticeable surface damage.

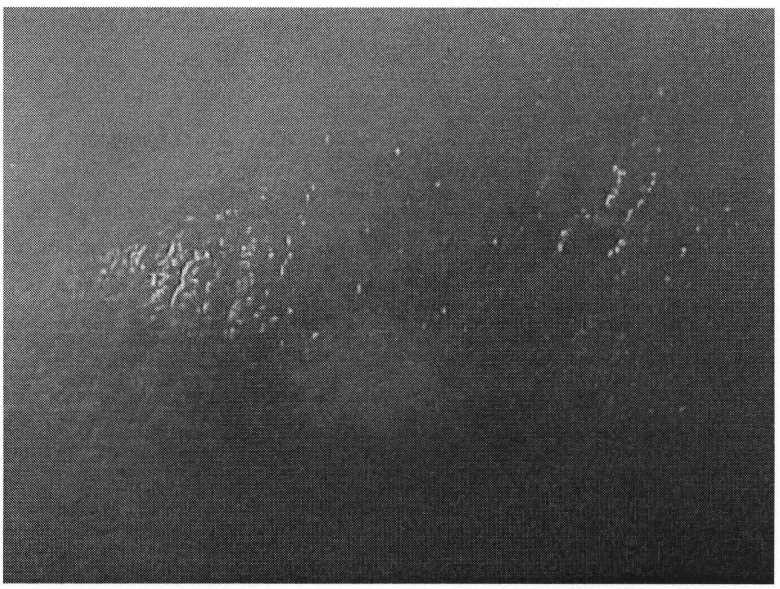

(a)

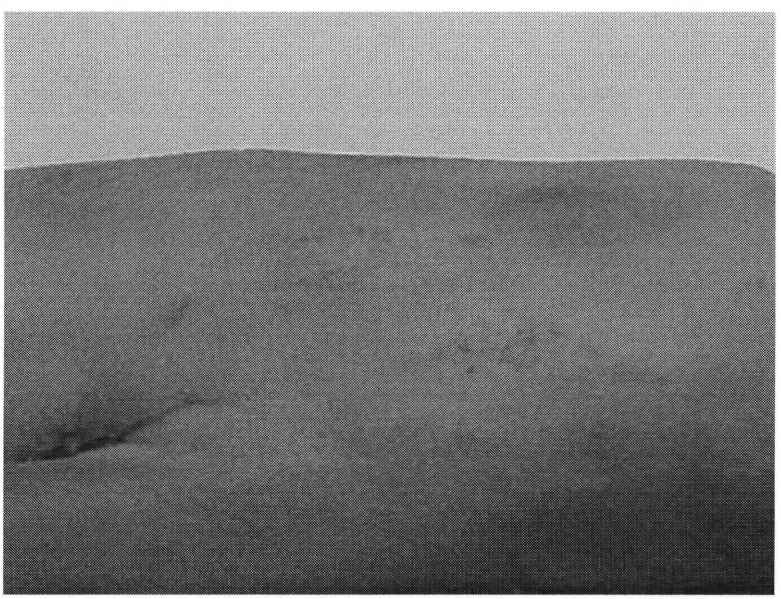

(b)

Figure E.26 (a) top (epidermis) layer of skin was removed from skin surface. No damage to bottom laying layers of skin was mentioned, and (b) top layer of pork skin was removed with more deep penetration into skin structure. This shows possibility to control the depth of penetration into the skin structure.

(a)

(b)

Figure E.27 (a) surface of chicken skin marked with waterproof marker, (b) skin surface after IJ treatment. There is no noticeable surface damage done to skin surface in the course of treatment. Marker spot was completely removed from treated surface.

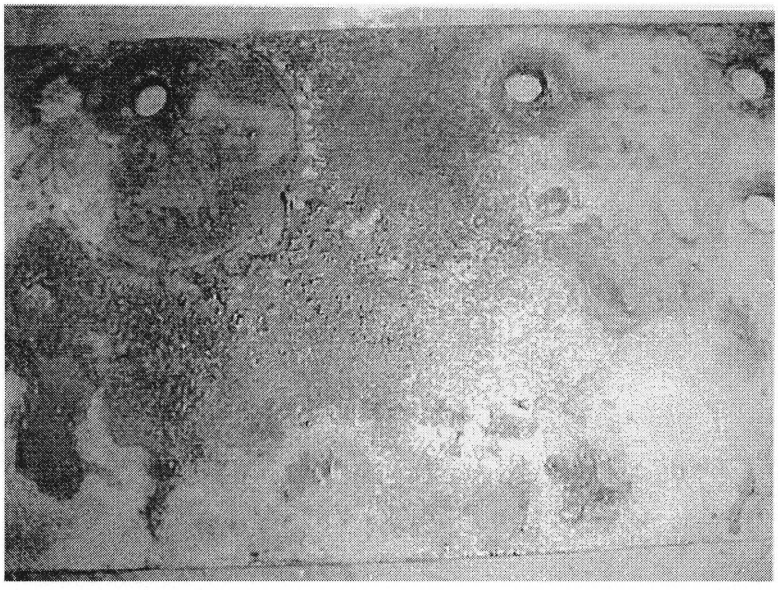

(a)

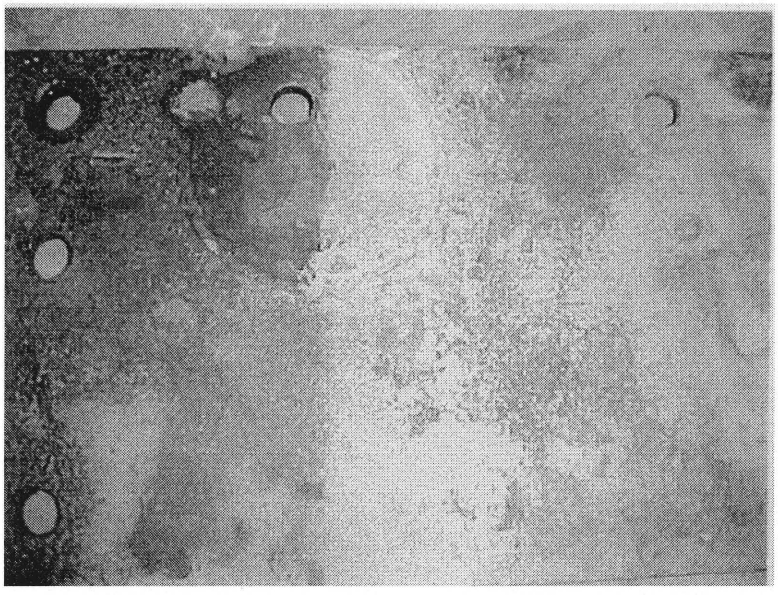

(b)

Figure E.28 (a) rusted carbon steel surface. Notice that newly formed rust layer is highly adhesive, and (b) carbon steel plate was partially derusted (middle part of the plate).

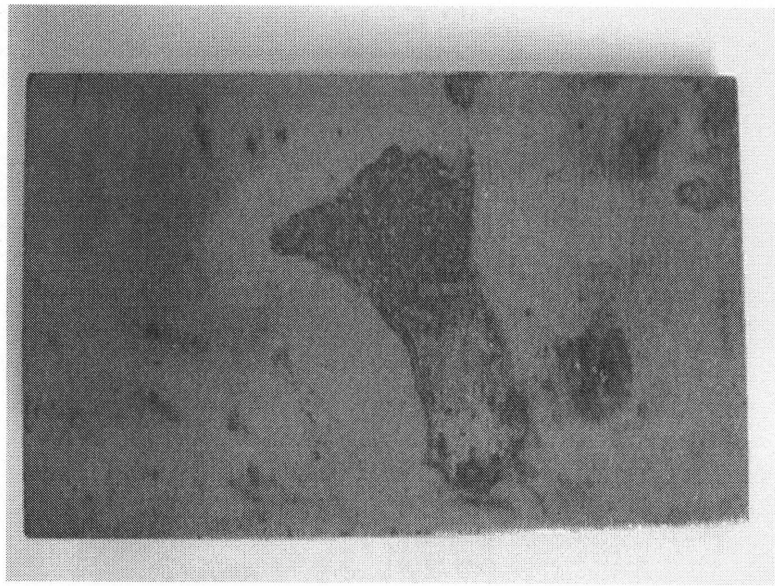

(a)

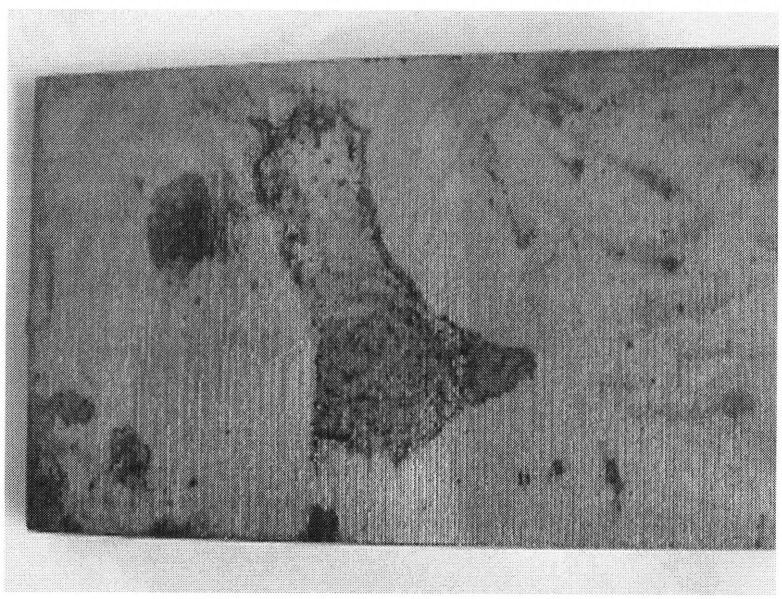

(b)

Figure E.29 (a) rusted carbon steel plate before the IAJ treatment, and (b) the same plate after the treatment.

APPENDIX F

EXPERIMENTAL RESULTS OF ICE PLUG DECOMPOSITION

The experimental database pertinent to the evaporator-auger system is presented below:

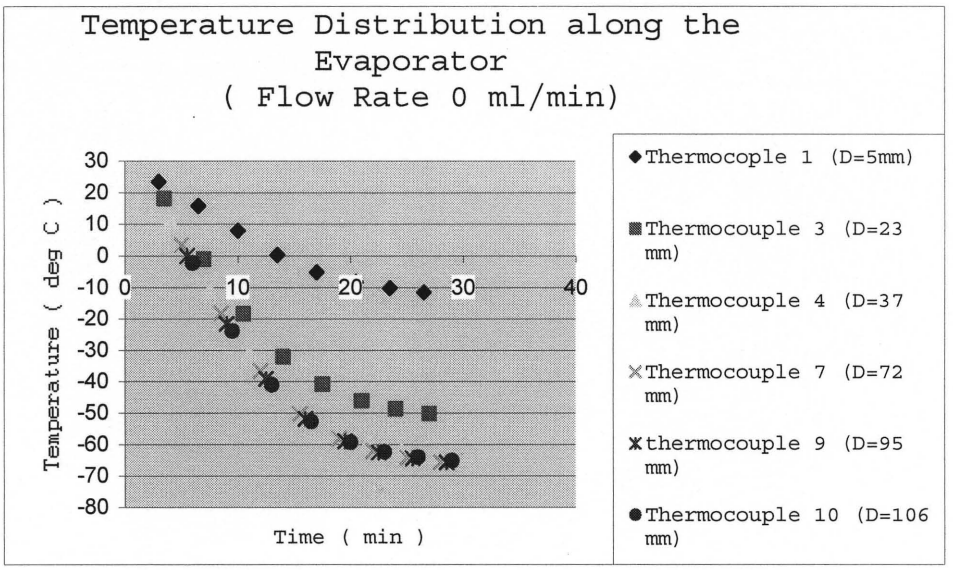

(a)

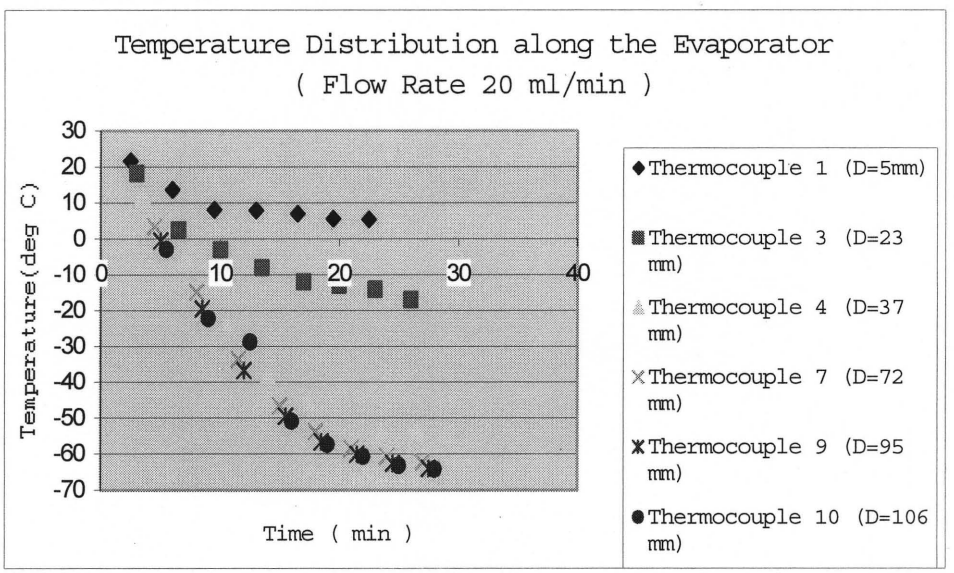

(b)

Figure F.1 Temperature distribution along the evaporator vs. time for six distinct water flow rates (Galden HT-55 cooling media): a) 0 ml/min, b) 20 ml/min, c) 60 ml/min, d) 80 ml/min, e) 100 ml/min, and f) 120 ml/min.

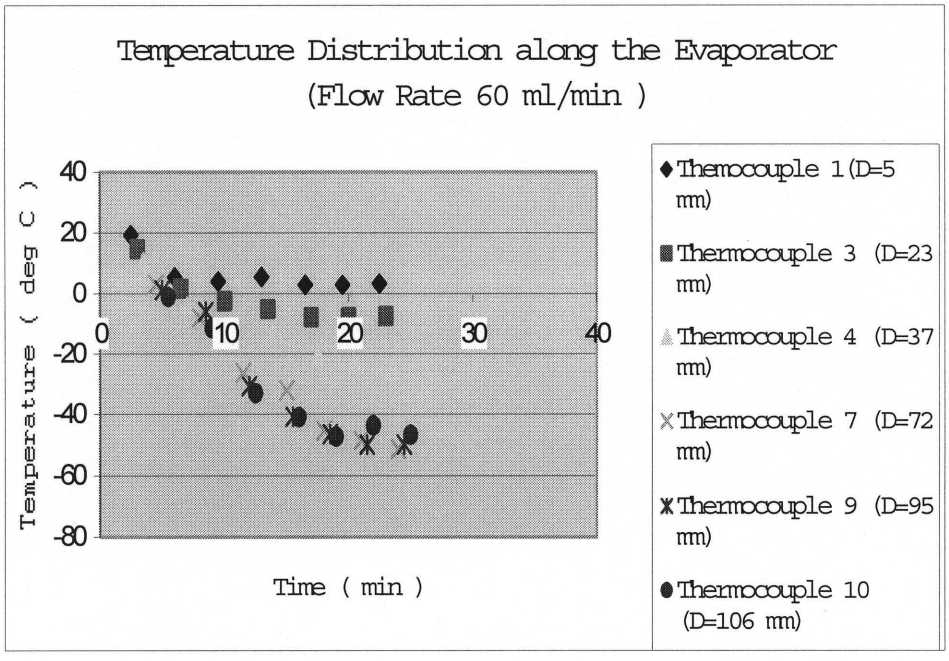

(c)

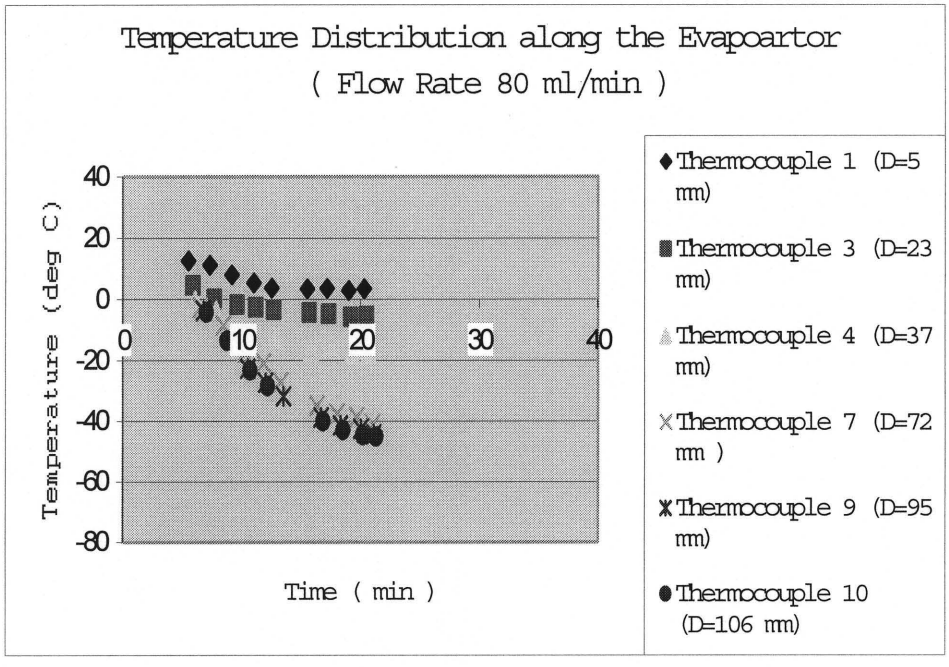

(d)

Figure F.1 Temperature distribution along the evaporator vs. time for six distinct water flow rates (Galden HT-55 cooling media): a) 0 ml/min, b) 20 ml/min, c) 60 ml/min, d) 80 ml/min, e) 100 ml/min, and f) 120 ml/min (continued).

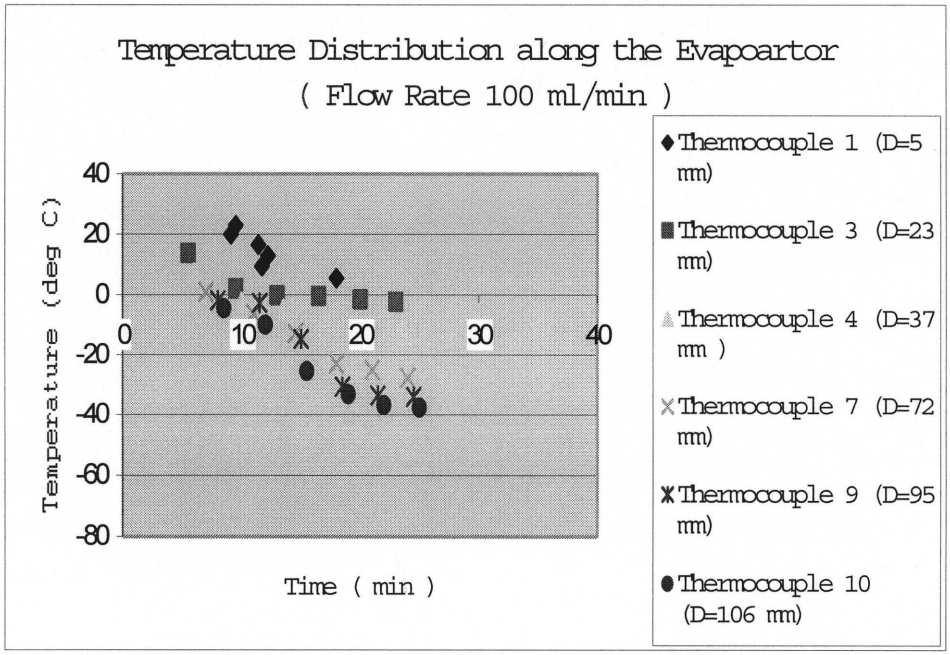

(e)

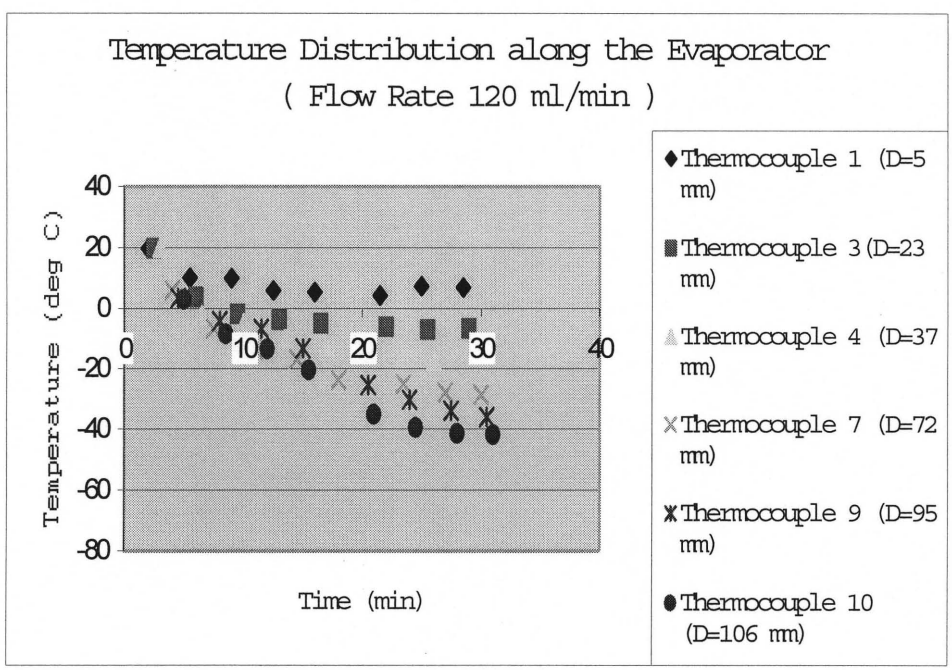

(f)

Figure F.1 Temperature distribution along the evaporator vs. time for six distinct water flow rates (Galden HT-55 cooling media): a) 0 ml/min, b) 20 ml/min, c) 60 ml/min, d) 80 ml/min, e) 100 ml/min, and f) 120 ml/min (continued).

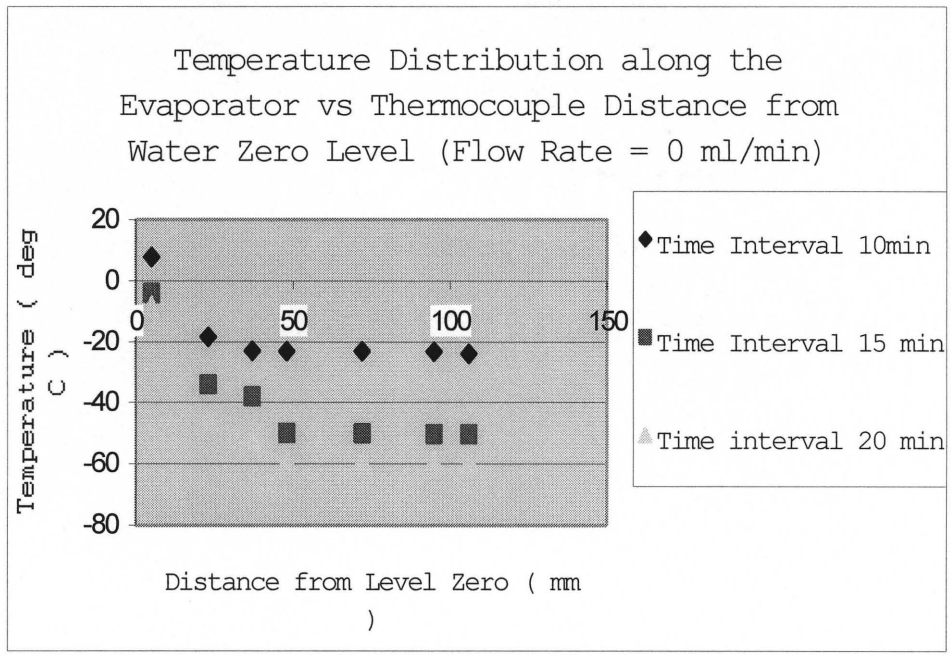

(a)

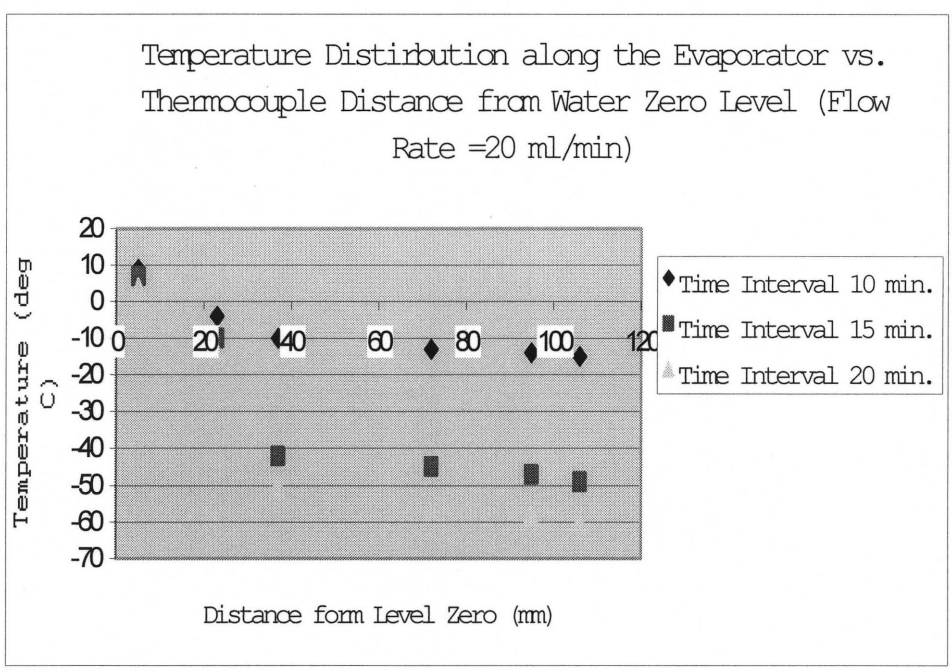

(b)

Figure F.2 Temperature distribution along the evaporator vs. thermocouple distance form water inlet level (Galden HT-55 cooling media) for the water flow rates of: a) 0 ml/min, b) 20 ml/min, c) 60 ml/min, d) 80 ml/min, e) 100 ml/min, and f) 120 ml/min.

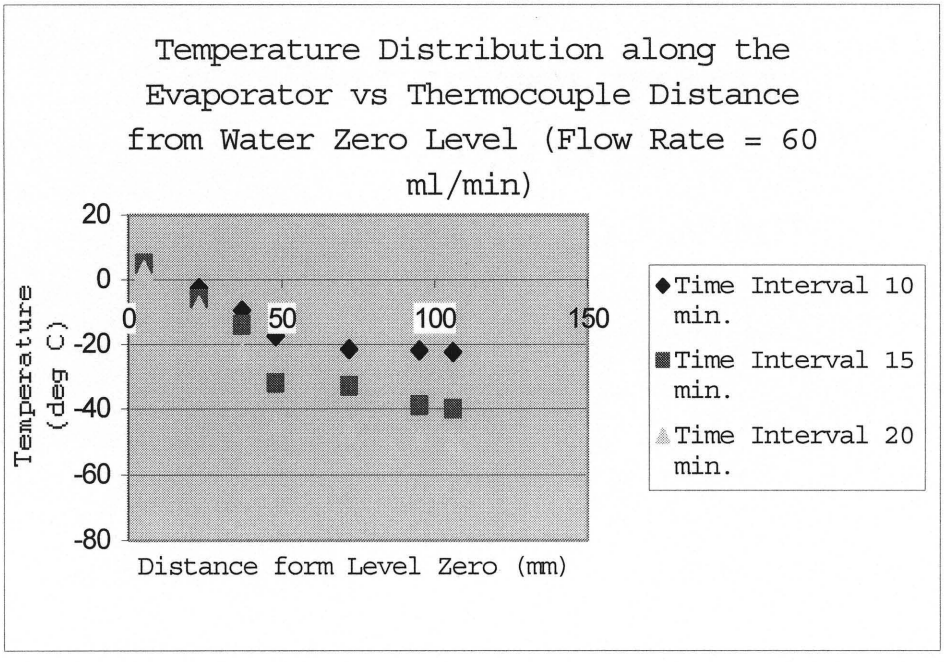

(c)

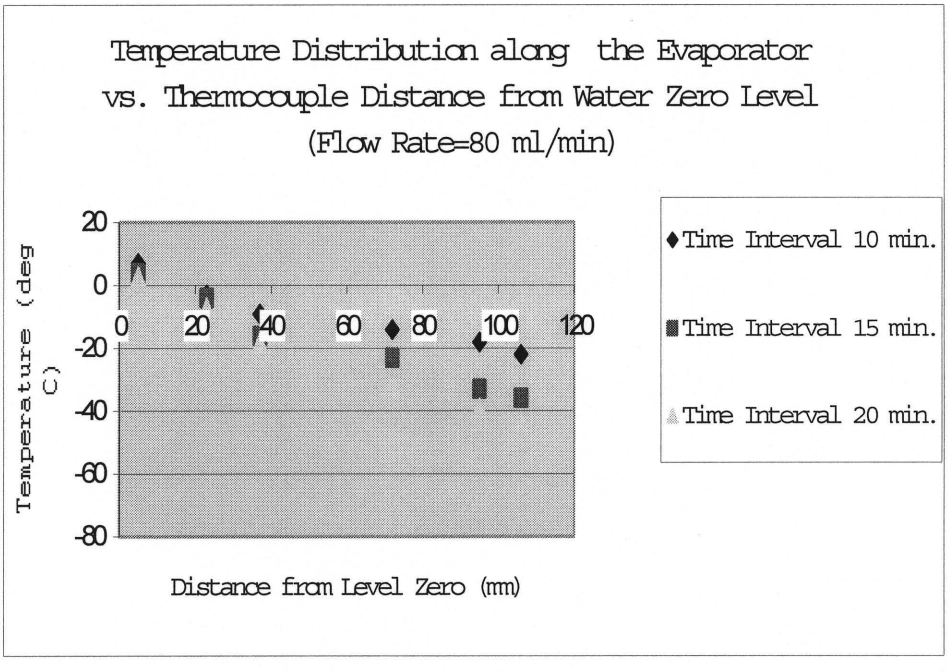

(d)

Figure F.2 Temperature distribution along the evaporator vs. thermocouple distance form water inlet level (Galden HT-55 cooling media) for the water flow rates of: a) 0 ml/min, b) 20 ml/min, c) 60 ml/min, d) 80 ml/min, e) 100 ml/min, and f) 120 ml/min (continued).

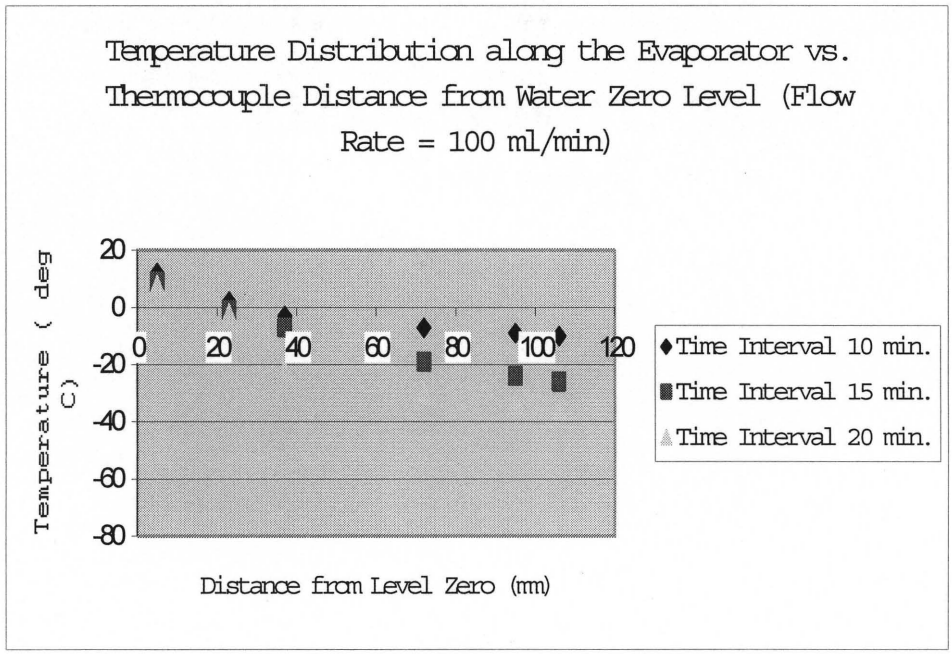

(e)

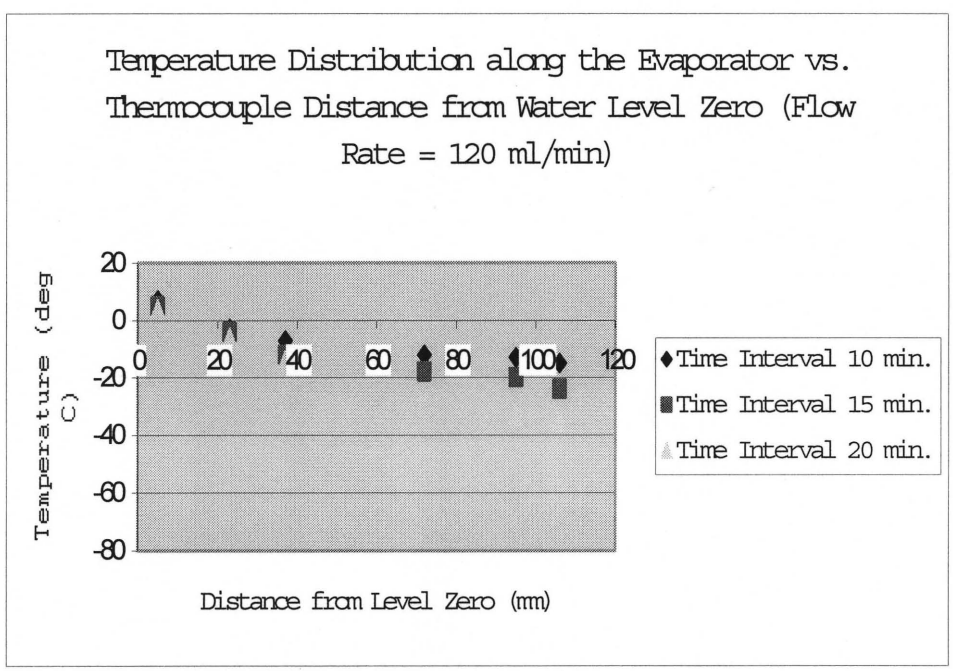

(f)

Figure F.2 Temperature distribution along the evaporator vs. thermocouple distance form water inlet level (Galden HT-55 cooling media) for the water flow rates of: a) 0 ml/min, b) 20 ml/min, c) 60 ml/min, d) 80 ml/min, e) 100 ml/min, and f) 120 ml/min (continued).

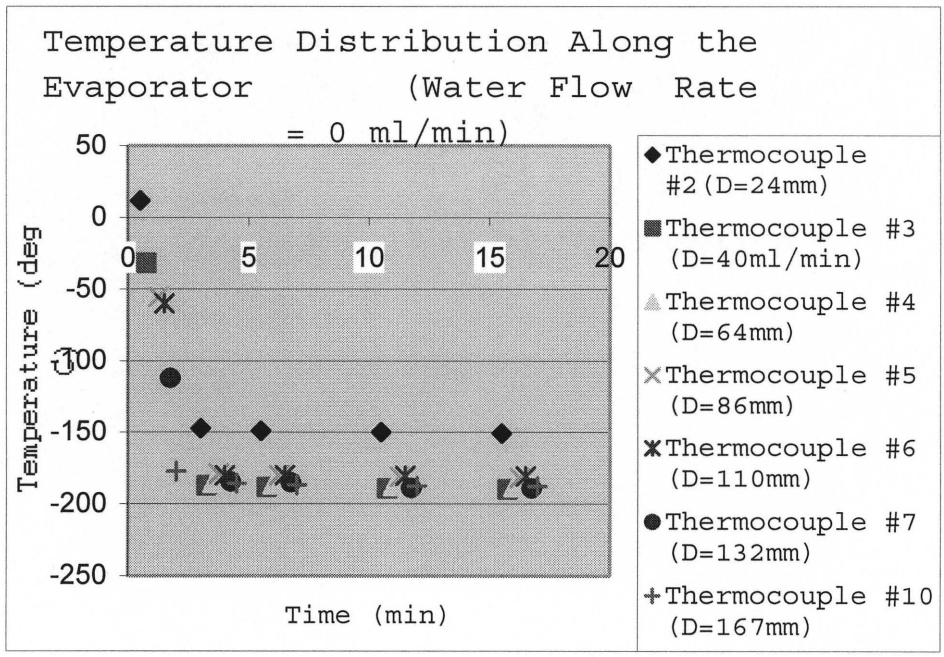

(a)

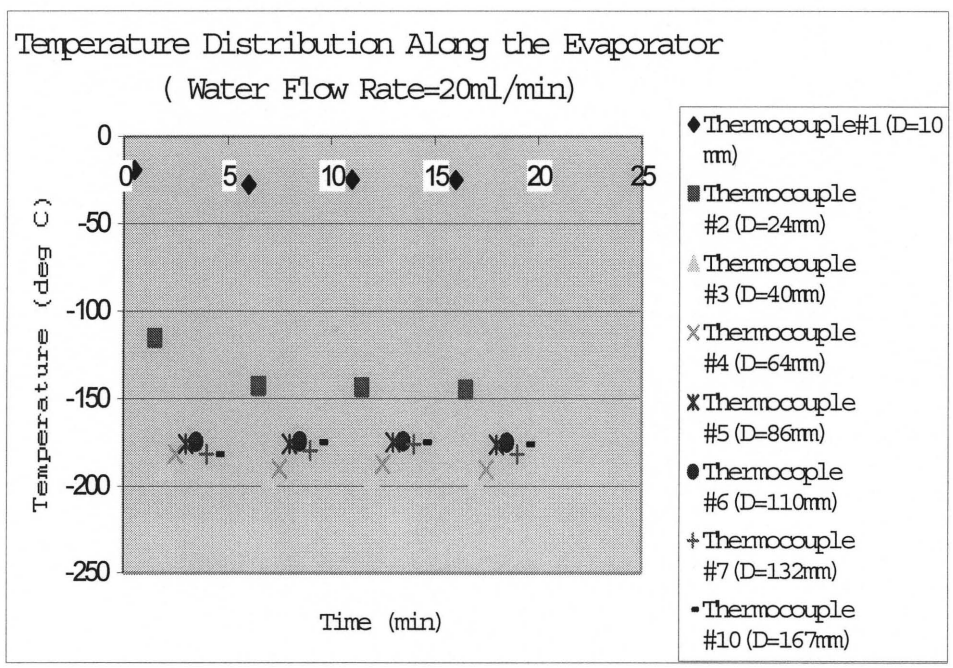

(b)

Figure F.3 Temperature distribution along the evaporator vs. time for the following six water flow rates (Galden HT-55 cooling media): a) 0 ml/min, b) 20 ml/min, c) 40 ml/min, d) 80 ml/min, e) 100 ml/min, and f) 150 ml/min.

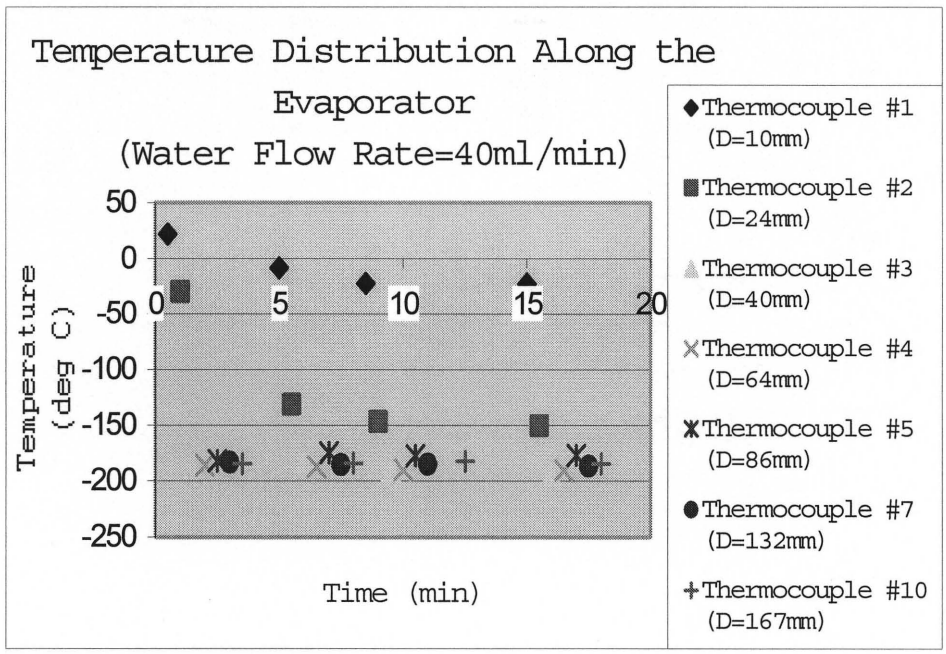

(c)

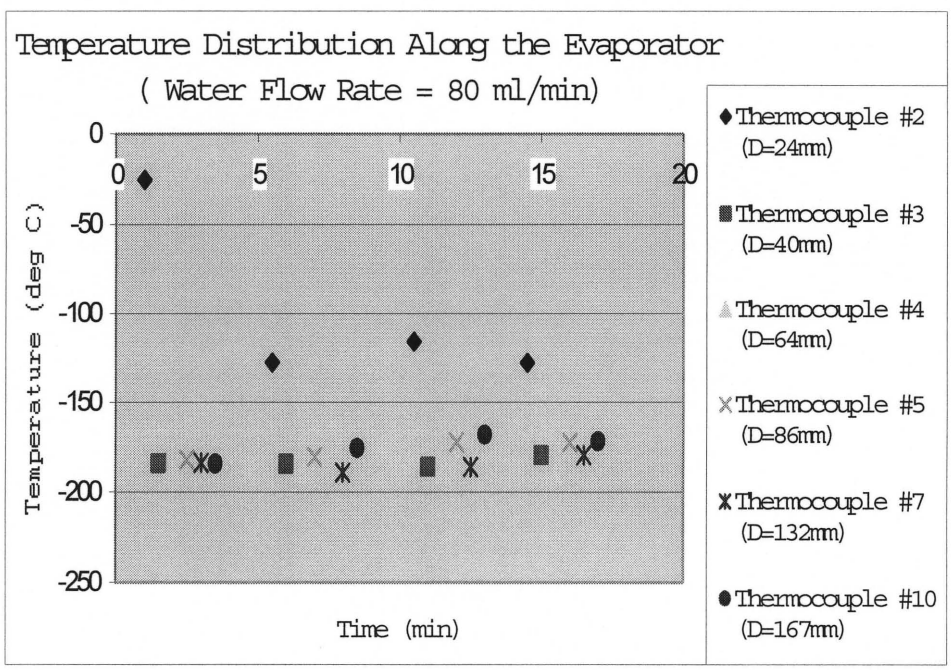

(d)

Figure F.3 Temperature distribution along the evaporator vs. time for the following six water flow rates (Galden HT-55 cooling media): a) 0 ml/min, b) 20 ml/min, c) 40 ml/min, d) 80 ml/min, e) 100 ml/min, and f) 150 ml/min (continued).

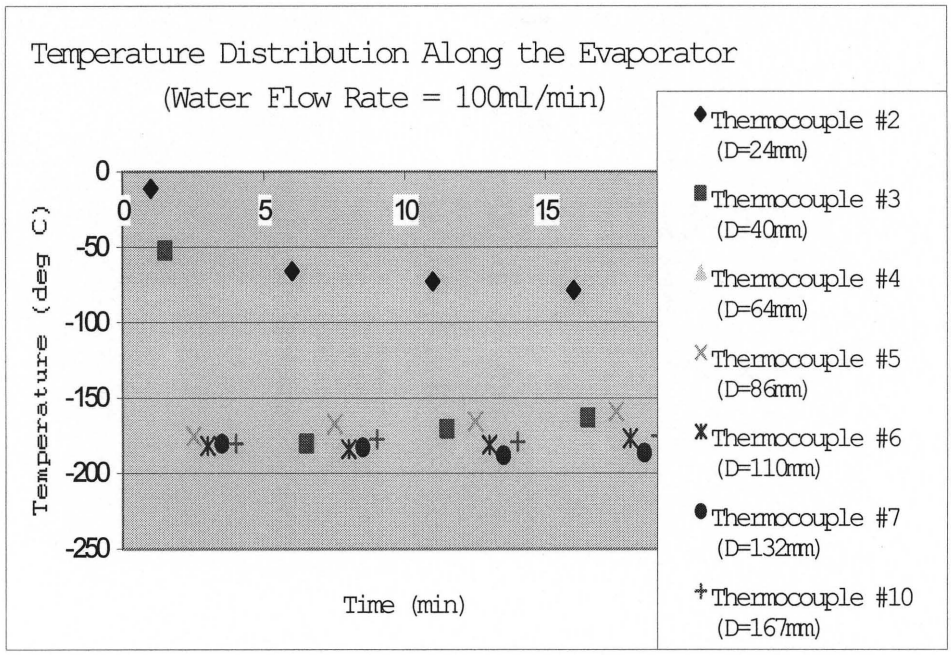

(e)

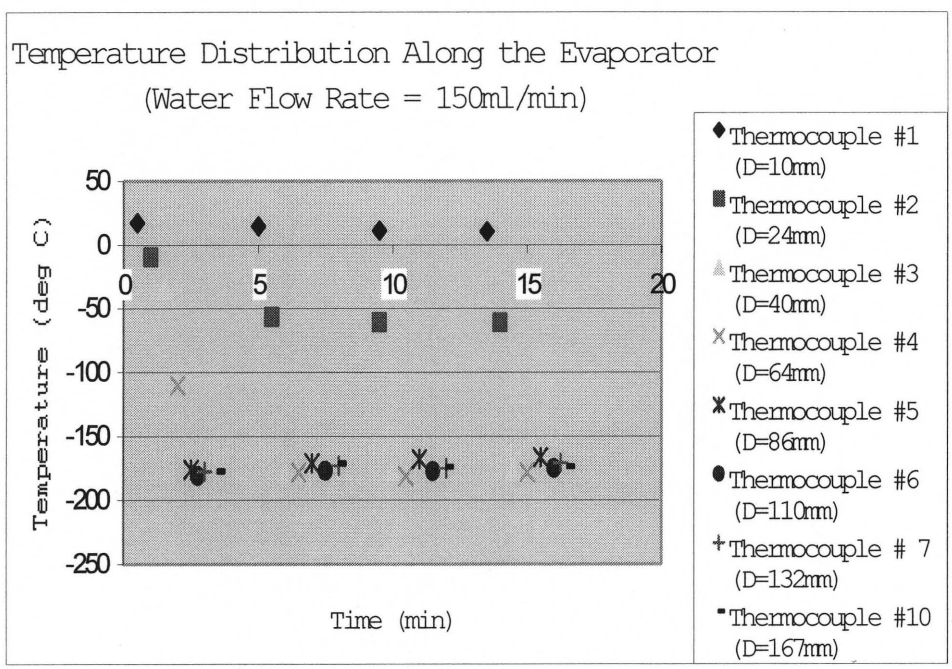

(f)

Figure F.3 Temperature distribution along the evaporator vs. time for the following six water flow rates (Galden HT-55 cooling media): a) 0 ml/min, b) 20 ml/min, c) 40 ml/min, d) 80 ml/min, e) 100 ml/min, and f) 150 ml/min (continued).

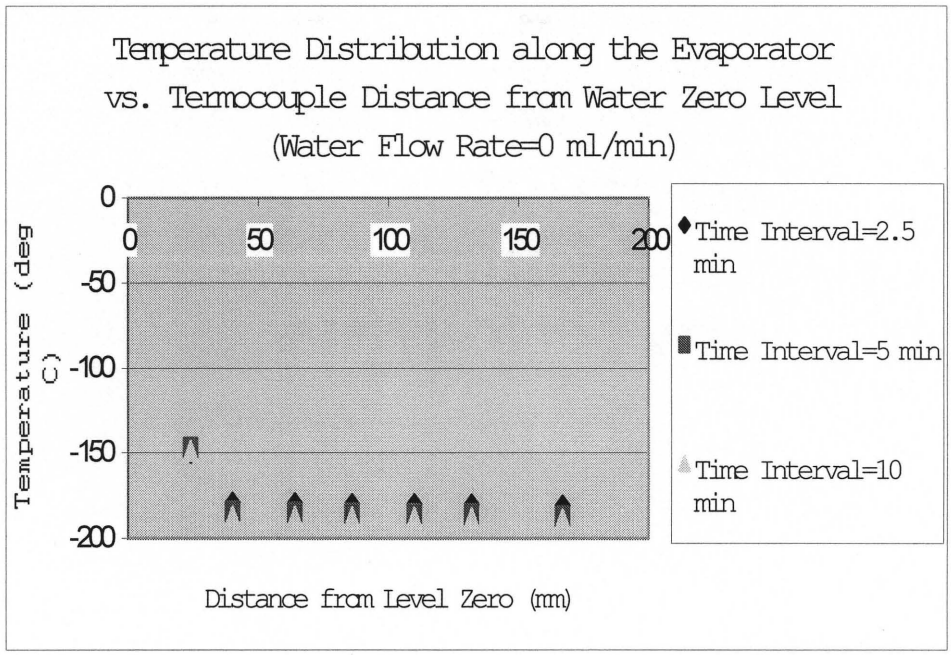

(a)

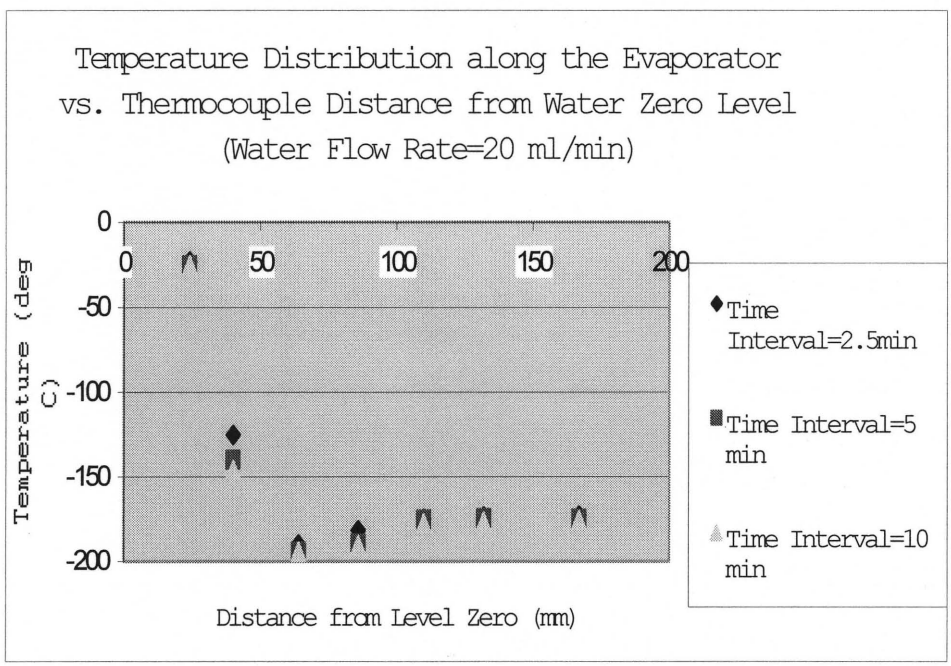

(b)

Figure F.4 Temperature distribution along the evaporator height for three fixed time duration and series of water flow rates: a) 0 ml/min, b) 20 ml/min, c) 40 ml/min, d) 80 ml/min, e) 100 ml/min, and f) 150 ml/min.

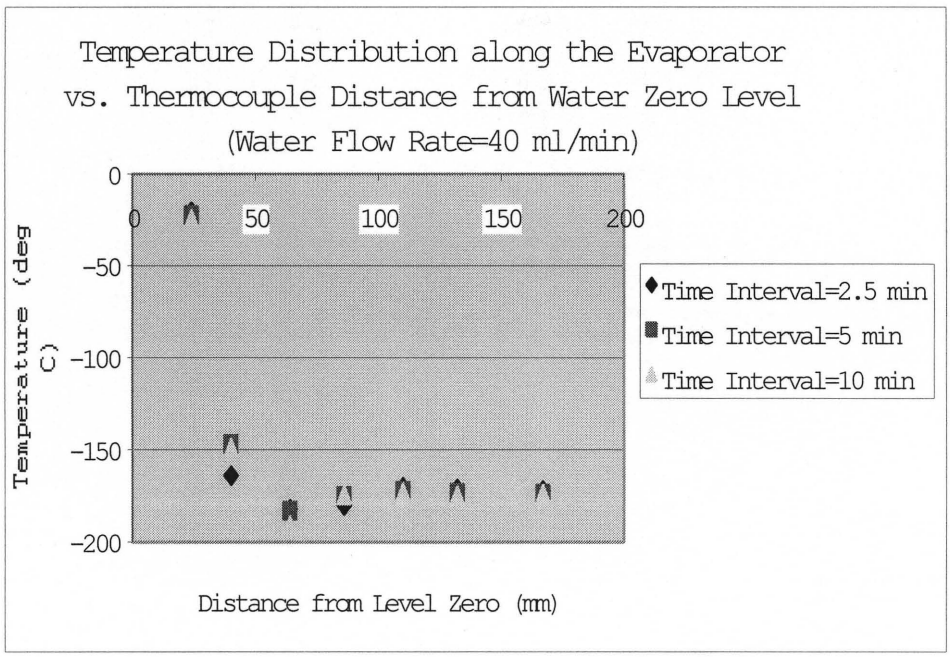

(c)

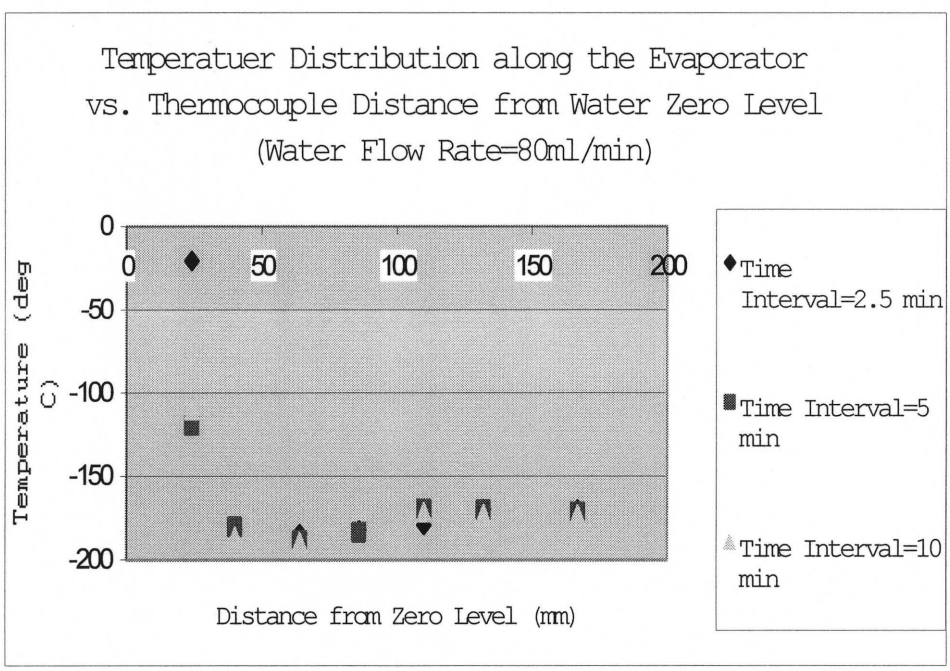

(d)

Figure F.4 Temperature distribution along the evaporator height for three fixed time duration and series of water flow rates: a) 0 ml/min, b) 20 ml/min, c) 40 ml/min, d) 80 ml/min, e) 100 ml/min, and f) 150 ml/min (continued).

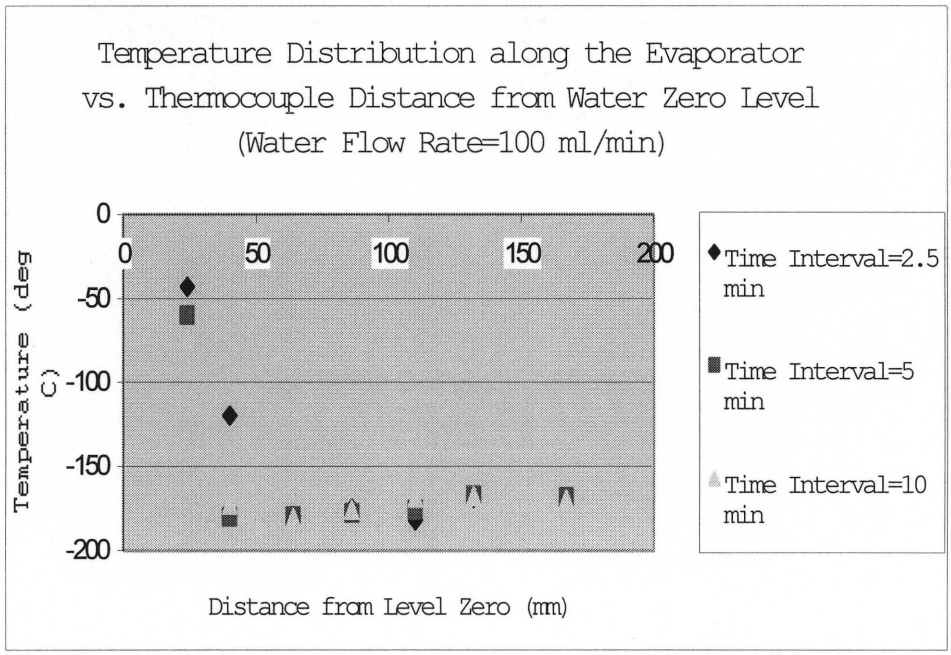

(e)

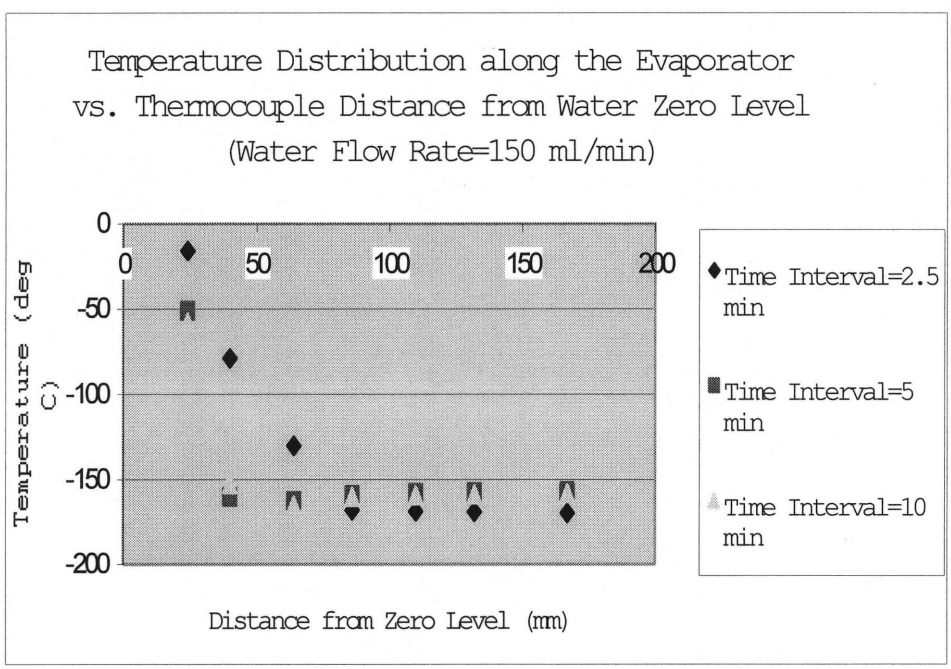

(f)

Figure F.4 Temperature distribution along the evaporator height for three fixed time duration and series of water flow rates: a) 0 ml/min, b) 20 ml/min, c) 40 ml/min, d) 80 ml/min, e) 100 ml/min, and f) 150 ml/min (continued).

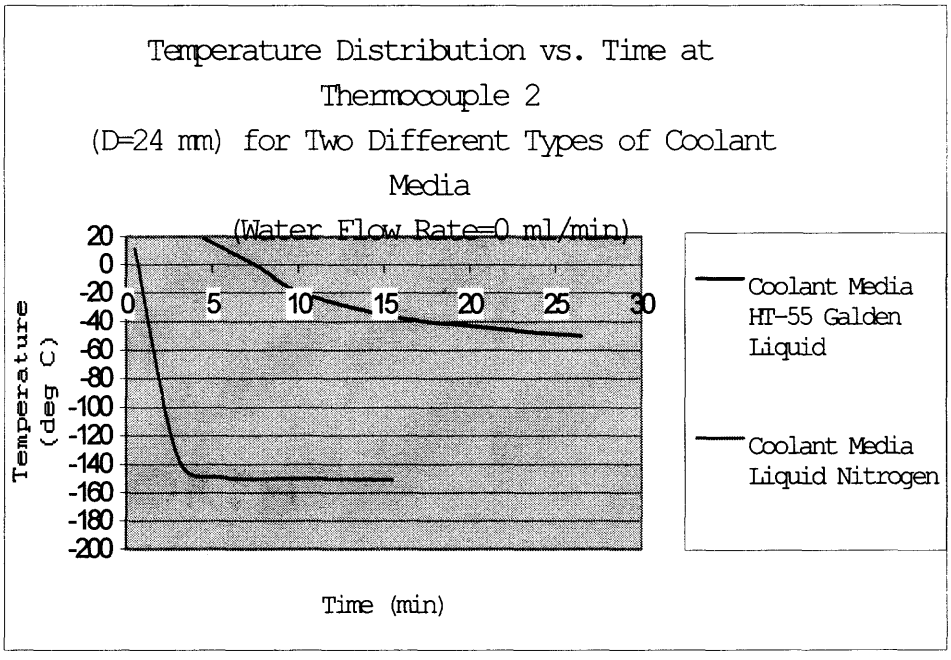

(a)

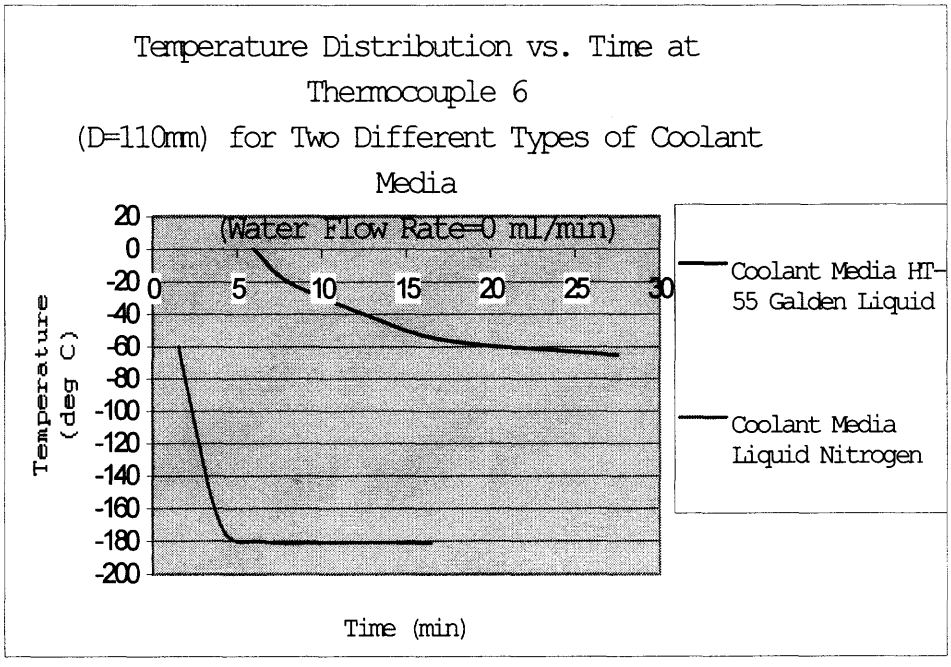

(b)

Figure F.5 Temperature readings at the thermocouple 2 and 6 (D=24 mm and 110 mm from water inlet level accordingly) for the Galden-55 and liquid nitrogen media and WFR=0 ml/min.

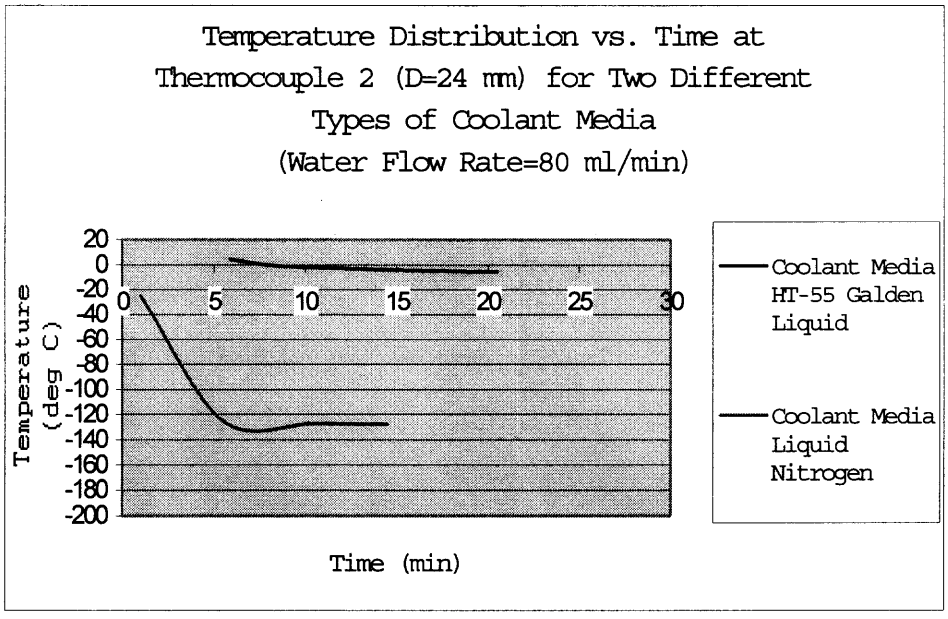

(a)

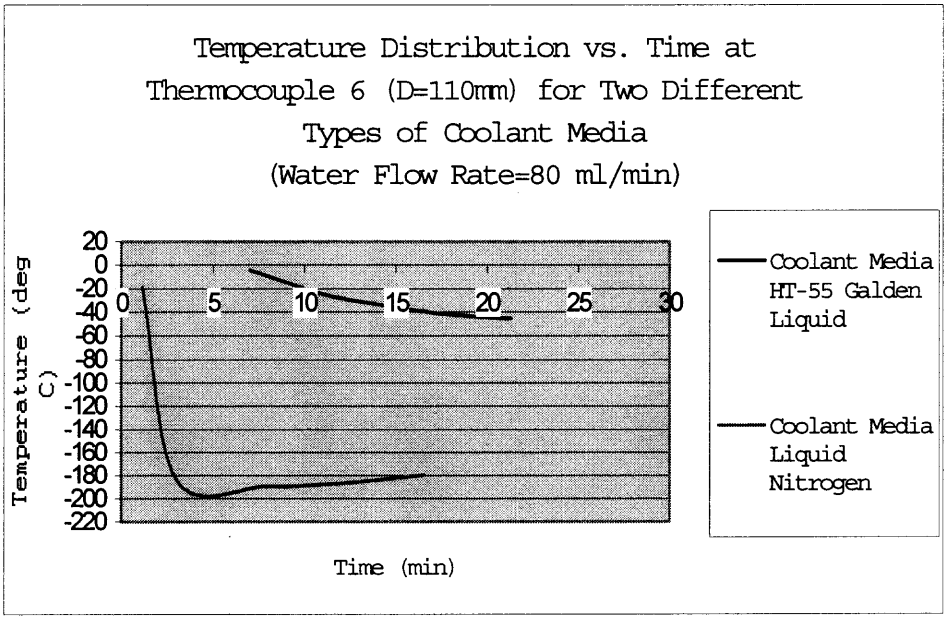

(b)

Figure F.6 Temperature readings at the thermocouple 2 and 6 (D=24 mm and 110 mm from water inlet level accordingly) for the Galden-55 and liquid nitrogen media and WFR=80 ml/min.

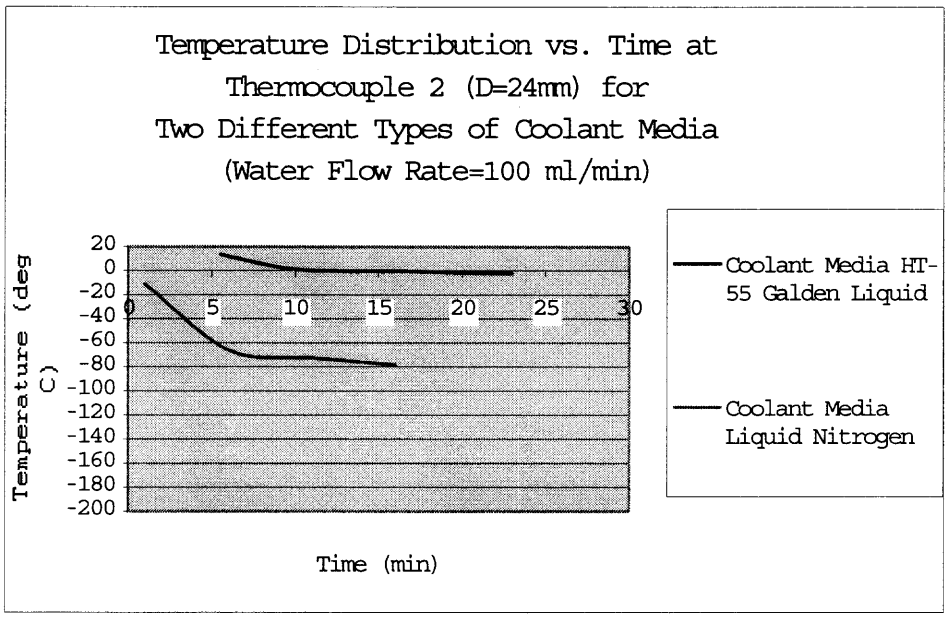

(a)

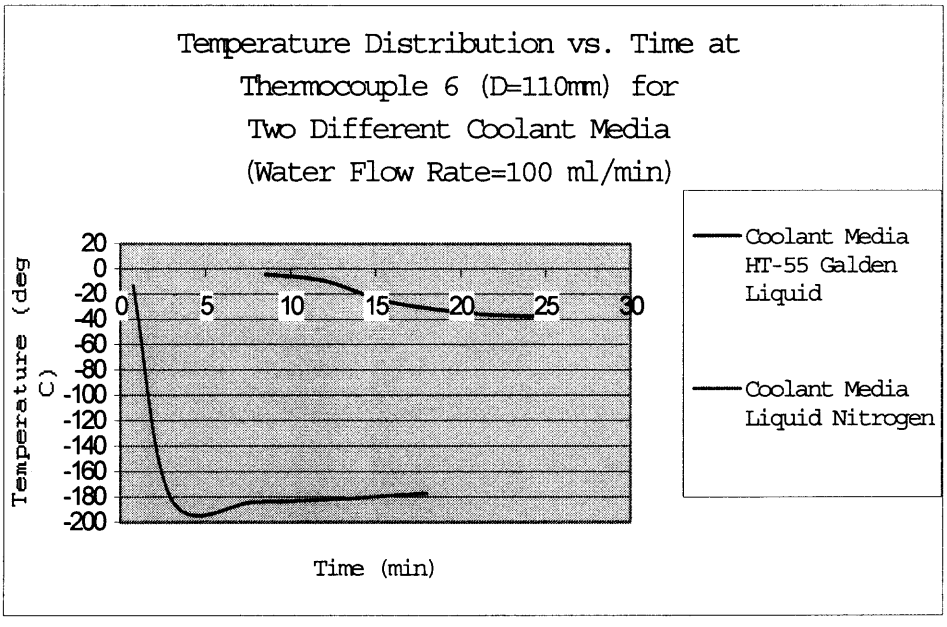

(b)

Figure F.7 Temperature readings at the thermocouple 2 and 6 (D=24 mm and 110 mm from water inlet level accordingly) for the Galden-55 and liquid nitrogen media and WFR=100 ml/min.

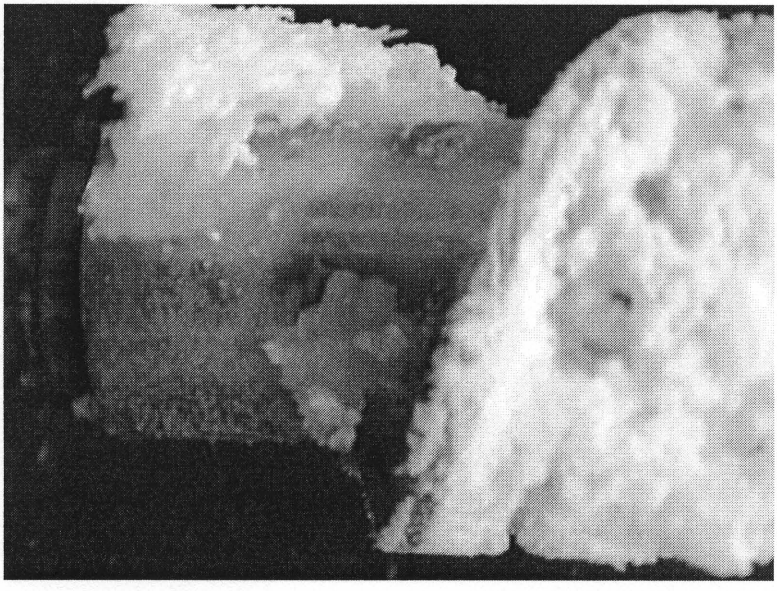

(a)

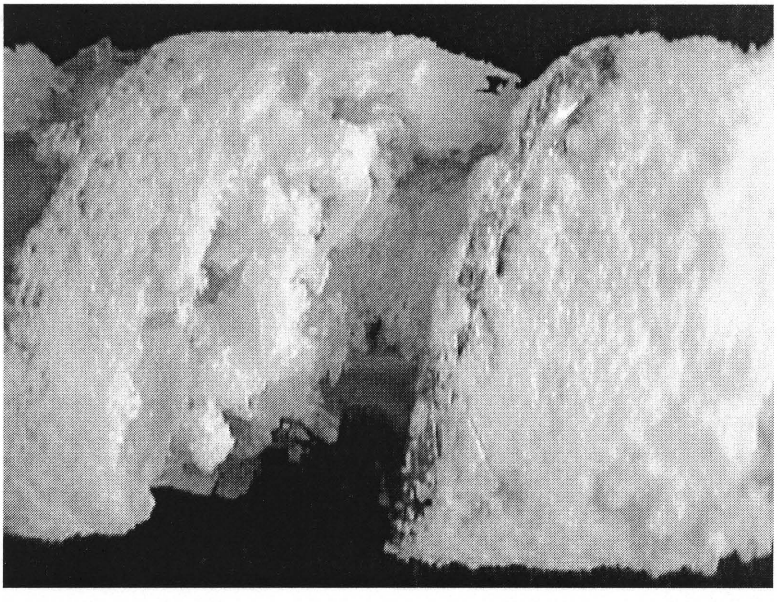

(b)

Figure F.8 Pictures show bottom and middle ice nucleation zones of the evaporator for single side cooling schema (liquid nitrogen is a cooling media, flow rate ~ 0.354 m^3/min) and WFR= 50 ml/min.

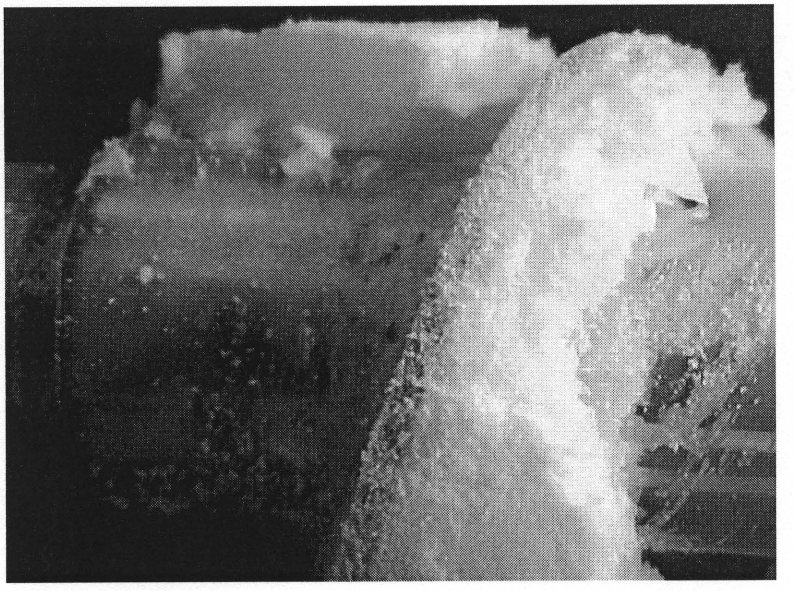

(a)

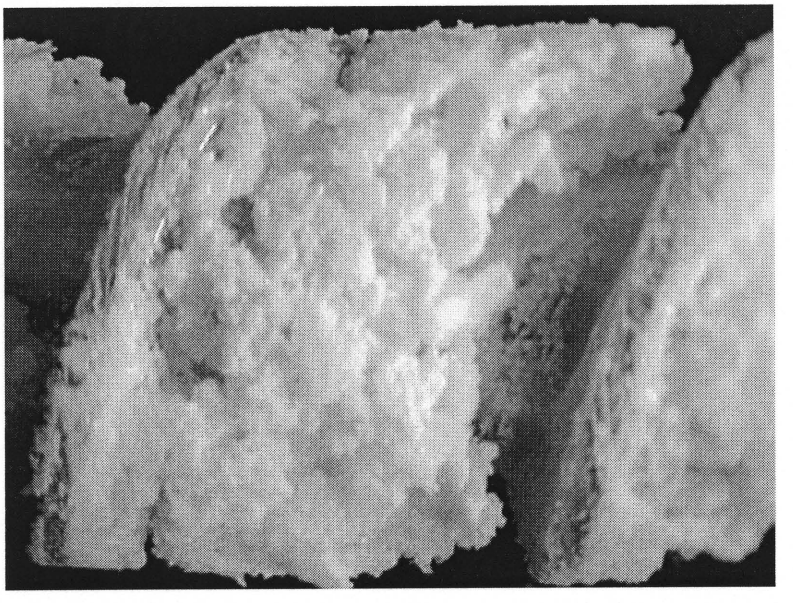

(b)

Figure F.9 Pictures show bottom and middle ice nucleation zones of the evaporator for single side cooling schema (liquid nitrogen is a cooling media, flow rate ~ 0.354 m^3/min) and WFR=100 ml/min.

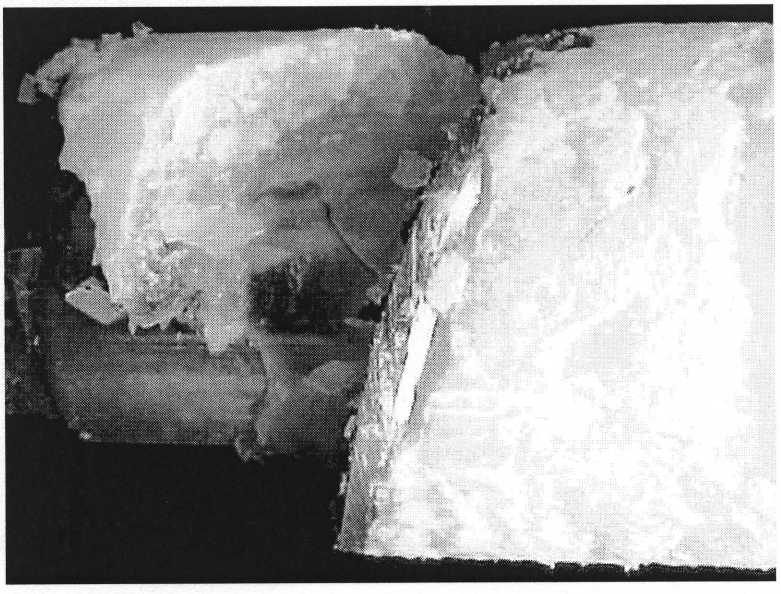

(a)

(b)

Figure F.10 Pictures show bottom and middle ice nucleation zones of the evaporator for single side cooling schema (liquid nitrogen is a cooling media, flow rate ~ 0.354 m^3/min) and WFR=150 ml/min.

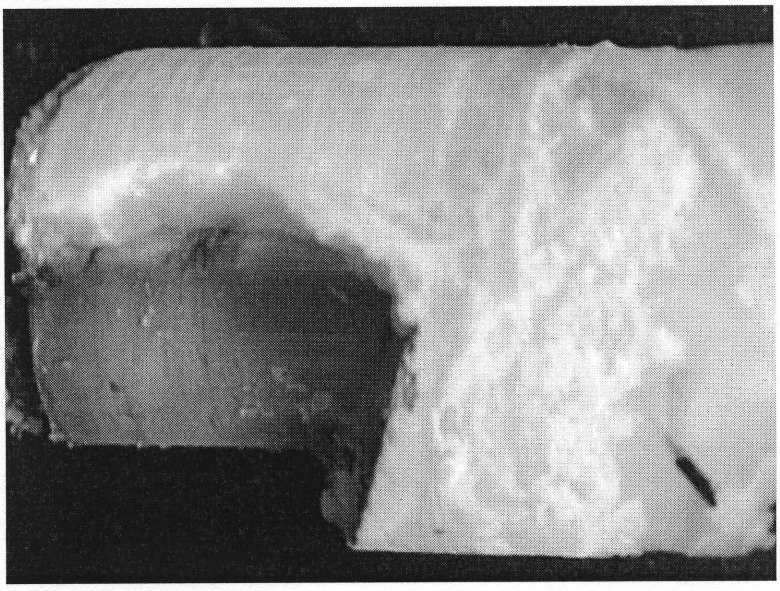

(a)

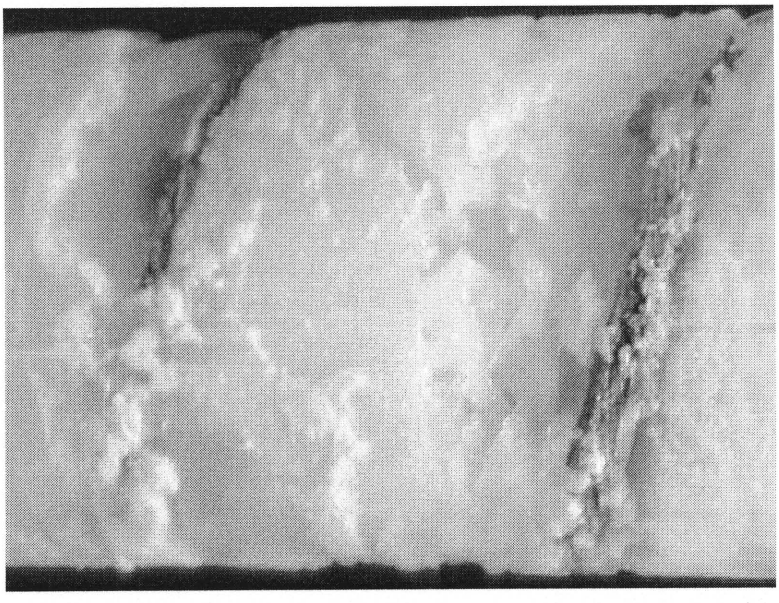

(b)

Figure F.11 Pictures show bottom and middle ice nucleation zones of the evaporator for single side cooling schema (liquid nitrogen is a cooling media, flow rate ~ 0.354 m^3/min) and WFR=200 ml/min.

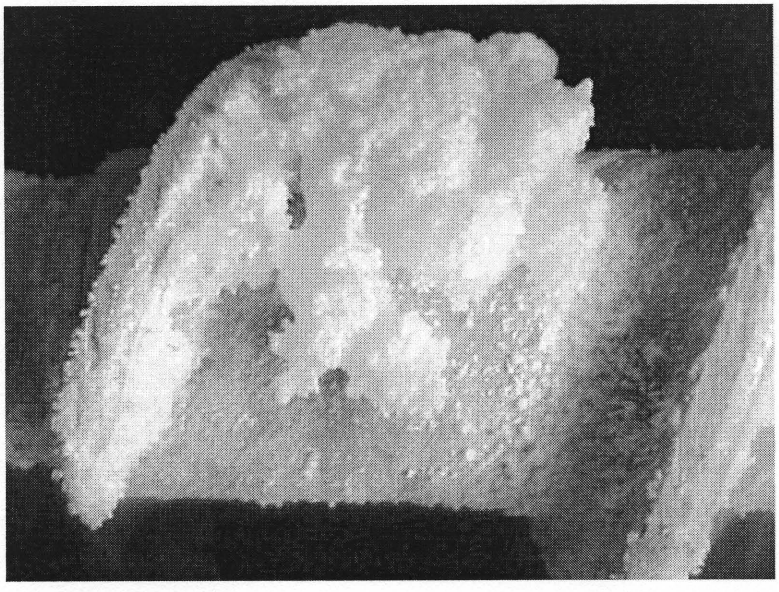

(a)

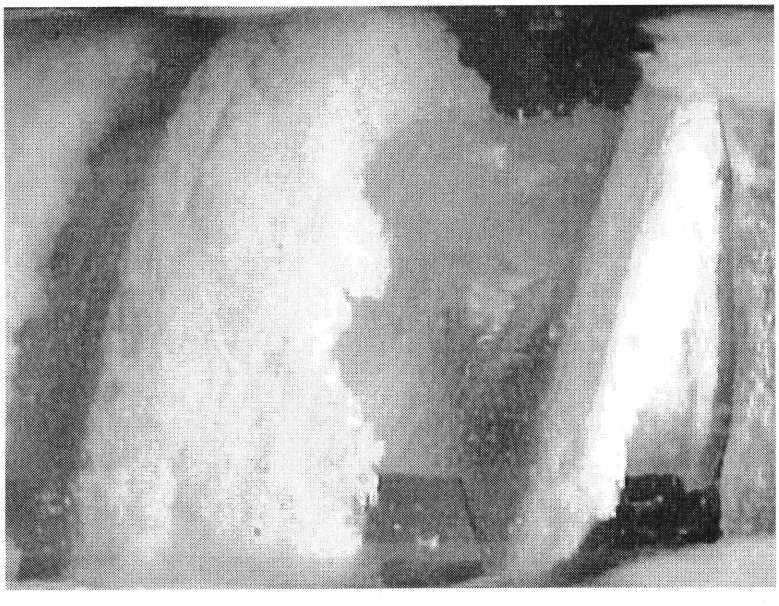

(b)

Figure F.12 Pictures show bottom and middle ice nucleation zones of the evaporator for dual side cooling schema (liquid nitrogen is a cooling media, flow rate ~ 0.354 m^3/min) and WFR=50 ml/min.

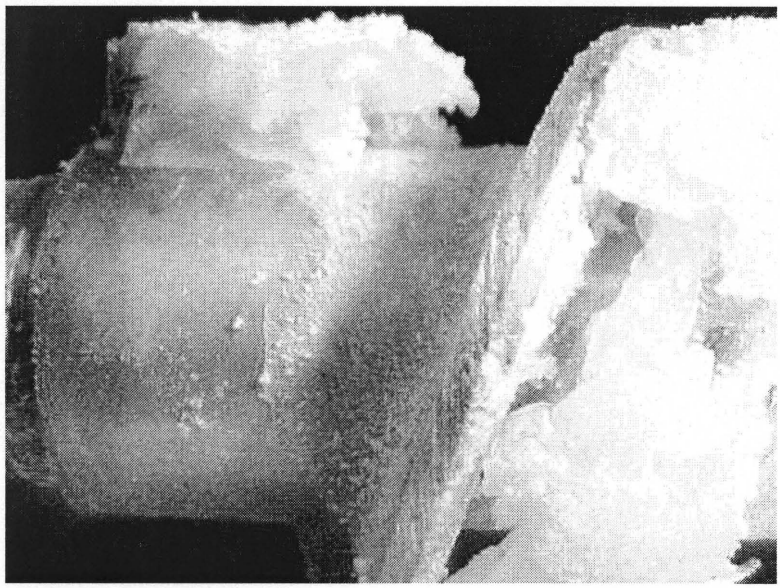

(a)

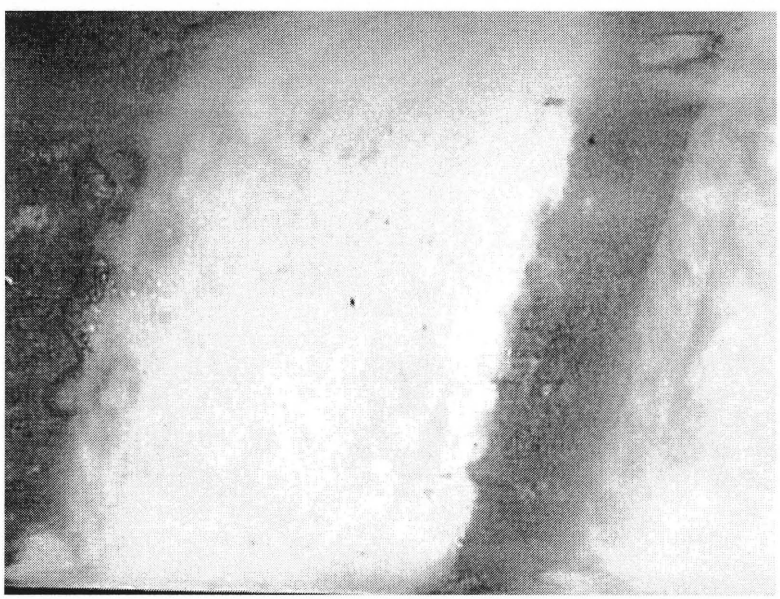

(b)

Figure F.13 Pictures show bottom and middle ice nucleation zones of the evaporator for dual side cooling schema (liquid nitrogen is a cooling media, flow rate ~ 0.354 m^3/min) and WFR=100 ml/min.

(a)

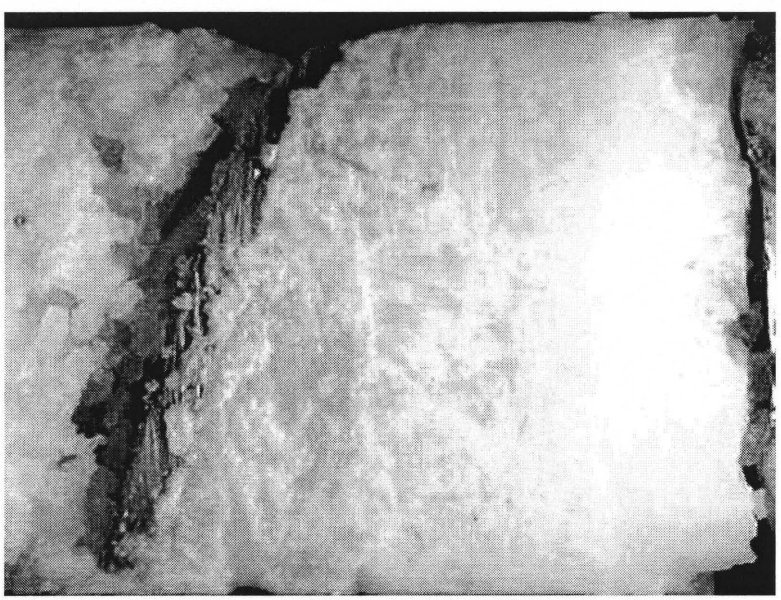

(b)

Figure F.14 Pictures show bottom and middle ice nucleation zones of the evaporator for dual side cooling schema (liquid nitrogen is a cooling media, flow rate ~ 0.354 m^3/min) and WFR=150 ml/min.

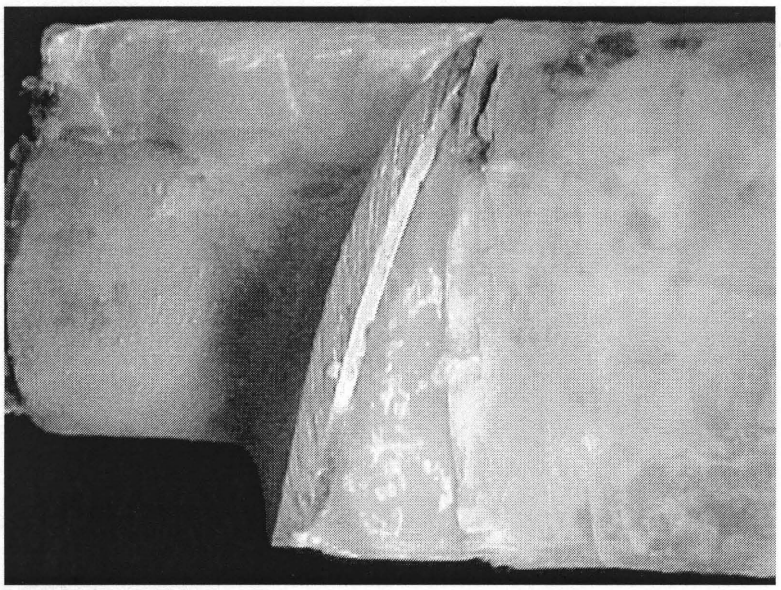

(a)

(b)

Figure F.15 Pictures show bottom and middle ice nucleation zones of the evaporator for dual side cooling schema (liquid nitrogen is a cooling media, flow rate ~ 0.354 m^3/min) and WFR=200 ml/min.

BIBLIOGRAPHY

Adapa S., Schmidt K., Jeon I., Herald T., Flores R., Mechanisms of ice crystallization and recrystallization in ice cream: a review, *Food Review International*, 16(3), 259-271, 2000.

Ahmad N., Thermal conductivity of ice, *Physics Status Solidi*, 181(1), 37-44, 1994.

Anisimov M. A., Tankaev R. U., Bogdanovich N. N., Vol'nitskaya E. P., Dmitrievskii S. A., Melting of ice in a porous medium, *Izvestia Vysshih Uchebnyh Zavedeniy*, Neft Gaz., 27(10), 83-8, 1984.

Ashby M. F., Hallam S. D., The failure of the brittle solids containing small cracks under compressive stress-states, *Acta Mettalurgica*, 34 (3), 497-510, 1986.

Babets K., Geskin E., "Optimization of Energy Utilization in the Course of Material Processing", *International Symposium on Advanced Thermodynamics and Energy Utilization*, University of Trente, Holland, August 2000.

Babets, K., Geskin, E., "Application of Fuzzy Logic for Modeling of the Waterjet Paint Stripping ", *An International Journal of Machining Science and Technology*, Volume 4, # 1, pp. 81-101, May 2000.

Batto R. A., Schulson E. M., On the ductile-to-brittle transition in ice under compression, *Acta Metallurgical Material*, 41(7), 2219-25,1993.

Bertolini D., Cassettari M., Salvetti G., Nucleation process and solidification rate of supercooled water, *Physical Script*, 38(3), 404-7, 1988.

Bilgram J., Guettinger H., Dynamical processes at the ice-water interface during solidification, *Journal of Glaciology*, 21(85), 537-45, 1978.

Bilgram J. H., Guettinger H., Kaenzig W., Fluctuations of the ice-water interface during solidification, *Physical Review Lett.*, 40(21), 1394-7, 1978.

Brill F., Sanitary ice making and dispensing apparatus, US Patent *6,334,328*, January 2000.

Byczynski D., Krumbiegel K., Pierskalla C., Reed W., Schlosser C., Ziminski J., Domestic clear ice maker, US Patent *6,148,621*, November 2000.

Cole D. M., Effect of grain size on the internal fracturing of polycrystalline ice, *CRREL Report No. 86-5*, 1986.

BIBLIOGRAPHY
(Continued)

Dolezal D., Apparatus and method for making ice, US Patent *6,145,324,* November 2000.

Donovan, P. J., Arakawa M., Petrenko V., Crack propagation in freshwater and saline ice, *Material Society Symposium Procedings*, 578 (Multiscale Phenomena in Materials-Experiments and Modeling), 321-326, 2000.

Ethington T., Pannhoff D., Huang M.,Lu Q., Low profile ice maker, US Patent *6,233,964,* May 2001.

Fletcher N.H., *The Chemical Physics of Ice*, Cambridge University Press, Cambridge, 1970.

Fujimoto T., Kawata A., Watanabe S., Otani Y., Apparatus for separation of ice/water and concentrated solutions using dynamic ice making, and ice slurry transport system, *Japan Kokai Tokyo Koho*, 5 pp, 1998.

Fukusako S., Recent advances in study of water-freezing and ice-melting problems, *Nippon Reito Kyokai Ronbunshu*, 7(1), 1-32, 1990.

Geskin E., Tismenetskiy L., Bakhromi E., F. Li, Investigation of Ice Jet Machining, *Proceedings of International Symposium on Electric Machining*, pp. 833-890, Lausanne, Switzerland, 1995.

Geskin E., Tismenetskiy L., Bakhromi E., Li F., Investigation of Icejet Machining, *Proceedings of 1995 NSF Design and Manufacturing Grantees Conference*, San Diego, 1995.

Geskin E., Tismenetskiy L., Li F., Investigation of Icejet Machining, *Proceedings of 1996 NSF Design and Manufacturing Grantees Conference*, Albuquerque, France, 1996.

Geskin E., Tismenetskiy L., Li F., Shishkin D., Investigation of Icejet Machining, *Proceedings of 1997 NSF Design and Manufacturing Grantees Conference*, Seattle, 1997.

Geskin E., Tismenetskiy L., Li F., Meng P., Shishkin D., Investigation of Icejet Machining, *Proceedings of 9th American Waterjet Conference*, Houston, TX, pp. 281-290, August 1997.

Geskin E., Shishkin D., Babets K., *Ice, Cryogenic and Polymer Added Jets* ", Chapter in the Book, *"Abrasive Water Jet, a View on Future"*, published by Institute for Industrial Technologies and Automation, June 1999.

BIBLIOGRAPHY
(Continued)

Geskin E., Shishkin D., Babets K., Investigation of Ice Jet Machining, *Proceedings of 1999 NSF Design and Manufacturing Grantees Conference*, Long Beach, January 1999.

GeskinE., Goldenberg B., Shishkin D., K. Babets K., "Ice Based Surface Decontamination," *Proceedings of Fourth DOE International Decommissioning Symposium,* Knoxville, TN, June 2000.

Geskin E., Goldenberg B., Shishkin D., Babets K., Petrenko O., "Water Based Machining Technology", *6th Annual Exhibition of The Coalition for National Science Funding*, Rayburn House Office Building, Washington, DC, May 2000.

Geskin,E.S. .Shishkin, D.V. Babets, E.K.," Ice, Cryogenic and Polymer Added Jets," Chapter in the book *"Abrasive Waterjet, A View on Future"*, Italian Institute of for Industrial Automation and Technology, Milan 1999.

Glushchenkov O., Petrenko V., Crack velocity measurements in sea ice, *Material Society Symposium Proceding,* 362 (Grain Size and Mechanical Properties-Fundamentals and Applications), 85-90, 1995.

Gold L. W., Dependence of crack formation on crystallographic orientation for ice. *Canadian Journal of Phys*ics , 44(11), 2757-64, 1996.

Handa Y. P., Zakrzewski M., Fairbridge C., Effect of restricted geometries on the structure and thermodynamic properties of ice, *Journal of Physical Chemistry*, 96(21), 8594-9, 1992.

Harima I., Ice Blasting Device and Manufacture of Ice Blasting Ice Grain, *Japanese Patent 04360766 A*, 1992.

Herb B., Visaisouk S., Ice Blast Technology for Precision Cleaning, in Precision Cleaning, *Witter Publishing Company*, Anaheim CA, pp. 172-179, 1996.

Hill G., Van Vlack B., Dent D., Misekow N., McDermott D., Stout R., Brown H., Ice maker, US Patent *5,992,167,* November 1999.

Hillig W.B., Kinetics of freezing of ice in the direction perpendicular to the basal plane. Growth Perfection Crystals, *Proceeding International Conference*, Cooperstown, N.Y., 350-60, 1958.

Hirata T., Ice crystal formation and desorption on cooled surface, Dennetsu, 38(152), 1999.

BIBLIOGRAPHY
(Continued)

Hobbs P.V., *Ice Physics*, Clarendon Press. Oxford, 1974.

Hoshizaki America, Manual. Inc.-Peachtree City, GA. 1998.

Huffman J., Petersen R., Henning M., Stettes G., Newkirk F., Apparatus and method for making and dispensing ice, US Patent *6,301,908,* October 2001.

Inaba H., Takeya K., Behavior of spherical ice particle in flowing supercooled water, *Nippon Kikai Gakkai Ronbunshu*, 60(580), 4151-8, 1994.

James W., Solidification kinetics of ice determined by the thermal-wave technique. *Journal of Physical Chemistry*, No. 1, 767-73, 1967.

Kamb B., Crystallography of Ice, *Physics and Chemistry of Ice*, Royal Society of Canada, Ottawa, 1973.

Kanno et al., Cleaning Device Using Fine Frozen Particles, US Patent *5,074,083*, 1991.

Kato S., Yamada H., Sakai T., Steward D., Flow-down ice maker, US Patent *6,112,533,* September 2000.

Kvajic G., Brajovic V., Anisotropy of growth of polycrystalline ice in constitutionally supercooled water, *Canadian Journal of Physics*, 49(14), 1861-4, 1971.

Lavrov V. V., Scale effects as indications of ice breaking mechanism, *Studies in Ice Physics and Ice Engineering*, 1973.

Li F., Geskin E., Tismenetskiy L., "Development of Icejet Machining Technology", *Proceedings of 8th American Water Jet Conference*, Houston, Texas, pp. 671-680, 1995.

Li F., Geskin E., Tismenetskiy L., "Development of Icejet Machining Technology", *Proceeding of XIII International Symposium on Waterjet Technology*, BHRA, Sardinia, Spain, pp. 725-734, 1996.

Liu B., et al, Research on the Preparation of the Ice Jet and its Cleaning Parameters, Jetting Technology, Ed. H. Louis, *Professional Engineering Publishing*, Ltd, London, UK, pp. 203-211, 1998.

Mantis H. T., Review of the properties of snow and ice, *SIPRE Rep.*, 1951.

Mesher T., Fluidized Stream Acceleration And Pressurizer Apparatus, US Patent *5,607,478*, 1997.

BIBLIOGRAPHY
(Continued)

Michael, B., *Ice Mechanics*, LES PRESSES DE L'UNIVERSITY OF LAVAL, Quebeq, 1978.

Miksch E., Solidification of ice dendrites in flowing supercooled water, *Transition of AIME*, 245(9), 2069-72, 1969.

Mochizuki K., Fujimoto T., Suda F., Supercooling solidification of aqueous binary solutions - fractal dimension of the dendritic ice, *Journal of Advanced Science*, 11(2), 111-112,1999.

Myers T. G., Hammond D. W., Ice and water film growth from incoming supercooled droplets, *International Journal of Heat Mass Transfer*, 42(12), 2233-2242, 1999.

Nakamura Y., Koshikawa N., Masaki M., Furukawa Y., Tomobe T., Kawasaki K., Kiguchiya S., Control of crystal growth direction of ice and apparatus for crystal growth of ice, *Japan Kokai Tokyo Koho*, 6 pp, 2000.

Neman-Nasser S., Horii H., Computation of induced non-planar crack extension with application to splitting, exfoliation and rock burst, Journal of Physical Research, 87, 6805-6821, 1982.

Niechcial R., Ice blasting cleaning system and method, US Patent *5,910,042,* June 1999.

Osman D., Buisine B., Thery B., Measure of Air Flow Rate According to the Mixing Chamber Design, In Jetting Technology-Applications and Opportunity, *BHR Group publication 21*, Sardinia, pp. 223-237, 1996.

Park Y., Enoki M., Numerical analysis approach for the crack propagation in ductile/brittle layered materials, *Nippon Kinzoku Gakkaishi*, 65(11), 1002-1007, 2001.

Paterson W. S. B., The Physics of Glaciers, Pergamon Press, *Journal of Glaciology*, published by the International Glaciological Society, Cambridge, 1981.

Petrenko V., Gluschenkov O., Crack velocities in freshwater and saline ice, Journal of Geophysical Res., [Solid Earth], 101(B5), 11,541-11,551, 1996.

Sakashita S., Ice making apparatus for freeze concentration, *Japan. Kokai Tokyo Koho*, 6 pp., 1999.

Sanderson T.J., *Ice Mechanics: risks to offshore structures*, Graham & Trotman, London, UK 1988.

BIBLIOGRAPHY
(Continued)

Schlosser C., Mueller L., McDougal G., Ice making machine, US Patent *5,752,393* , May 1998.

Schulson E. M., Hoxie S. G., Nixon W. A., The tensile strength of cracked ice, Philosophy Magazine, 59(2), 303-11, 1989.

Settles G., Supersonic Abrasive Ice blasting Apparatus, US Patent *5,785,581*, 1998.

Shapiro A., Tiemann J., Edelstein; William A., Methods and apparatus for detecting ice readiness, US Patent *6,311,503*, November 2001.

Shinichi H., Surface Cleaning Method and Device, *Japanese Patent 09225830 A*, 1997.

Shishkin D., Geskin E., Babets K., Application of Ice Particles for Precision Cleaning of Sensitive Surfaces, *International Symposium On Surface Contamination and Cleaning*, Newark, NJ, May 2001.

Shishkin D., Geskin E., Goldenberg B., Development of a Technology for Fabrication of Ice Abrasives, *International Symposium On Surface Contamination and Cleaning*, Newark, NJ, May 2001.

Shishkin D., Geskin E., Goldenberg B., A Practical Application of Ice Jet Technology, *Cleaner Times*, August 2001.

Shihskin D., Geskin E., Goldenberg B., "Application of Ice Particles for Precision Cleaning of Sensitive Surfaces", *ASME Transaction, Journal of Electronic Packaging Magazine*, 2002.

Shishkin D., Geskin E., Goldenberg B., "Development Technology for Fabrication of Ice Abrasives" *Proceedings of 14 American Waterjet Technology Conference*, Minneapolis, MN, August 2001.

Skupien D., Heat exchanging device, US Patent *5,857,515,* January 1999.

Sorour M. M., Hassab M. A., Madi M. B., Kandil F. T., Formation and melting of a vertical ice slab in an enclosure, *International Journal of Heat Mass Transfer*, 14(2), 167-77, 1987.

Szijcs J., A Method for Cleaning Surfaces, *European Patent 0 509 132 B1*, 1991.

Treadwell P., Ice dispenser, US Patent *6,257,465,* July 2001.

BIBLIOGRAPHY
(Continued)

Tomoji M., A Precision Cleaning Method, *Japanese Patent 04078477*, 1990.

Vaisman S. M., Kozitskii V. I., Milen'kii V. V., Mogil'nyi V. I., Smolenskaya S. B., Modeling of the freezing of ice plugs in a test pipeline, *Khimicheskoye Mashinostroenie*, Kiev, Ukraine, 46, 97-101, 1987.

Vissisouk S., Vixaysouk S., Particles Blasting Using Crystalline Ice, US Patent *5,367,838*, 1994.

Volynets A. Z., Safonov V. K., Fedoseev V. F., Some aspects of the theory of freezing of ice in cylindrical ice generators, *Kholod Tekhnologia*, (5), 37-40, 1978.

Voytkovsiy K. F., The mechanical properties of ice, *Izvestia Akadimii Nauk*, SSSR, 1996.

Wood G., Walton A.G., Homogeneous nucleation kinetics of ice from water, *Journal of Applied Physics*, 41(7), 3027-36, 1970.